Topochemical Reactions of Ruthenium and Rhodium Containing Oxide Phases

---

Lun Jin

Lincoln College

January 2019



A thesis submitted to the

Board of the Faculty of Physical Sciences

in partial fulfilment of the requirements

for the degree of Doctor of Philosophy

Topochemical Reactions of Ruthenium and Rhodium Containing Oxide Phases

This work is focussed on the topochemical reactions of Ru-containing and Rh-containing $n = 1$ Ruddlesden-Popper phases by using CaH_2 as a reducing agent, to form oxide-hydride phases, or finely divided Zr powder as an oxygen getter, to form anion-deficient reduced oxide phases. The chemical doping of $LaSr_3NiRuO_8$ and $LaSr_3NiRuO_4H_4$ is also been investigated.

Building on the work of the first Ru(II)-containing cation-ordered infinite layer phase $LaSrNiRuO_4$ prepared via topochemical reduction of its parent double perovskite $LaSrNiRuO_6$ by using CaH_2 as a reducing agent, the $n = 1$ Ruddlesden-Popper equivalent $LaSr_3NiRuO_8$ was prepared via traditional ceramic synthesis and its topochemical reactions were well-investigated. The initial screening for the reactivity of $LaSr_3NiRuO_8$ was carried out by treating it with CaH_2 in sealed silica ampoules and heated in the temperature range $350 \leq T/\,^{o}C \leq 460$. A number of distinct phases $LaSr_3NiRuO_7$, $LaSr_3NiRuO_6$ and $LaSr_3NiRuO_4H_4$ were observed before non-topochemical decomposition of the starting material occurred. However, it was impossible to isolate the first two reduced oxide phases in this case as the presence of the by-product H_2 gas strongly aided the formation of the oxide-hydride phase. $LaSr_3NiRuO_4H_4$ preserves the highly symmetric structure of its parent $LaSr_3NiRuO_8$ oxide phase, a body-centred tetragonal unit cell, with all oxide ions which originally residing in 'equatorial' anion sites being completely substituted by hydride ions. The measured structural and magnetic data, along with the computational study, are consistent with the presence of transition metal ions in remarkably low oxidation states (Ru^{2+} and Ni^{+}) in an extended solid and show no evidence of long-range magnetic ordering down to a temperature of 1.8 K. Since both $LaSr_3NiRuO_8$ and $LaSr_3NiRuO_4H_4$ are antiferromagnetic insulators, doping chemistry of them was investigated by manipulating the ratio between La and Sr. Structural analysis shows that doped materials are structurally similar to undoped ones, however, magnetic behaviour of doped phases is significantly different from undoped ones. Magnetisation data collected from doped phases suggest that electrons of the B-site cations are no longer localised once the ratio between La and Sr deviates from 1:3.

The successful isolation of the previously mentioned reduced oxide phase, $LaSr_3NiRuO_6$, was achieved by treating $LaSr_3NiRuO_8$ with Zr powder in a getter, as there was no source of H^- ions to form the competing oxide-hydride phase. $LaSr_3NiRuO_6$ adopts a body-centred orthorhombic structure, with ordered oxide vacancies along b-axis. The low temperature neutron powder diffraction data does not show any additional magnetic diffraction features, despite magnetisation data show strong evidence of a ferromagnetic ground state consisting of a d^9, S = ½ Ni^{1+} centre and a d^6, Ru^{2+} centre with two unpaired electrons ($S = 1$).

The topochemical reduction chemistry discussed above can be extended to the Co analogue $LaSr_3CoRuO_8$. Although both the reduced oxide phase $LaSr_3CoRuO_6$ and the oxide-hydride phase $LaSr_3CoRuO_4H_4$ adopt the same crystal structures as their corresponding Ni analogues, statistical and visual fits of refinements are worse in Co cases due to the presence of stacking faults ($n = 2$, 3 and 4 Ruddlesden-Popper phases and separate perovskite blocks) across lattices.

Analogous chemistry was explored for another 4*d* transition-metal, rhodium. Data collected from these samples revealed $La_2Sr_2CoRhO_8$ and $LaSr_3MnRhO_8$ had been converted into the oxide-hydride phases $La_2Sr_2CoRhO_6H_2$ and $LaSr_3MnRhO_6H_2$ respectively, in which 50% of the oxide ions in the 'equatorial' anion sites have been exchanged for hydride anions, converting the –AO–BO_2–AO– stacking sequence of the oxides into an –AO–$B(O_{0.5}H_{0.5})_2$–AO– sequence in the oxide-hydrides, with the oxide and hydride anions adopting a disordered configuration within the $B(O_{0.5}H_{0.5})_2$ sheets.

Declaration

The work described in this thesis was carried out at the Inorganic Chemistry Laboratory at the University of Oxford between October 2015 and December 2018 under the supervision of Professor Michael A. Hayward. All the work presented in this thesis is my own, except where I have either given reference to a published source or acknowledged help from a named person. None of the work has been submitted by the author for any other degree at any other university.

Lun Jin

January 2019

To Mom and Dad, and everyone who ever believed in me.

Acknowledgements

First, I would like to thank my supervisor Professor Michael A. Hayward for offering me the invaluable opportunity to come to Oxford and work with you on this exciting DPhil project. Your dedication into scientific research is truly admirable and has a huge impact on me. Without your guidance, patience, knowledge and care, this work would not have been completed.

I would like to thank the Leverhulme Trust Grant RPG-2014-366 for funding this work. Special thanks to my mom and dad for funding me to study in Oxford and complete my DPhil.

Also, I need to thank all the researchers who contributed to this work: Professor John E. McGrady and Dr. Dihao Zeng for DFT calculations; Professor Stephen J. Blundell for collecting μSR data; Professor Joke Hadermann and Maria Batuk for TEM study; Dr. P. Manuel and Dr. E. Suard for their assistance in collecting the neutron powder diffraction data; the Clarke, Battle and Goodwin groups and the I11 beam scientists at Diamond Light Source for helping to collect the synchrotron X-ray powder diffraction data.

Special thanks to Professor Kageyama and his research group in Kyoto University, for inviting me to come to visit and use high-pressure machines. I really felt welcome and had a good time during my trip in Japan.

Finally, I would like to thank all the members of MAH group that I have worked with over the past few years to make all the science not as tough as expected, specifically Dr. Midori E. Amano Patiño and Dr. Ronghuan Zhang for teaching me all the research and practical skills I ever needed to complete this work and for keeping me accompanied whenever I feel lonely or helpless.

Table of Contents

Topochemical Reactions of Ruthenium and Rhodium Containing Oxide Phases I

Declaration III

Acknowledgements VII

Table of Contents IX

Chapter 1 Introduction 1

1.1 Complex Transition-Metal Oxides 1

1.2 Topochemical Reactions of Complex Transition-Metal Oxides 2

1.2.1 Binary Metal Hydrides 3

1.2.2 Finely Divided Electropositive Metals 8

1.2.3 Flowing H_2 gas 11

1.3 Perovskite Structure and Tolerance Factor 12

1.4 Ruddlesden-Popper Structure 15

1.5 Hydride-for-Oxide Substitution 17

1.6 Basic Band Theory and the Hubbard Model 19

1.7 Electronic Behaviour of Complex Transition-Metal Oxides 22

Chapter 2 Experimental Methods and Techniques 25

2.1 Synthesis of Starting Materials 25

2.1.1 Ceramic Method 25

2.1.2 Citrate Gel Method 25

2.2 Binary Metal Hydride Reductions 26

2.2.1 Sealed Glass Ampoules 27

2.2.2 Venting Apparatus 28

2.2.3 Washing Reaction Mixtures 29

2.3 Zirconium Getter Reductions 30

2.4 Handling Air-sensitive Reactions and Compounds 31

2.4.1 Argon-filled Glove Box 31

2.4.2 Air-sensitive X-ray Powder Diffraction 32

2.5 Powder Diffraction 32
2.5.1 X-ray Powder Diffraction 34
2.5.2 Neutron Powder Diffraction 36
2.6 Rietveld Refinement 41
2.7 Thermogravimetric Analysis (TGA) 42
2.8 Bond Valences Sums 43
2.9 Muon-Spin Relaxation Spectroscopy (μSR) 43
2.10 SQUID Magnetometry 44
2.10.1 Standard Measurements 45
2.10.2 Ferrosubtraction Measurements 45
2.11 Magnetism 46
2.11.1 The Curie-Weiss law 47
2.11.2 Correlated Magnetic Behaviour and Magnetic Ordering 48
2.11.3 Super-exchange and the Goodenough-Kanamori Rules 48
2.12 Transmission Electron Microscopy 50
2.13 FAULTS Analysis 50

Chapter 3 Synthesis and Characterisation of $LaSr_3NiRuO_8$ 53

3.1 Introduction 53
3.2 Experimental 54
3.3 Results 55
3.3.1 Structural Characterisation of $LaSr_3NiRuO_8$ 55
3.3.2 Magnetic Characterisation of $LaSr_3NiRuO_8$ 60
3.4 Discussion 64
3.4.1 Cation Arrangement in $LaSr_3NiRuO_8$ 64
3.4.2 Slow-Cooled and Quenched $LaSr_3NiRuO_8$ Samples 65
3.5 Conclusion 67

Chapter 4 Synthesis and Characterisation of $LaSr_3NiRuO_4H_4$ 69

4.1 Introduction 69
4.2 Experimental 69
4.3 Results 70
4.3.1 Initial investigation of reactivity of $LaSr_3NiRuO_8$ towards CaH_2 70
4.3.2 Structural and Chemical Characterisation of $LaSr_3NiRuO_4H_4$ 75

4.3.3 Magnetic Characterisation of $LaSr_3NiRuO_4H_4$ 81
4.3.4 DFT Calculations of $LaSr_3NiRuO_4H_4$ 83
4.3.5 μ^+SR data of $LaSr_3NiRuO_4H_4$ 85
4.4 Discussion 86
4.4.1 Structural Peculiarity of $LaSr_3NiRuO_4H_4$ 86
4.4.2 Electronic Structure of $LaSr_3NiRuO_4H_4$ 90
4.4.3 Magnetic Characterisation of $LaSr_3NiRuO_4H_4$ 92
4.5 Conclusion 93

Chapter 5 A-Site Doping of $LaSr_3NiRuO_8$ Series 95

5.1 Introduction 95
5.2 Experimental 95
5.2.1 Synthesis of $La_xSr_{4-x}NiRuO_8$ ($0.5 \leq x \leq 1.5$) 95
5.2.2 Synthesis of $La_xSr_{4-x}NiRuO_4H_4$ ($0.5 \leq x \leq 1.5$) 96
5.3 Results 98
5.3.1 Structural Characterisation of $La_xSr_{4-x}NiRuO_8$ ($0.5 \leq x \leq 1.5$) 98
5.3.2 Magnetic Characterisation of $La_xSr_{4-x}NiRuO_8$ ($0.5 \leq x \leq 1.5$) 102
5.3.3 Structural Characterisation of $La_xSr_{4-x}NiRuO_4H_4$ ($0.5 \leq x \leq 1.5$) 107
5.3.4 Magnetic Characterisation of $La_xSr_{4-x}NiRuO_4H_4$ ($0.5 \leq x \leq 1.5$) 110
5.4 Discussion 115
5.4.1 Doping Limits of $La_xSr_{4-x}NiRuO_8$ and $La_xSr_{4-x}NiRuO_4H_4$ ($0.5 \leq x \leq 1.5$) 115
5.4.2 Reaction Pathways of Low-temperature Topochemical Reactions 116
5.4.3 Magnetic Behaviour of $La_xSr_{4-x}NiRuO_8$ and $La_xSr_{4-x}NiRuO_4H_4$ ($0.5 \leq x \leq 1.5$) 118
5.5 Conclusion 119

Chapter 6 Synthesis and Characterisation of $LaSr_3NiRuO_6$ 121

6.1 Introduction 121
6.2 Experimental 121
6.2.1 Reduced Oxide Phases Formed via CaH_2 Reduction 121
6.2.2 Reduced Oxide Phases Formed via Zr Getter Reduction 124
6.2.3 Preparation of the Large-Scale Neutron Sample 127
6.3 Results 128
6.3.1 Thermogravimetric Analysis of $LaSr_3NiRuO_6$ 128
6.3.2 Synchrotron X-Ray Powder Diffraction of $LaSr_3NiRuO_6$ 130

6.3.3 Room Temperature Neutron Powder Diffraction of $LaSr_3NiRuO_6$ 132
6.3.4 Magnetic Characterisation of $LaSr_3NiRuO_6$ 138
6.3.5 Low Temperature Neutron Powder Diffraction of $LaSr_3NiRuO_6$ 141
6.4 Discussion 147
6.4.1 Crystallographic Structure of $LaSr_3NiRuO_6$ 147
6.4.2 Zr Powder Getter versus CaH_2 149
6.4.3 Two-Phase Reduction Behaviour of $LaSr_3NiRuO_6$ 150
6.5 Conclusion 152

Chapter 7 $LaSr_3CoRuO_8$ and Its Topochemical Reductions 153

7.1 Introduction 153
7.2 Experimental 153
7.2.1 Synthesis of $LaSr_3CoRuO_8$ 153
7.2.2 Synthesis of $LaSr_3CoRuO_4H_4$ 154
7.2.3 Synthesis of $LaSr_3CoRuO_6$ 155
7.3 Results 156
7.3.1 Structural Characterisation of $LaSr_3CoRuO_8$ 156
7.3.2 Magnetic Characterisation of $LaSr_3CoRuO_8$ 160
7.3.3 Thermogravimetric Analysis of $LaSr_3CoRuO_6$ 163
7.3.4 Structural Characterisation of $LaSr_3CoRuO_6$ 165
7.3.5 Magnetic Characterisation of $LaSr_3CoRuO_6$ 171
7.3.6 Structural Characterisation of $LaSr_3CoRuO_4H_4$ 174
7.3.7 Magnetic Characterisation of $LaSr_3CoRuO_4H_4$ 192
7.3.8 μ^+SR data of $LaSr_3CoRuO_4H_4$ 194
7.4 Discussion 195
7.4.1 Structural Peculiarity of $LaSr_3CoRuO_xH_y$ Phases 195
7.4.2 Magnetic Characterisation of $LaSr_3CoRuO_xH_y$ Phases 197
7.4.3 Stacking Faults Found in $LaSr_3CoRuO_xH_y$ Phases 198
7.5 Conclusion 199

Chapter 8 Synthesis and Characterisation of Rh-Containing Oxide Phases 201

8.1 Introduction 201

8.2 Experimental 201
8.2.1 Synthesis of $LaSr_3MnRhO_8$ 201
8.2.2 Synthesis of $La_2Sr_2CoRhO_8$ 202
8.3 Results 203
8.3.1 Structural Characterisation of $LaSr_3MnRhO_8$ 203
8.3.2 Structural Characterisation of $La_2Sr_2CoRhO_8$ 208
8.3.3 Magnetic Characterisation of $LaSr_3MnRhO_8$ 213
8.3.4 Magnetic Characterisation of $La_2Sr_2CoRhO_8$ 217
8.4 Discussion 221
8.4.1 Cation Arrangement in Rh-containing n = 1 Ruddlesden-Popper Phases 221
8.4.2 Valence Transitions in Rh-containing n = 1 Ruddlesden-Popper Phases 222
8.5 Conclusion 224

Chapter 9 Synthesis and Characterisation of Rh-Containing Oxide-Hydride Phases 225

9.1 Introduction 225
9.2 Experimental 225
9.3 Results 228
9.3.1 Thermogravimetric Analysis of $LaSr_3MnRhO_6H_2$ and $La_2Sr_2CoRhO_6H_2$ 228
9.3.2 Structural Characterisation of $LaSr_3MnRhO_6H_2$ 230
9.3.3 Structural Characterisation of $La_2Sr_2CoRhO_6H_2$ 237
9.3.4 Magnetic Characterisation of $LaSr_3MnRhO_6H_2$ 243
9.3.5 Magnetic Characterisation of $La_2Sr_2CoRhO_6H_2$ 245
9.4 Discussion 248
9.4.1 The Role of Rhodium in Stabilizing Oxide-hydride Phases 248
9.4.2 The Anion-disorder in Rh-containing Oxide-hydride Phases 249
9.5 Conclusion 251

Chapter 10 Conclusions 253

Appendix 1 Table of Figures 257

Appendix 2 Additional Data for Chapter 5 265

Appendix 2.1 Synchrotron X-ray diffraction data of $La_xSr_{4-x}NiRuO_8$ ($0.5 \leq x \leq 1.5$) 265
Appendix 2.2 Magnetisation data of $La_xSr_{4-x}NiRuO_8$ ($0.5 \leq x \leq 1.5$) 270
Appendix 2.3 Synchrotron X-ray diffraction data of $La_xSr_{4-x}NiRuO_4H_4$ ($0.5 \leq x \leq 1.5$) ... 275
Appendix 2.4 Magnetisation data of $La_xSr_{4-x}NiRuO_4H_4$ ($0.5 \leq x \leq 1.5$) 280

Appendix 3 Bibliography 285

Chapter 1

Introduction

1.1 Complex Transition-Metal Oxides

Transition metal compounds have been of great and enduring interest to scientists in a wide range of disciplines, because of the ability of transition metals to adopt stable oxidation states with unpaired electrons in partially filled d-orbitals, which interact strongly with the ligands chemically bound to the metal. In case of solid-state oxides, transition metals are organized into regular arrays, whose unpaired d-electrons on neighbouring centres can couple with each other either via direct exchange mechanisms, or via superexchange interactions involving the valence orbitals of the bridging ligands like the oxygen 2*p* orbitals or hydrogen 1*s* orbitals, giving rise to the wide range of interesting physical and chemical properties, including magnetoresistance, high-temperature superconductivity, collective magnetism, ferroelectricity, unusual catalytic and photocatalytic behaviour.[1-5] These lead to a variety of applications of complex transition-metal oxides in areas such as catalysis, energy storage and information processing.[6-8] The synthesis of complex oxides has therefore been the subject of extensive study.

Traditional solid-state synthesis methods usually require high temperatures ($T \geq 1000$ °C) to overcome large energetic barriers of the diffusion of ions in solids. Therefore only the most thermodynamically stable phases can be produced by this method. As a result, only the limited repertoire of metal oxidation states and coordinated geometries which are most stable can be incorporated into complex transition-metal oxides.

1.2 Topochemical Reactions of Complex Transition-Metal Oxides

In order to widen the range of complex transition-metal oxides that can be prepared, synthetic routes which have access to kinetic controlled phases could be adopted, and hence result in the formation of metastable phases with novel metal oxidation states and coordination geometries. The product of topochemical reaction is the phase that is kinetically favoured rather than the one which is most thermodynamically stable. For kinetic control to be exerted, differential chemical reactivity must exist in a chemical system, i.e. in case of solid-state oxides, different ions within a lattice have different rates of diffusion.

Conventionally the electronic behaviour of complex oxides is modified by cation substitution, for example aliovalent cation substitution can be used to modify transition-metal oxidation states. However it is also possible to tune the physical and chemical properties of extended solid oxides by modifying the anion lattice, either by introducing anion vacancies, or by substituting or inserting non-oxide heteroanions such as hydride ions, nitride ions or halide ions.[9-16] Therefore low temperature synthetic routes allow the preparation of a large number of new, kinetically stabilized phases which are unattainable via high temperature routes.[17]

Typically, solid state binary metal hydrides, finely divided electropositive metals and flowing H_2 gas are the most common reagents used to reductively modify the anion lattice of the complex transition-metal oxides. In this work, binary metal hydrides such as CaH_2, and finely divided electropositive metals like zirconium are used to modify the anion lattice of parent complex transition-metal oxides to form oxide-hydride phases and reduced oxide phases respectively. The choice of the reducing agent depends on the nature of target reduced phases and the reaction temperature regime that optimizes the anion mobility inside a lattice with conservation of the cation framework.

1.2.1 Binary Metal Hydrides

Binary metal hydrides such as NaH, LiH and CaH_2 have already been widely employed in topochemical reductions of complex transition-metal oxides according to following reactions [1], [2] and [3]:

$$ABO_4 + x\text{NaH} \longrightarrow ABO_{4-x} + x\text{NaOH} \quad [1]$$

$$ABO_4 + 2x\text{LiH} \longrightarrow ABO_{4-x} + x\text{Li}_2\text{O} + x\text{H}_2 \quad [2]$$

$$ABO_4 + x\text{CaH}_2 \longrightarrow ABO_{4-x} + x\text{CaO} + x\text{H}_2 \quad [3]$$

Previous work has focused on the topochemical reductions of complex transition-metal oxides which lead to the preparation of extended phases containing 3*d* transition metals such as square planar Ni^+, Co^+, Mn^+ and Fe^{2+}.[15, 18-22] Some 4*d* and 5*d* transition metals like Ru, Rh and Ir have participated as well, however it appears that the topochemical reductions of complex oxides containing only 4*d* and 5*d* transition metals tend to decompose to binary oxides and metal elements unless the structure is stabilized by 3*d* transition metals.[11, 23]

1.2.1.1 Sodium Hydride

NaH is an effective solid-state reducing agent in the low-temperature regime (150 °C to 250 °C) which is essential for topochemical reductions of some fragile complex transition-metal oxides. For example, the topochemical reduction of perovskite phase $LaNiO_3$ via zirconium getter at 400 °C results in the formation of $La_2Ni_2O_5$ which only reduces the Ni centres from 3^+ to 2^+.[24] Further reduction of Ni centres to 1^+ requires a higher reaction temperature to drive the equilibrium to a more anion-deficient phase, however this leads to sample decomposition to La_2O_3 and elemental nickel. By using NaH as a solid-state reducing

agent which is in close physical contact with the parent perovskite phase $LaNiO_3$, the highly metastable reduced phase $LaNiO_2$ can be prepared by heating at 190 °C. This phase adopts an infinite layer structure consisting of sheets of corner-sharing $Ni(I)O_4$ square planes stacked in an alternating sequence with sheets of La^{3+} cations remained in A-sites (Figure 1.1). The deintercalation of oxide ions from the lattice necessarily involves the reduction of transition metal centres Ni (3^+ to 1^+) to maintain the charge neutrality of the system. NaOH is observed as the by-product of this reduction which can be readily removed by dissolving in a weak acid like methanol.[18]

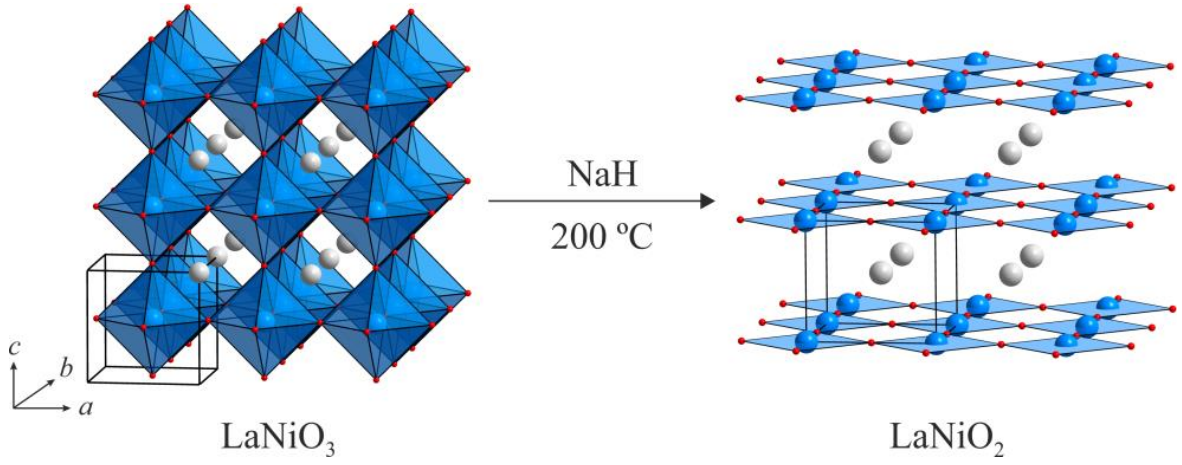


Figure 1.1. Topochemical reduction of $LaNiO_3$ with NaH to form the reduced oxide phase $LaNiO_2$ containing Ni^+ in square planes.[18]

1.2.1.2 Lithium Hydride

The low decomposition temperature of NaH with respect to Na and H_2, places an upper limit on the possible reaction temperatures at which this reagent can be used ($T \leq 250$ °C). Some systems are found to require higher reaction temperatures to facilitate oxygen diffusion. One of the candidate solid-state reducing agents functioning at higher temperature

regimes is LiH (250 °C to 600 °C). For example, the square planar Fe^{2+} centres found in the reduced oxide-halide phase $Sr_3Fe_2O_4Cl_2$ are formed by mixing its parent oxide-chloride phase $Sr_3Fe_2O_5Cl_2$ with an excess of LiH and heating in sealed Pyrex ampoules. The deintercalation of oxide ions is selective as it only introduces anion vacancies to the SrO layer of the parent oxide-chloride phase, hence the resulting reduced phase consists infinite sheets of corner-sharing Fe(II)O_4 square planes (Figure 1.2).[22] The by-products of this reaction are Li_2O, which can be readily removed by dissolving into a weak acid such as methanol, and H_2 gas which accumulates inside the reaction vessel and can potentially allow the preparation of oxide-hydride phases. However, there is always a concern that Li^+ ions might be inserted into the lattice during topochemical reactions which is very hard to detect by X-ray powder diffraction as has been observed in other phases[25, 26], so LiH reactions must be treated with cautious.

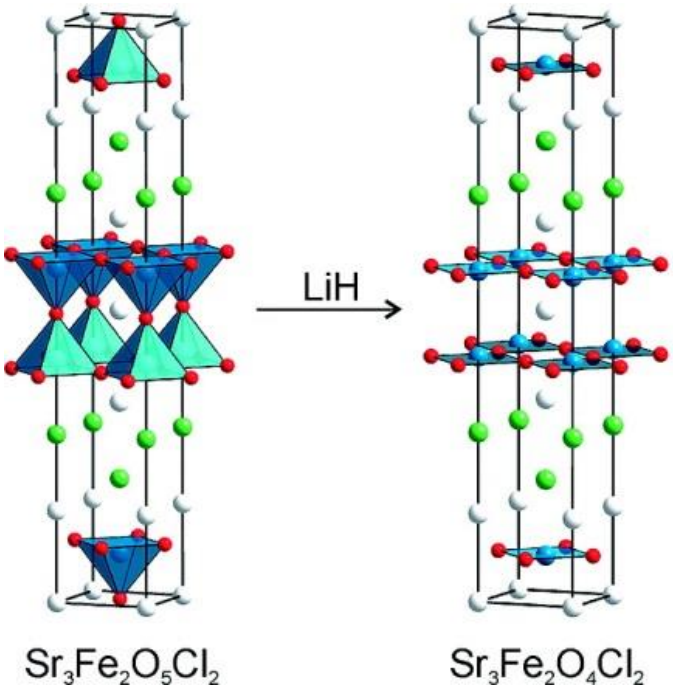


Figure 1.2. Topochemical reduction of $Sr_3Fe_2O_5Cl_2$ with LiH to form the reduced oxide-halide phase $Sr_3Fe_2O_4Cl_2$ containing square planar Fe^{2+}.[22]

1.2.1.3 Calcium Hydride

Another strong candidate for a solid-state reducing agent functioning at higher temperatures (250 °C to 600 °C) is CaH_2. Deintercalations of oxide ions are attainable via topochemical reductions of complex transition-metal oxides by using CaH_2 as a reducing agent. For example, some ruthenium containing complex oxides stabilized by 3d transition metals like iron and nickel have been successfully reduced to prepare Ru^{2+} metal centres in extended solid oxides by treating their parent perovskites with CaH_2 in the venting apparatus as mentioned in Chapter 2 Section 2.2.2, to prevent the accumulation of the by-product H_2 gas inside the reaction vessel[10, 11] by purging the system with an inert atmosphere like Ar (Figure 1.3). ABO_3 simple perovskites, $A_2B_2O_6$ double perovskites and A_2BO_4 n = 1 Ruddlesden-Popper phases all show the potential to be the starting materials in this topochemical reduction process.

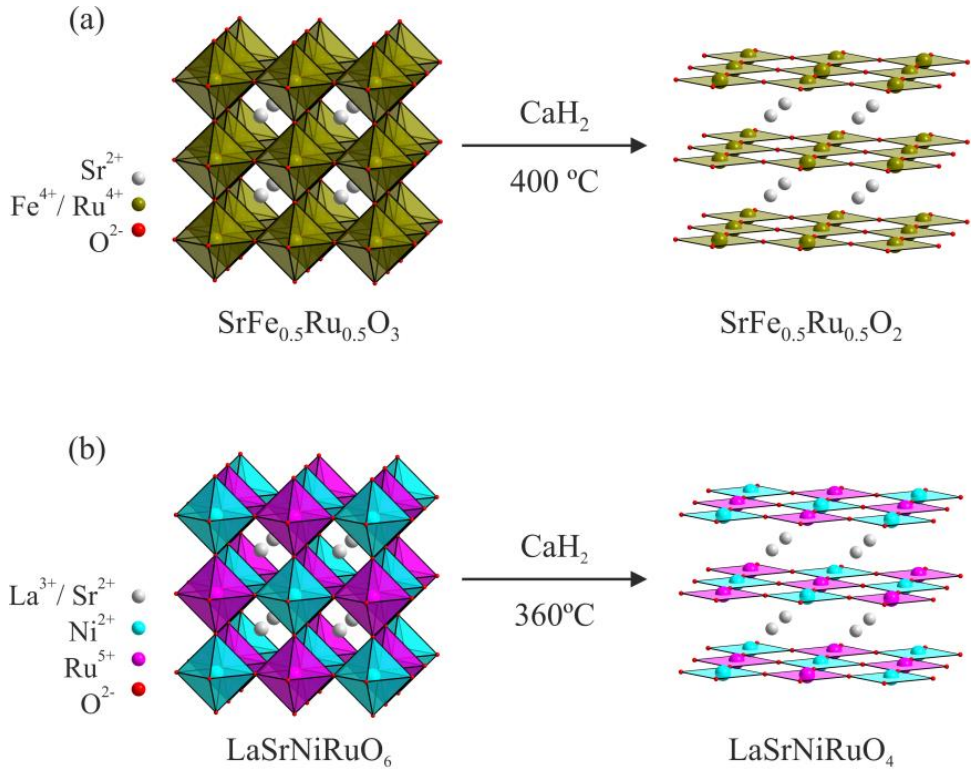


Figure 1.3. The reduction of (a) $SrFe_{0.5}Ru_{0.5}O_3$ and (b) $LaSrNiRuO_6$ via topochemical anion deintercalation using CaH_2.[10, 11]

In addition to the anion deintercalation reactions, due to the accumulation of H_2 gas as a by-product during reactions if the mixtures are sealed under vacuum within Pyrex or silica ampoules, the formation of oxide-hydride phases could be favoured as a result of anion exchange process in some cases like $LaSrCoO_3H_{0.7}$[15], $SrVO_2H$[14] (Figure 1.4) and $LaSr_3NiRuO_4H_4$[13] (Figure 1.5). Hydride-for-oxide substitution shows great potential in modifying properties of solid-state materials as discussed in Chapter 1 Section 1.5 and therefore it is one of the main focuses in my study. The anion-ordered oxide-hydride phase $LaSr_3NiRuO_4H_4$ prepared by reducing its parent oxide phase $LaSr_3NiRuO_8$ with an excess of CaH_2 has been described in details in Chapter 4.

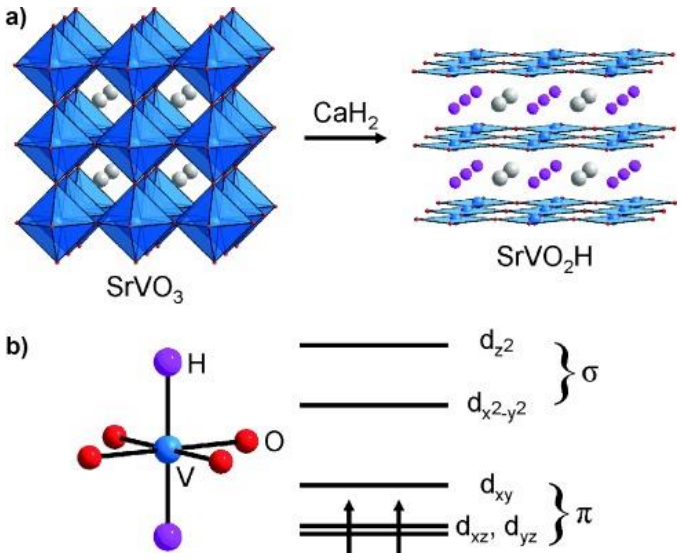


Figure 1.4. Topochemical reduction of $SrVO_3$ with CaH_2 to form the reduced oxide-hydride phase $SrVO_2H$ with H^- substituted into axial positions [14].

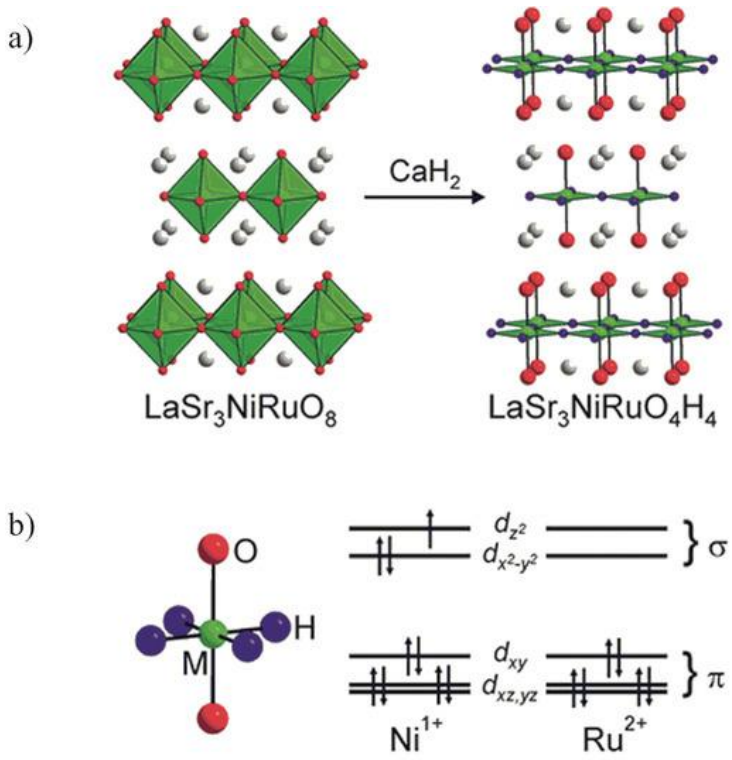


Figure 1.5. Topochemical reduction of $LaSr_3NiRuO_8$ with CaH_2 to form reduced oxide-hydride phase $LaSr_3NiRuO_4H_4$ with H^- substituted into equatorial positions [13].

1.2.2 Finely Divided Electropositive Metals

An alternative reduction method widely applied to complex transition-metal oxides utilizes finely divided electropositive metals as oxygen getters. When the anions in the lattice have appreciable mobility by heating the sample at suitable temperature, the oxygen content of a complex transition-metal oxide is in equilibrium with the partial pressure of O_2 in contact with the surface of the sample, according to reaction [4]:

$$MO_n \longleftrightarrow MO_{n-2x} + xO_2 \qquad [4]$$

In order to drive the equilibrium to the reduced phase, the reaction temperature needs to rise to favour the entropy change on reduction, but not to a point where the complex transition-metal oxides cannot afford it, i.e. the lattice starts to decompose. Alternatively, the equilibrium can be driven to the reduced phase by artificially lowering the oxygen partial pressure in the system, either by pumping the oxygen away or purging with an inert atmosphere, or using highly electropositive metals which will react rapidly with the partial pressure of oxygen above their surfaces to form variety of stable metal oxides as the by-products of the reactions.

The oxygen removed from the complex transition-metal oxide passes through the gas phase, hence the substrate oxide phase and the metal getter need to be in close proximity but not in contact with each other. Therefore this kind of set-up prevents the contamination of resulting reduced phase from by-products and unreacted metals and protects the sample from further purification techniques. In addition, as a result of the physically separated substrate oxide and metal getter, they can be heated to different temperatures. In other words, the metal getter can be heated to higher temperatures to facilitate faster oxygen consumption without heating the substrate transition-metal oxide to the same temperature.

For example, finely divided zirconium powder is a strong candidate to be used as a metal getter in topochemical reduction of perovskite $LaCoO_3$ as it can react rapidly with oxygen above the metal surface to 'getter' oxygen away from the system and thus drives the equilibrium towards reduced phase $LaCoO_{2.5}$ containing Co(II) metal centres according to the reaction [5]:

$$LaCoO_3 \longleftrightarrow LaCoO_{3-2x} + xO_2 + Zr \longleftrightarrow LaCoO_{2.5} + ZrO_y \quad [5]$$

The reduced phase $La_2Co_2O_5$ adopts the brownmillerite structure which is quite common for anion-deficient variants of the perovskite structure, consisting sheets of $Co(II)O_6$ octahedra stacked in an alternating sequence with sheets of $Co(II)O_4$ tetrahedra as shown in Figure 1.6.[27]

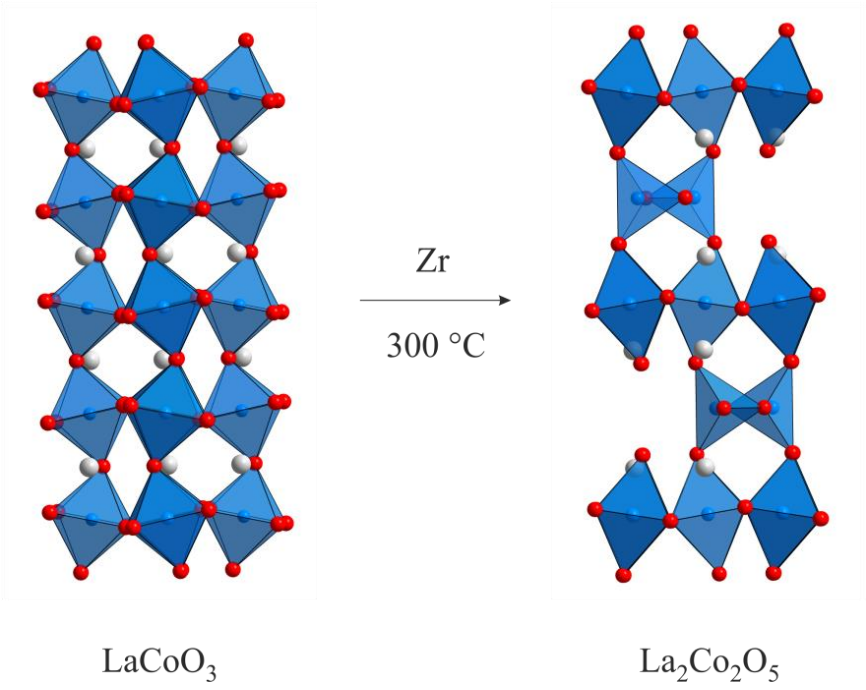


Figure 1.6. Topochemical reduction of $LaCoO_3$ with Zr getter to form the anion-deficient perovskite $La_2Co_2O_5$.[27]

There is another example of topochemical reductions of complex transition-metal oxides using aluminium as the oxygen getter, reported in Moriga *et al.*[28]. A range of oxygen-deficient phases $LaNiO_{3-x}$ ($0 \leq x \leq 0.5$) can be formed by treating their parent perovskite phase $LaNiO_3$ with aluminium metal getter and the oxygen content can be controlled by the reaction temperature or the amount of aluminium metal used. However, since aluminium's melting point is relatively low (660 °C), its reaction temperature window is not as wide as zirconium.

1.2.3 Flowing H_2 gas

Using flowing H_2 gas to reductively deintercalate oxide ions from complex transition-metal oxides, especially those with the cubic perovskite structure or its distorted variants, has been widely studied. A typical example is the topochemical reduction of $CaMnO_3$ by flowing H_2 gas to yield a reduced phase $CaMnO_{2.5}$ with ordered oxide vacancies according to reaction [6]:

$$CaMnO_3 + xH_2 \longleftrightarrow CaMnO_{3-x} + xH_2O \qquad [6]$$

The formation of water vapour as a by-product during the reaction is the driving force and the level of oxide ion deintercalation can be controlled by artificially adjusting the partial pressure of water within the system to synthesize a range of phases with composition $CaMnO_{3-x}$ ($0 \leq x \leq 0.5$).[29] In a reduction, the $Mn(IV)O_6$ octahedra in the parent oxide have been converted $Mn(III)O_5$ square-based pyramids (Figure 1.7), therefore not only the oxidation state of the Mn centre, but also its coordination number have been decreased by this topochemical reduction process.

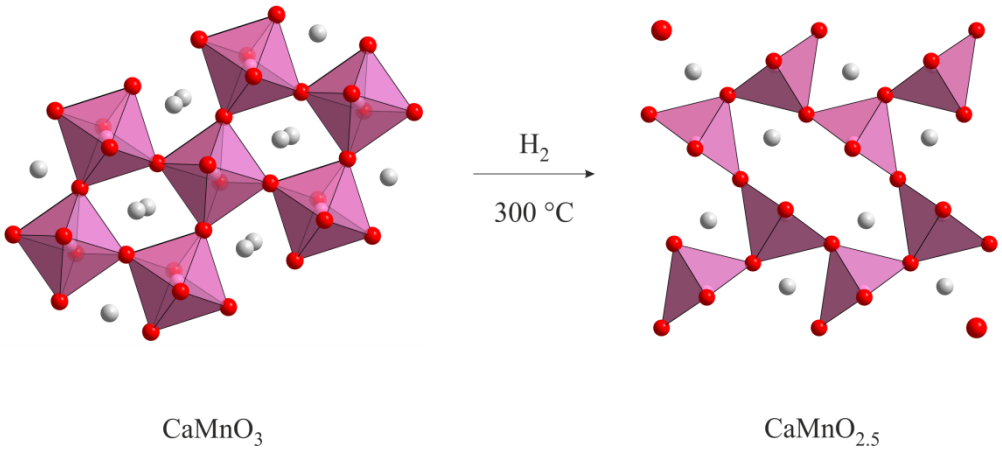


Figure 1.7. Topochemical reduction of $CaMnO_3$ with H_2 gas to form the anion-deficient perovskite $CaMnO_{2.5}$.[29]

Although flowing H_2 gas is the most obvious approach to carry out topochemical reductions of complex transition-metal oxides, and the oxygen content remained in the lattice can be controlled by reaction temperature, reaction time, partial pressure of H_2 above the sample and flow rate, it is not the best way due to the hazardous and practical issues associated with the set-up. Hence, there are too many variables to control which add a lot of uncertainties and difficulties to reproduce the desired reaction environment required by the target reduced phase.

1.3 Perovskite Structure and Tolerance Factor

Complex transition-metal oxides adopting perovskite structure with the general formula ABO_3, where A is an alkali metal, an alkaline earth metal or a lanthanide, and B is a transition metal, have attracted enduring and intensive attention.[30] The structure consists of corner-shared BO_6 octahedra forming a three-dimensional network, with the large A-site cations sitting in 12-fold cuboctahedral cavities.

Perovskites are quite flexible as they can accommodate different combinations of A-site and B-site cations (most of the metallic natural elements of the Periodic Table) [8], with almost no restrictions on their sizes, since the cooperative distortion of BO_6 octahedra will occur to compensate for the size mismatch between A-site and B-site cations if necessary. The 'flexibility' of perovskites can be quantitatively analysed by the Goldschmidt tolerance factor[31]:

$$t = \frac{< A - O >}{\sqrt{2} < B - O >} = \frac{r_A + r_O}{\sqrt{2}(r_B + r_O)}$$

Where $< A - O >$ and $< B - O >$ correspond to the bond lengths between the oxide ions and A/B-site cations and r_A, r_B and r_O are radius of A-cation, B-cation and anion (usually oxygen) respectively.

For an ideal cubic perovskite, the tolerance factor *t* equals to 1 as the size of A cations and B cations are perfectly matched. A typical example of cubic aristotype perovskite structure is $SrTiO_3$[32] as shown in Figure 1.8 (a) with perfectly matched cation sizes (Sr and Ti) to allow all Ti-O-Ti bond angles to be 180°, so the orbital overlap between the 3*d* transition metal orbitals and the 2*p* oxygen orbitals is maximised.

When $t < 1$, the A-site cation is smaller than the ideal size for the 12-fold cuboctahedral cavities created by the relevant B-site cation, and hence drives cooperative tilts and twists of BO_6 octahedra that form the three-dimensional network. The symmetry of perovskite can be lowered to orthorhombic[33], rhombohedral[34] or even trigonal ($FeTiO_3$, A and B cations have similar ionic radii)[35] from cubic and the B-O-B bond angles are smaller than 180°. For example, the size mismatch between the Ca and Ti cations in $CaTiO_3$[33] leads to a cooperatively twisted, corner-shared array of TiO_6 octahedra and the Ti-O-Ti bond angles are driven away from perfect 180° to accommodate smaller Ca^{2+} A-site cations as shown in Figure 1.8 (b).

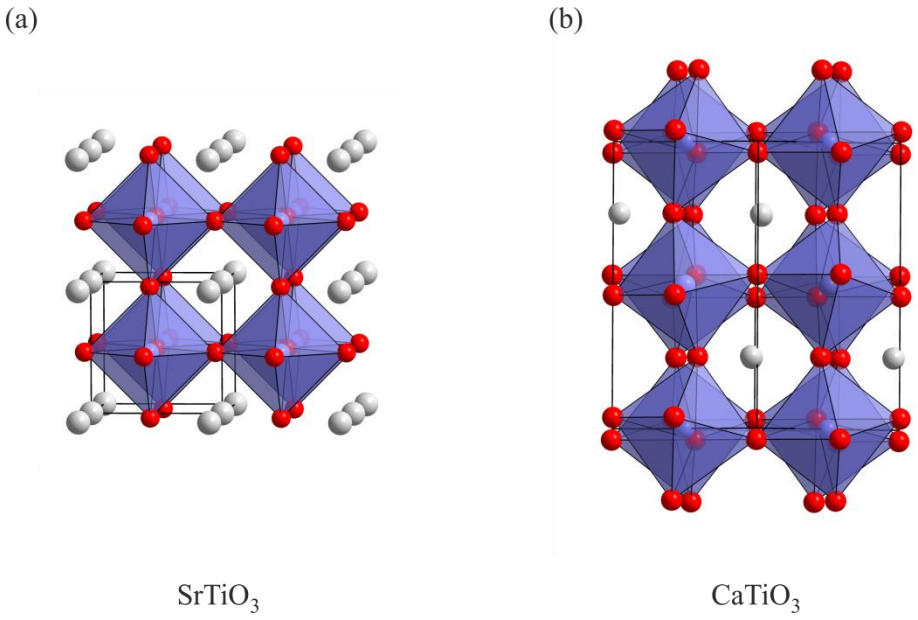


Figure 1.8. The ABO_3 perovskite type structure of (a) $SrTiO_3$ (*Pm*-3*m*) and (b) $CaTiO_3$ (*Pbnm*).[32, 33]

On the other hand, when $t > 1$, the A-site cation is larger than the ideal size for the 12-fold cuboctahedral cavities created by the relevant B-site cation, BO_6 octahedra tend to change their connectivity (from corner-sharing to face-sharing) to give a hexagonal variant of the original cubic structure, as shown in Figure 1.9.[36]

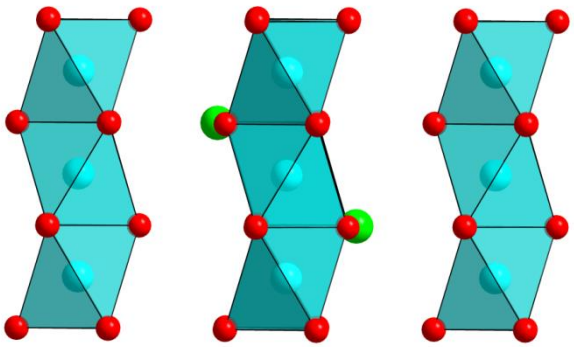


Figure 1.9. The structure of the hexagonal variant perovskite $BaNiO_3$ (*P*6$_3$/*mmc*).[36]

Since B-O-B bond angles affects the orbital overlap between the transition-metal *d* orbitals and the 2*p* oxygen orbital, and hence has influence on electronic and magnetic properties of perovskite, these properties can be tuned by modifying the Goldschmidt tolerance factor of perovskites, i.e. chemical substitutions can be exerted onto both cation sites and anion sites without the structure collapsing. The electronic and magnetic behaviour of perovskites strongly depend on metal-oxygen framework, which in this case, the oxidation states and coordination environment of transition metals can influent the nature and strength of metal-metal and metal-oxygen interactions. By understanding and controlling these factors, materials with specific electronic or magnetic properties can be designed.

1.4 Ruddlesden-Popper Structure

Ruddlesden-Popper structure is a layered variant of perovskite structure consisting of layers of two-dimensional perovskite blocks ABO_3 and intercalated cations forming rock-salt layers AO, and hence has a general formula $A_{n+1}B_nO_{3n+1}$ where A is an alkali metal, an alkaline earth metal or a lanthanide, B is a transition metal and n is the number of layers of corner-shared BO_6 octahedra stacked in the perovskite-type, therefore the general formula can also be written as $(AO)(ABO_3)_n$, of which the three-dimensional perovskite structure supposes to be the $n = \infty$ end phase.

In Ruddlesden-Popper structures with $n > 1$, the A-cations sit in two different sites, the 12-fold cuboctahedral sites residing in the perovskite blocks and the 9-coordinate sites residing in the rock-salt layer, the B-cations remain in the 6-coordinate sites to form the two-dimensional sheets of corner-shared BO_6 octahedra. A-cation order can potentially be allowed by these two different A-sites, especially when there are two or more A-cations with significantly different ionic radii or charges, like observed in many $n = 2$ Ruddlesden-popper phases and it is not surprising that the larger A-cation shows a strong preference in residing in the perovskite layer CN = 12 A-site and the smaller A-cation prefers to reside in the rock-salt layer CN = 9 A-site (Figure 1.10). For example, the perovskite A-sites in $YSr_2Mn_2O_7$ (r_{Y3+} = 1.215, r_{Sr2+} = 1.58) are exclusively occupied by Sr^{2+},[37] and similarly the perovskite A-sites in $Nd_2BaMn_2O_7$ (r_{Nd3+} = 1.303, r_{Ba2+} = 1.75) are preferentially occupied by Ba^{2+}.[38]

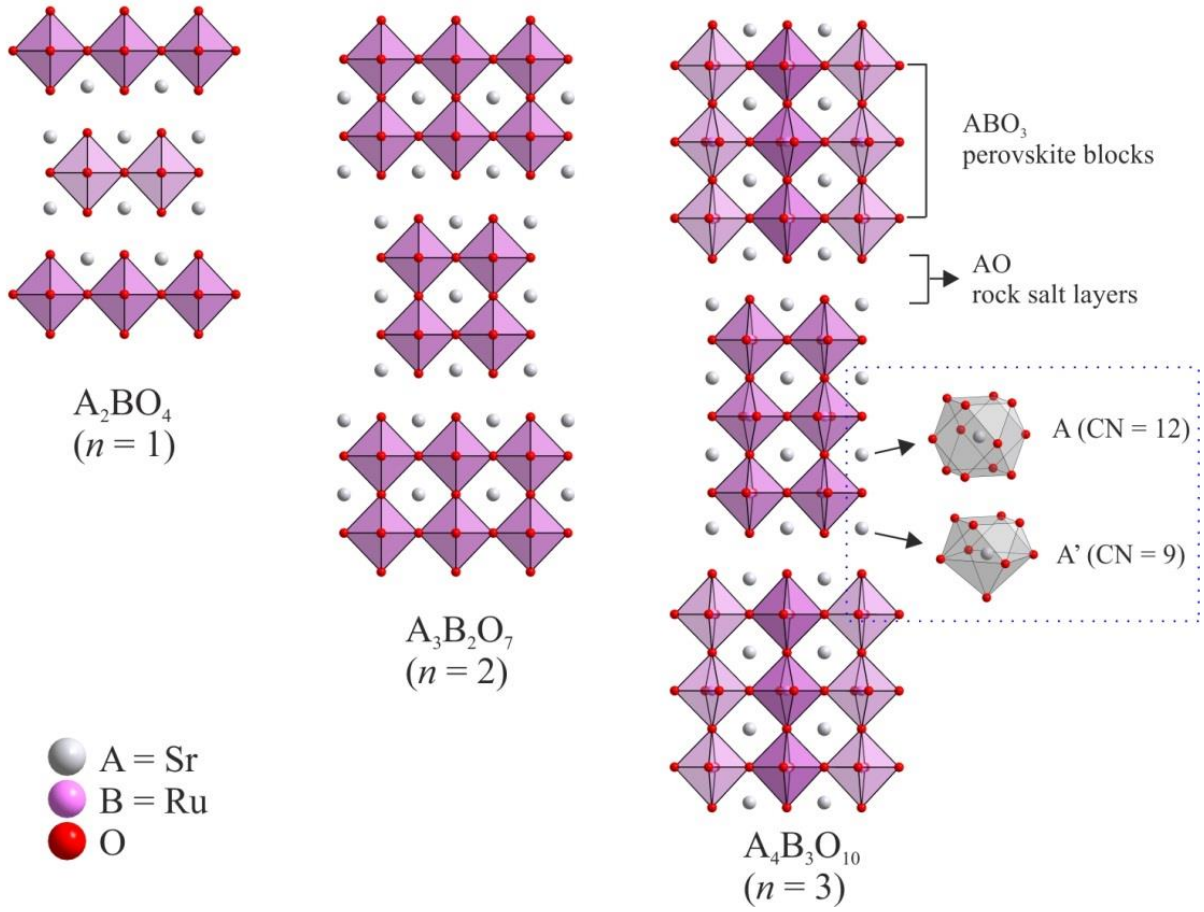


Figure 1.10. The Ruddlesden-Popper phases with *n* = 1, 2 and 3, along with coordination environments of two different A-sites.

Apart from the structural difference with respect to simple ABO_3 perovskite, Ruddlesden-Popper phase tends to be more robust during topochemical manipulations of lattice due to the presence of extra rock-salt layer AO. For example, the infinite layer phase $SrFe_{0.5}Ru_{0.5}O_2$ can be prepared by mixing its parent $SrFe_{0.5}Ru_{0.5}O_3$ oxide phase with CaH_2 and heating at 400 °C.[11] In contrast, the topochemical reductions of the Ruddlesden-Popper equivalents, $Sr_{n+1}(Fe_{0.5}Ru_{0.5})_nO_{3n+1}$ (n = 1 or 2) phases, with CaH_2 cannot reach completion at the same temperature.[23] Therefore Ruddlesden-Popper phases potentially undergo topochemical manipulations at wider temperature regime, hence it can open up more possibilities in material-design chemistry.

1.5 Hydride-for-Oxide Substitution

Since the electronic structure of the complex transition-metal oxides is strongly dependent on the lattice connectivity, in combination with the orbital overlapping and electron counts which defined by the oxidation state and local coordination geometry of transition-metal centres, hydride-for-oxide substitution, as a kind of anion exchange topochemical reactions, offers many attractive opportunities to modify the electronic properties of parent oxide phases.[17] For example, by utilising the hydride-for-oxide substitution, the insulating behaviour of $A^{II}TiO_3$ oxides is converted to the metallic conductivity found in corresponding $A^{II}TiO_{3-x}H_y$ oxide–hydrides.[39, 40]

The charge of a hydride ion is -1 while that of an oxide ion is -2, thus hydride-for-oxide substitution necessarily involves topochemical reduction of the chemical system, to form kinetically-controlled metastable phases, which gives access to unusually low oxidation states of transition metals that cannot be obtained via traditional high temperature synthetic routes. Also oxide ion is more electronegative than hydride ion, thus M-H bonds tend to have a higher degree of covalency compared to M-O bonds, and hence the different orbital mixing in M−H bonds compared to its parent M−O analogues leads to the qualitatively different band structures of oxide–hydride phases with respect to their corresponding parent oxide phases. Furthermore, magnetic coupling strengths can be strongly enhanced in oxide–hydride phases, proved by the high magnetic ordering temperatures observed for some reported oxide-hydride phases such as $LaSrCoO_3H_{0.7}$, $SrVO_2H$, and $SrCrO_2H$.[14, 15, 41] In addition, a much subtler difference between oxide and hydride ions is the lack of π-symmetry valence orbitals for the H^- anion. The orbital connectivity of the parent oxide phase can therefore be altered dramatically, especially if the oxide and hydride anions adopt an ordered arrangement. For example, the anion-ordered oxide–hydride $SrVO_2H$, where the hydride ions form V−H−V chains along the *z*-axis, is an antiferromagnetic insulator at ambient

pressure, but undergoes a metal-to-insulator transition when pressurized to about 50 GPa.[42] The resulting metallic state exhibits significant two-dimensional character because the hydride ions limit dispersion of the π-symmetry bands, which span the Fermi level, along the *z*-axis.[13]

Although hydride-for-oxide substitution offers many attractive features, only a handful of transition-metal oxide–hydride phases have been prepared and reported to date. The few reported systems can be categorised into two different groups, based on the mechanism by which the metastable oxide–hydride phase is stabilized with respect to decomposition to the elemental transition metal and water ($AMO_xH_y \rightarrow AO+M+H_2O$). Early transition-metal oxide–hydrides such as those containing titanium ($ATiO_xH_y$)[43], vanadium ($Sr_{n+1}V_nO_{3n-1}H_n$)[14], and chromium ($SrCrO_2H$)[41] can be thought of as ionically stabilized. These transition metals resist further reduction because of their low electronegativities, and their high oxidation states help to stabilize the H^- anion through columbic interactions. In contrast, late transition metals such as cobalt (as in $LaSrCo_3H_{0.7}$, $Sr_3Co_2O_{4.33}H_{0.84}$)[15, 44], stabilize the oxide–hydride phases through strong Co_{3d}–H_{1s}–O_{2p} covalent interactions[45].

Inspired from the idea that this strong Co_{3d}–H_{1s}–O_{2p} covalent interactions observed in cobalt oxide-hydrides has direct parallels to the strong σ-bonds observed in some molecular hydride systems of late 4*d* transition metals such as Ru and Rh (RuH_n with n = 1, 3, 6[46] and RhH_2[47]), it should be possible to prepare covalently stabilized oxide–hydride phases based on the same metals. Following this logic, we have chosen to explore the hydride-for-oxide substitution chemistry for a number of Ru/Rh-containing complex transition-metal oxides by using CaH_2 as a reducing agent and source of hydride ions. Detailed analysis of resulting oxide-hydride phases is presented in Chapter 4, 7 and 9.

1.6 Basic Band Theory and the Hubbard Model

The electrons of a single isolated atom occupy atomic orbitals with discrete energy levels; and when *N* atoms join together to form a molecule, or even a crystal lattice as the number of atoms *N* becomes larger and larger, their atomic orbitals overlap and each atomic orbital splits into *N* molecular orbitals with discrete energy levels. However, since the number of orbitals in extended solids is very large, they are very closely spaced in energy; therefore the energy difference between them can be neglected and can be considered as a continuous energy band (Figure 1.11).[48]

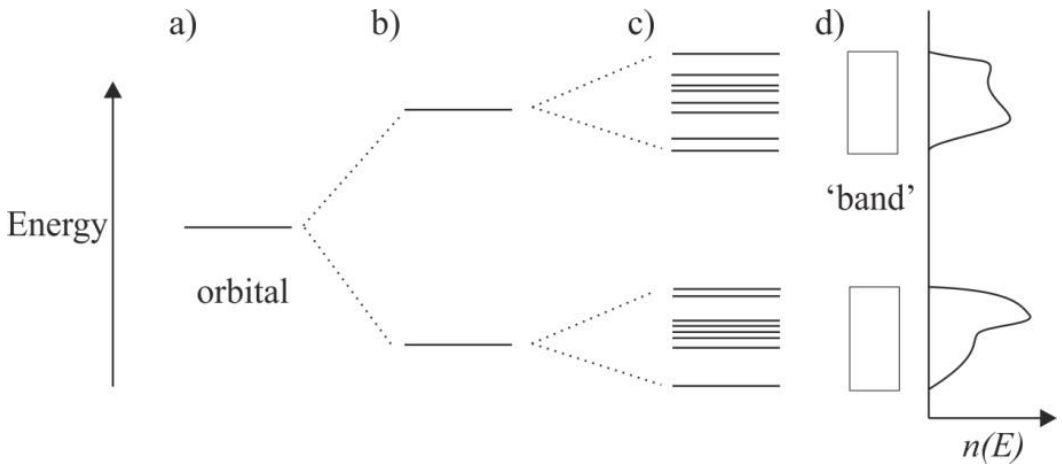


Figure 1.11. Orbital of a) an atom; b) a small molecule; c) a large molecule; becoming d) the band with the density of states in extended solids.[48]

The formation of bands is mostly a feature of valence electrons of atoms, which are the ones involved in chemical bonding and conducting electricity. The inner orbitals do not overlap as intensively as the valence orbitals, so the bands formed are very narrow and inner electrons are localised.

The occupancy of atomic orbitals determines the occupancy of a band and the energy of the highest occupied level is known as the *Fermi Level*. A partially filled band can result in

metallic conductivity as unpaired electrons near the Fermi level can be excited into orbitals where they are delocalised and can move freely as a charge carrier. However, many complex transition-metal oxides with partially-filled *d* bands are not metallic but antiferromagnetic insulators, like NiO and CoO.[48] This is due to the narrow bands formed by small interatomic orbital overlap, hence the on-site electron repulsions become unneglectable. Under these circumstances, basic band theory does not work as the electrons in partially filled *d* bands are localised by their mutual repulsion.

In order to describe the nature of the electronic behaviour of complex transition-metal oxides, the Hubbard model needs to be used as it represents one of the simplest ways to describe electron-electron interactions which are not considered in basic band theory. This model consists only two terms in the *Hubbard Hamiltonian*: a kinetic term allowing for tunnelling ('hopping') of electrons between sites in a lattice and typically denoted by the letter *t*; and a potential energy term *U* arising from the repulsion energy between two electrons on the same atom which can be thought of as the difference between the ionisation energy - *I* and the electron affinity - *A* (Figure 1.12). This Coulombic repulsion is assumed to be the only interaction between electrons in the Hubbard model.[30]

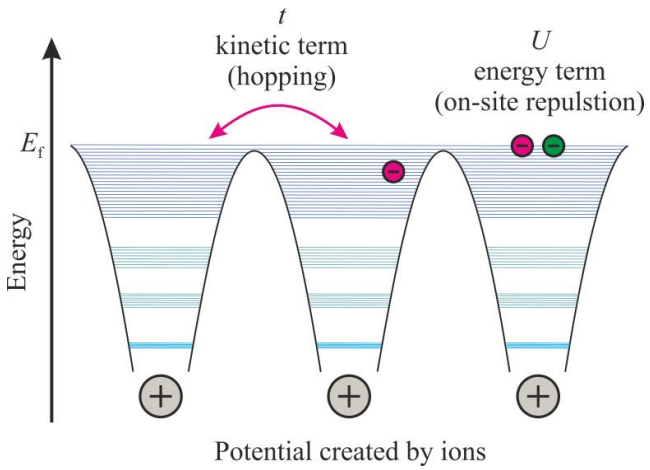


Figure 1.12. The hopping (*t*) and energy (*U*) terms in the Hubbard model.[48]

Therefore the Hubbard model describes the competition between chemical bonding (t) favouring itinerant electrons and short-range on-site Coulombic repulsion (U). The dominant energy term among these two can be determined by a dimensionless ratio of t/U.

The tunnelling of an electron from an atom to its neighbour costs an energy penalty U as a consequence of the on-site repulsion, which leads to the formation of sub-bands separated by the *Mott-Hubbard gap* U (Figure 1.13 (a)), making partially-filled bands insulating when the overlap is small, like observed in those *Mott-Hubbard insulators* NiO and CoO. As the interatomic orbital overlap increases, the sub-bands become broader and eventually they will meet when the band width W and the on-site electron repulsion U are approximately equal (Figure 1.13 (b)). Beyond this point, the band gap U becomes negligible and thus the system becomes metallic.[48]

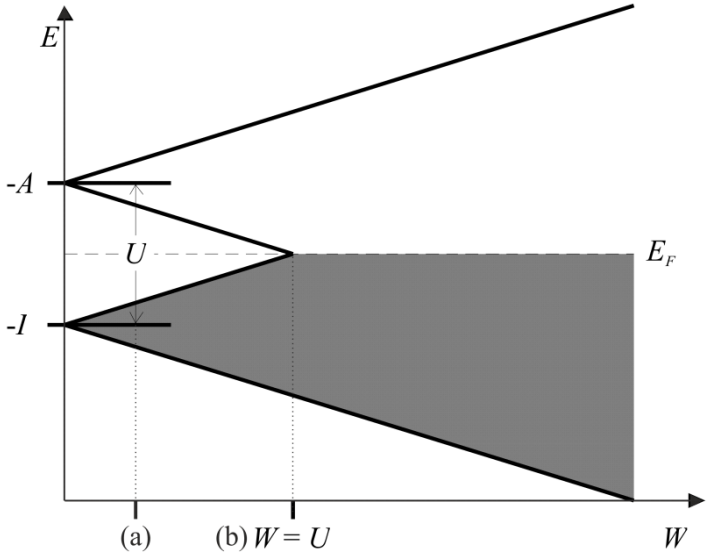


Figure 1.13. Hubbard sub-bands as a function of the band width *W*. On energy axis *E*, *-I* represents the ionisation energy and *-A* the electron affinity.[49]

1.7 Electronic Behaviour of Complex Transition-Metal Oxides

Previous work has focused on the topochemical reduction of complex transition-metal oxides which leads to the preparation of phases containing 3d transition metals in novel oxidation states and coordination geometries (square planar Ni^{+}, Co^{+}, Mn^{+} and Fe^{2+}) using NaH, LiH and CaH_2 as reducing agents.[18, 20-22] However these phases tend to be insulators for three reasons:

- Firstly the starting materials themselves are insulators as late 3d transition metals tend to have narrow electronic bands (small *W*) and large on-site electronic repulsions (large *U*) which leads to the localization of 3d electrons.
- Secondly, after reduction, electron counts of local transition metal centres have been increased, in hence *U* has been increased which disfavors the formation of electronic conducting materials.
- Finally, the extension of metal-oxygen bonds in reduced phases tends to drive the tilting and twisting of MO_x polyhedral, which lowers the overlap of d-orbitals between adjacent metal centres (smaller *W*).

Many interesting electronic properties of complex transition-metal oxides are due to the competition between several stabilizing effects when $W \approx U$. Therefore if we want to prepare topochemically reduced phases with metallic conductivity, we need to start with phases that have wider electronic band widths (larger *W*) and smaller on-site repulsion (smaller *U*) by introducing 4*d* or 5*d* transition metals into the system. For example, Sr_2RuO_4 has been shown to be close to antiferromagnetic, ferromagnetic and superconducting instabilities from the competing localization-delocalization interactions, and is known as a *p*-wave superconductor with a $T_c \sim 1.5$ K.[50]

The electronic behaviour of complex transition-metal oxides strongly correlates to their crystal structures as well. For example, the Ru-O-Ru bond angle is 180° in Sr_2RuO_4 phase

(Figure 1.14) [51, 52], but it deviates from 180° as a consequence of the tilted RuO_6 octahedra to accommodate smaller Ca cations in Ca_2RuO_4 phase (Figure 1.14). In contrast to the *p*-wave superconductor Sr_2RuO_4, Ca_2RuO_4 is a Mott insulator.[53] Another example is Sr_2IrO_4, in which tilting of the IrO_6 octahedra also leads to deviation from a perfect 180° Ir-O-Ir bond angle, again resulting in an insulating behaviour (Figure 1.14).[52, 54] However, substituting some Ru into B-sites to form a solid solution of $Sr_2Ru_xIr_{1-x}O_4$, leads to an insulator-to-metal transition at $x = 0.7$.[55]

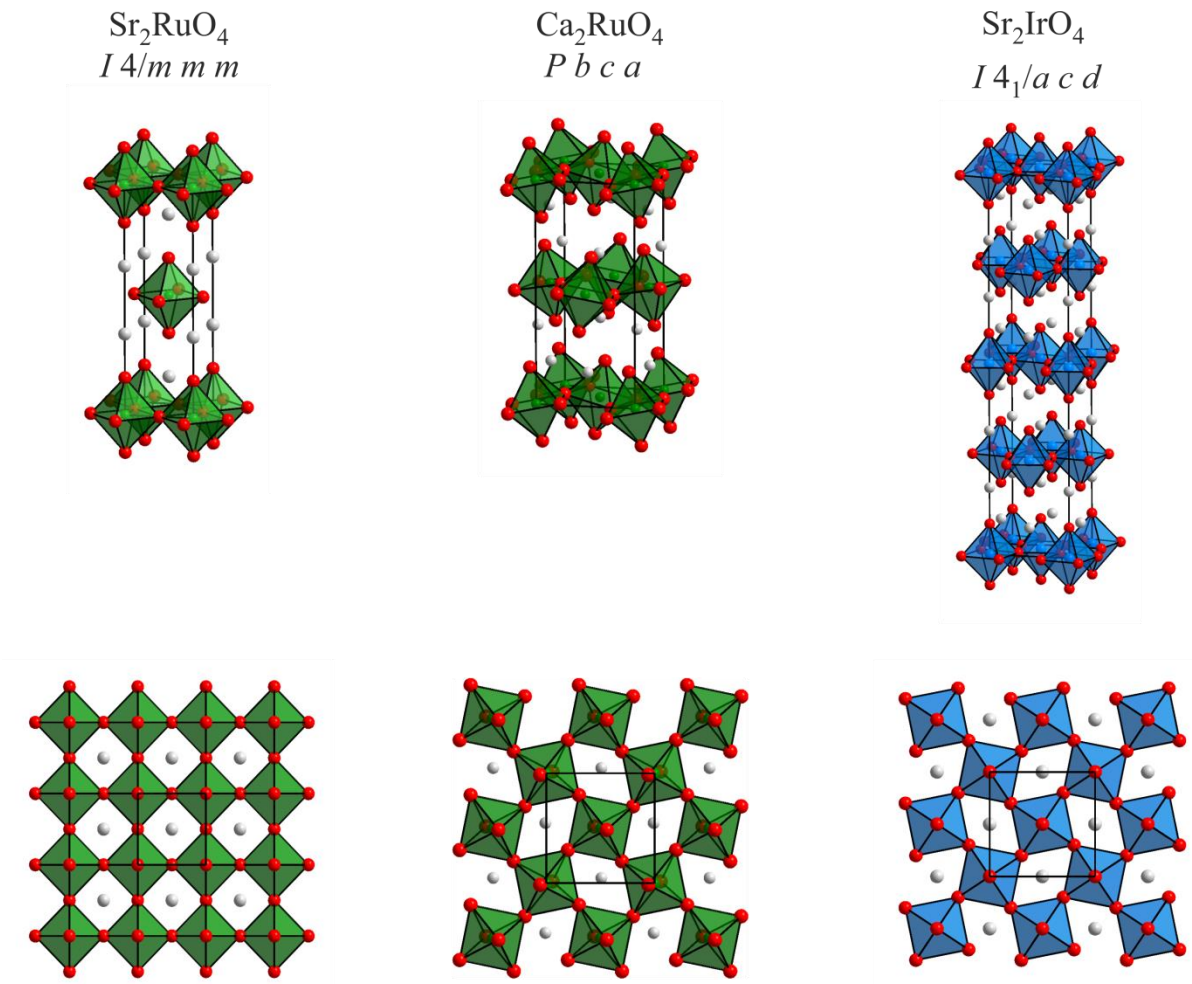


Figure 1.14. Structures of Sr_2RuO_4 (left), Ca_2RuO_4 (middle) and Sr_2IrO_4 (right).[56]

Apart from those parent oxide phases containing 4*d* or 5*d* transition metals, their topochemically reduced phases can be especially conductive as well because of competing interactions and correlated electronic behaviour. We have also noted in previous work, that 4*d* transition-metal oxide perovskites and Ruddlesden–Popper phases tend to decompose to yield elemental metals on reaction with CaH_2 unless they are stabilized by the presence of a 3*d* transition-metal ion.[11, 23] Therefore, topochemical reductions of complex transition-metal oxides $LaSr_3NiRuO_8$, $LaSr_3CoRuO_8$, $LaSr_3MnRhO_8$ and $La_2Sr_2CoRhO_8$ were attempted and resulting reduced oxide phases and oxide-hydride phases are analyzed in details and presented in Chapter 4-9.

Chapter 2

Experimental Methods and Techniques

2.1 Synthesis of Staring Materials

2.1.1 Ceramic Method

Conventional high-temperature ceramic synthesis techniques were used to prepare some of the thermodynamically stable solids discussed in this thesis. This procedure involves the thorough mixing of suitable quantities of appropriate starting reagents, such as binary metal oxides and carbonates, using an agate mortar and pestle. The resulting powders were slowly (1 °C/min) heated up to 1000 °C and heated for 24 hours to decompose any carbonates. Samples were then pressed into 13 mm diameter pellets under 5 tonnes of force, in order to minimise diffusion length in solids and improve grain contact of reagents, hence to speed up reaction rates. Then these pellets were heated to suitable high temperatures (usually above 1000 °C) to overcome large energetic barriers to diffusion within solids, under the selected atmosphere (air, Ar, O_2 etc.). Detailed reaction temperatures and atmospheres of this procedure for each sample are presented in appropriate chapters. After each firing, samples were thoroughly reground and re-pressed into pellets. Multiple heatings (each ~ 2 days) with intermittent grindings were normally required to reach a homogeneous single phase or equilibrium. Reaction progress was monitored via laboratory X-ray powder diffraction and reactions were judged to be complete when data collected after consecutive firings showed no change.

2.1.2 Citrate Gel Method

The citrate gel synthetic route, first described by M. Pechini in 1967[57], allows the preparation of samples requiring a higher degree of homogeneity, by dissolving suitable quantities of appropriate starting reagents, such as binary metal oxides and carbonates into a 1:1 solution of nitric acid in distilled water. An excess amount of citric acid (a common tridentate ligand which binds strongly to a wide variety of metal cations) was added to form metal-citrate chelating complexes, followed by a suitable amount of ethylene glycol. The mixture was then heated to drive the condensation polymerisation, with release of NO_x and water vapour, hence resulting in the formation of a polyester network containing a homogeneous array of coordinated metal cations. A highly viscous gel was thus formed, hence it was heated at 200 ~ 400 °C to combust most of organic components, until a loose black powder was obtained. The resulting powder was then slowly (1 °C/min) heated up to 1000 °C and heated for 24 hours to fully decompose any organic residues before pressing into pellets and heating under appropriate reaction conditions. The heating-grinding-pressing process was repeated until the reaction reached completion, confirmed by no more changes in X-ray patterns of two consecutive firings.

This method offers a strategy to reduce reaction time and lower reaction temperatures to a certain extent, and produces samples with a higher degree of homogeneity (important if following topochemical reactions are influenced by microscopic structures or short-range metal distributions), compared to conventional ceramic synthesis.

2.2 Binary Metal Hydride Reductions

Previous work has shown that binary metal hydrides, NaH, CaH_2 and LiH can be used to reduce a wide range of materials at relatively low temperatures ($180 \leq T/°C \leq 630$) to modify anion lattices of parent oxide phases.[18, 58, 59]

Topochemical reductions of n = 1 Ruddlesden-Popper phases, to form kinetically controlled metastable phases, were attempted by treating with NaH or CaH_2, according to following reaction schemes:

$$ABO_4 + x\text{NaH} \longrightarrow ABO_{4-x} + x\text{NaOH}$$

$$ABO_4 + x\text{CaH}_2 \longrightarrow ABO_{4-x} + x\text{CaO} + x\text{H}_2$$

Although Na-containing by-products can be easily removed from the sample (see Section 2.2.3), the low decomposition temperature of NaH places an upper limit on possible reaction temperatures (~ 250 °C), therefore it cannot be used as a reducing agent for systems requiring a higher reaction temperature regime to have the sufficient anion mobility. In addition, the reaction with NaH does not generate H_2 gas, so it cannot be used if oxide-hydride phases are target products. For the Rh-containing and Ru-containing oxides discussed in this thesis, CaH_2 is more commonly used than NaH, due to the relatively high reaction temperature regime provided and its ability to act as a hydride source.

The binary metal hydrides were kept in an argon-filled glove box due to their air and moisture-sensitive nature. Furthermore, any mixtures containing these reagents were also kept under an inert atmosphere at all times. Substrates to be reduced were typically ground with 2 stoichiometric equivalents of the chosen binary metal hydride in the glovebox and then placed within a suitable reaction vessel.

2.2.1 Sealed Glass Ampoules

Sealed glass ampoules were used for reactions with NaH, as no H_2 is produced during the reaction, or for reactions with CaH_2, which target products are oxide-hydride phases, as the H_2 produced needs to be trapped inside the vessel to act as a hydride source. Considering

the hazards associated with the production of H_2 gas, the size of sealed glass ampoules for CaH_2 reactions needs to be carefully chosen, based on the calculation of the maximum partial pressure of H_2 that can be generated during the reaction. The thorough mixture of the parent oxide phase and the chosen metal hydride were sealed under vacuum in either Pyrex (cheaper and easier to handle, but cannot be heated above 400 °C) or quartz ampoules, and then were heated to the desired temperatures at a slow ramp rate of 1-2 °C/min, to ensure that the temperature of the furnace did not overshoot the relatively low reaction temperature. After being held at the required temperature for a suitable length of time, the ampoules were scored with a glass cutting knife, pumped into a glovebox and opened inside the glovebox. The reaction mixture was reground, and the reaction progress was monitored by laboratory X-ray powder diffraction.

2.2.2 Venting Apparatus

The venting apparatus (Figure 2.1) was developed to allow a steady stream of argon flowed inside the vessel, to extract the H_2 gas evolved during the reaction when CaH_2 was using as a reducing agent. This approach was usually employed for the preparation of large-scale samples suitable for neutron diffraction experiments, or for the preparation of reduced oxide phases when the presence of H_2 gas does aid the formation of competing oxide-hydride phases. Reaction mixtures were prepared as described in Section 2.2, and then transferred into a Pyrex/silica tube closed by a Young's tap. After pumping out of the glovebox, instead of sealing the tube under vacuum, the Young's tap was connected to a steady argon flow. After purging the system for a while, it was heated to the desired temperatures at a slow ramp rate of 1-2 °C/min, with continuous flow of argon.

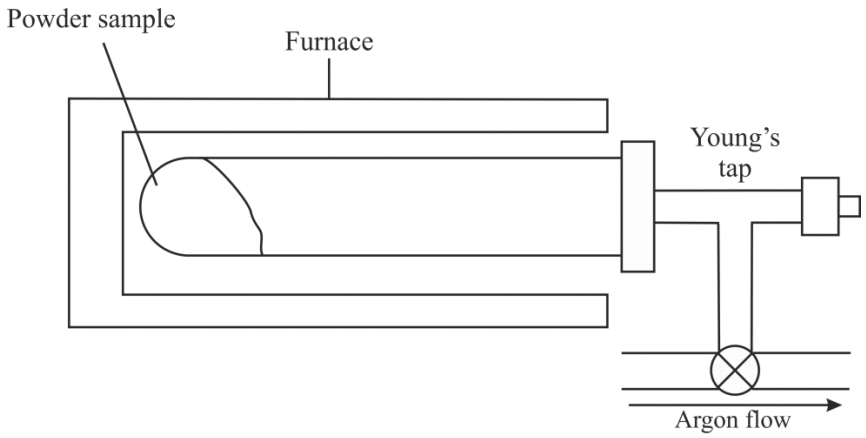


Figure 2.1. The schematic representation of the venting apparatus.

Between heating periods, the reaction vessel was evacuated before pumping into the glovebox. The reaction mixture was reground, and the reaction progress was monitored by laboratory X-ray powder diffraction.

2.2.3 Washing Reaction Mixtures

After the completion of topochemical reductions with binary metal hydrides, it was necessary to remove any unreacted hydrides and by-products from the reaction mixture, to obtain pure reduced phases. This was done by washing the reaction mixture under an inert atmosphere (N_2) using standard Schlenk techniques, with clean methanol (NaH or LiH reductions) or an acidic methanol (CaH_2 reductions). The standard acidic methanol (0.1 M) used was prepared by dissolving suitable amount of NH_4Cl (Fisher Scientific, > 99%) in clean methanol (Sigma-Aldrich, ≥ 99.9%). Samples were then recovered by filtration and washed with clean methanol to remove any remaining NH_4Cl residues, before drying under vacuum. The removal of all hydrides and by-products was confirmed by laboratory X-ray powder diffraction.

2.3 Zirconium Getter Reductions

Apart from binary metal hydrides, an alternative reduction method employed to reduce Ru-containing oxides was the zirconium getter reduction. This method works by using the finely-divided (maximised surface area) zirconium powder as an oxygen getter, which reacts rapidly with the partial pressure of oxygen above its surface, to form variety of stable metal oxides ZrO_x as the by-products of the reactions, hence artificially lowers the oxygen partial pressure in the system and drives the equilibrium to reduced phases.

Inside an argon-filled glove box, excess amount of the getter reagent, finely-divided Zr powder, was weighted and placed in the bottom of a quartz tube that had a small indent between 0.5 – 1 cm from the base of the tube. The substrate was placed in a smaller quartz thimble which was in turn loaded into the indented quartz tube. The quartz tube was sealed with a Young's tap and then pumped out of the glove box, followed by evacuating and sealing under vacuum to form an ampoule (Figure 2.2). This set-up ensured that the substrate would never be contaminated by the getter reagent or by-products, hence no further purification procedures were required. Then the reaction vessel was placed in a low temperature furnace and heated to the desired temperature at a slow ramp rate of 1-2 °C/min. After being held at the required temperature for a suitable length of time, the ampoule was scored with a glass cutting knife, pumped into a glovebox and opened inside the glovebox. The reaction mixture was reground, and the reaction progress was monitored by laboratory X-ray powder diffraction.

This method works well for yielding reduced oxide phases in this work, from their parent oxide phases, if the formation of competing oxide-hydride phases would be strongly aided by the presence of H_2 gas (the by-product of CaH_2 reductions).

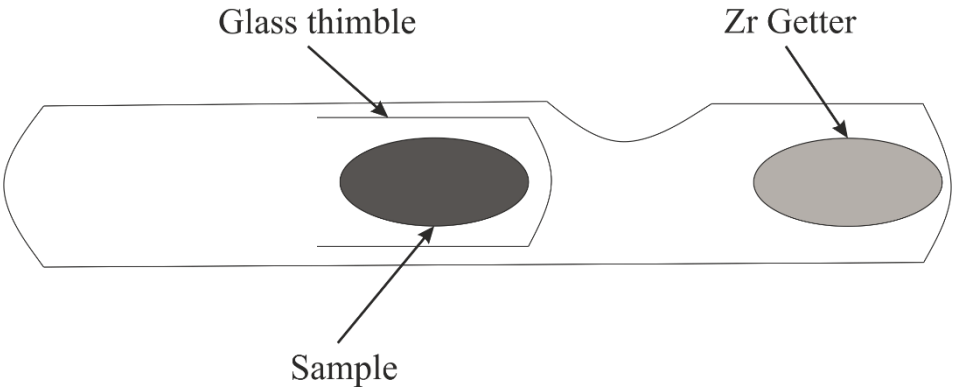


Figure 2.2. The schematic representation of the zirconium getter ampoule.

2.4 Handling Air-sensitive Reactions and Compounds

All the reduced oxide phases and oxide-hydride phases in this work slowly react with oxygen, and eventually re-oxidise back to their parent oxide phases if they have been exposed in air for sufficient long time. Also, the reducing reagents used, group I/II binary metal hydrides and zirconium powder readily react with oxygen and water in air to yield their respective oxides and hydroxides. Therefore, topochemical reductions involving these compounds must be carried out and analysed using techniques that exclude air and moisture.

2.4.1 Argon-filled Glove Box

Reaction mixtures for topochemical reductions were prepared under an inert atmosphere in an argon-filled glove box. The partial pressure of oxygen and water are normally below 10 ppm within the box, by constantly circulating the internal atmosphere over a column made of copper catalyst. The column has a finite capacity, therefore it needs to be regenerated by heating under a 5% H_2/N_2 gas flow once its limit has been reached.

2.4.2 Air-sensitive X-ray Powder Diffraction

X-ray powder diffraction data were collected from air-sensitive topochemical reaction mixtures, by using a sample holder shown in Figure 2.3. A glass slide was covered with a thin layer of Dow-Corning high vacuum grease, and under an inert atmosphere, a small amount of powder was evenly distributed over the greasy side of the slide. The slide was then sealed in the air-sensitive X-ray sample holder, with the sample side pointing upwards, by screwing on a brass cap, which compresses a rubber O-ring to form an air-tight environment.

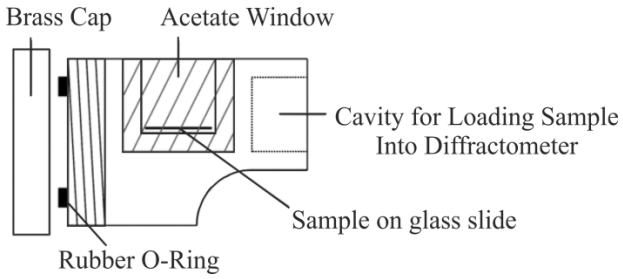


Figure 2.3. The schematic representation of an air-sensitive X-ray sample holder.

2.5 Powder Diffraction

Powder diffraction techniques are some of the most important and widely used methods for the characterisation of crystalline materials in solid-state chemistry. Both X-ray and neutron powder diffraction were the main methods used for the structural characterisation of the phases presented in this work.

Diffraction is a characteristic behaviour of waves which occurs when they irradiate scattering obstacles of comparable size to the wavelength. The spacing between the lattice

planes formed by periodically arranged atoms within a crystal, is comparable to wavelengths of X-ray and neutron radiations. The regular array of lattice planes acts as a diffraction grating to diffract incident radiations and produces a regular array of waves. In most directions, these waves will cancel out through destructive interference; however, a few specific directions will result in constructive interference. This is described as the Bragg's model of diffraction (Figure 2.4) and the geometrical conditions for it to be observed are given by Bragg's Law[60]:

$$\boldsymbol{n\lambda = 2d_{hkl}sin(\theta)} \qquad \textbf{2.1}$$

where n is an integer, λ is the wavelength of the incident beam, d_{hkl} is the interplanar distance and θ is the angle between the beam and the lattice planes depicted in Figure 2.4. Assuming that the source and detector in a diffraction experiment are at an infinite distance from the sample, then the incident and diffracted beams can be considered parallel.

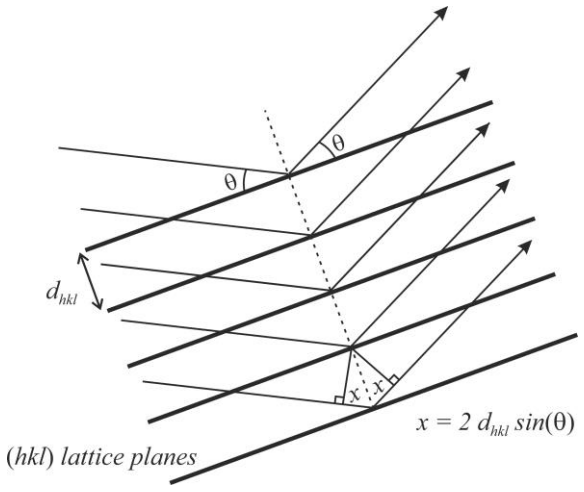


Figure 2.4. Bragg's construction for diffraction of monochromatic radiation by a set of parallel lattice planes.

In a diffraction pattern, the position of a given reflection is defined by the *d*-spacing (d_{hkl}), which is correlated to the unit cell dimensions. The intensity of a given reflection (I_{hkl}) is given by:

$$\boldsymbol{I_{hkl} \propto LmA|F_{hkl}|^2} \qquad \textbf{2.2}$$

where *L* is the sample-independent Lorentz-polarisation factor, *m* is the reflection multiplicity, *A* is the absorption factor and F_{hkl} is the structure factor, which depends on the crystal structure[61]. The structure factor, F_{hkl}, is an expression of how the content of the unit cell, i.e. the arrangement of atoms, influences the intensity of a reflection, I_{hkl}, according to the following equation:

$$\boldsymbol{F_{hkl} = \sum_n f_n(\theta) \cdot \exp[2\pi i(hx_n + ky_n + lz_n)] \cdot \exp(-8\pi^2 U_{iso_n} sin^2\,\theta_{hkl}/\lambda^2)} \qquad \textbf{2.3}$$

where f_n is the atomic scattering factor, x_n, y_n, z_n are the fraction coordinates of the atoms in the unit cell, and U_{iso_n} is the isotropic displacement parameter. The second exponential term describes how the intensity decreases as a function of the scattering angle θ.

2.5.1 X-ray Powder Diffraction

Powder X-ray diffraction is frequently used in solid state chemistry and it is a powerful tool to monitor the progress of reactions and determine the crystal structure and lattice parameters of product phases. X-ray radiation interacts with and is diffracted by the electron density of atoms in the material, thus a given atom's scattering factor (f_j) is therefore related to its atomic number (Z).[61]

2.5.1.1 Panalytical Empyrean and X'Pert Instruments

The Panalytical Empyrean and the Panalytical X'pert diffractometers were used to collect data suitable for routine inspections of reaction progress and characterisations of crystal structures, respectively. In these instruments, a Ge(111) monochromator was employed on the incident beam, hence only Cu $K_{\alpha 1}$ radiation was selected to hit the sample, and the beam optics can be adjusted by the choice of beam mask, anti-scatter and Soller slits. These instruments utilised Bragg-Brentano focussing geometry.

The Panalytical Empyrean instrument was used to track the progress of reactions and program parameters were varied to fit different scan angles and times, with respect to different samples. The Panalytical X'pert diffractometer was used to collect diffraction patterns with high qualities, by fitting with an angle-sensitive detector which works at a range of ± 1.5° from θ. This set-up gives an improved signal-to-noise ratio compared to the Empyrean diffractometer, and thus provides high-quality diffraction patterns which can be used for Rietveld Refinement (Section 2.6).

For both diffractometers, samples were prepared as follows:

- Air-sensitive samples were assembled as described in Section 2.4.2.
- Non air-sensitive samples were sprinkled onto a silicon wafer which was covered by a thin layer of Dow-Corning high vacuum grease. The silicon wafer was cleaved along the (110) plane which is a systematically absent diffraction peak, and therefore it did not interfere with actual diffraction patterns collected from samples. Then the wafer was assembled onto a spinning stage which rotates during measurements to minimise the effects of uneven sample distribution.

2.5.1.2 Synchrotron X-ray Powder Diffraction

Synchrotron radiation results from acceleration of charged particles, generated by electromagnetic radiation, which is forced to change direction around a curved path (by a magnetic field) and with speeds approaching the speed of light. Synchrotron X-ray radiations have a range of high frequencies, and high-quality powder diffraction data can be collected by using this radiation.[62]

The synchrotron X-ray powder diffraction data presented in this work were collected on the I11 beamline at the Diamond Light Source Facility in Didcot, Oxfordshire. The I11 beamline is a high-resolution powder diffraction beamline equipped with a source that produces X-rays ranging from 5 to 30 keV.[62] A Si (111) double-crystal-monochromator (DCM), which is made of two liquid nitrogen quenched Si (111) crystals, is used to select the energy of the incident beam. Samples are loaded and sealed in glass capillaries, which are securely placed in brass holders with a magnetic base. Then these holders are mounted onto a magnetic spinner stage that is pre-aligned to the centre of the diffractometer. The Position Sensitive Detector (PSD), which employed MYTHEN-II silicon microchip technology, was used to collect high-resolution, wide-angle range powder diffraction data from samples. The synchrotron X-ray powder diffraction data collected from I11 beamline were analysed by Rietveld Refinement (Section 2.6).

2.5.2 Neutron Powder Diffraction

As mentioned in Section 2.5.1, X-ray radiation interacts with and is diffracted by the electron density of atoms in the material, therefore determining the changes in the fractional occupancy or position of atomic sites occupied by light elements can be difficult and

unreliable, especially in the presence of relatively heavy elements. In contrast, neutron radiation interacts with the nuclei of atoms, and the neutron scattering lengths of atoms do not follow a liner relationship with atomic number, therefore light elements can be located with the presence of heavier elements. For example, the nuclei of both anions studied in this work, oxide and hydride, exhibit significantly different coherent scattering lengths (5.803 and -3.739 fm respectively) and thus are readily 'visible' in a neutron diffraction experiment.[63] Also, unlike the X-ray scattering form factor, the neutron scattering form factor is independent of the scattering angle, so diffraction peaks occurred at high angles in neutron diffraction patterns do not lose intensity and are more reliable to determine actual crystal lattices. In case of solid-state chemistry, the complete structural characterisation of samples cannot always be achieved by using X-ray powder diffraction only, hence neutron powder diffraction data need to be collected to finalise crystal structures and contents of unit cells.

In addition, neutron powder diffraction allows for the characterisation of the magnetic structure of materials that exhibit long-range magnetic ordering (showing additional magnetic diffraction features), because neutrons are half-integer spin particles and as such they are scattered by a lattice of ordered unpaired electrons. The intensity of the magnetic scattering is comparable to that of the nuclear scattering. However, in contrast with the latter, the form factor for the magnetic scattering has an angular dependence which decays even faster than the form factor of X-ray diffraction. This is because magnetic scattering results from the interaction (of neutrons) with the outer-most electrons.[64]

The magnetic scattering structure factor (F_{mag}^{hkl}) for an unpolarised neutron source can be expressed as follows[65]:

$$\boldsymbol{F_{mag}^{hkl} = \sum_j q_j p_j e^{2\pi i h x_j}} \qquad \textbf{2.4}$$

where q_j is the magnetic interaction vector, p_j is the magnetic form factor, h is the magnetic scattering vector and x_j is the position vector of magnetic atoms in the unit cell.

The observed intensity of a magnetic reflection ($I_{hkl,mag}$) is proportional to the square of the projection of the magnetic structure factor onto the scattering vector[65]:

$$\boldsymbol{I_{hkl,mag} = |F_{mag}^{hkl}|^2 cos^2 \alpha} \qquad \textbf{2.5}$$

where α is the angle between the magnetic scattering structure and the relevant lattice plane.

Given that the neutron scattering interaction is relatively weak, large scale samples were prepared for the experiments. Samples were loaded in vanadium cans which have a neglectable contribution to patterns, as vanadium exhibits a very low coherent scattering length of -0.3824 fm.[63]

Neutrons can be generated by nuclear reactor sources (in which the neutron radiation arises from a fission process), or by spallation sources (where the neutrons are expelled from a heavy metal target being hit by pulses of accelerated high-energy protons). The former is the source used at the Institut Laue-Langevin (ILL) in Grenoble, France, and the latter is used at ISIS neutron facility, Rutherford Appleton Laboratory in Oxfordshire, UK. The neutron powder diffraction data in this work were collected at these two facilities[66, 67] from two instruments: the WISH (ISIS) and the D2B (ILL).

2.5.2.1 WISH

WISH (Figure 2.5) is a long-wavelength diffractometer primarily designed for powder diffraction at long *d*-spacing in magnetic and large unit cell systems. WISH provides high resolution data over a *d*-spacing range from 0.7-17 Å with a single frame bandwidth of 8 Å. WISH uses pixelated ^{3}He detectors (4 banks) covering scattering angles from 10° to 170°.

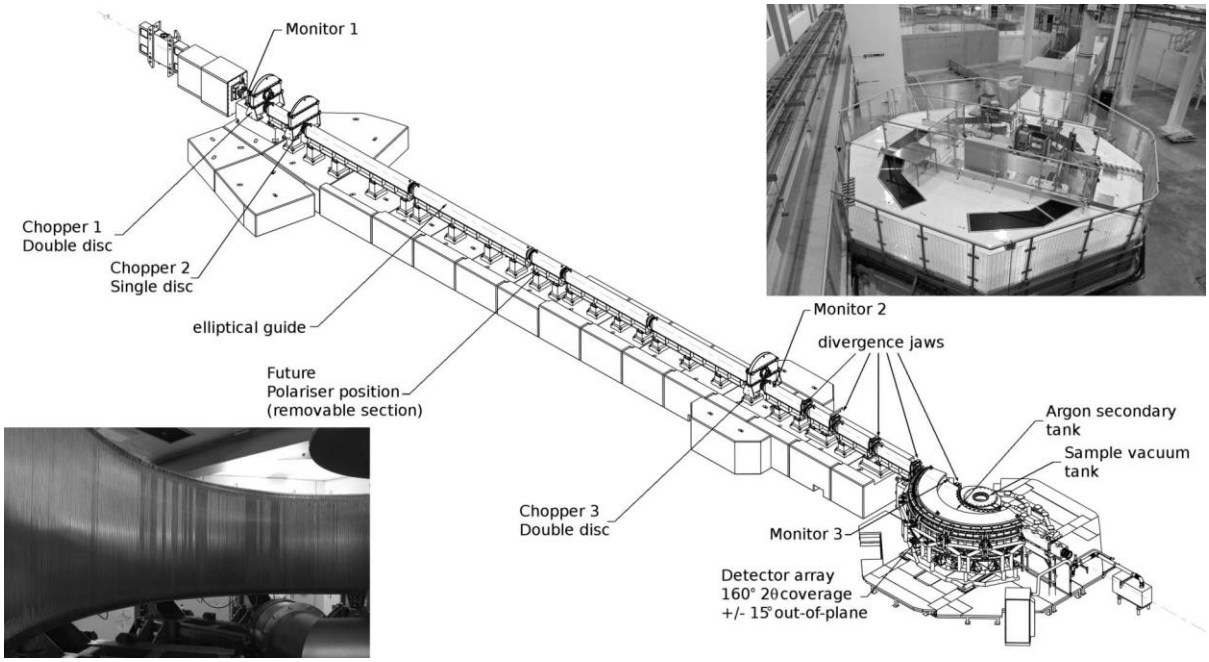


Figure 2.5. Engineering layout of the Wish diffractometer. The two pictures show the instrument in the TS2 experimental hall (right) and the large ^{3}He detector array inside the blockhouse (left).[68]

Pulses of protons are accelerated in a synchrotron until they reach 800 MeV and then fired at a tantalum target. This triggers an intra-nuclear cascade that produces a pulse of neutrons. The neutrons in these pulses have very high thermal energies and are slowed down by using a solid methane moderator before they reach the instrument, thus the neutrons have a suitable wavelength for time-of-flight diffraction measurements.

Time-of-flight diffractometers use an energy dispersive mode with detectors at fixed scattering angles around the sample to measure diffraction patterns as a function of the wavelength. The wavelength is related to the velocity of neutrons by using the de Broglie relationship:

$$\boldsymbol{\lambda = \frac{h}{m} \times \frac{t}{L}} \qquad \textbf{2.6}$$

where *h* is Planck's constant, *m* is the neutron mass, and *t* is the time taken to travel distance *L* from the moderator to the detector via the sample.

2.5.2.2 D2B

The D2B instrument (Figure 2.6) is a high-resolution powder diffractometer at ILL. The ILL neutron source provides neutrons with an extremely high intensity (energies in the meV range) from fission of ^{235}U. The fission process is sustained by lowering the energy of produced neutrons through a moderator filled with D_2O. The neutrons resulting from this moderation process are of suitable energies to perform diffraction experiments, with appropriate wavelengths (maximum flux at 1.2 Å) which can be further discriminated by using a crystal monochromator at each instrument.

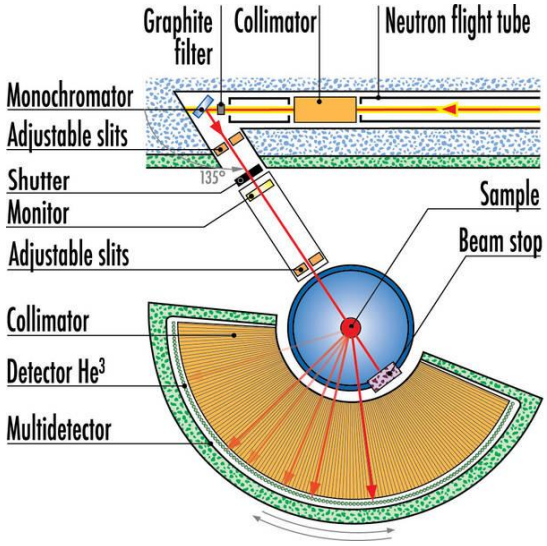


Figure 2.6. D2B diffractometer at ILL, Grenoble, France.[69]

The D2B instrument is a two-axis diffractometer with a high take-off angle (135°) for the monochromator. Scans were performed over the range $5 < 2\theta\ /° < 160$, with several scans being summed to give a diffraction pattern with a good signal-to-noise ratio, hence make sure that refinements of data can achieve good statistical fits. The wavelength of the incident neutron beam can be selected by rotation within the *hkl* plane of a Ge crystal monochromator and a wavelength of 1.5943 Å was used for all experiments in this thesis.

2.6 Rietveld Refinement

The Rietveld refinement was used to analyse X-ray and neutron powder diffraction data with the General Structure Analysis System (GSAS) suite of programs in this work.[70] The extraction of structural information is inherently difficult from powder diffraction data, as they only provide a one-dimensional view of a three-dimensional structure and hence result in loss of some information. For example, Miller planes with the same or similar *d*-spacing but different *hkl* values will have reflections overlapping with each other, all of which contribute intensity to a peak, hence exact structure factors cannot be calculated from reflection intensities. The Rietveld method allows for a predicted structural model, which is close to the real one, to be compared against the observed diffraction pattern, so that when the model is correct, the 'true' values of the intensities can be predicted.[71] By doing this, it enables overlapping peaks to be separated.

During a Rietveld refinement, the intensity of the reflections in the structural model are compared to those observed in the collected data via the relationship:

$$\boldsymbol{S = \sum_i w_i (y_{io} - y_{ic})^2} \qquad \textbf{2.7}$$

where w_i is the weighting factor, y_{io} is the observed intensity at point i in the diffraction pattern, and y_{ic} is the calculated intensity at point i. Diffraction and structural parameters are then refined against the experimental data, using a least squares optimisation technique to minimise the difference S.

The statistical fit of the model to the data is assessed using three parameters: the goodness of fit, χ^2, the profile factor, R_p, and the weighted profile factor, wR_p. These parameters are defined as follows:

$$\chi^2 = \frac{\sum w_i(y_{io}-y_{ic})^2}{n_{obs}-n_{var}} \quad \textbf{2.8}$$

$$R_p = 100\% \times \frac{\sum|y_{io}-y_{ic}|}{\sum y_{io}} \quad \textbf{2.9}$$

$$wR_p = 100\% \times \sqrt{\left(\frac{\sum w_i(y_{io}-y_{ic})^2}{\sum w_i y_{io}^2}\right)} \quad \textbf{2.10}$$

where n_{obs} is the number of observations in all histograms and n_{var} is the number of variables in the least squares refinement.

In this work, the extraction of structural information, including lattice parameters, atomic positions, site occupancy and peak profiles etc. is achieved by Rietveld refinements of collected powder diffraction data.

2.7 Thermogravimetric Analysis (TGA)

Thermogravimetric analysis was used to confirm the composition of topochemical reduced phases, especially the content of oxide ions remained in the lattice. All measurements were carried out using the Mettler Toledo TGA/DSC 1 STARe system. A small amount of sample (20 – 50 mg) was accurately weighed and placed into an alumina crucible, then loaded onto the instrument. The sample was heated under a steady flow of either 5%/95% H_2/N_2 (reductive TGA) or O_2 (oxidative TGA) at a suitable ramp rate, and held at the target temperature for sufficient amount of time to complete the reaction before cooling down. The mass change of the sample during the experiment was recorded as a function of temperature. After the experiment, X-ray powder diffraction data were collected from the resulting sample to examine its composition. Heating topochemical reduced phases under 5%/95% H_2/N_2 flow (reductive TGA), usually lead to fully decomposition into binary metal oxides or elemental metals, while under O_2 flow (oxidative TGA), they normally reoxidise back to their parent oxide phases. In both cases, from knowledge of the mass of the

sample at the beginning and end points, together with the compositions at the end point (from X-ray powder diffraction data), the amount of oxygen gained or lost was calculated, hence the initial composition of the topochemical reduced phase can be proposed.

2.8 Bond Valence Sums

The valence of an ion, V_i, can be estimated by considering the sum of the valences of all the individual bonds within the coordination sphere of the ion.[72] This approximation can be expressed as:

$$\boldsymbol{V_i = \sum_j v_{ij}} \qquad \textbf{2.11}$$

where the valence v_{ij} of a bond between atoms *i* and *j* is given by:

$$\boldsymbol{v_{ij} = e^{(R_{ij} - d_{ij})/b}} \qquad \textbf{2.12}$$

where *b* is an empirical constant (taken to be 0.37)[73], R_{ij} is the 'bond-valence parameter', and d_{ij} is the measured bond length.

2.9 Muon-Spin Relaxation Spectroscopy (μSR)

Muon-Spin Relaxation Spectroscopy (μSR) is an experimental technique based on the implantation of spin-polarized muons in matter and the detection of the influence of the atomic, molecular or crystalline surroundings on their spin motion. The motion of the muon spin is due to the magnetic field experienced by the particle and may provide information on the local environment. The decay of muon emits a *fast decay positron* (an anti-electron) preferentially along the direction of the muon's spin. The decay of positrons from 'a bunch' of muons deposited at the same conditions allows the determination of the statistical average direction of the spin polarisation of the implanted muon ensemble. The time evolution of the muon spin polarisation depends sensitively on the spatial distribution and dynamical fluctuations of the magnetic environment.[74]

The μSR data in this work were collected at the Paul Scherrer Institute in Switzerland, by Prof. Stephen J. Blundell, University of Oxford.

2.10 SQUID Magnetometry

The magnetic properties of samples in this work were measured using a Quantum Design MPMS XL Superconducting Quantum Interference Device (SQUID). SQUID magnetometers are extremely sensitive and are able to detect very small changes in a magnetic field by making use of the Josephson Effect. The SQUID contains superconducting rings with two weak link insulating barriers known as Josephson Junctions.[75] Cooper pairs are able to tunnel through these junctions and maintain their phase coherence in the absence of a magnetic field.[76]

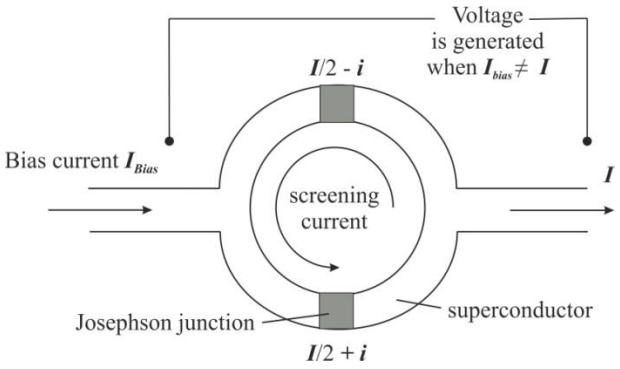


Figure 2.7. Schematic representation of the principal component in a SQUID magnetometer.[75]

When an external magnetic field is applied inside the ring, a current is induced in the coil in order to produce a magnetic field which opposes the applied one. This causes the critical current to be exceeded and breaks the superconductivity of the coils by impeding the tunnelling of the cooper pairs through the Josephson Junctions. The voltage which arises from the induced current is proportional to the magnetic moment of the sample placed in the coil and can be measured by the SQUID magnetometer.

For measurements in this work, samples of approximately 20 - 50 mg were weighed and placed in a gelatine capsule inside a drinking straw, with four empty capsules on either side. The outermost capsules were covered with a layer of diamagnetic tape to hold the sample in place. Air-sensitive samples were prepared in the glovebox and kept under an inert atmosphere until they could be loaded into the chamber of the SQUID. The straw was pierced with a needle multiple times, so it could be evacuated and then taped to the end of a long rod to be loaded into the SQUID.

2.10.1 Standard Measurements

For all parent oxide phases in this work, standard measurements were carried out to measure their magnetic properties. Zero-field-cooled (ZFC) and field-cooled (FC) data were collected using a magnetic field of 100 Oe over a temperature range of $5 \leq T / K \leq 300$. Measurements of field-cooled magnetisation isotherms as a function of field were also conducted at 300 K and 5 K over the field range of $-5 \leq H / T \leq 5$.

2.10.2 Ferrosubtraction Measurements

The magnetic properties of topochemical reduced phases in this work cannot be properly measured using the methods stated in Section 2.10.1, due to the inevitable presence of trace amount of ferromagnetic impurities (e.g. Ni or Co) in the samples prepared via topochemical reductions. A large field (3 T to 5 T) needs to be applied to saturate these ferromagnetic impurities during the magnetic characterisation, so the ferromagnetic behaviour contributed by these impurities would not mask the magnetic behaviour of the bulk phase, hence the paramagnetic susceptibility of the bulk phase can be properly measured. At 5 K increments between 5 K and 300 K, magnetisation-field isotherms were collected over the field range $3 \leq H / T \leq 5$ and the resultant magnetisation are plotted as a function of the

applied field. For each 5 K step the gradient of the plot obtained shows the paramagnetic susceptibility and the intercept gives the saturated ferromagnetic moment. Combined the whole range temperature data, a field-cooled plot can be made which shows the temperature dependence of the sample's magnetisation. A graphic representation of the principles of ferrosubtraction measurements is shown in Figure 2.8.

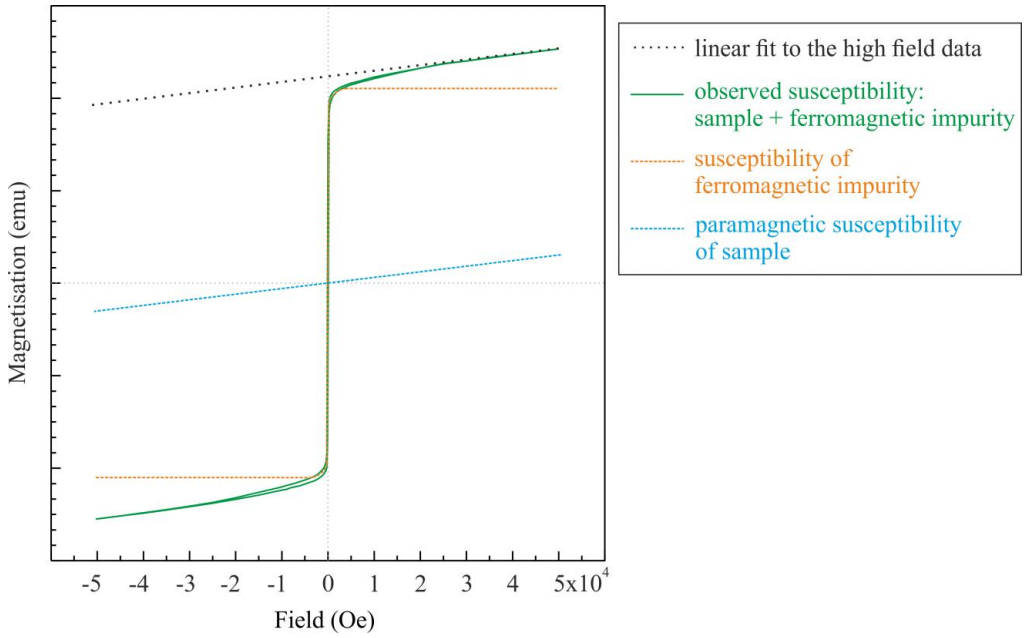


Figure 2.8. Schematic representation of a magnetisation-field isotherm of a sample consisting of a paramagnetic phase and a ferromagnetic impurity phase. The dotted line indicates the region used for a ferrosubtraction experiment.

2.11 Magnetism

Magnetism in solids arises from the electron spins of individual atoms, the combined effect of which gives the overall magnetic properties of the material. In the presence of an external magnetic field, these spins tend to align themselves along the applied field.

2.11.1 The Curie-Weiss law

The alignment of electron spins in a paramagnetic material in the presence of an external magnetic field is related to its paramagnetic susceptibility. The relationship between the temperature of the material and the paramagnetic susceptibility is described by the Curie Law:

$$\boldsymbol{\chi_m = \frac{C}{T}} \qquad \textbf{2.13}$$

where χ_m is the paramagnetic susceptibility, C is the Curie constant and T is the temperature.

The Curie Law operates under the assumption that the individual magnetic moments do not interact, but in reality, this only applies to magnetically dilute materials. Systems that express correlated behaviour such as ferromagnets and anti-ferromagnets cannot be described using the Curie Law. Magnetic behaviour of these materials is more accurately described by a corrected version of the Curie Law, which is called the Curie-Weiss Law:

$$\boldsymbol{\chi_m = \frac{C}{T-\theta} + K} \qquad \textbf{2.14}$$

where θ is the Weiss constant, a measure of the strength of magnetic interactions; K is the constant to account for any temperature independent part; and all other symbols are the same as in the Curie Law.

By plotting $1/\chi_m$ against temperature, values of C and θ can be obtained. The Curie constant is related to the spin only magnetic moment of the sample according to:

$$\boldsymbol{C = \frac{N_A \mu_B^2 \mu^2}{3k_B} \approx \frac{\mu^2}{8}} \qquad \textbf{2.15}$$

$$\boldsymbol{\mu = g\sqrt{s\,(s+1)}} \qquad \textbf{2.16}$$

where N_A is Avogadro's constant, μ_B is the Bohr magneton, k_B is the Boltzmann constant, μ is the magnetic moment, g is the gyromagnetic ratio and s is the sum of the spin quantum numbers of the electrons in the system.

By using the Curie constant extracted from experimental data and the spin-only formula, the spin states and the oxidation states of transition metal centres in the sample can be predicted.

2.11.2 Correlated Magnetic Behaviour and Magnetic Ordering

Some materials show behaviours in which there are strong interactions between electron spins, this is called correlated magnetic behaviour and leads to different types of magnetic ordering. These materials do not obey the Curie-Weiss law and possess a spontaneous moment.

Ferromagnetism arises when the localised magnetic moments align parallel to each other and hence results in a net magnetic moment. In contrast, anti-ferromagnetism arises when localised magnetic moments align anti-parallel to each other and hence results in zero net magnetic moment as all spins cancel out. If the angle between spins is not 180°, there is a small spontaneous net moment, and this is known as canted-antiferromagnetism. Ferrimagnetism is where localised magnetic moments of unequal magnitude align anti-parallel to each other and hence results in a net magnetic moment, which is much smaller than in ferromagnetically ordered materials.

2.11.3 Super-exchange and the Goodenough-Kanamori Rules

In transition metal oxides, the distance between metal centres is too far for direct orbital interactions with each other. However, the oxide/hydride ions act as bridges to mediate the magnetic coupling of spins by super-exchange. The strength of the super-exchange interaction depends on the bond angle, principal quantum number of the metal *d*-orbital and length of the M-O/H bond.

The system of semi-empirical rules developed by Goodenough and Kanamori[77], based on Anderson's work[78], can be used to predict the magnetic coupling that arises from super-exchange interactions between electrons in the *d*-orbitals of magnetic ions, separated by a ligand. According to the Goodenough-Kanamori rules, an M-O-M 180º super-exchange interaction (where M is a magnetic ion with partially filled *d*-orbitals) results in a strong antiferromagnetic coupling (Figure 2.9 left). On the other hand, an M-O-M 90º super-exchange interaction results in a weak ferromagnetic coupling (Figure 2.9 right).

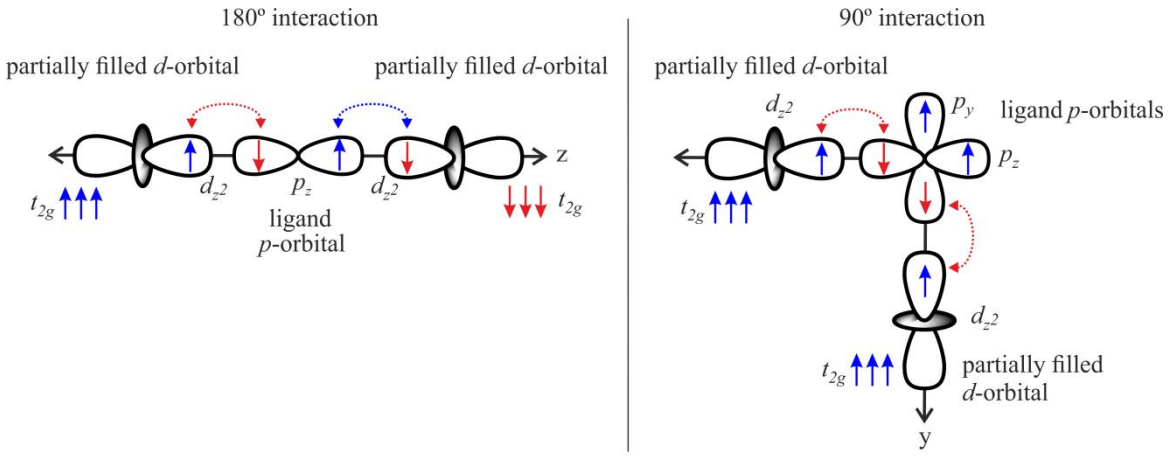


Figure 2.9. A schematic representation of super-exchange interactions of M-O-M in 180° (left) and 90° (right) arrangements.

The super-exchange interaction in the 180° arrangement is more important with regards to the work presented in this thesis and leads to the following predictions:

- The interaction between a half-filled orbital and either a filled or an empty orbital, favours ferromagnetic coupling.
- The interaction between two half-filled orbitals or between a filled and an empty orbital, favours antiferromagnetic coupling.

2.12 Transmission Electron Microscopy

Transmission electron microscopy (TEM) is a microscopy technique in which a beam of electrons is transmitted through a specimen to form an image. The specimen is most often an ultrathin section less than 100 nm thick or a suspension on a grid. An image is formed from the interaction of the electrons with the sample, as the beam is transmitted through the specimen, and then magnified and focused onto an imaging device. TEM are capable of imaging at a significantly high resolution and capture fine details as small as a single column of atoms.

In this work, this technique was used to resolve the crystal structure of the oxide-hydride phase $LaSr_3CoRuO_4H_4$, as a consequence of unpleasant fitting of collected powder diffraction data against the simple body-centred tetragonal unit cell (space group *I*4/*mmm*). Electron diffraction (ED) patterns were acquired on a FEI Tecnai transmission electron microscope operated at 200 kV. High angle annular dark field (HAADF) scanning transmission electron microscopy (STEM) images were acquired using a probe aberration corrected FEI Titan 80-300 "cubed" microscope operated at 300 kV. Samples for TEM analysis were prepared in the glove box filled with argon by grinding the material and dipping the copper TEM grid into the dry powder. The vacuum transfer holder was used to transfer the grids from the glove box to the microscope.

2.13 FAULTS Analysis

FAULTS is a Fortran90 program to simulate and refine X-ray powder diffraction (XRD) and neutron powder diffraction (ND) patterns of crystal systems with any type of coherent planar defect (e.g. stacking faults etc.). This program is based on the DIFFaX (Diffracted Intensity From Faulted Xtals) program[79, 80] and on the library CrysFML (Crystallographic Fortran Modules Library)[81, 82].

The FAULTS program behaves like a Rietveld refinement program in which the model for calculating the profile intensities is not a simple crystallographic three-dimensional periodic structure. The minimized function with respect to the set of free parameters collected in the array $\boldsymbol{a}$, like in the Rietveld method, is

$$\chi^2 = \sum_{i=1}^{n} w_i \left[y_i - y_{c,i}(\boldsymbol{a}) \right]^2 \qquad \textbf{2.17}$$

in which the calculated profile intensity at the point $i, y_{c,i}(\boldsymbol{a})$, is the convolution of the theoretically calculated intensity with the resolution function of the diffractometer, and w_i is the inverse of the variance of the observed profile intensity y_i.[83]

The FAULTS program was used to analyse the stacking faults (the intergrowth of n = 2 RP phase and the separate perovskite blocks throughout the main n = 1 RP phase) presented in the oxide-hydride phase $LaSr_3CoRuO_4H_4$, and tried to account for the imperfections found in fitting peak shapes of diffraction patterns against the simple body-centred tetragonal unit cell (space group *I*4/*mmm*) confirmed by TEM results.

In order to run simulations in the FAULTS program, the input control file (*.flts) must be written by the user, which involves the title section, the instrumental and size broadening section, the structural section, the layers section, the stacking section, the transitions section and the calculation section. The additional experimental section is only necessary in case a refinement needs to be done. The resulted diffraction patterns (*.dat) can be visualised by software such as WinPLOTR in FullProf Suite.

In the input control file, two kinds of layers were set up, the major n = 1 RP phase $LaSr_3CoRuO_4H_4$ (layer 1) and the minor n = 2 RP phase $LaSr_2CoRuO_3H_4$ (layer 2). The stacking type was set to be recursive and the number of layers was set to be infinite. In the transitions section, transition probabilities of layer 1 to layer 1, layer 1 to layer 2, layer 2 to layer 1 and layer 2 to layer 2 were specified and varied to investigate the dependence of

resulting diffraction patterns on these probabilities. A schematic representation of these two types of layers and how they can be stacked together is shown in Figure 2.10.

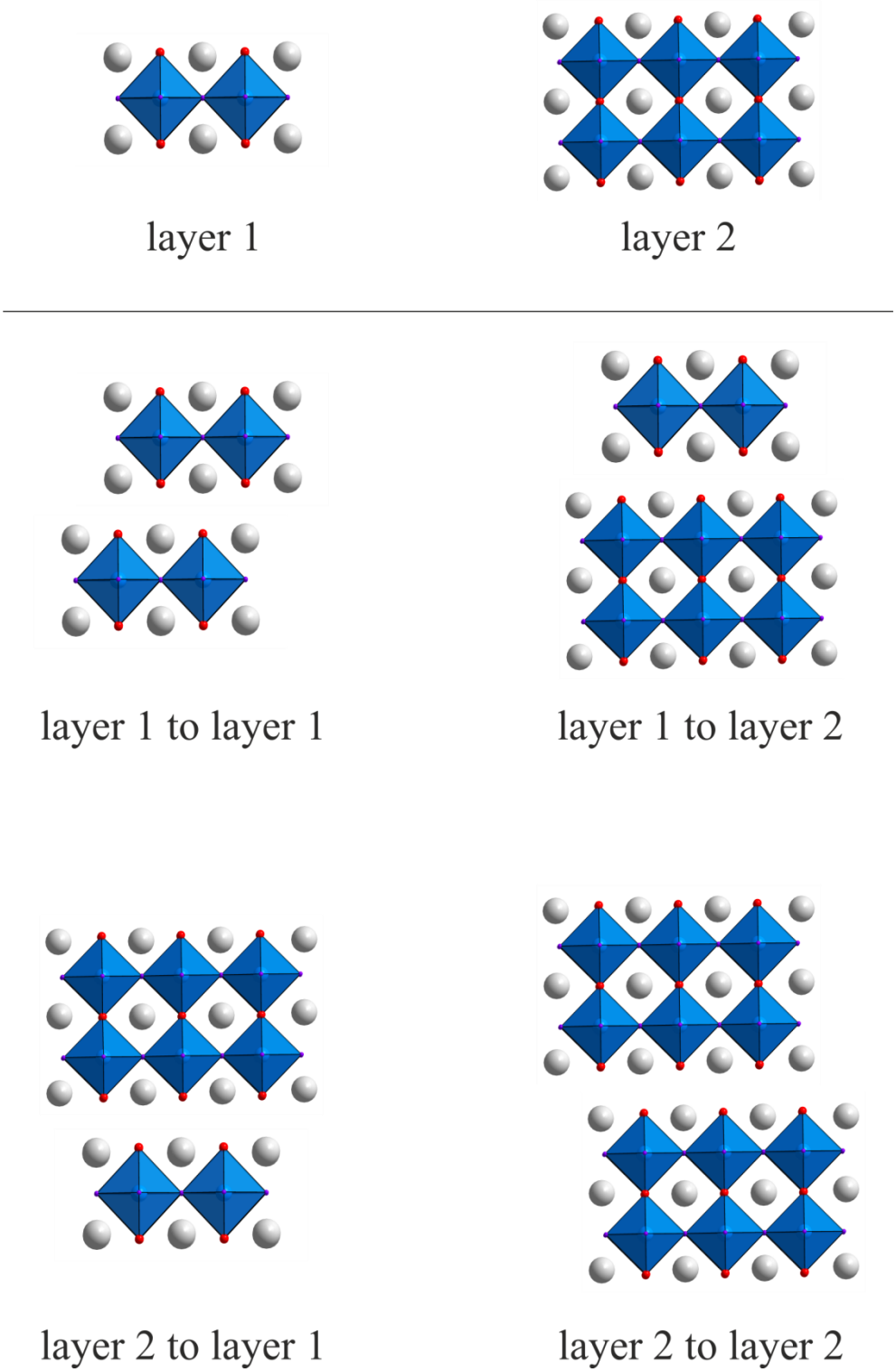


Figure 2.10. A schematic representation of two types of layers and four different stacking situations.

Chapter 3

Synthesis and Characterisation of $LaSr_3NiRuO_8$

3.1 Introduction

The low-temperature topochemical reactions of complex transition-metal oxides using solid-state reducing agents such as binary metal hydrides and finely divided electropositive metals have enabled the preparation of a wide range of metastable phases containing transition metals with novel oxidation states and coordinated geometries, as discussed in Chapter 1 Section 1.2. These metastable phases giving rise to various interesting electronic and magnetic properties such as multiferroic behaviour, high-temperature superconductivity and metal-to-insulator transitions.[6, 8, 49, 84]

Attempts to topochemically reduce 4*d* and 5*d* complex transition-metal oxides usually result in reduction to the metal elements. However, coupling the reduction of 4*d* and 5*d* transition metal cations to the formation of robust, stable frameworks containing 3*d* transition metal cations prevents them from being reduced all the way to their elemental state.

For example, the first reported example of Ru^{2+} in an extended transition-metal oxide is found in the topochemical reduction of perovskite $Sr(Fe_{0.5}Ru_{0.5})O_3$ to $Sr(Fe_{0.5}Ru_{0.5})O_2$ with CaH_2. The disordered arrangement of the Fe^{2+} and Ru^{2+} metal centres results in frustration of the magnetic couplings and spin glass behaviour, preventing a detailed exploration of the interactions between the 3*d* and 4*d* electronic states. The topochemical reductions of equivalent $n = 1$ and $n = 2$ Ruddlesden-Popper phases $Sr_2(Fe_{0.5}Ru_{0.5})O_4$ and $Sr_3(Fe_{0.5}Ru_{0.5})_2O_7$ with CaH_2 have been investigated as well, resulting formation of phases with compositions $Sr_2(Fe_{0.5}Ru_{0.5})O_{3.35}$ and $Sr_3(Fe_{0.5}Ru_{0.5})_2O_{5.67}$ respectively, both consist of two-phase mixtures of topochemically reduced phases with slightly different oxygen contents.

It is proposed that this phase separation is the result of short-range iron-ruthenium inhomogeneity in the starting materials.[23]

Similar to Fe/Ru perovskite example described above, the first Ru(II)-containing cation-ordered infinite layer phase $LaSrNiRuO_4$ is prepared via topochemical reduction of its parent double perovskite $LaSrNiRuO_6$ by using CaH_2 as a reducing agent. The ordered arrangement adopted by the nickel and ruthenium cations in $LaSrNiRuO_4$ allows magnetic couplings between 3*d* and 4*d* electronic states to be studied for the first time in an extended oxide.[10]

Building on previous work, further investigations for isolation of Ruddlesden-Popper phases containing pure, highly reduced Ru^{2+} metal centres were carried out. In particular, the possibility of reducing the n = 1 Ruddlesden-Popper phase $LaSr_3NiRuO_8$ to form anion-deficient phases and oxide-hydride phase was well-investigated.

3.2 Experimental

Samples of $LaSr_3NiRuO_8$ were synthesized by a high-temperature ceramic method as described in Chapter 2 Section 2.1.1. Suitable stoichiometric ratios of La_2O_3 (99.999%, dried at 900°C), $SrCO_3$ (99.994%), RuO_2 (99.99%, dried at 800°C) and NiO (99.998%) were ground together using an agate mortar and pestle, transferred into an alumina crucible, and then heated at a rate of 1 ºC min^{-1} to 1000°C in air to decompose the carbonate. The sample was reground, pressed into pellets and then heated for 3 periods of 48 hours at 1200 °C in air, with grinding between heating periods. The reaction progress was monitored by laboratory X-ray diffractometer and once the reaction was deemed complete, synchrotron X-ray powder diffraction data and neutron powder diffraction data were collected from the resulting phase.

3.3 Results

3.3.1 Structural Characterisation of $LaSr_3NiRuO_8$

3.3.1.1 Synchrotron X-Ray Powder Diffraction

Synchrotron X-ray powder diffraction data (Chapter 2 Section 2.5.1.2) was collected from a sample of $LaSr_3NiRuO_8$. These data could be readily indexed using a body-centred tetragonal unit cell (space group *I4/mmm*) with lattice parameters: a = 3.89044(2) Å and c = 12.62974(7) Å. A structural model was constructed, based on an n = 1, A_2BO_4 Ruddlesden-Popper phase with a 1 : 3 La : Sr solid-solution on the A-site and a 1 : 1 Ni : Ru solid-solution on the B-site. This model was refined against the data to achieve a good statistical fit. The refined plots are shown in Figure 3.1 with detailed structural parameters listed in Table 3.1 and 3.2.

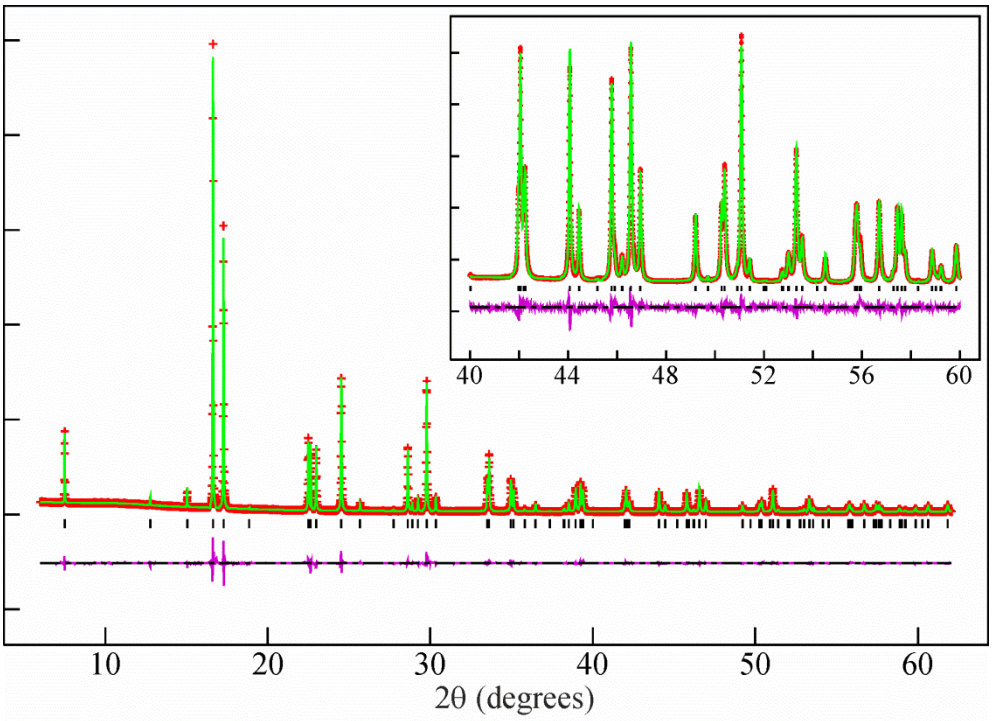


Figure 3.1: Rietveld refinement of $LaSr_3NiRuO_8$ using *I 4/m m m* model against synchrotron X-ray powder diffraction data. Observed (red), calculated (green), and difference plots (pink) are shown.

Atom	Wyckoff Position	*x*	*y*	*z*	Fraction	U_{iso} equiv. ($Å^2$)
La/Sr(1)	4*e*	0	0	0.35709(2)	0.25/0.75	0.0113
Ni/Ru(1)	2*a*	0	0	0	0.5/0.5	0.0040
O(1)	4*e*	0	0	0.1656(1)	1	0.0162
O(2)	4*c*	0.5	0	0	1	0.0082
$LaSr_3NiRuO_8$ space group *I*4/*mmm* (#139) Formula weight : 689.53 g mol^{-1}, Z = 2 *a* = 3.8904(1) Å, *c* = 12.6297(1) Å, Volume = 191.16(1) $Å^3$						
Radiation source: Synchrotron X-ray, λ = 0.82626(1) Temperature: 298 K χ^2 = 9.87; *wRp* = 5.67%; *Rp* = 3.63%.						

Table 3.1: Structural parameters from the refinement of $LaSr_3NiRuO_8$ against synchrotron X-ray powder diffraction data collected at 298K.

Atom	U_{11}	U_{22}	U_{33}
La/Sr(1)	0.01366(22)	0.01366(22)	0.00648(28)
Ni/Ru(1)	0.00257(32)	0.00257(32)	0.00487(47)
O(1)	0.0199(12)	0.0199(12)	0.0085(21)
O(2)	0.0009(19)	0.0162(22)	0.0072(20)

Table 3.2. Anisotropic displacement factors from the structural refinement of $LaSr_3NiRuO_8$ against synchrotron X-ray powder diffraction data collected at 298 K.

3.3.1.2 Neutron Powder Diffraction

The neutron powder diffraction measurement at ambient temperature was carried out at D2B diffractometer in ILL (Chapter 2 Section 2.5.2.2). The body-centred tetragonal unit cell shown in Figure 3.2 (space group *I*4/*mmm*) was used to refine the data. The refinement converged readily to a give good statistical fit for ambient temperature data. The observed, calculated, and difference plots are shown in Figure 3.3. Full details of the structural parameters are given in Table 3.3, anisotropic displacement factors are given in Table 3.4 and selected bond lengths are given in Table 3.5.

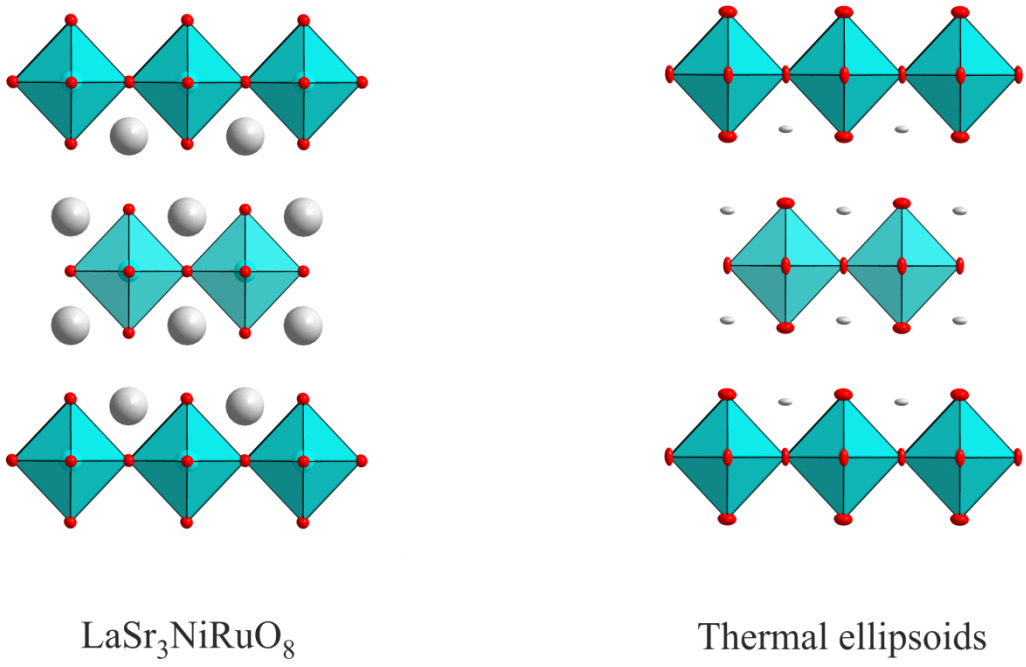
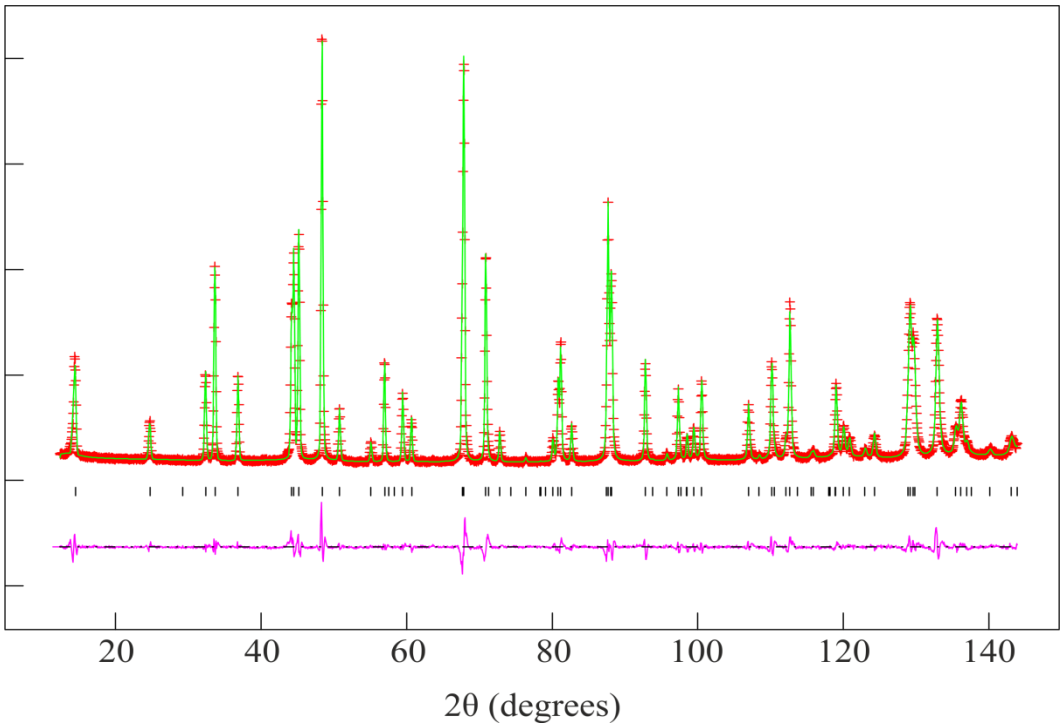


Figure 3.2. Crystal structure of $LaSr_3NiRuO_8$ (space group *I*4/*mmm*) with thermal ellipsoids displayed.



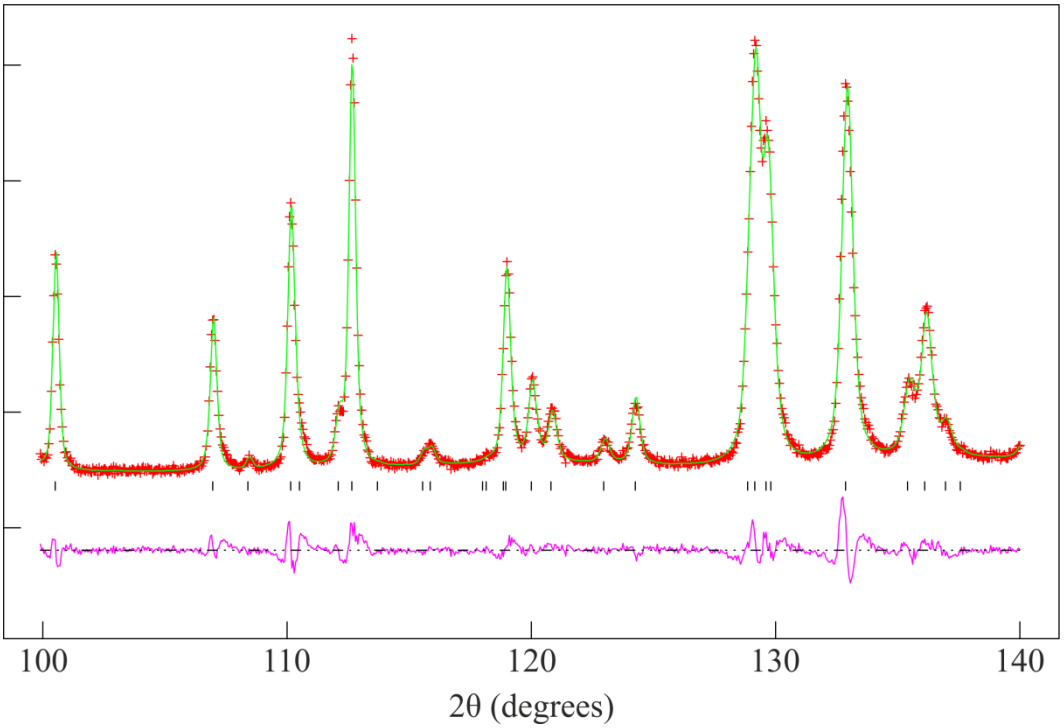


Figure 3.3. Observed, calculated and difference plots from the refinement of $LaSr_3NiRuO_8$ against neutron powder diffraction data collected at 298 K, full range (top) and high angles (bottom).

Atom	Wyckoff Position	*x*	*y*	*z*	Fraction	U_{iso} equiv. ($Å^2$)
La/Sr(1)	4*e*	0	0	0.3565(1)	0.25/0.75	0.0058
Ni/Ru(1)	2*a*	0	0	0	0.5/0.5	0.0013
O(1)	4*e*	0	0	0.1628(2)	1	0.0095
O(2)	4*c*	0.5	0	0	1	0.0046
$LaSr_3NiRuO_8$ space group *I*4/*mmm* (#139) Formula weight : 689.53 g mol^{-1}, Z = 2 *a* = 3.8887(1) Å, *c* = 12.6265(4) Å, Volume = 190.94(1) $Å^3$						
Radiation source: Neutron Powder Diffraction, λ = 1.5943(2) Temperature: 298 K χ^2 = 5.633; *wRp* = 5.75%; *Rp* = 4.27%.						

Table 3.3. Structural parameters from the refinement of $LaSr_3NiRuO_8$ against neutron powder diffraction data collected at 298 K.

Atom	U_{11}	U_{22}	U_{33}
La/Sr(1)	0.00921(63)	0.00921(63)	0.0024(11)
Ni/Ru(1)	0.00374(72)	0.00374(72)	0.0004(14)
O(1)	0.01501(70)	0.01501(70)	0.0062(18)
O(2)	0.0040(11)	0.0032(12)	0.0132(14)

Table 3.4. Anisotropic displacement factors from the structural refinement of $LaSr_3NiRuO_8$ against neutron powder diffraction data collected at 298 K.

Cation	Anion	length (Å)
La/Sr(1)	O(1)	2.446(3) × 1
	O(1)	2.761(1) × 4
	O(2)	2.658(1) × 4
Ni/Ru(1)	O(1)	2.056(3) × 2
	O(2)	1.944(1) × 4

Table 3.5. Selected bond lengths from the refined structure of $LaSr_3NiRuO_8$.

3.3.2 Magnetic Characterisation of $LaSr_3NiRuO_8$

Zero-field-cooled and field-cooled magnetization data collected from $LaSr_3NiRuO_8$ as a function of temperature in an applied field of 100 Oe using a SQUID magnetometer (Chapter 2 Section 2.10), are shown in Figure 3.4 (top). Data in the range $150 < T / K < 300$ can be fitted to the Curie-Weiss law ($\chi = C/(T - \theta)$) to yield values of $C = 2.73(1)$ cm^3 K mol^{-1}, $\theta = +91.5(2)$ K, hence a value of $\mu^2 = 21.84$ μ_B can be calculated. The zero-field-cooled and field cooled data diverge below T = 55 K, consistent with the onset of canted antiferromagnetic order. Magnetization data collected at 300 K as a function of applied field is linear and passes through the origin. Analogous data collected at 5 K after cooling in an applied field of 5000 Oe exhibit hysteresis consistent with weak ferromagnetism (Figure 3.4 (bottom)).

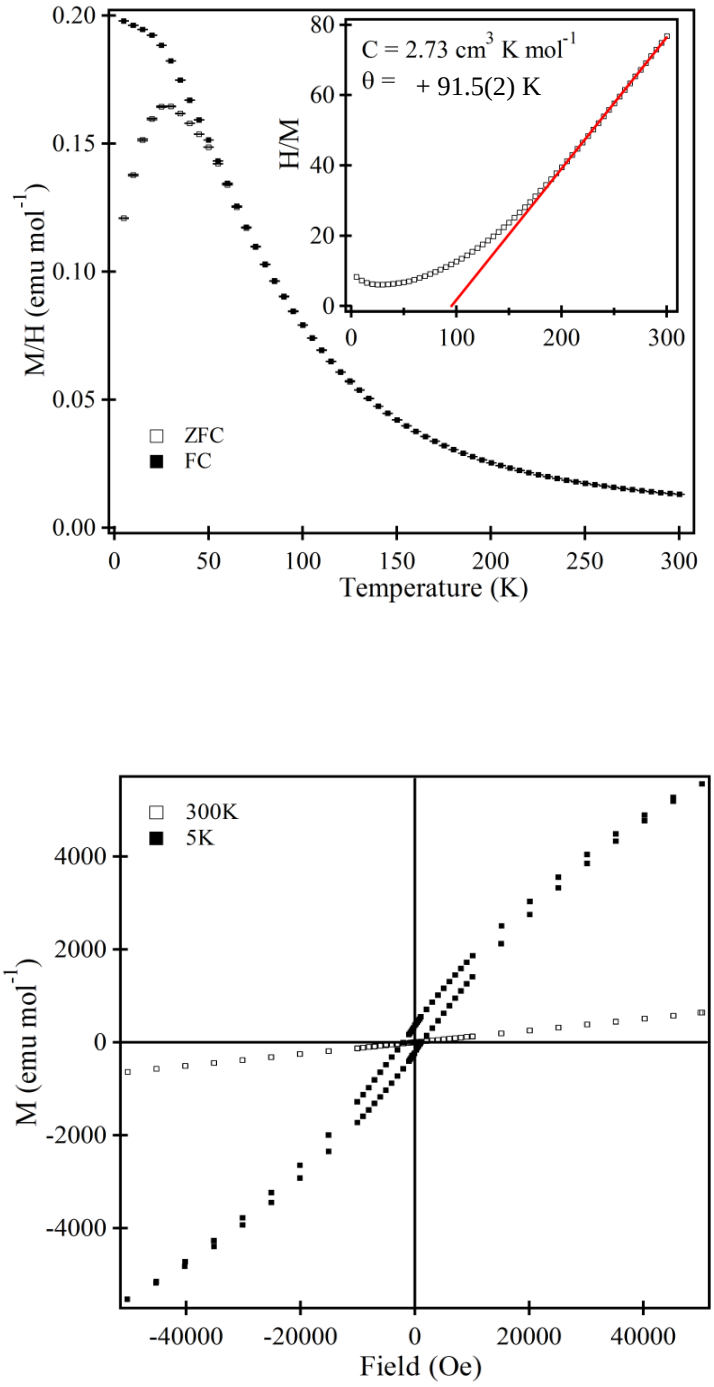


Figure 3.4. Zero-field-cooled and field-cooled magnetisation data collected in an applied field of 100 Oe. Inset shows fit to the Curie-Weiss law (top); Magnetisation data collected as a function of applied field (bottom) from $LaSr_3NiRuO_8$.

By considering the chemical formulation of $LaSr_3NiRuO_8$, it should consist of either Ni^{2+} and Ru^{5+}, or Ni^{3+} and Ru^{4+} if we assume electrons are localised for these B-site transition metal cations (Figure 3.5).

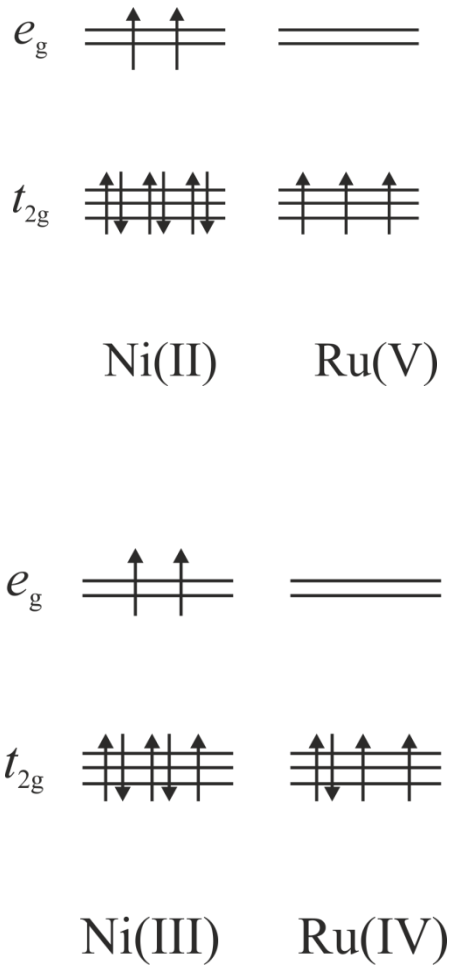


Figure 3.5. Predicted spin states of B-site transition metal cations in $LaSr_3NiRuO_8$.

In the first case which $LaSr_3NiRuO_8$ contains Ni^{2+} and Ru^{5+} centres, with spin states of $S = 1$ and $S = {}^3/_2$ respectively, the calculated value of $\mu^2 = 21.84\ \mu_B$ observed from experimental data is approximately 95.0% of the expected value of $\mu^2 = 23\ \mu_B$ derived from

spin-only formula, which agrees reasonably well. In the second case which $LaSr_3NiRuO_8$ contains Ni^{3+} and Ru^{4+} centres, with spin states of $S = {}^3/_2$ and $S = 1$ respectively, the value of the expected moment μ^2 derived from spin-only formula should be 23 μ_B as well. Therefore the magnetic moment cannot be used to predict which combination it should be as the expected moments are the same for both combinations. However, several hole-doped versions of $LaSr_3NiRuO_8$ have been prepared (presented in Chapter 5), where part of Ni centres is more likely to be oxidized than Ru centres, and the process of oxidising Ni^{3+} to Ni^{4+} is more energetically expensive than oxidising Ni^{2+} to Ni^{3+}. Therefore the combination of Ni^{2+} and Ru^{5+} centres stands out based on the oxidizing behaviour of Ni centres in doped $LaSr_3NiRuO_8$ series.

Goodenough Kanamori rules[85] would predict strong ferromagnetic interactions between half-filled Ni^{2+} e_g orbitals and empty Ru^{5+} e_g orbitals, as well as between filled Ni^{2+} t_{2g} orbitals and half-filled Ru^{5+} t_{2g} orbitals, but magnetisation data collected using a SQUID magnetometer shows a low saturated magnetic moment consistent with canted antiferromagnetic interactions at low temperature. Similar magnetic behaviour has also been seen in the magnetisation data collected from the equivalent perovskite phase.[86] A possible explanation of this complicated magnetic behaviour could be that there are both types of magnetic ordering in the material. It could have ferromagnetic ordering within each layer between Ni and Ru centres, but with layers stacked antiferromagnetically to result in such a low saturated moment. Further Pair Distribution Function (PDF) analysis is required to investigate its detailed cation arrangement as it may adopt a paracrystalline order with rigorous Ni/Ru order within each perovskite sheet, but no order between layers as they are not rigidly connected along *c* axis like its cation-ordered double perovskite analogue $LaSrNiRuO_6$.[10]

3.4 Discussion

3.4.1 Cation Arrangement in $LaSr_3NiRuO_8$

The cation arrangement in the n = 1 Ruddlesden-Popper phase $LaSr_3NiRuO_8$ remains mysterious so far. From diffraction point of view, there are no extra peaks which cannot be described by the simple body-centred tetragonal unit cell mentioned in Section 3.3.1, indicate no sign of cation-ordering in this phase. However, from the magnetisation data collected using a SQUID magnetometer, it shows strong evidence for an antiferromagnetic ground state.

Unlike its equivalent double perovskite, $LaSrNiRuO_6$, which adopts a chequer-board ordered arrangement of Ni and Ru centres as shown in Figure 3.6 (b)[10], the n = 1 Ruddlesden-Popper phase $LaSr_3NiRuO_8$ shows no indication of B-site cation ordering, despite the large charge difference between Ni^{2+} and Ru^{5+} centres should favour an ordered arrangement. A simple body-centred tetragonal unit cell (space group *I4/mmm*) with single A-cation site and single B-cation site can perfectly describe the crystallographic structure of $LaSr_3NiRuO_8$, consisting of a 1 : 3 La : Sr solid-solution on the A-site and a 1 : 1 Ni : Ru solid-solution on the B-site.

In contrast, if the n = 1 Ruddlesden-Popper phase $LaSr_3NiRuO_8$ is cation-disordered, like the case of simple perovskite $SrFe_{0.5}Ru_{0.5}O_3$ (Figure 3.6 (a)), it should have similar magnetic frustration and spin-glass behaviour[11], which are not observed in the magnetisation data collected using a SQUID magnetometer.

Therefore Pair Distribution Function (PDF) analysis is required to investigate the detailed cation arrangement in the n = 1 Ruddlesden-Popper phase $LaSr_3NiRuO_8$.

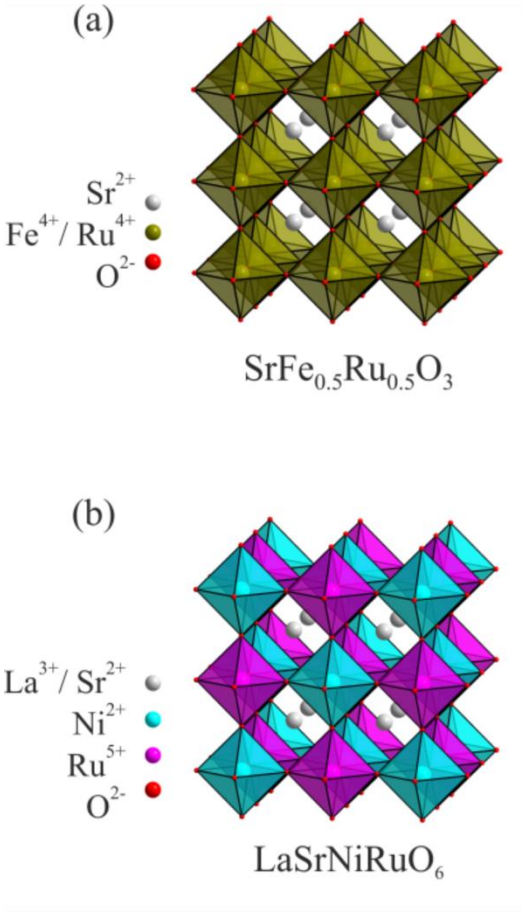


Figure 3.6. Crystallographic structures of (a) cation-disordered simple perovskite $SrFe_{0.5}Ru_{0.5}O_3$ and (b) cation-ordered double perovskite $LaSrNiRuO_6$ [10, 11].

3.4.2 Slow-Cooled and Quenched $LaSr_3NiRuO_8$ Samples

From previous study, we found that although the slow-cooled and quenched $LaSrNiRuO_6$ samples are chemically identical, the difference in cooling rates results in microstructural differences between slow-cooled and quenched samples as the cooling rates applied in the synthesis of the materials affect the growth of crystalline domains. These microstructural differences could be reflected by the close inspection of peak shapes in high-resolution XRD patterns. Peak shapes are shaper and better-defined in slow-cooled samples

while they are broader and closer-overlapped in quenched ones. This observation could be explained by the phase transition reported in literature for this double perovskite $LaSrNiRuO_6$ [87], which involves the change from the monoclinic crystal system of space group $P2_1/n$ to a trigonal crystal system of space group $R\text{-}3$ upon heating above the transition temperature of 670 K (396.85 °C). Slow-cooling results in the growth of the monoclinic crystalline domains that form upon cooling, and are trapped before they are allowed to grow in the quenched sample.

$LaSrNiRuO_6$ that was rapidly cooled, exhibits smaller crystalline domains compared to slow-cooled samples and makes the topochemical reduction proceed to completion before any non-topochemical decompositions happen. However, the slow-cooled sample requires higher reaction temperatures as the build-up in lattice strain during the reduction lifts the reaction energy barrier, which overcome the energy needed for the competing decomposition reaction. Therefore materials that were slow cooled cannot reach complete reduction to form the pure infinite layer phase $LaSrNiRuO_4$.[10]

Inspired by the differences in microstructure and topochemical reactivity for slow-cooled and quenched $LaSrNiRuO_6$ samples, different rates of cooling, slow-cooled inside the furnace by 5 °C min^{-1}, quenched to ambient temperature on the bench and quenched in liquid nitrogen were applied to three identical samples of $n = 1$ Ruddlesden-Popper phase $LaSr_3NiRuO_8$.

By comparing the synchrotron X-ray powder diffraction data of these three samples, no obvious peak broadening or asymmetry could be observed, unlike in the $LaSrNiRuO_6$ case. Therefore different rates of cooling applied to $LaSr_3NiRuO_8$ do not result in microstructural differences because $LaSr_3NiRuO_8$ does not undergo similar phase transition in the temperature range we have explored so far.

The topochemical reactivity of these three samples towards CaH_2 has been investigated as well. They do not show any differences in their reactivity as their reduction profiles look similar to each other and the distinct phases achieved are the same at each reaction temperature.

Therefore slow-cooled and quenched $LaSr_3NiRuO_8$ samples are chemically and microstructurally identical, and they have no differences in topochemical reactivity towards CaH_2.

3.5 Conclusion

The n = 1 Ruddlesden-Popper phase $LaSr_3NiRuO_8$ has been prepared via a traditional high-temperature ceramic synthetic route from binary metal oxides and metal carbonates. Both synchrotron X-ray powder diffraction data and ambient temperature neutron powder diffraction data could be readily indexed by a simple body-centred tetragonal unit cell (space group *I4/mmm*) with lattice parameters a = 3.8887(1) Å, c = 12.6265(4) Å. There are no phase transitions within the temperature range we have explored so far, BO_6 octahedrals remain undistorted and the high symmetry unit cell can be used to index patterns throughout the whole temperature range.

The magnetisation data collected using a SQUID magnetometer show strong evidence of a canted antiferromagnetic ground state consisting of Ni^{2+} and Ru^{5+} centres, with spin states of S = 1 and $S = {}^{3}/_{2}$ respectively, but Goodenough Kanamori rules[85] would predict strong ferromagnetic interactions between them. Therefore it could have ferromagnetic ordering within each layer between Ni^{2+} and Ru^{5+} centres, but with layers stacked antiferromagnetically to result in such a low saturated moment. The detailed cation

arrangement of $LaSr_3NiRuO_8$ (whether it is a paracrystalline material or not) needs to be confirmed by Pair Distribution Function (PDF) analysis.

Topochemical manipulations of $LaSr_3NiRuO_8$ have been intensively studied and show the potential to form various distinct phases with different oxygen and hydrogen contents. Outcomes and detailed analysis are presented in the following Chapter 4 and 6.

In addition, partially oxidizing or reducing B-site cations have been achieved by manipulating the ratio between La and Sr to form a series of doped versions of $LaSr_3NiRuO_8$ and their topochemical reactivity towards CaH_2 has been investigated as well. Outcomes and detailed analysis are presented in the following Chapter 5.

Chapter 4

Synthesis and Characterisation of $LaSr_3NiRuO_4H_4$

4.1 Introduction

As discussed in Chapter 1 Section 1.2, in order to widen the range of complex transition-metal oxides that can be prepared, synthetic routes which have access to kinetic controlled phases can be adopted, and hence result in the formation of phases with novel metal oxidation states and coordination geometries which could potentially exhibit a wide variety of interesting physical and chemical properties.

The attempted topochemical reduction of the n = 1 Ruddlesden-Popper phase $LaSr_3NiRuO_8$ with the solid-state binary metal hydride CaH_2, in sealed ampoules yields compositions in the range of $LaSr_3NiRuO_{8-x}$ ($0 \leq x \leq 2$) at different reaction temperatures (350 °C – 460 °C) and the final reduced phase achieved as the result of hydride-for-oxide ion substitution is $LaSr_3NiRuO_4H_4$, according to reaction [1]:

$$LaSr_3NiRuO_8 + 4\ CaH_2 \longrightarrow LaSr_3NiRuO_4H_4 + 4\ CaO + 2\ H_2 \qquad [1]$$

Detailed characterisations of this oxide-hydride phase will be described in this chapter.

4.2 Experimental

The starting material n = 1 Ruddlesden-Popper phase $LaSr_3NiRuO_8$, has been prepared by the traditional high-temperature ceramic synthesis as described in Chapter 2 section 2.1.1. A sample of $LaSr_3NiRuO_4H_4$ suitable for analysis by neutron powder diffraction was prepared by grinding together approximately 1.5 g of $LaSr_3NiRuO_8$ with 0.4 g of CaH_2 in an

argon filled glovebox using an agate mortar and pestle. The resulting powders were sealed in a silica ampoule and heated at 450 °C for 3 periods of 7 days, with the sample being reground between heating periods. Once the reaction was deemed complete, the reaction mixture was washed, under nitrogen, with 8 × 25 ml of 0.1 M solution of NH_4Cl in methanol in order to remove the CaO formed as a by-product of the reaction and any unreacted CaH_2. This was then followed by washing with 5 × 25 ml of clean methanol to dissolve NH_4Cl residues. The sample was then dried under vacuum.

4.3 Results

4.3.1 Initial investigation of reactivity of $LaSr_3NiRuO_8$ towards CaH_2

Small scale test reactions were performed by mixing ~300 mg of $LaSr_3NiRuO_8$ with 8 mole equivalents of CaH_2 in an argon-filled glove box. The mixtures were then sealed under vacuum in silica ampoules and heated in the temperature range $350 \leq T / ºC \leq 460$. X-ray powder diffraction was used to monitor the reaction progress. CaO was observed as the by-product of this reduction which can be readily removed by dissolving into a weak acid like NH_4Cl in methanol. Since H_2 gas was accumulated inside the reaction vessels, the capacity of the ampoules used was carefully chosen to prevent the high pressure building up in the apparatus. In order to describe the whole reduction profile, temperature intervals of 25 °C were chosen and the changes observed in XRD patterns with respect to different reaction temperatures are summarized in Table 4.1. The symmetry of the main phase observed in XRD patterns was lowered from tetragonal to orthorhombic once the deintercalation of oxide ions started. A number of distinct phases $LaSr_3NiRuO_7$, $LaSr_3NiRuO_6$ and $LaSr_3NiRuO_4H_4$ were observed before non-topochemical decomposition of the starting material occurred (Figure 4.1) [88].

Reaction condition	Symmetry of the main lattice	Lattice parameters (estimated)/ Å	Description	Chemical composition
Starting material	Tetragonal	*a* = 3.89 *b* = 3.89 *c* = 12.63	Nice sharp 103 and 110 peaks, very crystalline	$LaSr_3NiRuO_8$
350 °C	Orthorhombic	*a* = 3.89 *b* = 3.81 *c* = 12.70	Visible broadening and splitting of 103 peak	$LaSr_3NiRuO_{8-x}$
375 °C	Orthorhombic	*a* = 3.89 *b* = 3.81 *c* = 12.70	Further broadening and splitting of 103 peak	$LaSr_3NiRuO_{8-x}$
400 °C	Orthorhombic	*a* = 3.91 *b* = 3.79 *c* = 12.70	103 peak splitting into 103 and 013	$LaSr_3NiRuO_{7.01(3)}$
425 °C	Orthorhombic	*a* = 3.84 *b* = 3.57 *c* = 13.00	Further splitting between 103 and 013 peaks	$LaSr_3NiRuO_{5.98(2)}$
450 °C	Tetragonal	*a* = 3.62 *b* = 3.62 *c* = 13.32	New tetragonal phase with smaller *ab*-plane	$LaSr_3NiRuO_4H_4$
460 °C	N/A	N/A	Decomposition	La_2O_3 etc.

Table 4.1. Results from initial investigation of topochemical reduction of $LaSr_3NiRuO_8$ with CaH2 in sealed silica ampoules.

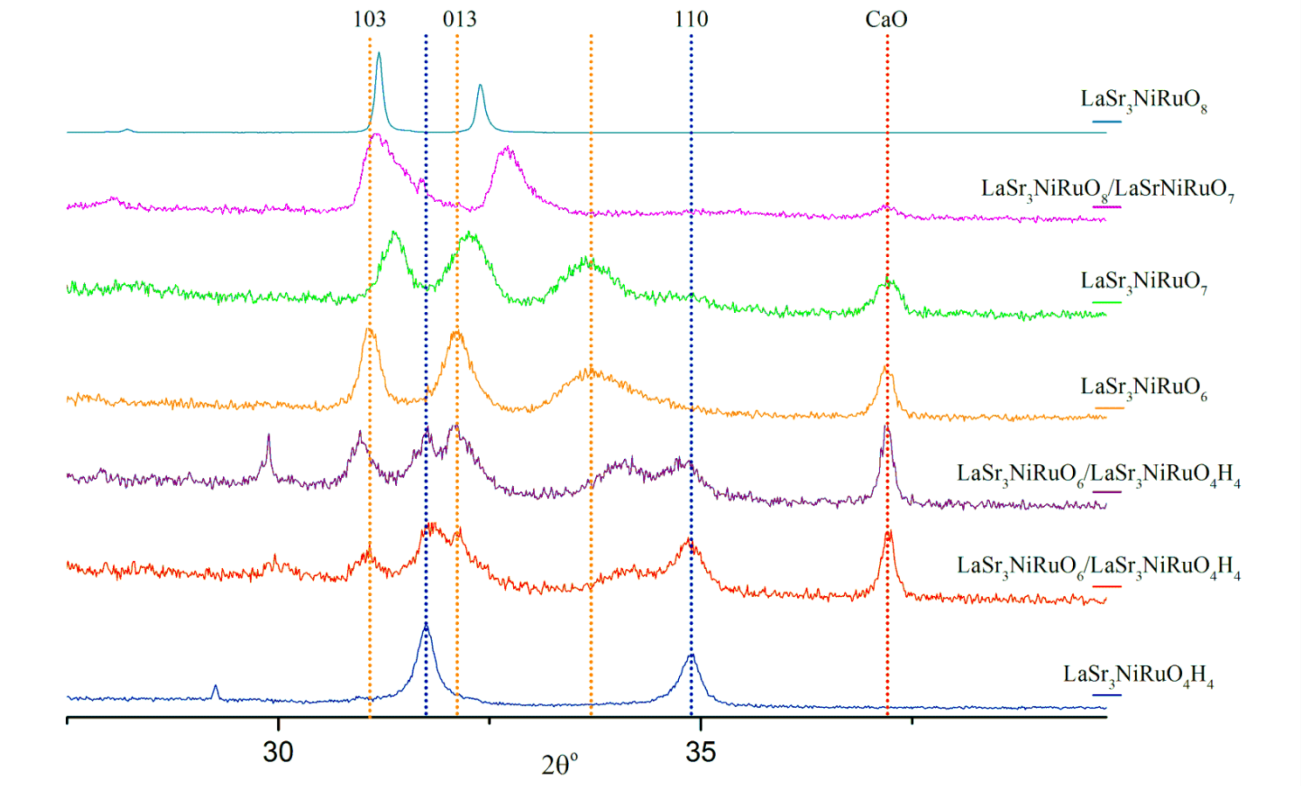


Figure 4.1. Topochemical reduction profile of $LaSr_3NiRuO_8$ with CaH_2 to form a range composition of $LaSr_3NiRuO_{8-x}$.

The first distinct reduced phase observed is $LaSr_3NiRuO_7$ at 400 °C which could be roughly indexed by an orthorhombic cell with slight elongation in *a* and *c* axis and shrinking of the *b* axis compared to its tetragonal parent oxide phase $LaSr_3NiRuO_8$. The original 103 peak in the starting material has already become two peaks 103 and 013. The phase composition was determined by an oxidative thermogravimetric analysis (TGA), as described in Chapter 2 Section 2.7, under a steady oxygen flow which showed a mass gain of approximately one oxygen to reoxidize back to the starting material $n = 1$ Ruddlesden-Popper phase $LaSr_3NiRuO_8$.

After pushing the reaction harder by raising the reaction temperature to 425 °C, oxide ions in the lattice have greater mobility so further reductive deintercalation occurs. A second distinct reduced phase which could be readily indexed by a new body-centred orthorhombic cell (a = 3.84 Å, b = 3.57 Å, c = 13.00 Å) is formed and oxidative thermogravimetric analysis suggests a composition of $LaSr_3NiRuO_6$.

In order to see whether the second distinct phase $LaSr_3NiRuO_6$ is the most reduced phase can be formed with CaH_2 or not, the temperature was raised to 450 °C. However, instead of undergoing non-topochemical decomposition, a new phase forms, which has the same tetragonal symmetry as the starting material, $LaSr_3NiRuO_8$, but with a significantly smaller a-b plane and larger c lattice parameter. The third distinct reduced phase could be readily indexed by using a body-centred tetragonal unit cell with lattice parameters a = 3.6226(2) Å, c = 13.317(1) Å. The reaction temperature is raised again to 460 °C and the resulting product is found to be decomposed into La_2O_3 and other binary oxides, therefore the third distinct phase appears to be the most reduced analogue of the parent oxide phase which can reach with CaH_2 as the reducing agent.

In order to determine the chemical content of a-b plane in this smaller tetragonal cell, a survey of bond lengths in the literature was carried out (Table 4.2)[14, 41, 45, 86] to compare with the bond length in the third distinct reduced phase.

Composition of Material	Average bond length/ Å	Type of bond
$LaSr_3NiRuO_{8-x}$ (450 °C)	1.811(1)	M-?-M
$LaSr_3NiRuO_8$	1.9451(1)	M-O-M
$LaSrNiRuO_4$	1.729(1)	M-□-M
	2.000(6)	M-O-M
$LaSrCoO_3H_{0.7}$	1.8016(3)	Co-H-Co
$SrVO_2H$	1.8301(4)	V-H-V
Sr_2VO_3H	1.8301(4)	V-H-V
$SrCrO_2H$	1.91720*	Cr-O/H-Cr
*bond length averaged over the hydride and oxide bonds. Oxide hydride site occupancy 0.663(2)/0.337(2)		

Table 4.2. Survey of metal-oxide and metal-hydride bond lengths in literatures from known compounds.[14, 41, 45, 86]

From Table 4.2, the third distinct phase $LaSr_3NiRuO_{8-x}$ formed at 450 °C has an average bond length to be 1.811(1) Å which is clearly too short for an M-O-M bond and too long for an M-□-M bond, however it falls into the range of average bond lengths of M-H-M cases. In order to prove the presence of hydride ions inside the lattice, neutron powder diffraction data is required as hydride ion has a negative neutron scattering (H^1 neutron scattering length = -3.73 fm) which is clearly different from oxide ion. Also since hydride ion has only two electrons which is too light compared to other elements in the phase, it is 'invisible' in X-ray powder diffraction data.

4.3.2 Structural and Chemical Characterisation of $LaSr_3NiRuO_4H_4$

4.3.2.1 Neutron Powder Diffraction

Neutron powder diffraction measurements performed at ambient temperature and low temperature were carried out at WISH diffractometer, ISIS (Chapter 2 Section 2.5.2.1) and the ambient data collected was refined against a model based on the structure of its parent oxide phase $LaSr_3NiRuO_8$ (space group *I*4/*mmm*), but gave a poor fit until the occupancies of the anion sites were refined. It was observed that the 'equatorial' anion site occupancy rapidly refined to a negative value, indicating the presence of hydrogen at this position (H^1 neutron scattering length = -3.73 fm). Once the atom on this site had been changed to a hydride ion, the occupancy refined to unity, within error, confirming the stoichiometry of the phase as $LaSr_3NiRuO_4H_4$ (Figure 4.2). The refined plots are shown in Figure 4.3 with detailed structural parameters in Table 4.3, 4.4 and 4.5.

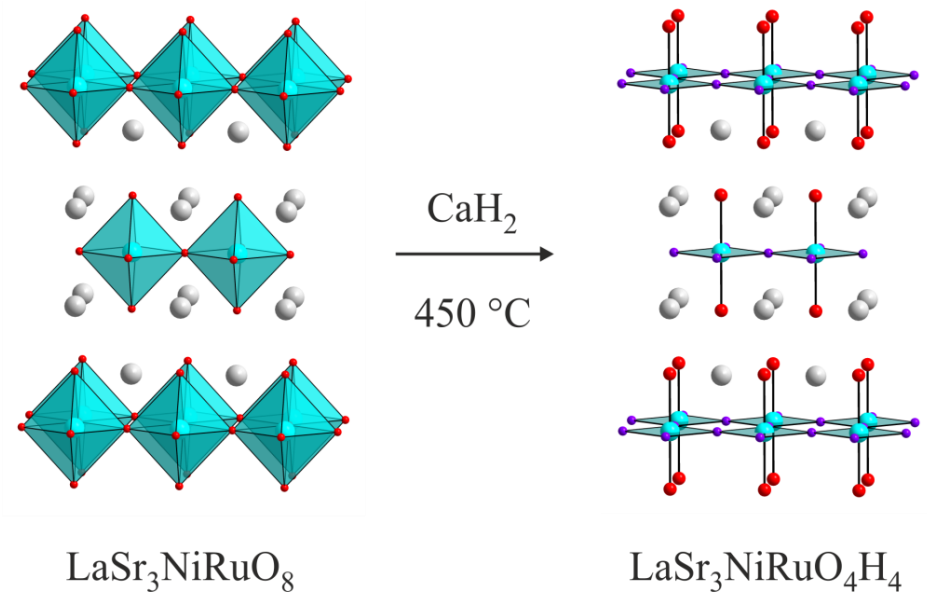


Figure 4.2. Topochemical reduction of $LaSr_3NiRuO_8$ with CaH_2 to form reduced oxide-hydride phase $LaSr_3NiRuO_4H_4$ with H^- substituted into equatorial positions.

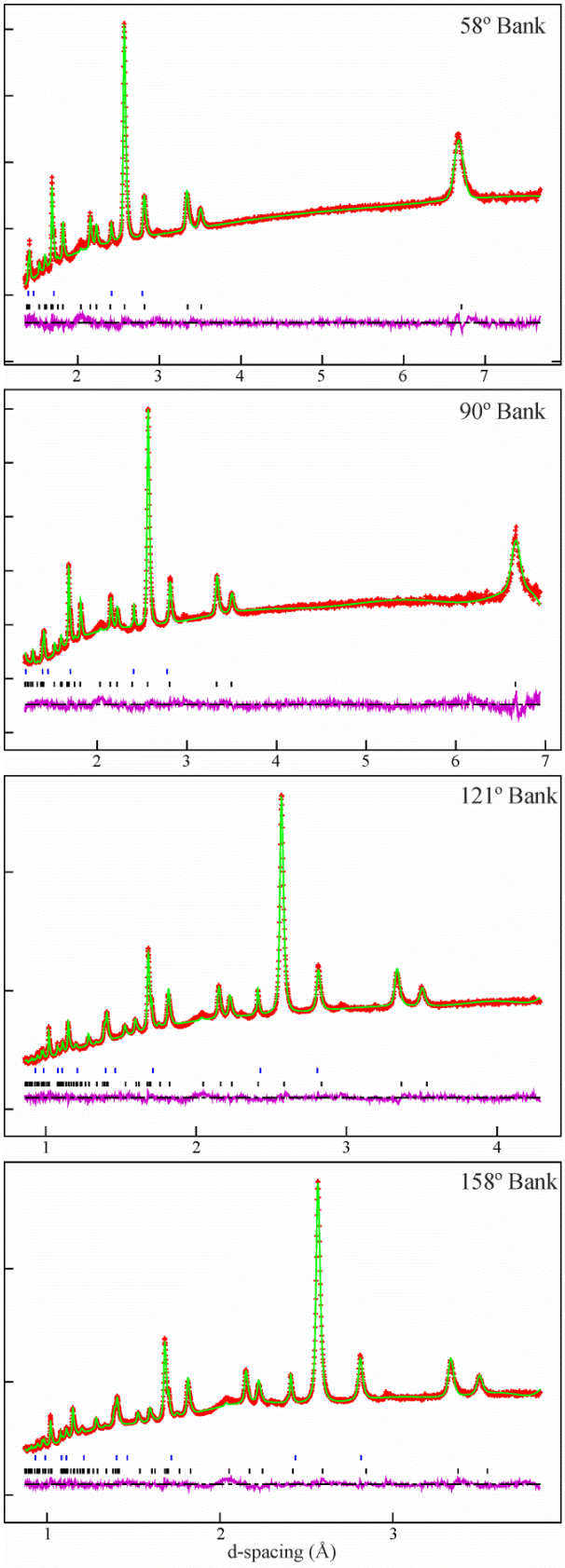


Figure 4.3. Observed, calculated and difference plots from the refinement of $LaSr_3NiRuO_4H_4$ against neutron powder diffraction data collected at 298 K. Lower tick marks indicate peak positions of the majority phase, upper tick marks CaO.

Atom	Wyckoff Position	*x*	*y*	*z*	Fraction	U_{iso} equiv.(Å^2)
La/Sr(1)	4*e*	0	0	0.3528(1)	0.25/0.75	0.011
Ni/Ru(1)	2*a*	0	0	0	0.5/0.5	0.034
O(1)	4*e*	0	0	0.1658(2)	1	0.027
H(1)	4*c*	0.5	0	0	1	0.069
$LaSr_3NiRuO_4H_4$ space group *I*4/*mmm* (#139) Formula weight : 629.57 g mol^{-1}, Z = 2 Mass fraction: 97.3(2)% *a* = 3.6226(2) Å, *c* = 13.317(1) Å, Volume = 174.77(4) Å^3						
CaO space group *Fm*-3*m* (#225) Formula weight : 56.07 g mol^{-1}, Z = 4 Mass fraction: 2.7(2)% *a* = 4.8129(4) Å, Volume = 111.48(2) Å^3						
Radiation source: Neutron time of flight Temperature: 298 K χ^2 = 3.855; *wRp*= 1.78%; *Rp* = 1.36%.						

Table 4.3. Structural parameters from the refinement of neutron powder diffraction data collected from $LaSr_3NiRuO_4H_4$ at 298 K.

Atom	U_{11}	U_{22}	U_{33}
La/Sr(1)	0.0068(11)	0.0068(11)	0.0194(25)
Ni/Ru(1)	0.0333(16)	0.0333(16)	0.0354(37)
O(1)	0.0205(10)	0.0205(10)	0.0409(23)
H(1)	0.0595(33)	0.0899(32)	0.0584(31)

Table 4.4. Anisotropic displacement factors from the refinement of neutron powder diffraction data collected from $LaSr_3NiRuO_4H_4$ at 298 K.

Cation	Anion	length (Å)
La/Sr(1)	O(1)	2.490(3) × 1
	O(1)	2.574(1) × 4
	H(1)	2.669(1) × 4
Ni/Ru(1)	O(1)	2.208(3) × 2
	H(1)	1.811(1) × 4

Table 4.5. Selected bond lengths from the refined structure of $LaSr_3NiRuO_4H_4$.

Low temperature neutron powder diffraction data were collected at 30 K, 20 K, 10 K and 2 K, but no additional features were observed which indicates the absence of long-range magnetic ordering.

4.3.2.2 Synchrotron X-Ray Powder Diffraction

Since the WISH diffractometer used above is primarily designed for neutron powder diffraction at long *d*-spacing in magnetic and large unit cell systems, its relatively low resolution at short *d*-spacing for small unit cell systems like $LaSr_3NiRuO_4H_4$, cannot fully confirm the tetragonal symmetry of the unit cell. Therefore synchrotron X-ray powder diffraction data were collected from this oxide-hydride phase as its extremely high resolution will reveal any extra peaks that do not belong to this high symmetry tetragonal unit cell and if the oxide-hydride phase requires a larger or distorted unit cell.

Synchrotron X-ray powder diffraction data (Chapter 2 Section 2.5.1.2) were collected from a large-scale neutron sample of $LaSr_3NiRuO_4H_4$. The data could be readily indexed using a body-centred tetragonal unit cell (space group *I*4/*mmm*) with lattice parameters: a = 3.6226(2) Å, c = 13.317(1) Å, as described in Section 4.3.2.1. The equatorial anion sites were left empty as hydride ion is too 'light' to be observed in synchrotron X-ray powder diffraction data and contributes nearly nothing to the pattern. This model was refined against the data to achieve a good statistical fit (χ^2 = 124.6; *wRp* = 4.39%; *Rp* = 3.21%.).

Observed, calculated and difference plots from the Rietveld refinement of $LaSr_3NiRuO_4H_4$ (space group *I*4/*mmm*) against synchrotron X-ray powder diffraction data are shown in Figure 4.4. There are no extra peaks which cannot be indexed by this high symmetry model and fittings to peak shapes are quite satisfied, even for peaks at high angles as showed in the embeded plot for zoom-in area $46 \leq 2\theta / ° \leq 60$, suggest BO_2H_4 octahedra in this phase remain undistorted.

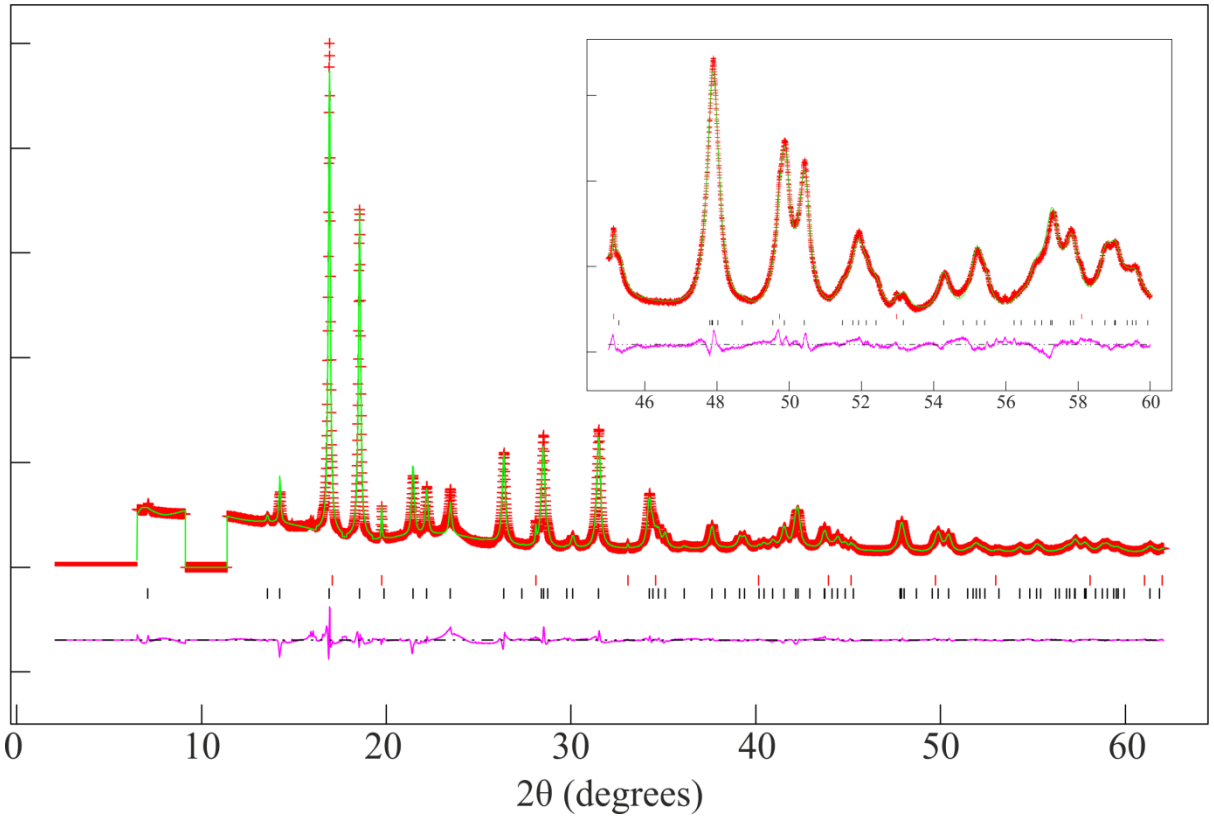


Figure 4.4. Observed, calculated and difference plots from the refinement of $LaSr_3NiRuO_4H_4$ (space group *I*4/*mmm*) against synchrotron X-ray powder diffraction data collected at 298 K. Lower tick marks indicate peak positions of the majority phase, upper tick marks CaO.

The good fit of synchrotron X-ray powder diffraction data by a simple body-centred tetragonal unit cell (space group *I*4/*mmm*) confirms that the oxide-hydride phase $LaSr_3NiRuO_4H_4$ adopts the same crystallographic structure as its parent oxide phase $LaSr_3NiRuO_8$, with a significant contraction in *a*-*b* plane due to the complete exchange of equatorial oxide ions to hydride ions, which has already been confirmed by the neutron powder diffraction data collected from WISH diffractometer in ISIS.

4.3.3 Magnetic Characterisation of $LaSr_3NiRuO_4H_4$

Magnetisation data was collected using a superconducting quantum interference device (SQUID) by using a technique called ferronagnetic subtraction (Chapter 2 Section 2.10). Due to the inevitable presence of trace amount of ferromagnetic Ni impurity in the sample prepared via topochemical reaction with CaH_2, a large field (3 T to 5 T) was applied to saturate elemental Ni during the magnetic characterisation, so the ferromagnetic behaviour contributed by Ni impurity would not mask the magnetic behaviour of the bulk phase. At 5 K increments between 5 K and 300 K, magnetisation-field isotherms were collected over the field range $3 \leq H / T \leq 5$ and the resultant magnetisation are plotted as a function of the applied field. For each 5 K step the gradient of the plot obtained shows the paramagnetic susceptibility and the intercept gives the saturated ferromagnetic moment. Combined the whole range temperature data, a field-cooled plot can be made, the Curie constant was extracted as $C = 0.374(2)$ cm^3 K mol^{-1} and the Weiss temperature as $\theta = -21.4(3)$ K, and hence yields a value of μ^2 to be 2.992 μ_B which corresponds to 1 unpaired electron in total (Figure 4.5 & 4.6).

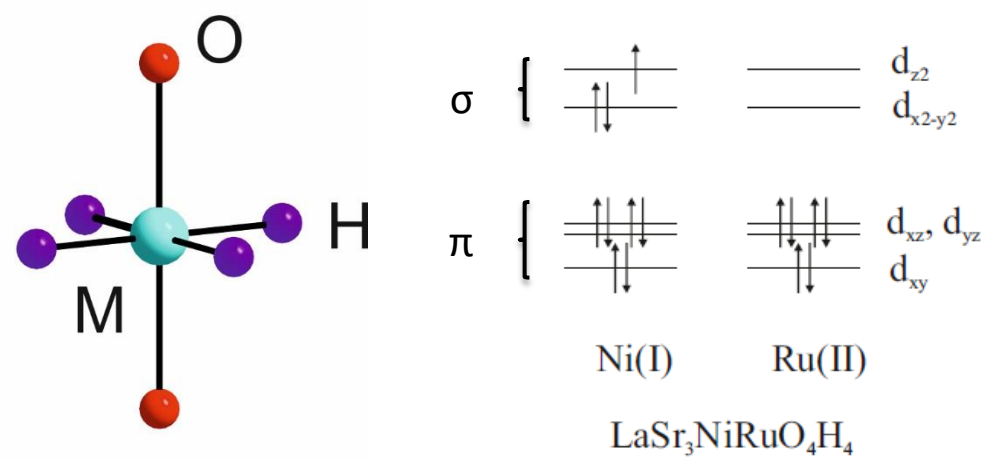


Figure 4.5. The O_2H_4 coordination of Ni^+ and Ru^{2+} results in S = ½ and S = 0 spin states, respectively.

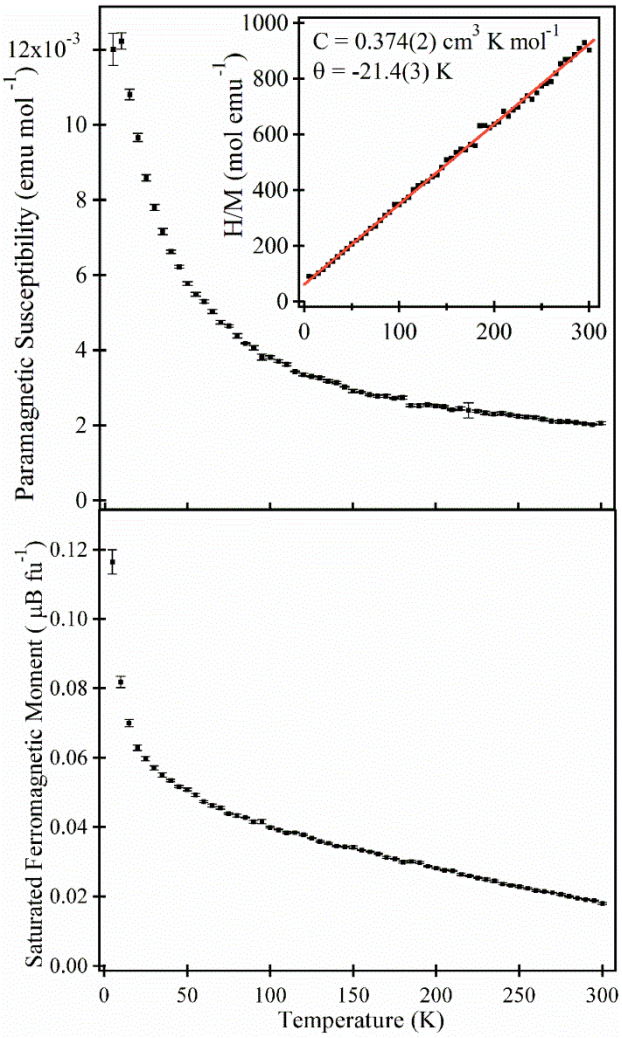


Figure 4.6. The paramagnetic susceptibility (top) and saturated ferromagnetic moment (bottom) of $LaSr_3NiRuO_4H_4$ collected as a function of temperature. Inset: the fit to the Curie–Weiss law in the temperature range 10 < *T* / K < 300.

The magnetisation data collected suggests B-site cations in the parent oxide phase have been reduced to Ni^{1+} (high-spin d^9) with 1 unpaired electron and diamagnetic Ru^{2+} (low-spin d^6). These states merit the closest predicted value to the experimental Curie constant. On cooling below T ~ 10 K the paramagnetic susceptibility of $LaSr_3NiRuO_4H_4$ goes through a local maximum and this is accompanied by an increase in the saturated ferromagnetic moment of the sample. These data in combination suggest the oxide-hydride phase probably adopts an antiferromagnetic ground state.

4.3.4 DFT Calculations of $LaSr_3NiRuO_4H_4$

In order to explore the nature of the magnetic coupling in $LaSr_3NiRuO_4H_4$, Density Function Theory (DFT) calculations were performed by Prof. John E. McGrady and his DPhil student Dihao Zeng (Department of Chemistry, Physical and Theoretical Chemistry Laboratory, University of Oxford).

All density functional calculations were performed using the VASP software package (VASP 5.3). The PBE functional was used, along with Hubbard *U* values (U_{eff}) of 6.0 eV on Ni and 3.0 eV on Ru to describe the effect of strong correlations. A plane-wave cut-off of 600 eV was imposed in all cases, and the Brillouin zone was sampled on a 5 × 5 × 3 *Γ*-centred grid. A 2√2 x 2√2 x 1 expansion of the primitive unit cell was used (Figure 4.7), which contains eight formula units. Neither the B-site transition metal ions (Ni^{1+}/Ru^{2+}) nor the A-site cations (Sr^{2+}/La^{3+}) are distinguished by the modelling of the crystallographic data. We have therefore chosen to impose chequerboard order on the Ni/Ru layer: *i.e*. each Ru is surrounded by four Ni and *vice versa*, and the positions of Ni and Ru alternate along the *c* axis. The eight La^{3+} ions in the 2√2 x 2√2 x 1 expanded cell were positioned such that the distances between them are maximised. Several alternative arrangements were tested, with minimal impact on the lattice parameters or the projected density of states (DOS). The DOS shown in Figure 4.8 corresponds to a magnetic configuration where all Ni^{1+} spins are parallel within a Ni/RuH_2 layer, but alternate layers are antiferromagnetically aligned (shown by the red arrows in Figure 4.7). The DOS for a completely ferromagnetic arrangement was essentially identical. We were unable to converge to a configuration where the spins on Ni^{1+} are aligned anti-parallel to each other. This probably reflects the weak coupling between next nearest-neighbour Ni^{1+} ions *via* the intervening RuH_4 units. Optimized lattice parameters from the calculations are *a* = 3.6374 Å, *c* = 13.418 Å compared to crystallographic values of *a* = 3.6226 Å and *c* = 13.317 Å, respectively.

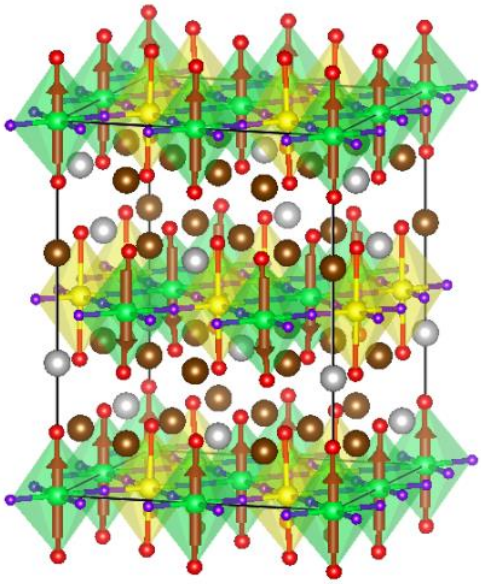


Figure 4.7. 2√2 x 2√2 x 1 expanded unit cell used in the computational model. Grey: La; Brown: Sr; Green: Ni; Yellow: Ru; Red: O; Purple: H.

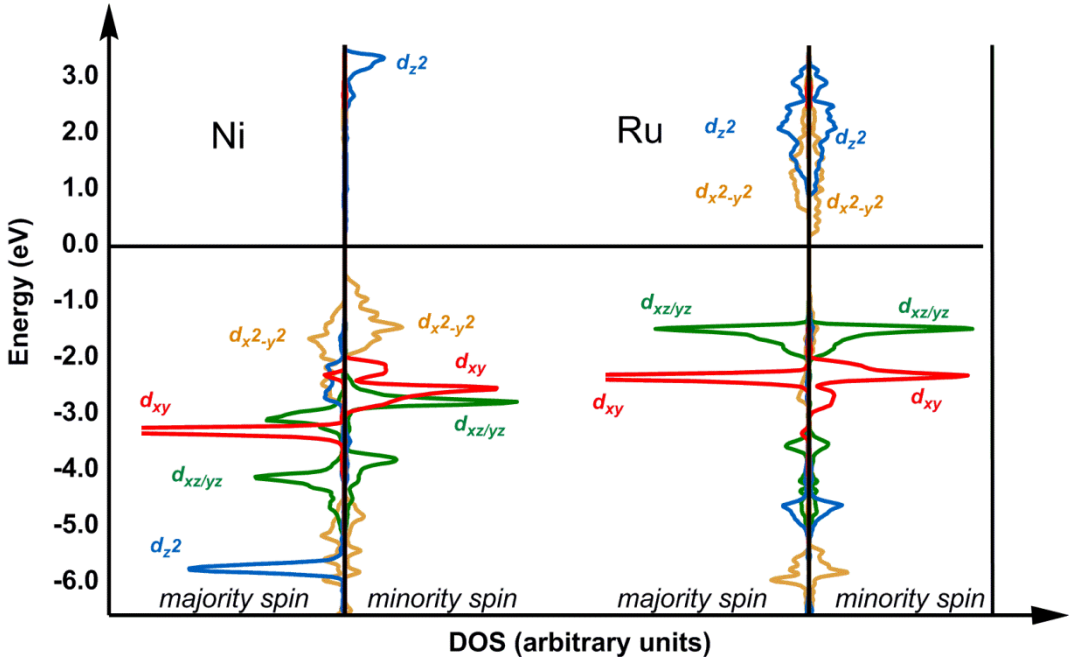


Figure 4.8. Spin-polarized projected density of states (Ni and Ru) for $LaSr_3NiRuO_4H_4$ (U_{eff}(Ni)=6.0 eV, U_{eff}(Ru)=3.0 eV). The Ni^+ ions are coupled ferromagnetically within the $NiRuH_2$ layers, but coupling between adjacent layers is antiferromagnetic.

The density functional theory calculation confirmed the simple electronic configuration determined by magnetisation data collected using the SQUID magnetometer (Figure 4.5), Ru^{2+} adopts a low-spin d^6, $S = 0$ state, while Ni^{1+} adopts an $S = ½$ state with a 'hole' in its d_{z2} orbital. The density of states, projected onto the individual angular momentum components of the Ni and Ru *d* orbitals (Figure 4.8), shows only the minority-spin component of Ni d_{z2} above the Fermi level: the bands formed by the other 9 spin orbitals are occupied. The strong splitting of the majority-spin and minority-spin components of the Ni bands is consistent with the presence of a single unpaired electron on the Ni^+ centres (0.91 μ_B). The Ru centres, in contrast, are diamagnetic, with minority-spin and majority-spin components of $d_{xz/yz}$ and d_{xy}/d_{z2} occupied in a typical low-spin t_{2g}^6 (Ru^{2+}) arrangement.

4.3.5 μ^+SR data of $LaSr_3NiRuO_4H_4$

As a result of the conflict between low temperature neutron powder diffraction data and magnetisation data, we have collected μ^+SR data as an independent probe to investigate local magnetic ordering (μ^+SR data were collected at the Paul Scherrer Institute in Switzerland by Prof. Stephen J. Blundell, University of Oxford).

Plots of the asymmetry of μ^+SR data collected from $LaSr_3NiRuO_4H_4$ at various temperatures are shown in Figure 4.9 and there is no indication of magnetic ordering down to a temperature of 1.8 K, which in agreement with the low temperature neutron powder diffraction data collected (2 K). The muon polarization simply relaxes with a rate which increases as the sample is cooled, consistent with fluctuations that slow down on cooling, but not to the point where a long range order is obtained, i.e. the asymmetry plot does not oscillate. This suggests that if $LaSr_3NiRuO_4H_4$ does adopt an antiferromagnetic ground state, the ordering temperature is extremely low.

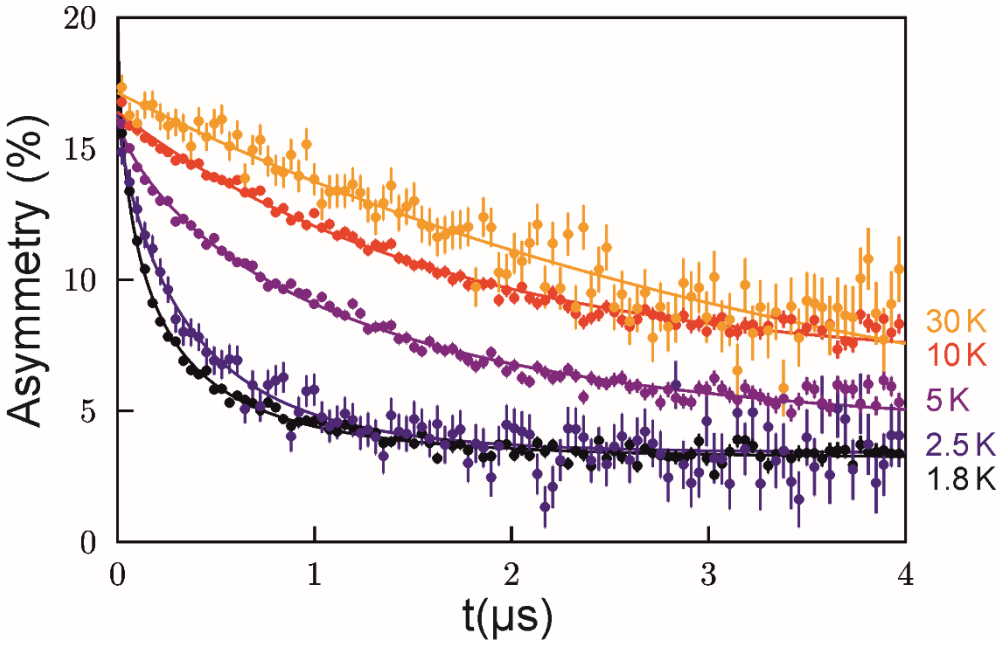


Figure 4.9. Plots of the asymmetry of μ^+SR data collected from $LaSr_3NiRuO_4H_4$ at various temperatures.

4.4 Discussion

4.4.1 Structural Peculiarity of $LaSr_3NiRuO_4H_4$

The topochemical reduction of n = 1 Ruddlesden-Popper phase $LaSr_3NiRuO_8$ with solid state binary metal hydride CaH_2 in sealed ampoules eventually yields an anion-ordered oxide-hydride phase $LaSr_3NiRuO_4H_4$, with the Ru and Ni cations located in a plane containing only hydride ligands, and the coordination spheres of the corner-linked square-planar MH_4 units in this plane are completed by two axial oxide ions that link the planes to the neighbouring (La/Sr)O layers. The −(La/Sr)O−(Ni/Ru)O_2−(La/Sr)O− stacking sequence of the parent oxide is converted into a −(La/Sr)O−(Ni/Ru)H_2−(La/Sr)O− sequence. In contrast, the anion-ordered oxide-hydride phase $SrVO_2H$ prepared via the topochemical reaction of its parent perovskite phase $SrVO_3$ with CaH_2, consists of sheets of apex-linked

$V^{3+}O_4$ squares and their coordination spheres are completed by two axial hydride ions sit in the neighbouring SrH layers. These two anion-ordered oxide-hydride phases are both formed by using CaH_2 as a solid-state reducing agent and a source of H^-, however the hydride ions in $LaSr_3NiRuO_4H_4$ end up in 'topologically distinct' anion sites, which in this case, forms corner linked square planes containing B-site cations that completely devoid of oxide ions.

This interesting structural selectivity is quite common in Ruddlesden-Popper phases[89] as they offer a number of different anion sites that can be described as topologically distinct rather than simply crystallographically distinct, because they are situated at different positions within the structural network and cannot be made equivalent by simply removing a symmetry-breaking tilting or twisting distortion. These 'topologically distinct' anion sites allow a degree of selectivity to be imposed in topochemical reactions and provide a methodology to design materials with desired pattern of ordered oxide vacancies or non-oxide heteroanions like hydride, nitride and halides in a rational manner.[89]

Anions situated in topologically distinct coordination sites tend to exist in different chemical environments, therefore removal of them can exert different consequences on cations in one specific site. Hence in this case, which anions are moved or substituted during the topochemical reduction process of $LaSr_3NiRuO_8$, can be quantitatively analysed by calculated anion bond valence sums (Table 4.6) of O(1) and O(2) shown in Figure 4.10, as these BVS values reflect the degree of influence exerted on the A-site cations (1:3 La/Sr, BVS A) and B-site cations (1:1 Ni/Ru, BVS B) respectively by oxide ions in each 'topologically distinct' anion site.

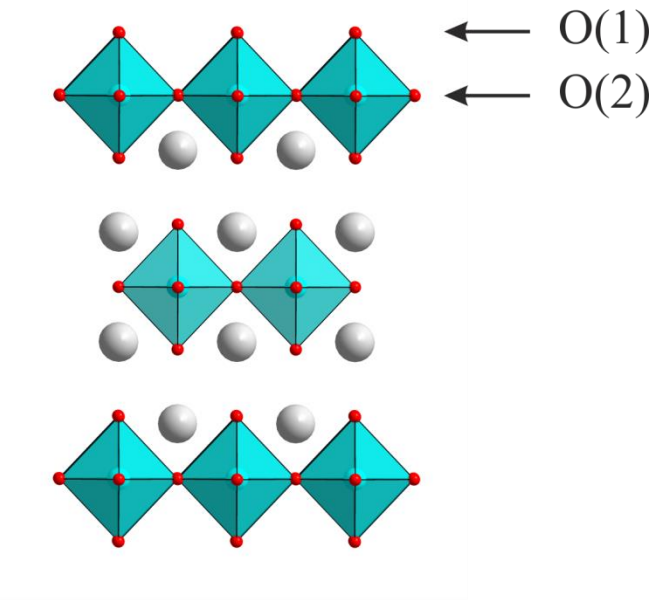


Figure 4.10. The topologically distinct anion sites in the *n* = 1 Ruddlesden-Popper phase $LaSr_3NiRuO_8$.

Anion	Anion BVS	$LaSr_3NiRuO_8$
O(1)	BVS A BVS B	1.172 1.013
	(BVS B) – (BVS A)	**- 0.159**
O(2)	BVS A BVS B	0.980 2.742
	(BVS B) – (BVS A)	**+ 1.762**

Table 4.6. The calculated anion bond valence sums of the *n* = 1 Ruddlesden-Popper phase $LaSr_3NiRuO_8$.

During topochemical reductions, B-site cations are reduced while the oxidation states of A-site cations remain unchanged. The best compromise between the two largely incompatible requirements of the two classes of cations is to deintercalate or substitute oxide ions which will lead to the greatest change in the bonding environment of B-cation with the smallest change in that of A-cation. The compromise can be quantified as the term (BVS B) – (BVS A) showed above in Table 4.6. The value of this term is more positive for O(2), the equatorial oxide ion, compared to that of O(1) which is the apical oxide ion, hence O(2) is the chosen one to be deintercalated or substituted during the modification of the anion lattice in $LaSr_3NiRuO_8$ if Ni^{2+}/Ru^{5+} centres need to be reduced. This outcome predicts hydride ions should prefer to reside in equatorial anion sites, which agrees with neutron powder diffraction data, as the coordination environment of O(1) is A_5B while that of O(2) is A_4B_2, both are six-coordinated, but O(2) has a greater impact on B-site cations, simply because it is coordinated with one more B-site cation compared to O(1).

Therefore in topochemical reactions of $LaSr_3NiRuO_8$ with CaH_2, hydride ions are favoured to substitute into equatorial anion sites which used to be occupied by O(2) in the parent oxide phase, hence result in the formation of the anion-ordered oxide-hydride phase $LaSr_3NiRuO_4H_4$ containing this unique structural motif, Ru and Ni cations located in a plane that contains hydride ligands only and the coordination spheres of the corner-linked square-planar MH_4 units in this plane are completed by two axial oxide ions that link the planes to the neighbouring (La/Sr)O layers.

4.4.2 Electronic Structure of $LaSr_3NiRuO_4H_4$

As discussed in Section 4.4.1, the ordered arrangement of oxide ions and hydride ions found in the oxide-hydride phase $LaSr_3NiRuO_4H_4$ generates a unique structural motif where in the MH_2 planes containing the transition metals are completely devoid of oxide ions, with obvious parallels to the CuO_2 sheets present in the high-temperature superconducting cuprates $La_{2-x}M_xCuO_{4+\delta}$ (M = Ba, Sr). However, the oxide-hydride phase is a typical antiferromagnetic insulator and does not show any superconductivity in the temperature range that has been explored so far. The contrast in conductivity might be explained by a close inspection in electronic structure of the oxide-hydride phase $LaSr_3NiRuO_4H_4$, with comparison to the high-temperature superconducting cuprates.

Among the cuprates showing high-T_c superconductivity, the system $La_{2-x}M_xCuO_{4+\delta}$ (M = Ba, Sr) first discovered by Bednorz and Müller[4], is one of the most suitable systems to study the electronic structure of high-temperature superconductors. The undoped compound La_2CuO_4 is an antiferromagnetic insulator, the same as the oxide-hydride phase $LaSr_3NiRuO_4H_4$ (resistivity measurements performed by a multimeter on cold-pressed powder samples yielded values greater than 5 MΩcm, consistent with insulating behaviour). This is due to strong electronic correlation effects on the Cu^{2+} centres (d^9) which force the compound with metallic half-filled band to become a charge-transfer insulator.[90] However, upon Ba/Sr-for-La doping, antiferromagnetism disappears and an insulator-to-metal transition occurs near $x = 0.06$[91] and superconductivity is observed with a maximum T_c near $x = 0.15$, driven by delocalisation of electrons.[92]

Combining DFT calculation results and the electronic configuration of Ni^{1+} and Ru^{2+} centres, a schematic electronic band structure of the oxide-hydride phase $LaSr_3NiRuO_4H_4$ can be made and studied (Figure 4.11).

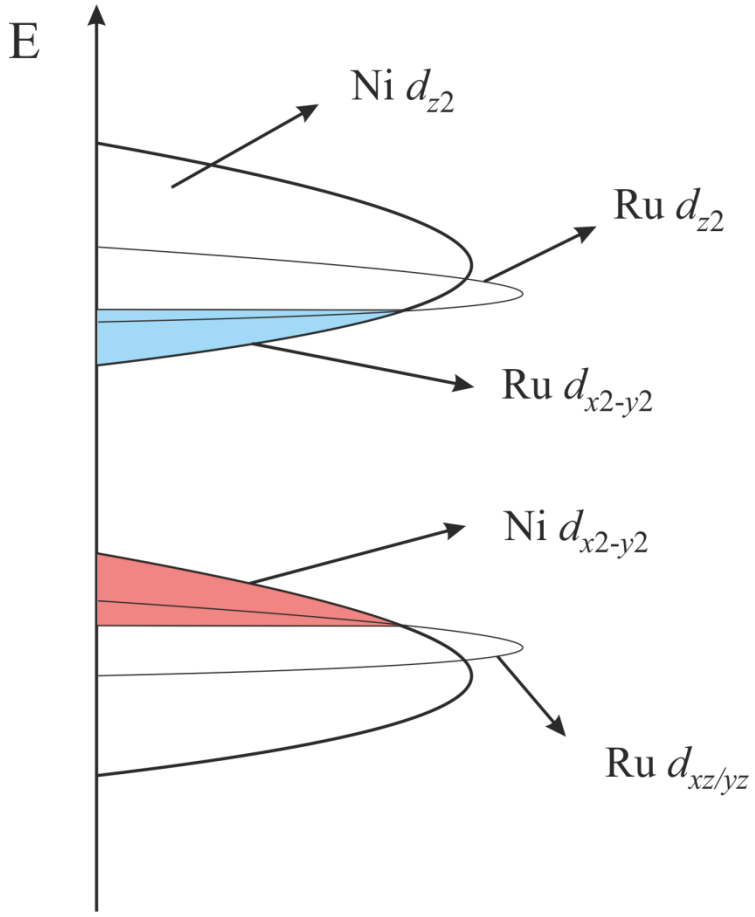


Figure 4.11. The schematic electronic band structure of the oxide-hydride phase $LaSr_3NiRuO_4H_4$.

Unlike the half-filled Cu^{2+} d_{x2}-$_{y2}$ orbital in high-temperature superconducting cuprates, the d_{x2}-$_{y2}$ orbital of Ni^{1+} is fully occupied while that of Ru^{2+} is completely empty, both resulting in non-conductive behaviour because of the absence of delocalised electrons. These d_{x2}-$_{y2}$ orbitals are important and worth investigating as they match the symmetry of H^- 1*s* orbital, thus can overlap with it quite well.

The doping of the antiferromagnetic insulator La_2CuO_4 by Ba or Sr yields the formation of high-T_c superconductors as they induce delocalisation of electrons, the analogy is to

modify the ratio between La and Sr in the oxide-hydride phase $LaSr_3NiRuO_4H_4$. For La-rich compositions, $La_{1+x}Sr_{3-x}NiRuO_4H_4$, B-site cations are partially reduced (e^- doped), thus some Ru^{2+} are reduced to Ru^{1+} by putting electrons into empty Ru d_{x2}-$_{y2}$ orbitals (filled by blue colour in Figure 4.11). In contrast, for Sr-rich compositions, $La_{1-x}Sr_{3+x}NiRuO_4H_4$, B-site cations are partially oxidised (hole doped), thus some Ni^{1+} are oxidised to Ni^{2+} by generating holes in filled Ni d_{x2}-$_{y2}$ orbitals (filled by red colour in Figure 4.11).

In both La-rich and Sr-rich cases, the d_{x2}-$_{y2}$ orbital would become partially filled and becomes the valence orbital which can well-overlap with H^- 1*s* orbital, like the half-filled Cu^{2+} d_{x2}-$_{y2}$ orbital interacting with the O^{2-} 2*p* orbital in high-temperature superconducting cuprates. Therefore the doped oxide-hydride phases $La_xSr_{4-x}NiRuO_4H_4$ might be candidates for high-temperature superconductors. Detailed information about these doped phases is presented in Chapter 5.

4.4.3 Magnetic Characterisation of $LaSr_3NiRuO_4H_4$

A disordered Ni/Ru lattice might be expected to exhibit spin-glass behaviour, as observed for $Sr_{n+1}(Fe/Ru)_nO_{3n+1}$ phases. However, magnetisation data collected using a SQUID magnetometer indicates none of the $LaSr_3NiRuO_xH_y$ phases are spin-glasses at low temperature, and shows no convincing evidence for an antiferromagnetic ground state as well. In addition, low temperature neutron powder diffraction data show no additional magnetic diffraction features that would support the presence of a long-range magnetic ordered state and plots of asymmetry of μ^+SR data collected do not oscillate down to a temperature of 1.8 K.

One possible explanation is the apparent weakness of the magnetic coupling between Ni^{1+} d_{z2} orbital and hydride 1*s* orbital due to poor overlapping as a result of shape mismatch. And the magnetic coupling between Ni^{1+} centres is very weak as well because of the long distance between them. Also the relatively small size of the Ni moment (S = ½) may account for our failure in observing additional magnetic diffraction features under circumstances with zero applied magnetic field, which unlike in the SQUID case, the measured magnetic interactions between Ni^{1+} centres through a linear hydride and diamagnetic ruthenium superexchange pathway in the oxide-hydride phase are amplified by a large external field applied (3 T ~ 5 T) during the measurement (Figure 4.12).

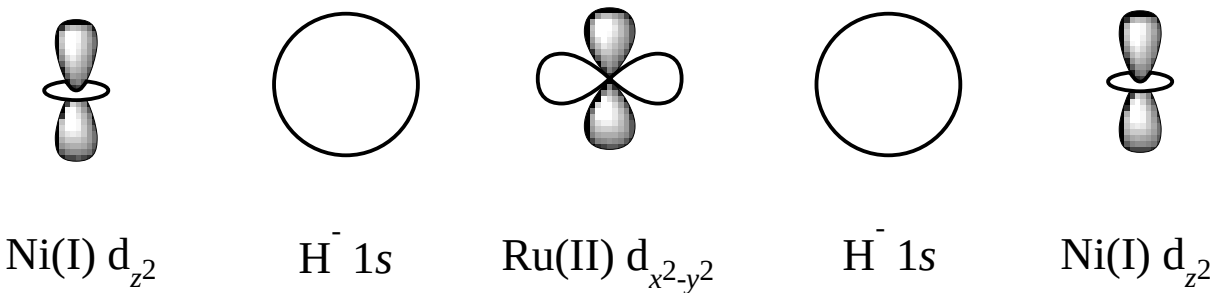


Figure 4.12. Orbital overlapping through a linear Ni-H-Ru-H-Ni superexchange pathway in $LaSr_3NiRuO_4H_4$.

4.5 Conclusion

The idea of forming an oxide-hydride phase containing the 4*d* transition metal Ru is initiated by the covalently stabilized oxide-hydride phase $LaSrCoO_3H_{0.7}$[15]. The strong Co_{3d}-H_{1s}-O_{2p} covalent interactions has direct parallels to the strong σ-bonds observed in molecular hydride systems of late 4*d* and 5*d* transition metals such as Ru, suggesting that it should be possible to prepare covalently stabilized oxide–hydride phase based on the same metal.

Topochemical reduction of the n = 1 Ruddlesden-Popper phase $LaSr_3NiRuO_8$ with the solid-state binary metal hydride CaH_2, in sealed ampoules at 450 °C yields the novel anion-ordered oxide-hydride phase $LaSr_3NiRuO_4H_4$ via anion exchange process. The structure of this new reduced oxide-hydride phase preserves the simple body-centred tetragonal unit cell (space group *I*4/*mmm*) of its parent oxide phase with lattice parameters: a = 3.6226(2) Å, c = 13.317(1) Å. There are no phase transitions observed while we cooled down the sample and this model can be used to describe the structure of $LaSr_3NiRuO_4H_4$ through the whole temperature range $2 \leq T/K \leq 298$ with no distortions of octahedra.

From previous work, perovskites and Ruddlesden–Popper phases containing only 4*d* transition metals tend to decompose to yield metals in the elemental state when reacting with CaH_2 unless they are stabilized by the presence of 3*d* transition metals. For example, reaction of $SrRuO_3$ with CaH_2 yields SrO and Ru but $SrFe_{0.5}Ru_{0.5}O_3$ and $LaSrNiRuO_6$ yield $SrFe_{0.5}Ru_{0.5}O_2$ and $LaSrNiRuO_4$, respectively.[10, 11] The formation of $LaSr_3NiRuO_4H_4$ in the topochemical reaction of $LaSr_3NiRuO_8$ demonstrates that the La-Sr-Ni-O lattice is sufficiently robust to resist non-topochemical decomposition, and can thus stabilize the formation of Ru^{2+} centres in an extended solid. This allows for the preparation of the anion-ordered $LaSr_3NiRuO_4H_4$ phase, to the best of our knowledge, the first reported example of an oxide–hydride phase containing a 4*d* transition metal, and the 1:1 ratio of hydride to oxide is the highest yet reported, also the presence of a plane that contains hydride ligands only is a unique feature in the oxide–hydride chemistry.

The measured structural and magnetic data, along with the computational study, are consistent with the presence of transition metal ions in remarkably low oxidation states (Ru^{2+} and Ni^{+}) in an extended solid and show no evidence of long-range magnetic ordering down to a temperature of 1.8 K.

Chapter 5

A-Site Doping of $LaSr_3NiRuO_8$ Series

5.1 Introduction

The undoped n = 1 Ruddlesden-Popper phase $LaSr_3NiRuO_8$ and its reduced oxide-hydride phase $LaSr_3NiRuO_4H_4$ are both antiferromagnetic insulators, the same as the undoped compound La_2CuO_4. However, upon Ba/Sr-for-La doping of La_2CuO_4, high-T_c superconductivity was found in the $La_{2-x}M_xCuO_{4+\delta}$ (M = Ba, Sr) system. As first discovered by Bednorz and Müller[4], antiferromagnetism disappears and an insulator-to-metal transition occurs near x = 0.06[91] and superconductivity is observed with a maximum T_c near x = 0.15, driven by delocalisation of electrons.[92] Inspired by the insulator-to-metal transition found in superconducting cuprates as a result of A-site doping, manipulations of the ratio of La and Sr in the n = 1 Ruddlesden-Popper phase $LaSr_3NiRuO_8$ were carried out, to form phases of composition $La_xSr_{4-x}NiRuO_8$ ($0.5 \leq x \leq 1.5$) which were subsequently reacted with CaH_2.

5.2 Experimental

5.2.1 Synthesis of $La_xSr_{4-x}NiRuO_8$ ($0.5 \leq x \leq 1.5$)

Samples of $La_xSr_{4-x}NiRuO_8$ ($0.5 \leq x \leq 1.5$) were synthesized by a high-temperature ceramic method as described in Chapter 2 Section 2.1.1. Suitable stoichiometric ratios of La_2O_3 (99.999%, dried at 900°C), $SrCO_3$ (99.994%), RuO_2 (99.99%, dried at 800°C) and NiO (99.998%), for each composition respectively, were ground together using an agate mortar and pestle, transferred into an alumina crucible, and then heated at a rate of 1 ºC min^{-1} to 1000°C in air to decompose the carbonate. The samples were reground, pressed into pellets

and then heated for 3 periods of 48 hours at 1200°C in air, with grinding between heating periods. The reaction progress was monitored by laboratory X-ray diffractometer and once the reaction was deemed complete, synchrotron X-ray powder diffraction data were collected from the resulting phase.

5.2.2 Synthesis of $La_xSr_{4-x}NiRuO_4H_4$ ($0.5 \leq x \leq 1.5$)

Samples of $La_xSr_{4-x}NiRuO_4H_4$ ($0.5 \leq x \leq 1.5$) were prepared by grinding together approximately 0.5 g of the respective parent $La_xSr_{4-x}NiRuO_8$ ($0.5 \leq x \leq 1.5$) oxide phase with 0.13 g of CaH_2 in an argon filled glovebox using an agate mortar and pestle. The resulting powders were sealed in silica ampoules and heated at suitable temperatures (Table 5.1) for 2 periods of 7 days, with the sample being reground between heating periods. Once the reaction was deemed complete, the reaction mixture was washed, under nitrogen, with 6 × 25 ml of 0.1 M solution of NH_4Cl in methanol in order to remove the CaO formed as a by-product of the reaction and any unreacted CaH_2. This was then followed by washing with 3 × 25 ml of clean methanol to dissolve NH_4Cl residues. The sample was then dried under vacuum.

***x* (content of La)**	**Topochemical Reaction Temperature (°C)**
0.5	410
0.6	420
0.7	430
0.8	450
0.9	450
1.0	450
1.1	460
1.2	470
1.3	470
1.4	470
1.5	470

Table 5.1. Topochemical reaction temperatures of $La_xSr_{4-x}NiRuO_8$ ($0.5 \leq x \leq 1.5$) with CaH_2 in sealed silica ampoules, yielding respective oxide-hydride phases.

Although all the doped parent oxide phases are formed at the same reaction temperature (1200 °C) as the undoped x = 1.0 analogue, their corresponding oxide-hydride phases are formed at slight different temperatures. In general, all La-rich (x > 1.0) parent oxide phases are more robust or less reactive, and require higher reaction temperatures (above 450 °C) to fully convert into corresponding oxide-hydride phases, while some of La-deficient ($x \leq 0.7$) parent oxide phases are more fragile or more reactive, and form corresponding oxide-hydride phases at lower reaction temperatures (below 450 °C). In addition, small amount of a mixture of elemental Ni and Ru is always observable in La-deficient (x < 1.0) oxide-hydride phases after washing, while it is not observable in any La-rich (x > 1.0) ones.

5.3 Results

5.3.1 Structural Characterisation of $La_xSr_{4-x}NiRuO_8$ ($0.5 \leq x \leq 1.5$)

Synchrotron X-ray powder diffraction data (Chapter 2 Section 2.5.1.2) were collected from samples of $La_xSr_{4-x}NiRuO_8$ ($0.5 \leq x \leq 1.5$). These data could be readily indexed using the same body-centred tetragonal unit cell (space group *I4/mmm*), as their undoped analogue $LaSr_3NiRuO_8$, with slight variations in lattice parameters. Although neutron powder diffraction data were not collected for these doped phases, atomic positions of oxide ions are still relatively reliable as the oxide ions contribute to over 20% of the total electron count. Data collected from all compositions were refined against this model to achieve good statistical fits. The refined plots of $La_{1.4}Sr_{2.6}NiRuO_8$ were shown in Figure 5.1 as a representative and others can be found in Appendix.2.1.

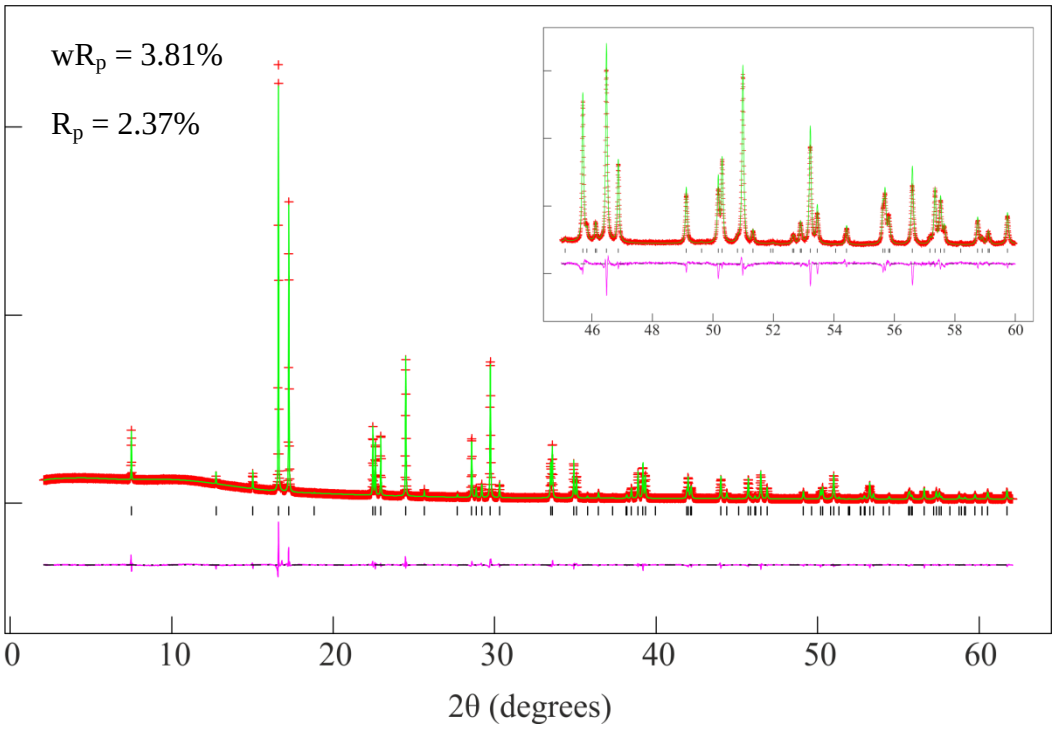


Figure 5.1. Rietveld refinement of synchrotron X-ray powder diffraction data collected from $La_{1.4}Sr_{2.6}NiRuO_8$ against *I4/mmm* model. Observed (red), calculated (green), and difference plots (pink) are shown.

Lattice parameters extracted from refinements of synchrotron X-ray powder diffraction data collected from samples of $La_xSr_{4-x}NiRuO_8$ ($0.5 \leq x \leq 1.5$) are summarized below in Figure 5.2. The blue dashed lines in Figure 5.2 represent the undoped compound $LaSr_3NiRuO_8$, hence right-hand-side (RHS) areas represent La-rich compounds and left-hand-side (LHS) areas represent La-deficient compounds. These error bars extracted from refinements reflect more of precision (the 4th or 5th decimal place) rather than accuracy, thus they are not really physically meaningful.

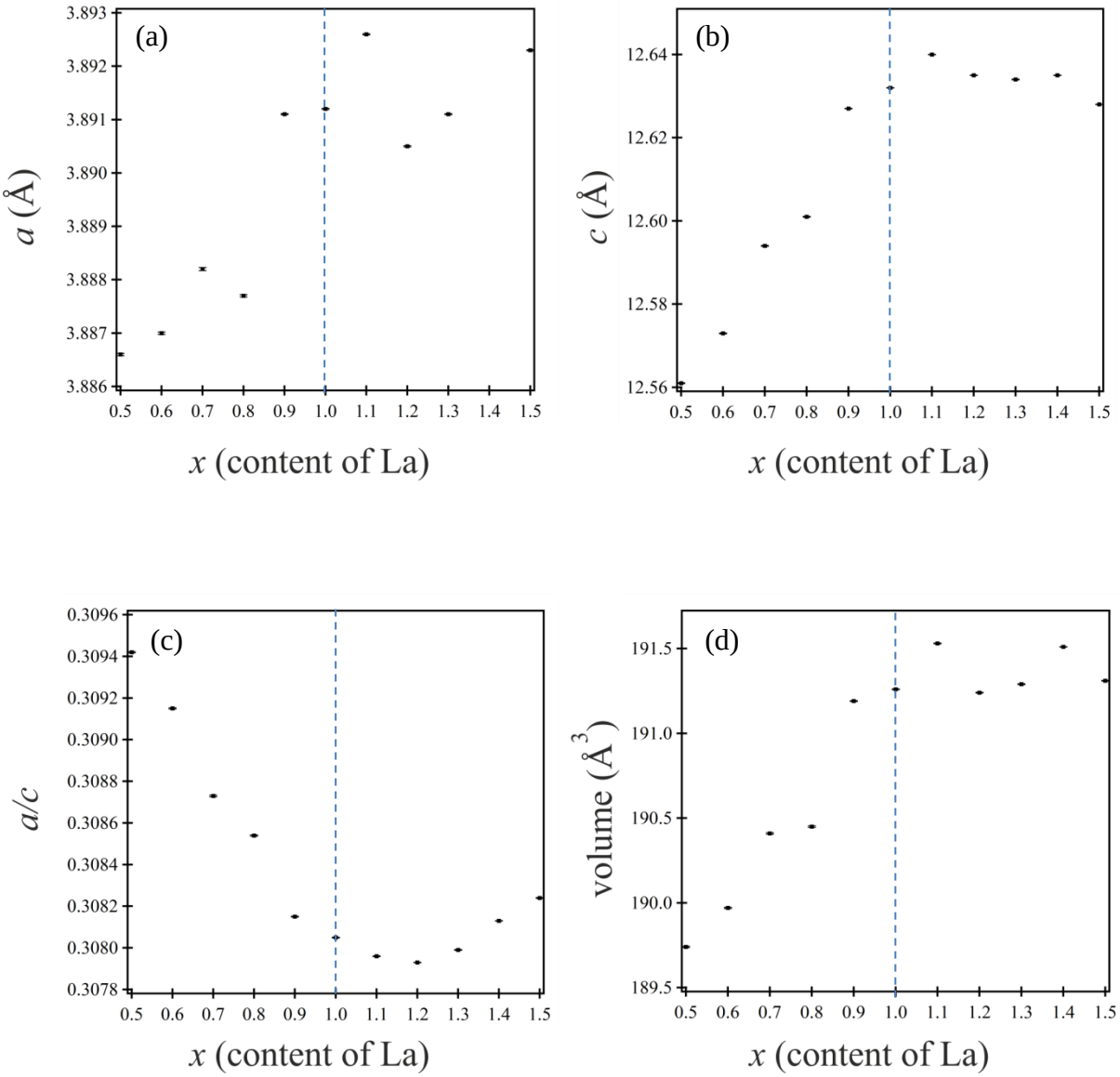


Figure 5.2. Plot (a) *a*; (b) *c*; (c) *a/c*; and (d) volume against *x* in $La_xSr_{4-x}NiRuO_8$ ($0.5 \leq x \leq 1.5$) series of compounds.

In general, changes in lattice parameters in this series of compounds are quite subtle (third decimal place for *a* and second decimal place for *c*), since only the ratio between La and Sr has been manipulated. The lattice parameters of La-rich compounds ($x > 1.0$) are similar to the undoped compound $LaSr_3NiRuO_8$, while unit cells of La-deficient ones ($x < 1.0$) do become smaller as more La^{3+} is replaced by Sr^{2+} (Figure 5.2).

The magnetisation data collected from the undoped compound $LaSr_3NiRuO_8$ suggest a combination of Ni^{2+} and Ru^{5+} for B-site cations (Chapter 3 Section 3.3.2), therefore upon substituting some La^{3+} by Sr^{2+}, part of Ni^{2+} is oxidized to Ni^{3+} (LHS areas, $x < 1.0$), and correspondingly, upon substituting some Sr^{2+} by La^{3+}, part of Ru^{5+} is reduced to Ru^{4+} (RHS areas, $x > 1.0$). Hence, in addition to the size difference between La^{3+} and Sr^{2+}, differences in ionic radii of Ni^{2+}/Ni^{3+} and Ru^{5+}/Ru^{4+} also contribute to changes in lattice parameters. Ionic radii of these A-site and B-site cations have been summarized below in Table 5.2.[93]

Cations	Coordination number	Ionic Radius (Å)
La^{3+}	9	1.216
Sr^{2+}	9	1.31
Ni^{2+} (high-spin d^8)	6	0.69
Ni^{3+} (high-spin d^7)	6	0.6
Ru^{5+} (low-spin d^3)	6	0.565
Ru^{4+} (low-spin d^4)	6	0.62

Table 5.2. Ionic Radii of A-site and B-site cations in $La_xSr_{4-x}NiRuO_8$ ($0.5 \leq x \leq 1.5$) series of compounds[93].

Although the ionic radius of La^{3+} is 0.094 Å smaller than Sr^{2+}, the size expansion gained from reducing Ru^{5+} to Ru^{4+} (0.055 Å) approximately compensates the contraction attributed to La-for-Sr substitution, despite the size difference between Ru^{5+}/Ru^{4+} is smaller than that of La^{3+}/Sr^{2+} (0.055 Å < 0.094 Å), resulting in La-rich compounds (x > 1.0) having similar lattice parameters with the undoped compound $LaSr_3NiRuO_8$. In contrast, the size contraction gained from oxidising Ni^{2+} to Ni^{3+} (0.090 Å) outweighs the expansion attributed to Sr-for-La substitution, as the size difference between Ni^{2+}/Ni^{3+} is similar to that of La^{3+}/Sr^{2+} (0.090 Å ≈ 0.094 Å), hence leads to overall contraction of unit cells for La-deficient compounds (x < 1.0). These observations suggest that the sizes of B-site cations have greater influence on lattice parameters than the sizes of A-site cations for n = 1 Ruddlesden-Popper phases.

5.3.2 Magnetic Characterisation of $La_xSr_{4-x}NiRuO_8$ ($0.5 \leq x \leq 1.5$)

Zero-field-cooled and field-cooled magnetization data were collected from samples of $La_xSr_{4-x}NiRuO_8$ ($0.5 \leq x \leq 1.5$) as a function of temperature in an applied field of 100 Oe using a SQUID magnetometer (Chapter 2 Section 2.10). The magnetisation data of $La_{0.6}Sr_{3.4}NiRuO_8$ were shown in Figure 5.3 as a representative and others can be found in Appendix.2.2. Data in suitable temperature ranges are fitted to the Curie-Weiss law ($\chi = C/(T - \theta)$) to yield values of the Curie constant, C, and the Weiss temperature, θ, for each composition respectively, which are plotted below in Figure 5.4.

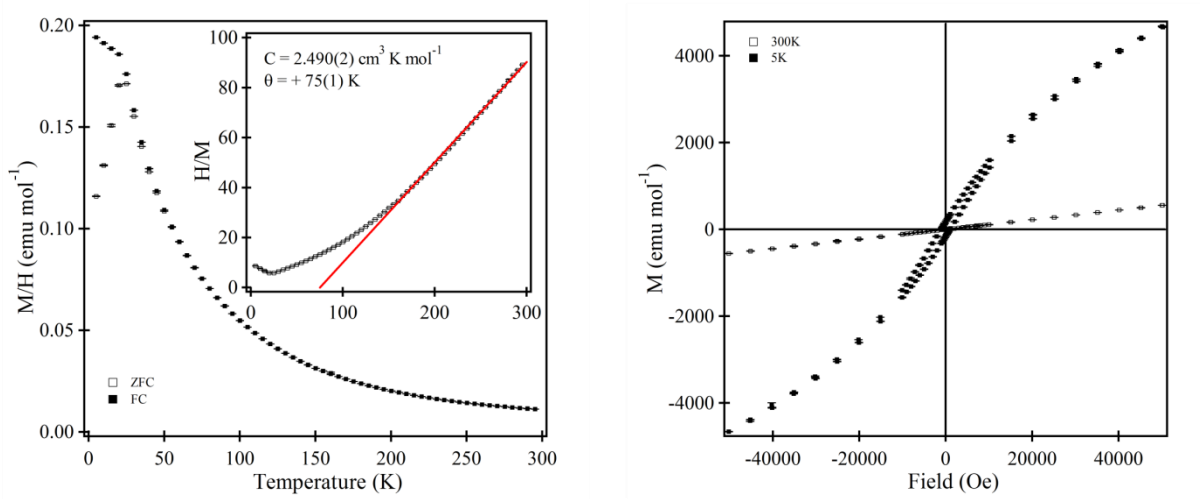


Figure 5.3. Zero-field-cooled and field-cooled magnetisation data collected in an applied field of 100 Oe. Inset shows fit to the Curie-Weiss law (left); Magnetisation data collected as a function of applied field (right) from $La_{0.6}Sr_{3.4}NiRuO_8$.

In general, all these doped phases exhibit canted antiferromagnetic behaviour, like the undoped compound $LaSr_3NiRuO_8$, with the diverging between ZFC and FC data occurred below temperature T = 50 K, and the temperature-dependent magnetisation data of each composition which can be fitted to the Curie-Weiss law were within similar temperature ranges ($150 < T / K < 300$).

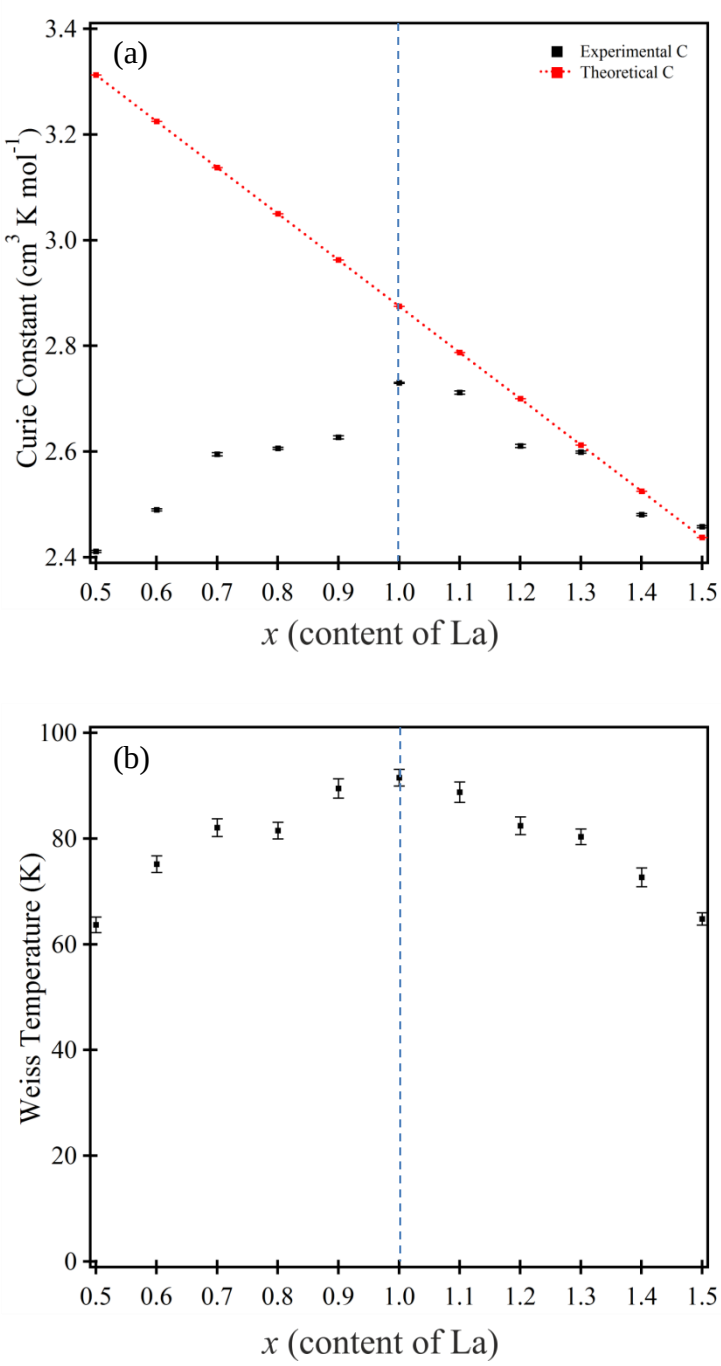


Figure 5.4. Plot of (a) Curie Constant; and (b) Weiss Temperature against *x* in $La_xSr_{4-x}NiRuO_8$ ($0.5 \leq x \leq 1.5$) series of compounds.

The blue dashed lines in Figure 5.4 represent the undoped compound $LaSr_3NiRuO_8$, hence right-hand-side (RHS) areas represent La-rich compounds and left-hand-side (LHS) areas represent La-deficient compounds. In Figure 5.4 (a), values of theoretical Curie constant (if a linear relationship between oxidation states of B-site cations and the magnetic behaviour of the phase is assumed) are represented in red, to compare with values of experimental Curie constant (black) extracted from magnetisation data collected from each composition. For RHS, values of experimental C approximately agree with theoretical C, but for LHS, they vary in the opposite direction. Weiss temperature decreases almost proportionally with respect to *x*, suggesting magnetic interactions between spins become weaker as long as the ratio between La and Sr deviates from 1:3.

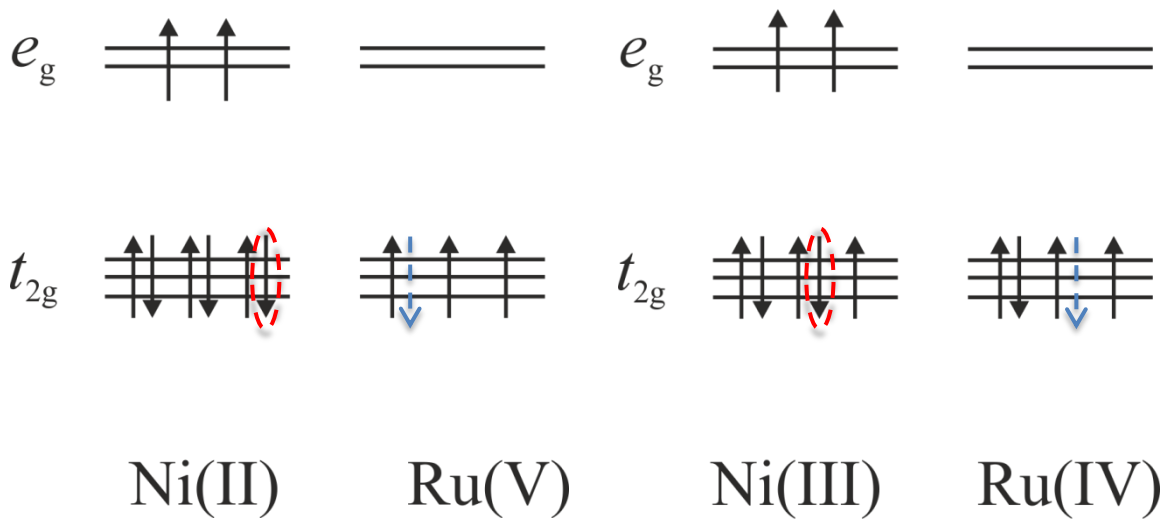


Figure 5.5. Predicted spin states of B-site transition metal cations in $La_xSr_{4-x}NiRuO_8$ ($0.5 \leq x \leq 1.5$) series of compounds.

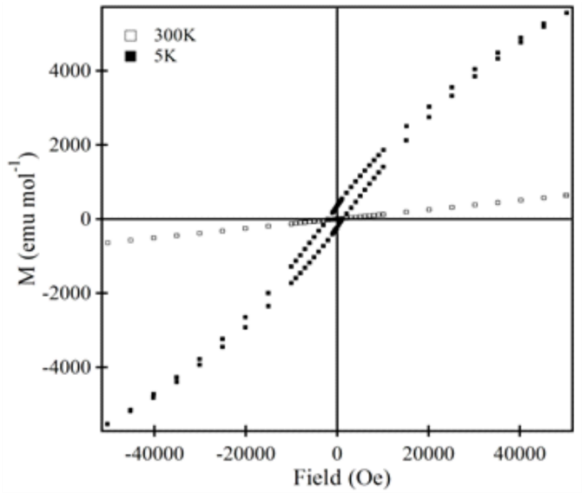
Although magnetisation data collected from the undoped compound $LaSr_3NiRuO_8$ suggest initial (before A-site doping) oxidation states of B-site cations should be Ni^{2+} and Ru^{5+}, the two possible combinations (Ni^{2+}/Ru^{5+} and Ni^{3+}/Ru^{4+}) are still both considered here (Figure 5.5).

For RHS areas of both plot (a) and (b) in Figure 5.4, La-for-Sr substitutions result in electron-doping of the system (La-rich compounds), hence B-site cations get reduced, in this case it is more likely to reduce part of Ru^{5+} to Ru^{4+} (or reduce part of Ru^{4+} to Ru^{3+}) by adding an extra electron into Ru t_{2g} orbitals, as represented by blue dashed arrows in Figure 5.5. Therefore the number of unpaired electrons in the system becomes smaller, leading to the decrease in Curie constant and Weiss temperature as expected.

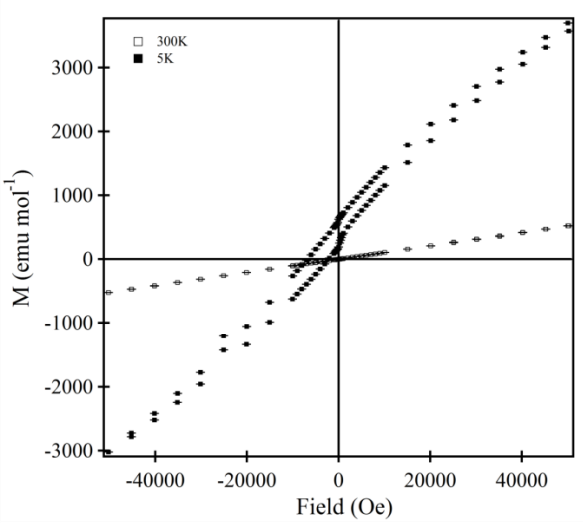
For LHS areas of both plot (a) and (b) in Figure 5.4, Sr-for-La substitutions result in hole-doping of the system (La-deficient compounds), hence B-site cations get oxidized, in this case it is more likely to oxidise part of Ni^{2+} to Ni^{3+} (or oxidise part of Ni^{3+} to Ni^{4+}) by removing an electron from Ni t_{2g} orbitals, as highlighted by red dashed circles in Figure 5.5. Therefore the number of unpaired electrons in the system becomes larger, in principle it should lead to an increase in Curie constant and Weiss temperature. However, experimental data show the decrease in Curie constant and Weiss temperature again, which contradict to predicted results based on spin-only interactions. These observations show that electrons of the B-site cations may no longer be localised, once the ratio of La and Sr is deviates from 1:3.

Magnetization data collected from samples of $La_xSr_{4-x}NiRuO_8$ ($0.5 \leq x \leq 1.5$) at 300 K and 5 K (after cooling in an applied field of 5 T) as a function of applied field using a SQUID magnetometer (Chapter 2 Section 2.10), are shown in Appendix.2.2. Magnetisation data collected at 300 K are linear and pass through the origin, and analogous data collected at 5 K exhibit hysteresis consistent with weak ferromagnetism for all compositions of

$La_xSr_{4-x}NiRuO_8$ ($0.5 \leq x \leq 1.5$), like the undoped compound $LaSr_3NiRuO_8$ (Figure 5.6 (a)). However, for compositions of $1.3 \leq x \leq 1.5$, besides normal hysteresis, 5 K data do show some magnetic frustration (Figure 5.6 (b)), which is diagnostic for the spin-glass behaviour, and the frustration does become stronger as more La^{3+} is substituted for Sr^{2+}. These observations suggest the appearance of B-site cation disordering as a result of reducing part of Ru^{5+} to Ru^{4+}, hence the charge difference between Ni and Ru is not large enough to maintain its cation ordering.



(a) $LaSr_3NiRuO_8$



(b) $La_{1.5}Sr_{2.5}NiRuO_8$

Figure 5.6. Magnetisation data collected as a function of applied field from (a) $LaSr_3NiRuO_8$ and (b) $La_{1.5}Sr_{2.5}NiRuO_8$.

5.3.3 Structural Characterisation of $La_xSr_{4-x}NiRuO_4H_4$ ($0.5 \leq x \leq 1.5$)

Synchrotron X-ray powder diffraction data (Chapter 2 Section 2.5.1.2) were collected from samples of $La_xSr_{4-x}NiRuO_4H_4$ ($0.5 \leq x \leq 1.5$). These data could be readily indexed using the same body-centred tetragonal unit cell (space group *I4/mmm*), as their undoped analogue $LaSr_3NiRuO_4H_4$, with slight variations in lattice parameters. Therefore, although neutron powder diffraction data were not collected for these doped oxide-hydride phases, these phases could still be considered to have Ni/Ru located in a plane containing only hydride ligands, and the coordination spheres of the corner-linked square-planar MH_4 units in this plane are completed by two axial oxide ions that link the planes to the neighbouring (La/Sr)O layers. Data collected from all compositions were refined against this model to achieve good statistical fits. The refined plots of $La_{1.3}Sr_{2.7}NiRuO_4H_4$ were shown in Figure 5.7 as a representative and others can be found in Appendix.2.3.

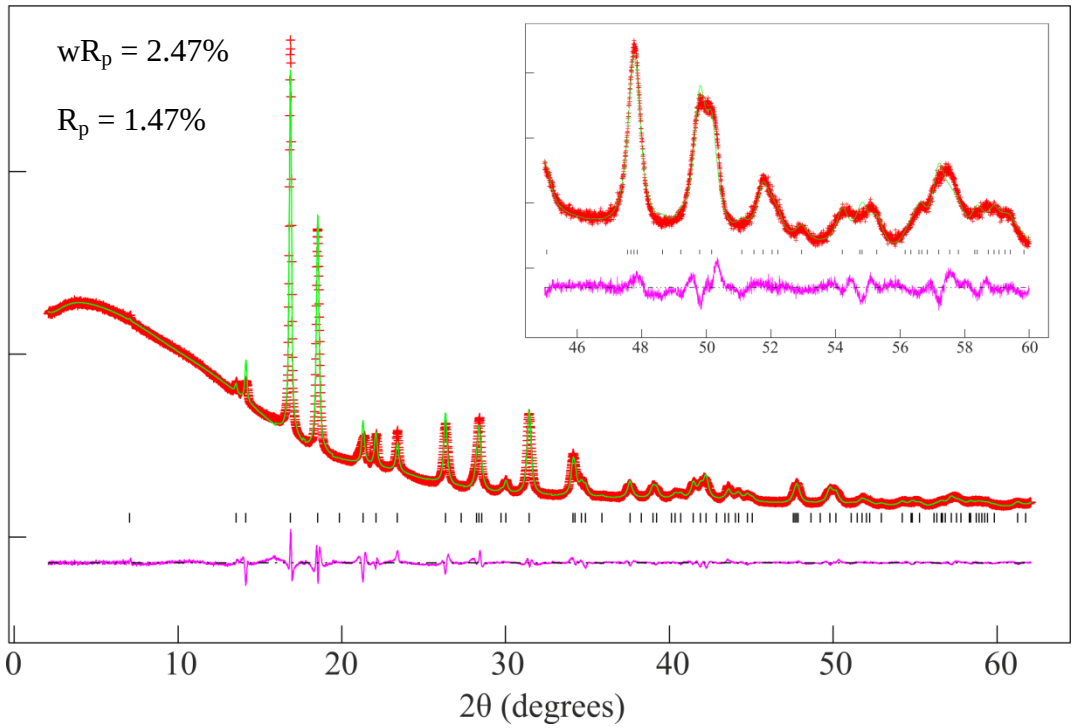


Figure 5.7. Rietveld refinement of synchrotron X-ray powder diffraction data collected from $La_{1.3}Sr_{2.7}NiRuO_4H_4$ against *I4/mmm* model. Observed (red), calculated (green), and difference plots (pink) are shown.

Lattice parameters extracted from refinements of synchrotron X-ray powder diffraction data collected from samples of $La_xSr_{4-x}NiRuO_4H_4$ ($0.5 \leq x \leq 1.5$) are summarized below in Figure 5.8. The blue dashed lines in Figure 5.8 represent the undoped compound $LaSr_3NiRuO_4H_4$, hence right-hand-side (RHS) areas represent La-rich compounds and left-hand-side (LHS) areas represent La-deficient compounds. Data points of $x = 1.5$ are clearly anomalies (as highlighted in red dashed circles in Figure 5.8) which indicate that instead of $La_{1.5}Sr_{2.5}NiRuO_4H_4$, it may be reduced to something else.

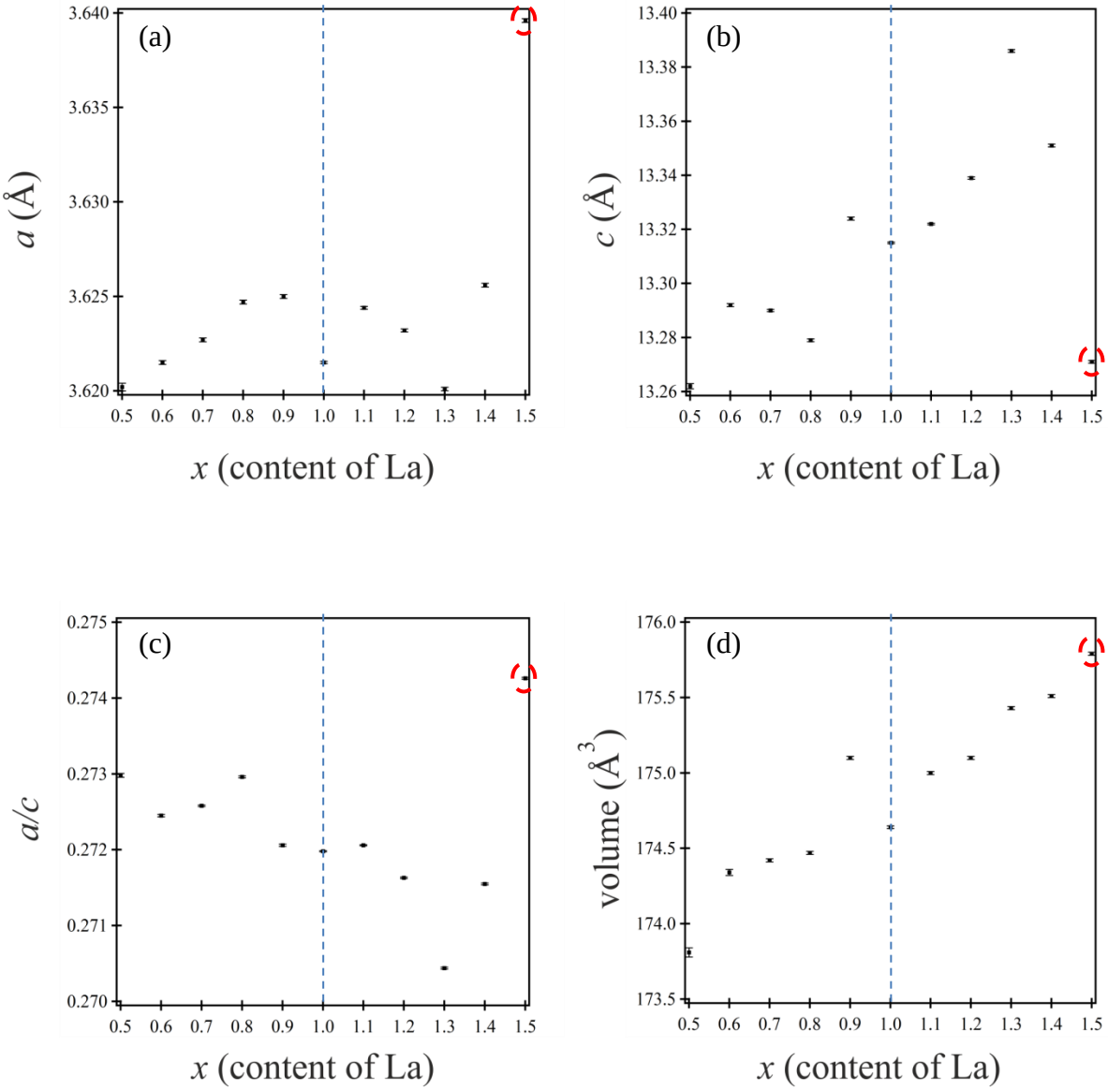


Figure 5.8. Plot (a) *a*; (b) *c*; (c) *a/c*; and (d) volume against *x* in $La_xSr_{4-x}NiRuO_4H_4$ ($0.5 \leq x \leq 1.5$) series of compounds.

For x = 0.5 and x = 1.5 phases, lattice parameters are less reliable, as these two end members really approach to the doping limit of the structure, so samples are not as pure and homogeneous as other phases.

In general, changes in the lattice parameter a in this series of oxide-hydride phases are quite subtle, only fluctuate within the range of $3.620 \leq a/\text{Å} \leq 3.625$.

For La-rich compounds (x > 1.0, RHS), both the lattice parameter c and the volume of cell generally show an increasing trend, with respect to the increase in x (content of La). According to ionic radii stated in Table 5.2, La^{3+} (r = 1.216 Å) is smaller than Sr^{2+} (r = 1.31 Å), therefore the contraction of unit cell should be expected, as more La^{3+} is substituted into the lattice, which contradicts what has been observed. Hence, the size expansion gained from reducing part of Ru^{2+} to Ru^{1+} is more dominant than the size contraction brought by replacing some of larger Sr^{2+} with smaller La^{3+}.

For La-deficient compounds (x < 1.0, LHS), both the lattice parameter c and the volume of cell generally show a decreasing trend, with respect to the decrease in x (content of La). The expansion of unit cell should be expected, if only the size difference between A-site cations are considered, as more Sr^{2+} is substituted into the lattice, which again contradicts what has been observed. Hence, the size contraction gained from oxidising part of Ni^{1+} to Ni^{2+} is more dominant than the size expansion brought by replacing some of smaller La^{3+} with larger Sr^{2+}.

Therefore, the hypothesis raised in Section 5.3.1, that the sizes of B-site cations have greater influence on lattice parameters than the sizes of A-site cations for n = 1 Ruddlesden-Popper phases, apply for these oxide-hydride phases as well.

5.3.4 Magnetic Characterisation of $La_xSr_{4-x}NiRuO_4H_4$ ($0.5 \leq x \leq 1.5$)

Magnetisation data were collected from samples of $La_xSr_{4-x}NiRuO_4H_4$ ($0.5 \leq x \leq 1.5$) by using a SQUID magnetometer and a technique called ferromagnetic subtraction (Chapter 2 Section 2.10). Due to the inevitable presence of trace amount of ferromagnetic Ni impurity in the sample prepared via topochemical reaction with CaH_2, a large field (3 T to 5 T) was applied to saturate elemental Ni during the magnetic characterisation, so the ferromagnetic behaviour contributed by Ni impurity would not mask the magnetic behaviour of the bulk phase. At 5 K increments between 5 K and 300 K, magnetisation-field isotherms were collected over the field range $3 \leq H / T \leq 5$ and the resultant magnetisation are plotted as a function of the applied field. For each 5 K step the gradient of the plot obtained shows the paramagnetic susceptibility and the intercept gives the saturated ferromagnetic moment. Combined the whole range temperature data, a field-cooled plot can be made, hence the Curie constant and the Weiss temperature of each composition can be extracted by fitting data in suitable temperature ranges to the Curie-Weiss law ($\chi = C/(T - \theta)$). The magnetisation data of $La_{0.8}Sr_{3.2}NiRuO_4H_4$ were shown in Figure 5.9 as a representative and others can be found in Appendix.2.4.

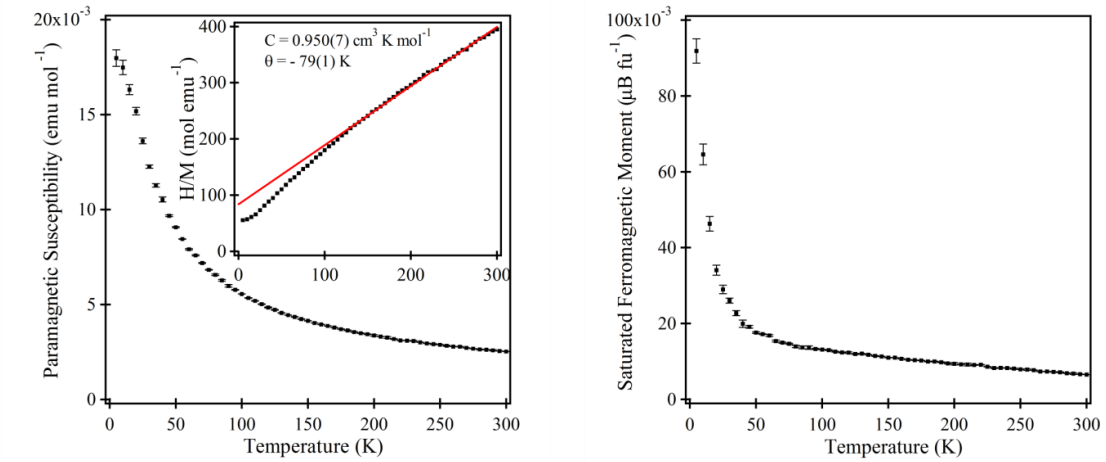


Figure 5.9. The paramagnetic susceptibility (left) and saturated ferromagnetic moment (right) of $La_{0.8}Sr_{3.2}NiRuO_4H_4$ collected as a function of temperature. Inset: the fit to the Curie–Weiss law in the temperature range $115 < T / K < 300$.

In general, all these doped oxide-hydride phases exhibit antiferromagnetic behaviour, like the undoped compound $LaSr_3NiRuO_4H_4$. However, the temperature-dependent magnetisation data collected from $LaSr_3NiRuO_4H_4$ can be fitted to the Curie-Weiss law through the whole temperature range ($10 < T / K < 300$), while the temperature-dependent magnetisation data of these doped analogues do show some deviations from the Curie-Weiss fit, especially below temperature $T \approx 115$ K.

The Curie constant and the Weiss temperature of each composition are summarized below in Figure 5.10. The blue dashed lines in Figure 5.10 represent the undoped compound $LaSr_3NiRuO_4H_4$, hence right-hand-side (RHS) areas represent La-rich compounds and left-hand-side (LHS) areas represent La-deficient compounds. In Figure 5.10 (a), values of theoretical Curie constant (if a liner relationship between oxidation states of B-site cations and the magnetic behaviour of the phase is assumed) are represented in red, to compare with values of experimental Curie constant (black) extracted from magnetisation data collected from each composition.

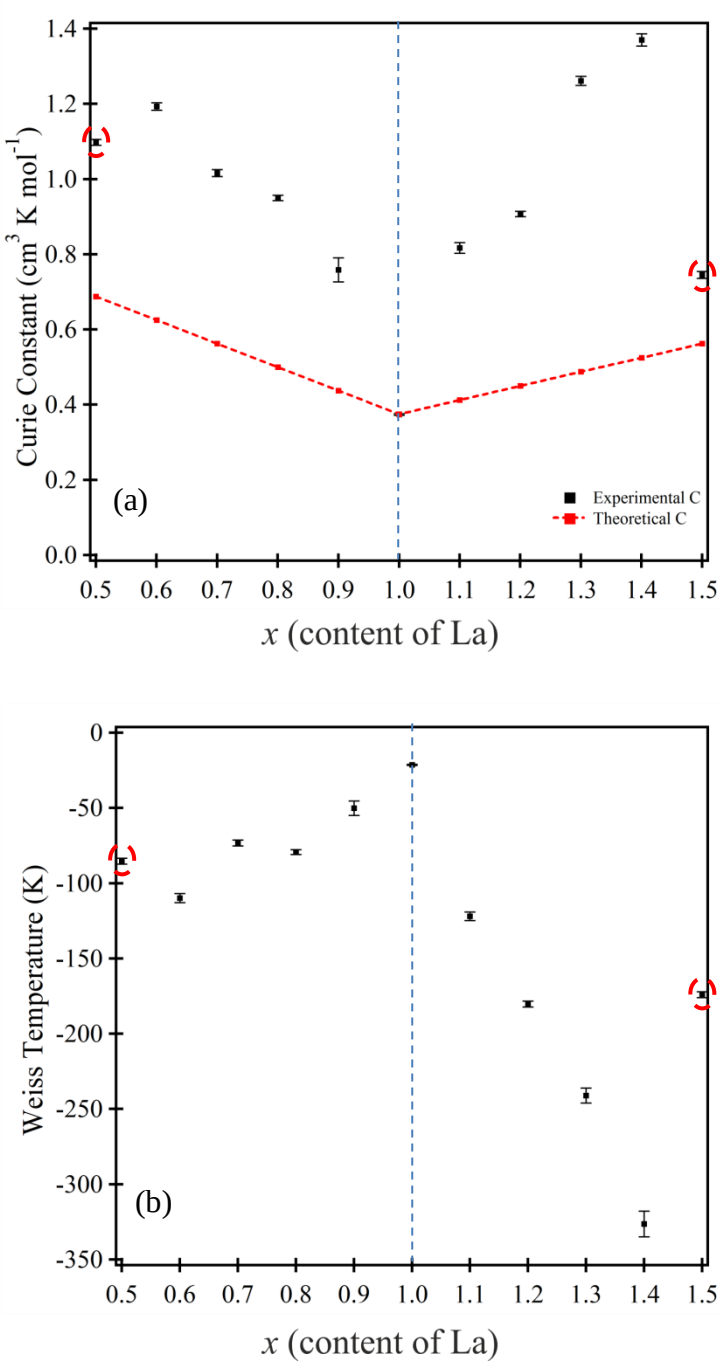


Figure 5.10. Plot of (a) Curie Constant; and (b) Weiss Temperature against *x* in $La_xSr_{4-x}NiRuO_4H_4$ ($0.5 \leq x \leq 1.5$) series of compounds.

Apart from two end members (x = 0.5 and 1.5, as highlighted in red dashed circles), changes in experimental Curie constants generally follow the trend expected, i.e. for RHS they increase with respect to the increase in x (content of La) and for LHS they increase with

respect to the decrease in *x*. However, the magnitude of changes is significantly larger than what is predicted, based on the assumption of localised electrons of B-site cations and spin-only interactions between them (as represented in red in Figure 5.10 (a)).

For RHS area of Figure 5.10 (a), La-for-Sr substitutions result in electron-doping of the system (La-rich compounds, $x > 1$), hence B-site cations get reduced, in this case it is more likely to reduce part of Ru^{2+} to Ru^{1+} by adding an extra electron into the Ru d_{x2-y2} orbital, as represented by the blue dashed arrow in Figure 5.11. Therefore the number of unpaired electrons in the system becomes larger, leading to the increase in Curie constants.

For LHS area of Figure 5.10 (a), Sr-for-La substitutions result in hole-doping of the system (La-deficient compounds, $x < 1$), hence B-site cations get oxidised, in this case it is more likely to oxidise part of Ni^{1+} to Ni^{2+} by removing one paired-up electron from the Ni d_{x2-y2} orbital, as highlighted by the red dashed circle in Figure 5.11. Therefore the number of unpaired electrons in the system becomes larger, leading to the increase in Curie constants as well.

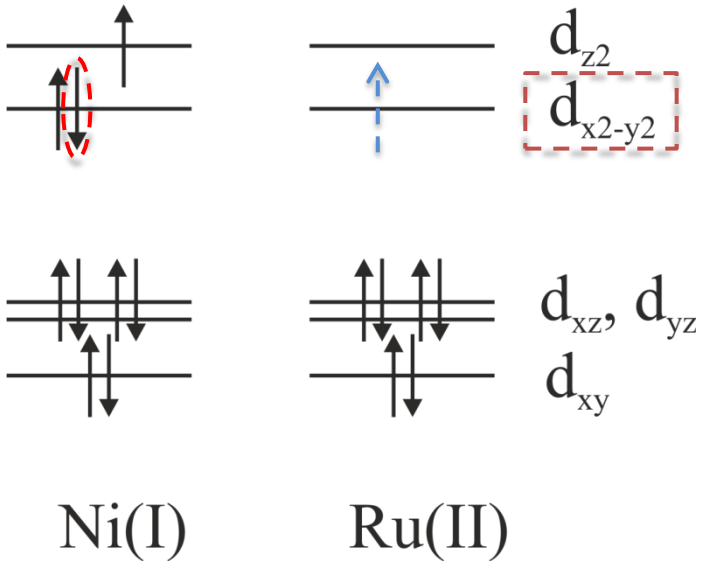


Figure 5.11. Predicted spin states of B-site transition metal cations in $La_xSr_{4-x}NiRuO_4H_4$ ($0.5 \leq x \leq 1.5$) series of compounds.

In both cases, the d_{x2-y2} orbital, as highlighted by the brown dashed box in Figure 5.11, becomes magnetically active, while before doping it is magnetically silent. It is important because the magnetically active d_{x2-y2} orbital can enhance the strength of magnetic coupling significantly (Figure 5.12), as it better matches the shape of the hydride 1*s* orbital compared to the original Ni d_{z2} orbital (La-deficient compounds, $x < 1$), or it makes the Ru (diamagnetic before doping) magnetically active in the superexchange pathway (La-rich compounds, $x > 1$). Therefore it is not surprising that the magnitude of Weiss temperatures of doped phases increase compared to the undoped analogue, as a consequence of strongly enhanced magnetic coupling strength. Also for La-rich compounds (RHS), the increase is more dramatic than the other side, as magnetically active Ru centres really shorten the distance of superexchange.

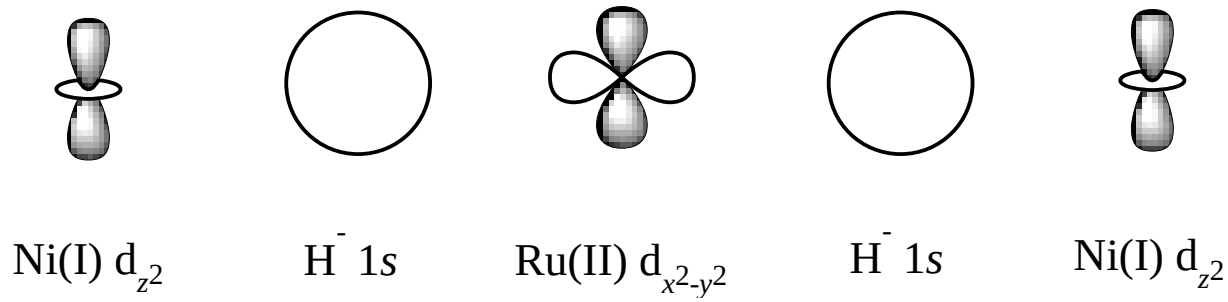


Figure 5.12. Orbital overlapping through a linear Ni-H-Ru-H-Ni superexchange pathway in $LaSr_3NiRuO_4H_4$.

In conclusion, magnetic data collected from samples of $La_xSr_{4-x}NiRuO_4H_4$ ($0.5 \leq x \leq 1.5$) suggest that, as long as the ratio between La and Sr deviates from 1:3, electrons of the B-site cations may no longer be localised, and no matter electron-doping or hole-doping the system, magnetic coupling strength are significantly enhanced for this series of compounds.

5.4 Discussion

5.4.1 Doping Limits of $La_xSr_{4-x}NiRuO_8$ and $La_xSr_{4-x}NiRuO_4H_4$ ($0.5 \leq x \leq 1.5$)

The chemical 'doping' concept has been applied in many complex transition-metal oxide and oxide-hydride phases, in order to generate itinerant electrons, which drives the transition-metal ions into non-integer or mixed-valent states, hence results in remarkably different physical properties, such as insulator-to-metal transitions or even superconductivity, compared to their undoped analogues.[4, 91, 92]

The cation-ordered double perovskite analogue, $LaSrNiRuO_6$, is found to be able to accommodate chemical 'doping' to a certain extent, by successfully preparing a range of $La_{1+x}Sr_{1-x}NiRuO_6$ ($-0.25 \leq x \leq 0.375$) phases using the citrate gel method described in Chapter 2 Section 2.1.2. However, upon topochemical reduction of these parent perovskite phases, only compositions of x = -0.15, -0.05, +0.05, +0.1 and +0.25 can be successfully reduced to infinite layer $La_{1+x}Sr_{1-x}NiRuO_4$ phases.[94]

Inspired by successful doping of $LaSrNiRuO_6$ and $LaSrNiRuO_4$ phases, manipulations between La and Sr for their n = 1 Ruddlesden-Popper equivalents were investigated. It is found that $LaSr_3NiRuO_8$ can accommodate chemical 'doping' to a greater extent, compared to its perovskite analogue, by forming single phases of $La_xSr_{4-x}NiRuO_8$ ($0.5 \leq x \leq 1.5$) under the same reaction conditions. It is not surprising that the n = 1 Ruddlesden-Popper phase has greater ability to accommodate chemical 'doping', as its structure is not rigidly connected along z direction.

The topochemical reduction chemistry of the undoped compound $LaSr_3NiRuO_8$ can also be applied to these doped phases, by using CaH_2 as a reducing agent, with slight variations of the reaction temperature (listed in Table 5.1). It is found that, unlike perovskite

analogues, the whole range of parent oxide phases can be reduced to oxide-hydride phases, i.e. $La_xSr_{4-x}NiRuO_4H_4$ ($0.5 \leq x \leq 1.5$) phases are formed in the similar fashion.

However, for La-rich compounds, reaction energy barriers have increased, as complete conversions from oxides to oxide-hydrides occur at elevated reaction temperatures (460 °C for $x = 1.1$ and 470 °C for $1.2 \leq x \leq 1.5$). There are significant amount of reduced oxides left in samples when reaction mixtures are heated at 450 °C, which is the optimum reaction temperature for the undoped compound. In contrast, La-deficient compounds tend to become more fragile, with respect to more La^{3+} substituted by Sr^{2+}, as reflected in the lowering optimum reaction temperatures. For $x = 0.9$ and 0.8, lattices can still hold together at 450 °C when they are treated with CaH_2, but for $0.5 \leq x \leq 0.7$, parent oxide phases already undergo non-topochemical decompositions at this temperature.

In general, both $La_xSr_{4-x}NiRuO_8$ and $La_xSr_{4-x}NiRuO_4H_4$ show greater ability to accommodate chemical 'doping' than their perovskite analogues because $n = 1$ Ruddlesden-Popper phases have not rigid connections along z direction and hence have more degree of freedom.

5.4.2 Reaction Pathways of Low-temperature Topochemical Reactions

Doped compounds do not necessarily undergo the same reaction pathway as their undoped analogues in topochemical reactions, especially when the reaction pathway is sensitive to electron counts of cations, which is normally changed as a consequence of cation substitutions.

For example, attempts to electron-dope the Fe^{2+} phase $SrFeO_2$ via rare-earth substitution for strontium reveal that $RE_xSr_{1-x}FeO_{3-\delta}$ is reduced to $RE_xSr_{1-x}FeO_{2+x/2}$,

maintaining an oxidation state of Fe^{2+} in the reduced phase.[95] In addition, attempts to hole-dope the anion-ordered, tetragonal oxide-hydride phase $SrVO_2H$ (formed in topochemical reduction of $SrVO_3$ by using CaH_2 as a reducing agent), by substituting 5% of the vanadium for titanium, reveal similar but more dramatic responses. Instead of forming tetragonal $SrV_{0.95}Ti_{0.05}O_2H$ phase, the analogous reaction conditions applied to the hole-doped $SrV_{0.95}Ti_{0.05}O_3$ yields a cubic $SrV_{0.95}Ti_{0.05}O_{1.5}H_{1.5}$ phase, with disordered distribution of O^{2-}/H^-.[96]

In both cases, the differences in reactivity in response to seemingly minor changes in compositions suggest that, the products of low-temperature topochemical reactions of these phases are selected under kinetic control, and depend sensitively on the electron counts of transition metals. Therefore even small changes in the composition can dramatically alter the relative rates of the competing pathways that exist under low-temperature conditions.

However, the sensitivity to cation substitution observed in above cases is not universal in topochemical reactions. For example, topochemical reductions of cation-ordered double perovskite $LaSrNiRuO_6$ and n = 1 Ruddlesden-Popper phase $LaSr_3NiRuO_8$ can be applied to their doped analogues and yield same corresponding reduced phases under similar reaction conditions, as discussed in Section 5.4.1. Therefore, low-temperature topochemical reactions of these parent oxide phases are 'similar' to typical high-temperature ceramic synthesis, i.e. the products of a reaction are determined by thermodynamic stability, and small compositional changes tend not to change the thermodynamic parameters to the extent that some other competing phase becomes more stable; that is to say, these phases can generally accommodate chemical 'doping' to certain extents, as their reaction pathways are not too sensitive to electron counts, and conservations of structures are more dominant here.

5.4.3 Magnetic Behaviour of $La_xSr_{4-x}NiRuO_8$ and $La_xSr_{4-x}NiRuO_4H_4$ ($0.5 \leq x \leq 1.5$)

The crystal structures are generally conserved for doped parent oxide phases and reduced oxide-hydride phases, but their magnetic behaviour has been altered dramatically, as long as the ratio between La and Sr deviates from 1:3.

For doped parent oxide phases, $La_xSr_{4-x}NiRuO_8$ ($0.5 \leq x \leq 1.5$), Curie constants extracted from experimental data of La-rich compounds ($x > 1$) approximately coincide with predicted ones, based on the assumption that, there is a liner relationship between oxidation states of B-site cations and the magnetic behaviour of the phase, i.e. electrons of transition metals are localised and spins only interact with themselves. In contrast, Curie constants of La-deficient compounds ($x < 1$) change in the opposite direction compared to predicted ones, which we have not come up with a perfect explanation so far. Weiss temperatures of doped parent oxide phases have not changed dramatically, but they do tend to decrease no matter after electron-doping or hole-doping the system. In addition, magnetisation-isotherm data collected at 5 K start to show frustrated magnetic behaviour after 'doping' to a certain extent and the frustration does become stronger as more La^{3+} is substituted for Sr^{2+}.

For doped reduced oxide-hydride phases, $La_xSr_{4-x}NiRuO_4H_4$ ($0.5 \leq x \leq 1.5$), although Curie constants extracted from experimental data change in the same direction as predicted, for both La-rich and La-deficient compounds, magnitudes of changes are unexpected large, such as doubled or even tripled for small compositional changes. Also absolute values of Weiss temperatures increase dramatically with respect to small amount of chemical 'doping', especially for La-rich compounds. These observations suggest that, the involving of the d_{x2-y2} orbital of Ni/Ru in magnetic coupling strongly enhances its strength in the linear Ni-H-Ru-H-Ni superexchange pathway, either from the orbital-shape matching point of view or the distance point of view.

5.5 Conclusion

The n = 1 Ruddlesden-Popper phase $LaSr_3NiRuO_8$ can accommodate chemical 'doping' to a great extent by forming single phases of $La_xSr_{4-x}NiRuO_8$ ($0.5 \leq x \leq 1.5$) under the same reaction condition. All compositions of doped parent oxide phases can be reduced to the corresponding oxide-hydride phases, $La_xSr_{4-x}NiRuO_4H_4$ ($0.5 \leq x \leq 1.5$), when they are treated with CaH_2, just like the undoped analogue, at slightly varied reaction temperatures. The body-centred tetragonal unit cells (space group *I4/mmm*) used to index $LaSr_3NiRuO_8$ and $LaSr_3NiRuO_4H_4$ can be used to describe the corresponding doped phases, with slight variations in lattice parameters.

Although these doped parent oxide phases and oxide-hydride phases are structurally similar to undoped ones, their magnetic behaviour has been altered dramatically, by even small amount of compositional changes, which suggests that electrons of the B-site cations are no longer localised once the ratio between La and Sr deviates from 1:3.

Unfortunately, chemical 'doping' of this series of compounds has not resulted in qualitative changes in conductivity, i.e. they are all still antiferromagnetic insulators, just like undoped ones. This is because electronic bands are too narrow for these n = 1 systems and electrons in the e_g band of $La_xSr_{4-x}NiRuO_8$ are still localised by strong on-site repulsion. In addition, upon hydride-for-oxide substitution, the degeneracy of the e_g band is broken chemically and splits into a d_{x2-y2} band and a d_{z2} band in the oxide-hydride phase, $La_xSr_{4-x}NiRuO_4H_4$. As a result, it makes the already narrow e_g band even narrower, which is not helpful for delocalising electrons. Therefore, switching to an n = 2 Ruddlesden-popper phase (wider bands) is another open and worthwhile possibility for future research, as it might induce the expected insulator-to-metal transition.

Chapter 6

Synthesis and Characterisation of $LaSr_3NiRuO_6$

6.1 Introduction

Low temperature topochemical reduction of complex transition-metal oxides has enabled the preparation of a wide range of novel metastable materials, which have been the subject of extensive study, as discussed in Chapter 1 Section 1.2.

The topochemical deintercalation of anions in complex transition-metal oxides necessarily involves reduction of transition metal centres to reach unusual low oxidation states, and modifies their coordination environments which results in qualitatively different lattice connectivity compared to parent oxide phases, especially when those anion vacancies are ordered. These topochemically reduced oxide phases, which exhibit interesting electronic and magnetic properties and their tunability makes these materials ideal for synthesis by design.[97-99]

Successful isolation of the pure reduced oxide phase $LaSr_3NiRuO_6$ was achieved by using finely divided electropositive metal Zr as an oxygen getter to reductively deintercalate oxide ions from lattice according to reaction [1]:

$$LaSr_3NiRuO_8 \longleftrightarrow LaSr_3NiRuO_{8-2x} + xO_2 + Zr \longrightarrow LaSr_3NiRuO_6 + ZrO_y \quad [1]$$

Detailed characterisations of this reduced oxide phase will be described in this chapter.

6.2 Experimental

6.2.1 Reduced Oxide Phases Formed via CaH_2 Reduction

The starting material n = 1 Ruddlesden-Popper phase, $LaSr_3NiRuO_8$, has been prepared by the traditional high-temperature ceramic synthesis as described in Chapter 2 section 2.1.1. The attempted topochemical reduction of the n = 1 Ruddlesden-Popper phase $LaSr_3NiRuO_8$ with the solid-state binary metal hydride CaH_2 in sealed ampoules yields compositions in the range $LaSr_3NiRuO_{8-x}$ ($0 < x < 2$) at different reaction temperatures (350 °C – 460 °C). Before the final reduced oxide-hydride phase $LaSr_3NiRuO_4H_4$ was observed, two distinct reduced oxide phases $LaSr_3NiRuO_7$ and $LaSr_3NiRuO_6$ were formed at reaction temperatures of 400 °C and 425 °C respectively. Although these reaction temperatures are classified as the optimum conditions for the formation of these two reduced oxide phases via CaH_2 reduction, pure phases were never successfully isolated. For example, the target reduced oxide phase $LaSr_3NiRuO_6$ isolated from CaH_2 reduction is clearly a mixture of two or more phases if a close inspection of synchrotron X-ray powder diffraction data is taken. This is especially clear when the peak shapes are examined (Figure 6.1).

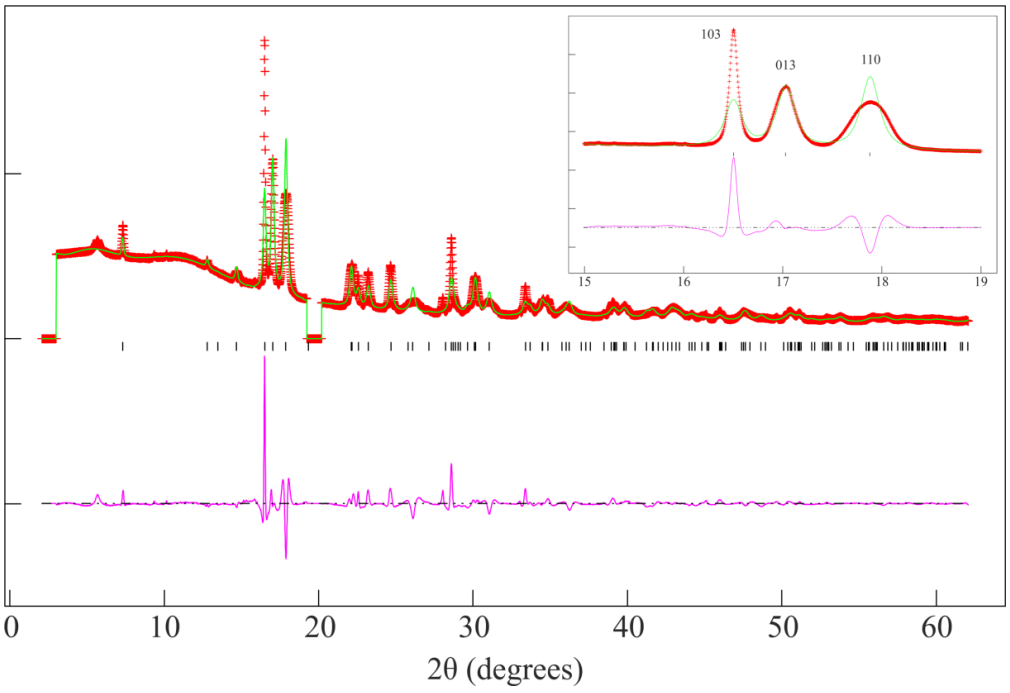


Figure 6.1. Observed, calculated and difference plots from the refinement of synchrotron X-ray powder diffraction data (*Immm*) collected from $LaSr_3NiRuO_6$ (formed at 425 °C in CaH_2 reduction).

The difference plot observed in the Rietveld refinement of synchrotron X-ray powder diffraction data collected from the reduced oxide phase $LaSr_3NiRuO_6$ (formed at 425 °C via CaH_2 reduction) against a simple body-centred orthorhombic unit cell (*Immm*) reveals that the 103 peak is much sharper, and the 110 peak is much broader, than expected, as highlighted in the embedded plot. Therefore it is highly likely that the phase isolated at this temperature is the mixture of the reduced oxide phase $LaSr_3NiRuO_6$ and an oxide-hydride phase e.g. $LaSr_3NiRuO_4H_4$, as reductions were carried out in sealed ampules and H_2 gas was formed as a by-product which strongly favours the formation of the oxide-hydride phase.

The H_2 gas which accumulates inside reaction vessels during CaH_2 reduction seems to be the key to form the oxide-hydride phase, but it is something needs to be avoided if the reduced oxide is the target phase. After switching to the 'venting' system described in Chapter 2 section 2.2.2, argon is purged through the system, to drive away the H_2 gas formed by CaH_2. However, this does not appear to change the reaction outcome as the formation of oxide-hydride phase is so strongly preferred, thus as long as there is H_2 gas generated inside the system, there will always be some oxide-hydride phase formed along with the target reduced oxide phase $LaSr_3NiRuO_6$. Therefore the solid state reducing agent was switched to NaH (which forms NaOH as the by-product during reactions, not H_2), to avoid the formation of H_2 gas, but the reaction temperature regime provided by NaH is too low to have appreciable anion mobility in the starting material $LaSr_3NiRuO_8$, thus no reaction was observed. Hence, a reductant which does not generate H_2 gas during the reduction, and which can function at similar temperature regime to CaH_2 needs to be selected, for example Zr powder. The detailed investigation of optimum reduction conditions for the use of Zr powder as an oxygen getter is presented in the following section 6.2.2. This approach eventually yields a much purer sample of the target reduced oxide phase $LaSr_3NiRuO_6$ by

eliminating the possibility of forming the oxide-hydride phase as there is no H^- source in the whole apparatus.

6.2.2 Reduced Oxide Phases Formed via Zr Getter Reduction

A small amount of $LaSr_3NiRuO_8$ was reduced by Zr powder as a test in order to find out the optimum reaction conditions. X-ray powder diffraction and thermogravimetric analysis were used to monitor reaction progress. A relatively high reaction temperature range was chosen due to the entropy-driven nature of the oxygen-releasing process, and according to the previous CaH_2 reduction profile, the system would not have appreciable anion mobility below 400 °C. In order to describe the whole reduction profile, temperature intervals of 25 °C were chosen and several distinct phases such as $LaSr_3NiRuO_{7.75}$, $LaSr_3NiRuO_7$ and $LaSr_3NiRuO_6$ were observed before non-topochemical decomposition of the starting material occurred (Table 6.1).

In general, reductions by Zr powder getter happened at higher temperatures compared to equivalent CaH_2 reactions because the substrate and metal are no longer in physical contact with each other and that slows down the reaction rate significantly. The $LaSr_3NiRuO_7$ phase was observed in the range 425 °C - 450 °C, with the $LaSr_3NiRuO_6$ phase not observed until 500 °C - 510 °C which is significantly above the non-topochemical decomposition temperature in the CaH_2 case (460 °C). Fortunately, due to the absence of a hydride ion source, the $LaSr_3NiRuO_6$ phase formed was much ‘cleaner’ compared to the analogue formed in CaH_2 reduction and more suitable for further detailed characterisations (Figure 6.2).

Reaction condition	Structure of the main lattice	Lattice parameters (estimated)/ Å	Description	Chemical composition
Starting material	Tetragonal	*a* = 3.89 *b* = 3.89 *c* = 12.63	Nice sharp 103 and 110 peaks, very crystalline	$LaSr_3NiRuO_8$
400 °C	Orthorhombic	*a* = 3.92 *b* = 3.81 *c* = 12.66	Visible splitting of 103 peak	$LaSr_3NiRuO_{7.75(1)}$
425 °C	Orthorhombic	*a* = 3.91 *b* = 3.79 *c* = 12.70	Further splitting of 103 peak	$LaSr_3NiRuO_{7.04(2)}$
450 °C	Orthorhombic	*a* = 3.91 *b* = 3.79 *c* = 12.70	No visible changes	$LaSr_3NiRuO_{7.02(1)}$
475 °C	Orthorhombic	*a* = 3.86 *b* = 3.62 *c* = 12.93	Starts to shift to O_6	$LaSr_3NiRuO_{7-x}$
500 °C	Orthorhombic	*a* = 3.84 *b* = 3.57 *c* = 13.00	Further splitting between 103 and 013 peaks	$LaSr_3NiRuO_{6.08(3)}$
510 °C	Orthorhombic	*a* = 3.84 *b* = 3.57 *c* = 13.00	No visible changes	$LaSr_3NiRuO_{6.05(1)}$
520 °C	N/A	N/A	Decomposition	La_2O_3 etc.

Table 6.1. Results from initial investigation of topochemical reduction of $LaSr_3NiRuO_8$ with Zr powder getter.

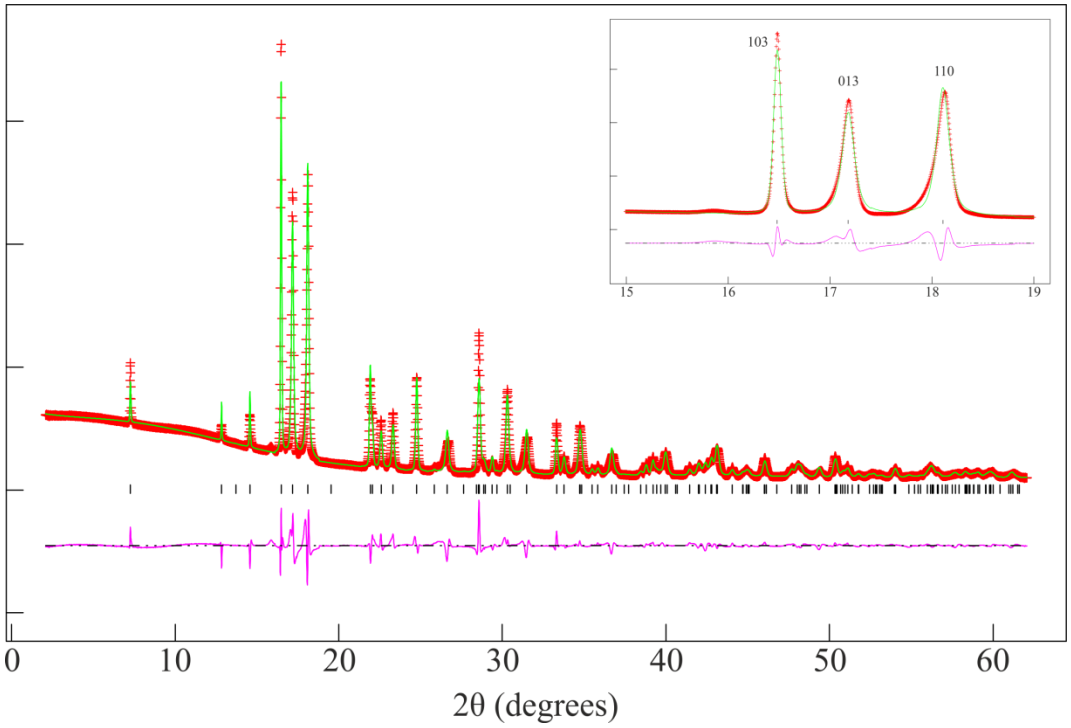


Figure 6.2. Observed, calculated and difference plots from the refinement of synchrotron X-ray powder diffraction data (*Immm*) collected from $LaSr_3NiRuO_6$ (formed at 500 - 510 °C in Zr powder reduction).

The difference plot observed in the Rietveld refinement of synchrotron X-ray powder diffraction data collected from the reduced oxide phase $LaSr_3NiRuO_6$ (formed at 500 - 510 °C in Zr powder reduction) against the same simple body-centred orthorhombic unit cell (*Immm*) shows the sample is much closer to be a homogeneous single phase. For example, the fitting to peak shapes of 103, 013 and 110 peaks has been significantly improved compared to the analogue isolated from CaH_2 reduction, as highlighted in the embedded plot of Figure 6.2.

6.2.3 Preparation of the Large-Scale Neutron Sample

A sample of $LaSr_3NiRuO_6$ suitable for analysis by neutron powder diffraction was prepared by putting approximately 1.5 g of $LaSr_3NiRuO_8$ in a smaller inner tube with 1.0 g of Zr powder in a larger outer tube to set up apparatus as described in Chapter 2 section 2.3 in an argon filled glovebox. The resulting reaction vessel was sealed under vacuum and heated at 500 °C for 2 periods of 7 days and then 510 °C for 2 periods of 7 days, with the substrate being reground, reacted Zr and ZrO_x being replaced by fresh Zr powder, and the reaction progress being monitored by laboratory X-ray diffractometer between heating periods. Since the substrate is not contaminated by any by-products or unreacted reducing agent, it does not require any further purification procedures.

6.3 Results

6.3.1 Thermogravimetric Analysis of $LaSr_3NiRuO_6$

The composition of the $LaSr_3NiRuO_{8-x}$ samples was determined from oxidative thermogravimetric analysis in a steady O_2 flow as described in Chapter 2 section 2.7. The composition of the reduced oxide phase formed at 500 – 510 °C was confirmed to be approximately $LaSr_3NiRuO_6$ by both the small test sample and the large neutron sample. Data shown in Figure 6.3 are plots of mass gain against temperature and the final phase achieved was confirmed to be the original parent oxide phase $LaSr_3NiRuO_8$ by laboratory X-ray diffractometer. Therefore the oxygen content in reduced phases can be calculated by the mass gain during the experiment as deintercalated oxide ions have been re-inserted into the crystal lattice to reoxidize back to the starting material $LaSr_3NiRuO_8$ (Table 6.2).

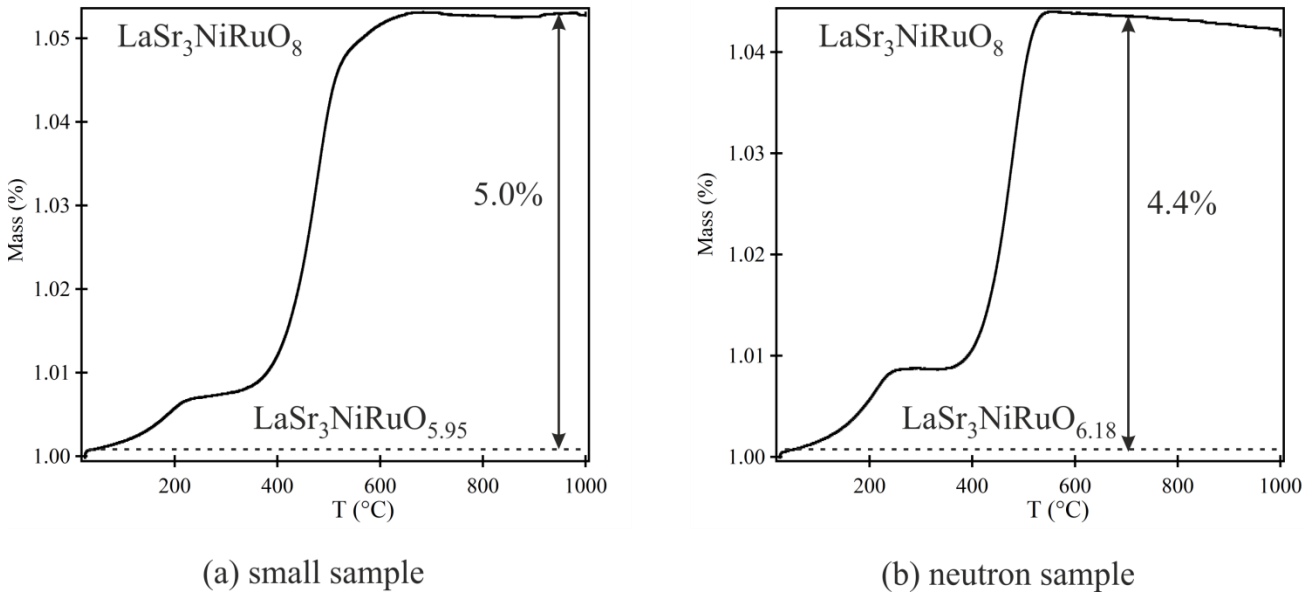


Figure 6.3. Plots of mass gain against temperature collected from (a) small sample and (b) neutron sample of $LaSr_3NiRuO_6$.

Oxidative Thermogravimetric Analysis			
RMM of $LaSr_3NiRuO_8$: 689.53 g/mol			
Sample	**Mass gain (%)**	**RMM (g/mol)**	**Oxygen content**
(a) small sample	5.0	656.70	5.95(4)
(b) neutron sample	4.4	660.47	6.18(3)

Table 6.2. Summary of thermogravimetric analysis data collected from (a) small sample and (b) neutron sample of $LaSr_3NiRuO_6$.

The RMM of reduced phases are calculated by the following equation [2]:

RMM of $LaSr_3NiRuO_8$ ÷ (1 + mass gain %) = RMM of the reduced phase [2]

The exact molar mass of $LaSr_3NiRuO_6$ should be 657.53 g/mol which is approximately the same as the value got from the small test sample (656.70 g/mol). However, the large scale neutron sample is not as pure as the small test sample because during the reduction the substrate and Zr powder are not in physical contact with each other, so it is extremely difficult to achieve a homogeneous phase with complete reduction, when the sample size is scaled up for neutron experiments. The oxygen content in the large-scale neutron sample is slightly higher than 6 which agrees with the presence of the minority phase $LaSr_3NiRuO_{7-x}$ that can be indexed in both synchrotron X-ray powder diffraction data and neutron powder diffraction data showed below in Section 6.3.2 and 6.3.3.

6.3.2 Synchrotron X-Ray Powder Diffraction of $LaSr_3NiRuO_6$

Synchrotron X-ray powder diffraction data (Chapter 2 Section 2.5.1.2) was collected from a large-scale neutron sample of $LaSr_3NiRuO_6$. The data were firstly indexed using a body-centred orthorhombic unit cell with lattice parameters: a = 3.84679(6) Å, b = 3.57881(7) Å and c = 13.0252(2) Å. A structural model was constructed, based on an n = 1, A_2BO_4 Ruddlesden-Popper phase with a 1:3 La:Sr solid-solution on the A-site, a 1:1 Ni:Ru solid-solution on the B-site and the two equatorial oxide ions deintercalated. This model was refined against the synchrotron X-ray powder diffraction data collected at room temperature and the single-phase refinement converged smoothly to give a relatively good statistical fit (χ^2 = 293.1; *wRp* = 7.25%; *Rp* = 4.60%).

A close inspection of the single-phase refinement reveals that most of peaks are slightly asymmetric (Figure 6.4 (a)), suggesting there is a secondary phase, which should have similar structure and lattice parameters compared to the primary one, as corresponding peaks are overlapped. Combining the TGA result (oxygen content = 6.18 for the large-scale neutron sample) showed in Section 6.3.1, a two-phase refinement with the secondary phase being a less reduced analogue $LaSr_3NiRuO_{7-x}$ (some oxide ions left behind in the equatorial anion-sites along *b*-axis as a result of incomplete reduction) was carried out, and it significantly improved the statistical fit (χ^2 = 98.46; *wRp* = 4.20%; *Rp* = 2.60%) compared to the single-phase refinement. Also the difference plot is more satisfying as this two-phase model accounts for the slight asymmetry of peaks and better described peak shapes in the pattern (Figure 6.4 (b)).

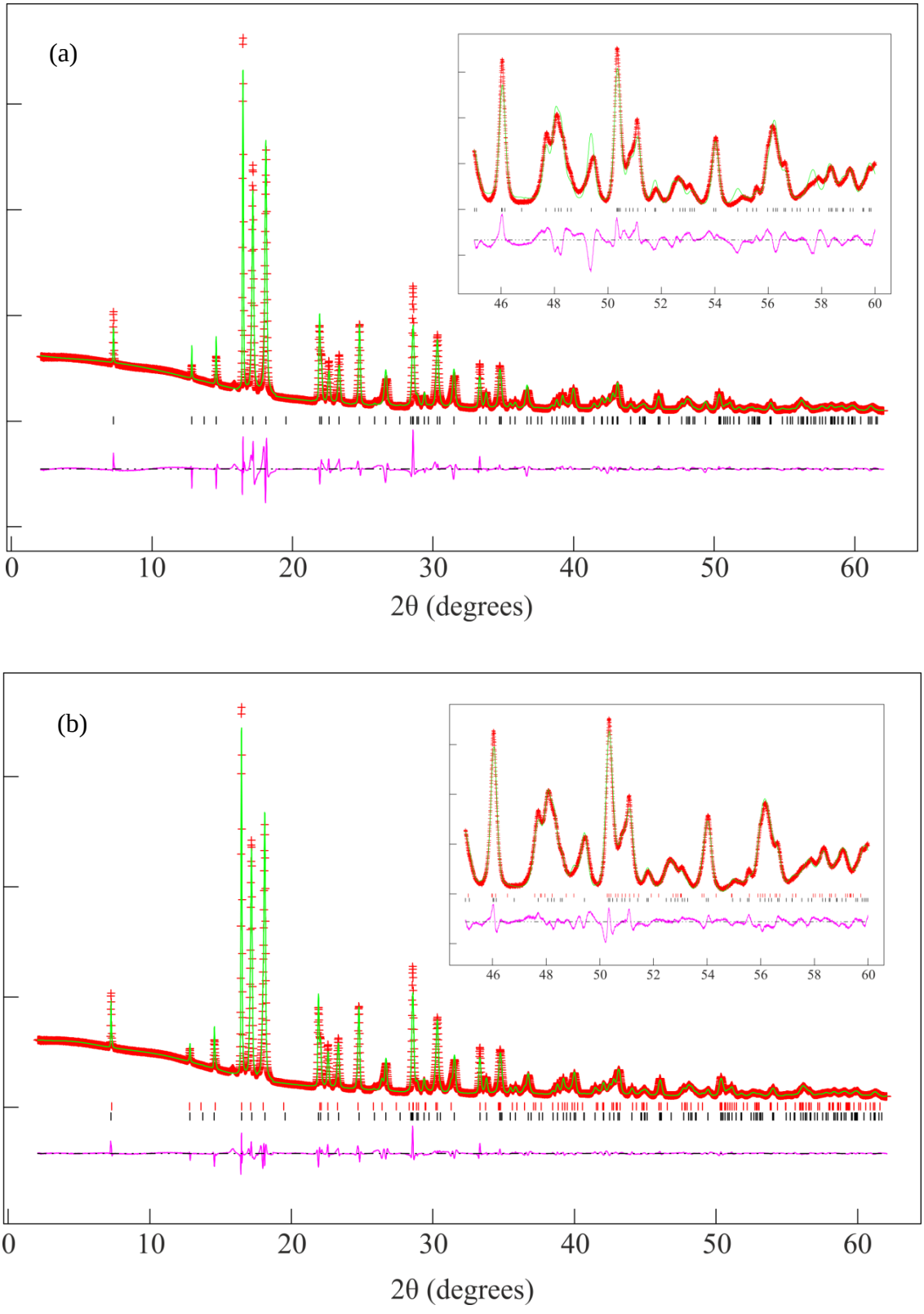


Figure 6.4. Observed, calculated and difference plots from the (a) single-phase and (b) two-phase refinement of synchrotron X-ray powder diffraction data (space group *Immm*) collected from $LaSr_3NiRuO_6$ at 298 K. Lower tick marks indicate peak positions of the majority phase, upper tick marks minority phase $LaSr_3NiRuO_{7-x}$.

6.3.3 Room Temperature Neutron Powder Diffraction of $LaSr_3NiRuO_6$

The neutron powder diffraction measurement at room temperature was carried out at D2B diffractometer in ILL (Chapter 2 Section 2.5.2.2). The body-centred orthorhombic unit cell previously described in Section 6.3.2 (Figure 6.5) was used to refine the neutron data collected from the reduced oxide phase $LaSr_3NiRuO_6$, formed in the topochemical reduction of its parent oxide phase $LaSr_3NiRuO_8$ by using Zr powder as an oxygen getter. While the model accounted for all the peaks, some reflections were too broad to be properly defined as showed in Figure 6.6 (a). Standard anisotropic peak broadening models led to an improvement in the fit to the data, but still did not fully describe the variation in peak shapes. The imperfect fit to peak shapes by a single-phase model suggests the sample containing more than one phase, which agrees with the TGA result and synchrotron X-ray powder diffraction data collected from the same sample. The single-phase refinement still converged readily to give a relatively good statistical fit (χ^2 = 4.670; *wRp* = 6.35%; *Rp* = 4.73%).

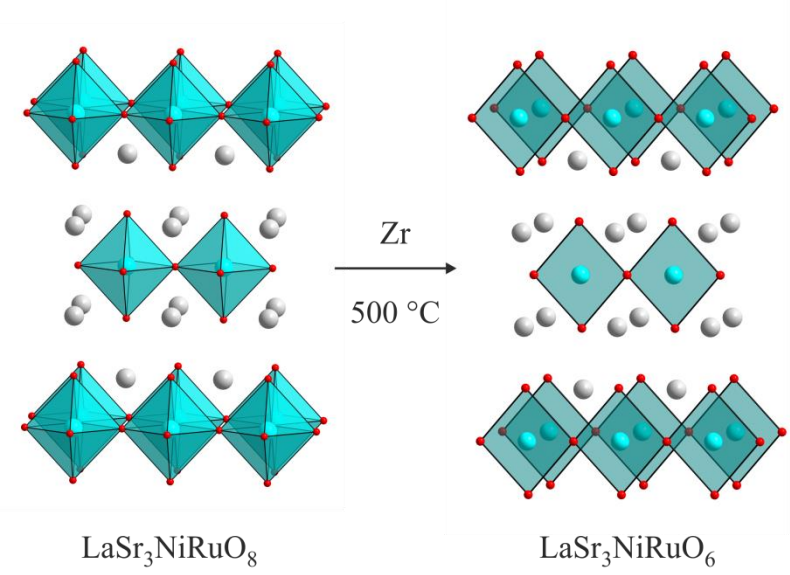


Figure 6.5. Topochemical reduction of $LaSr_3NiRuO_8$ with Zr powder to form reduced oxide phase $LaSr_3NiRuO_6$ with ordered oxide vacancies along *b*-axis.

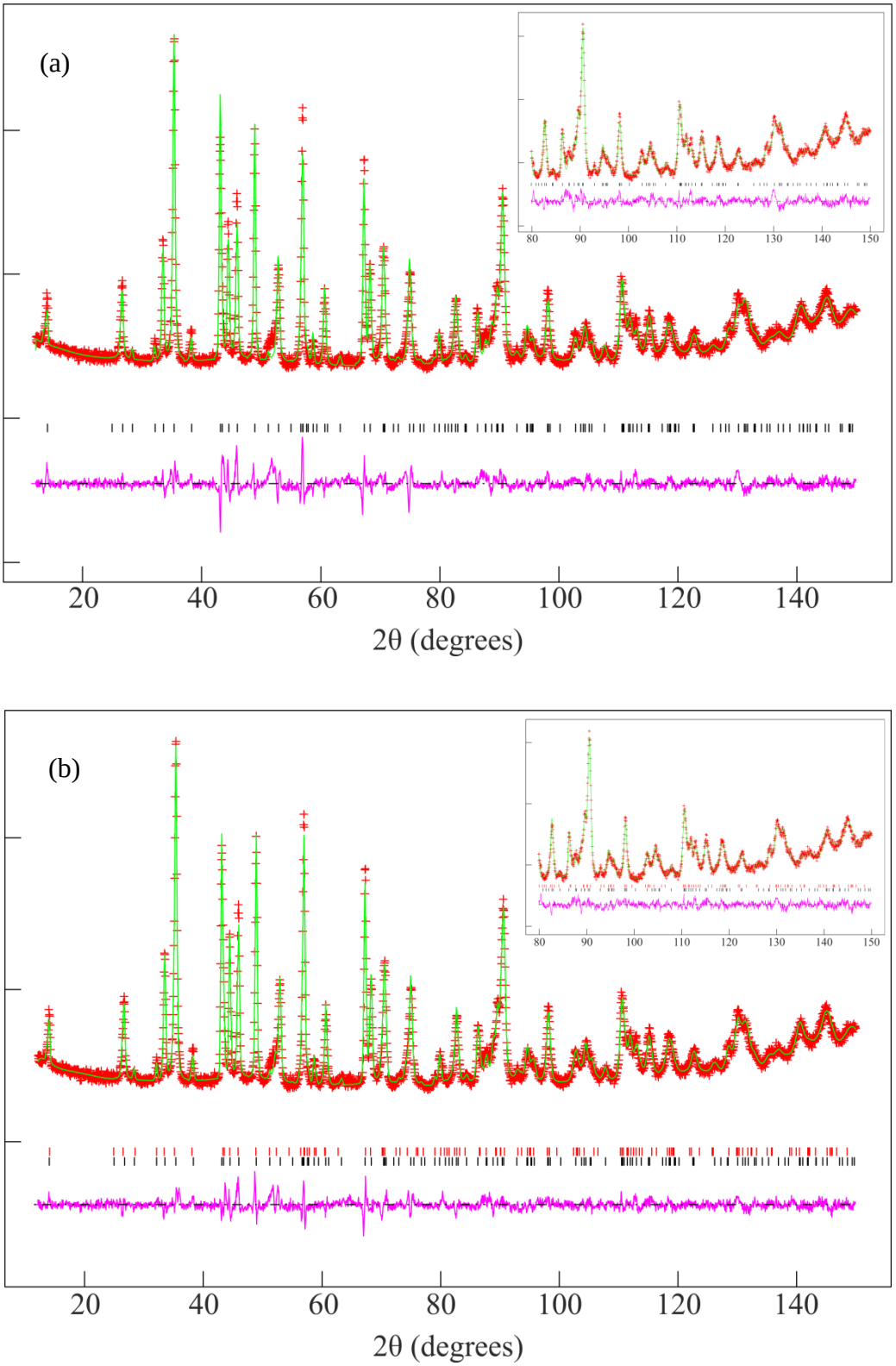


Figure 6.6. Observed, calculated and difference plots from the (a) single-phase and (b) two-phase refinement of neutron powder diffraction data (space group *Immm*) collected from $LaSr_3NiRuO_6$ at 298 K. Lower tick marks indicate peak positions of the majority phase, upper tick marks minority phase $LaSr_3NiRuO_{7-x}$.

A much improved fit to the neutron powder diffraction data collected was achieved by using a two-phase model based on the same body-centred orthorhombic structure, with the secondary phase being a less reduced analogue $LaSr_3NiRuO_{7-x}$. The structural lattice parameters of two phases were allowed to refine independently, and the secondary phase appeared to have a slightly larger unit cell than the primary phase, as a consequence of its higher oxygen content. This two-phase refinement converged readily to give an improved statistical fit (χ^2 = 2.871; *wRp* = 4.97%; *Rp* = 3.72%) and visual fit (Figure 6.6 (b)) as the variation in peak shapes was better described in this case. Full details of the structural parameters are given in Table 6.3, anisotropic displacement factors are given in Table 6.4 and selected bond lengths are given in Table 6.5.

The bond lengths extracted from the room-temperature structure of the reduced oxide phase $LaSr_3NiRuO_6$ (Table 6.5) suggest that the Ni/RuO_4 squares are quite distorted, i.e. in a 'diamond' shape, as the Ni/Ru-O(2) bond length is only 90.9% of the Ni/Ru-O(1) bond length. A similar phenomenon has been seen in the equivalent cation-ordered infinite layer phase $LaSrNiRuO_4$ where the checker-board arranged RuO_4 squares (Ru-O(1) bond length = 97.1% of Ru-O(2) bond length) and NiO_4 squares (Ni-O(1) bond length = 98.9% of Ni-O(2) bond length) are both slightly distorted.[10] In contrast, $SrFe_{0.5}Ru_{0.5}O_2$, the first extended oxide phase to contain Ru^{2+} centres, consists of perfect squares of Fe/RuO_4 unit with all Fe/Ru-O bonds being identical.[11]

Atom	Wyckoff Position	*x*	*y*	*z*	Fraction	U_{iso} equiv. (Å^2)
La/Sr(1)	4*i*	0	0	0.3544(1)	0.25/0.75	0.0071
Ni/Ru(1)	2*a*	0	0	0	0.5/0.5	0.0110
O(1)	4*i*	0	0	0.1626(2)	1	0.0102
O(2)	2*b*	0.5	0	0	1	0.0191
$LaSr_3NiRuO_6$ space group *Immm* (#71) Formula weight : 657.52 g mol^{-1}, Z = 2 Mass fraction: 76.1(2)% *a* = 3.8474(2) Å, *b* = 3.5762(2) Å, *c* = 13.0168(9) Å, Volume = 179.10(3) Å^3						
$LaSr_3NiRuO_{7-x}$ space group *Immm* (#71) Formula weight : 673.53 – δ g mol^{-1}, Z = 2 Mass fraction: 23.8(1)% *a* = 3.855(1) Å, *b* = 3.6251(9) Å, *c* = 12.946(2) Å, Volume = 180.95(6) Å^3						
Radiation source: Neutron Powder Diffraction, λ = 1.5943(2) Temperature: 298 K χ^2 = 2.871; *wRp* = 4.97%; *Rp* = 3.72%.						

Table 6.3. Structural parameters from the refinement of neutron powder diffraction data collected from $LaSr_3NiRuO_6$ at 298 K.

Atom	U_{11}	U_{22}	U_{33}
La/Sr(1)	0.0071(14)	0.0079(18)	0.0061(14)
Ni/Ru(1)	0.0033(17)	0.0216(23)	0.0080(17)
O(1)	0.0079(14)	0.0213(20)	0.0014(19)
O(2)	0.0059(23)	0.0336(39)	0.0178(29)

Table 6.4. Anisotropic displacement factors from the structural refinement of neutron powder diffraction data collected from $LaSr_3NiRuO_6$ at 298 K.

Cation	Anion	length (Å)
La/Sr(1)	O(1)	2.497(3) × 1
	O(1)	2.636(1) × 4
	O(2)	2.606(1) × 2
Ni/Ru(1)	O(1)	2.117(3) × 2
	O(2)	1.924(1) × 2

Table 6.5. Selected bond lengths from the room temperature refined structure of $LaSr_3NiRuO_6$.

Although much improved refinements were achieved against both synchrotron X-ray powder diffraction data and neutron powder diffraction data collected from the large-scale neutron sample, by adding a less reduced analogue $LaSr_3NiRuO_{7-x}$ as a minority phase, a single-phase refinement against neutron powder diffraction data by using a monoclinic unit cell was carried out to see whether this lower-symmetry unit cell could account for the abnormal broadening of some reflections in the pattern. However, not only the statistical fit (χ^2 = 8.646; *wRp* = 8.65%; *Rp* = 6.28%), but also the visual fit (Figure 6.7) got worse compared to the two-phase refinement described above.

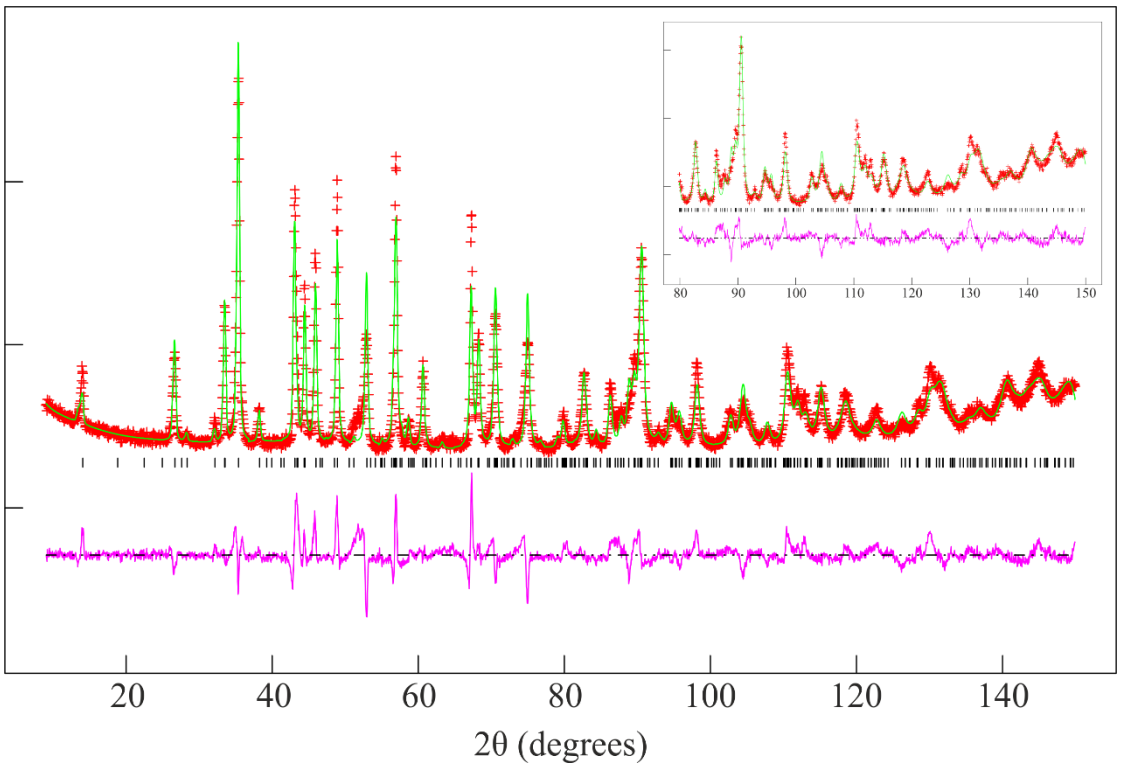


Figure 6.7. Observed, calculated and difference plots from the single-phase refinement of neutron powder diffraction data (space group *C*2/*c*) collected from $LaSr_3NiRuO_6$ at 298 K.

6.3.4 Magnetic Characterisation of $LaSr_3NiRuO_6$

Magnetisation data was collected from the superconducting quantum interference device (SQUID) by using a technique called ferromagnetic subtraction (Chapter 2 Section 2.10). Due to the inevitable presence of trace amount of ferromagnetic Ni impurity in the sample prepared via topochemical reaction with Zr powder, a large field (3 T to 5 T) was applied to saturate elemental Ni during the magnetic characterisation, so the ferromagnetic behaviour contributed by Ni impurity would not mask the magnetic behaviour of the bulk phase. At 5 K temperature increments between 5 K and 300 K, magnetisation-field isotherms were collected over $3 \leq H/T \leq 5$ and the resultant magnetisation are plotted as a function of the applied field. For each 5 K step the gradient of the plot obtained shows the paramagnetic susceptibility and the intercept gives the saturated ferromagnetic moment from any impurities.

Unlike the oxide-hydride phase $LaSr_3NiRuO_4H_4$ formed with CaH_2, this reduced oxide phase $LaSr_3NiRuO_6$ goes through a local maximum which is accompanied by an increase in the saturated ferromagnetic moment of the sample, and then its paramagnetic susceptibility becomes nearly independent with respect to temperature, consistent with a paramagnetic to ferromagnetic transition when the sample is cooled below T = 80 K. Combined the whole range temperature data, a field-cooled plot can be made, from data in the range $100 \leq T / K \leq 300$, the Curie constant was extracted as $C = 1.252(5)$ cm^3 K mol^{-1} and the Weiss temperature as $\theta = + 68(1)$ K (Figure 6.8). These data in combination suggest the reduced oxide phase should adopt a ferromagnetic ground state.

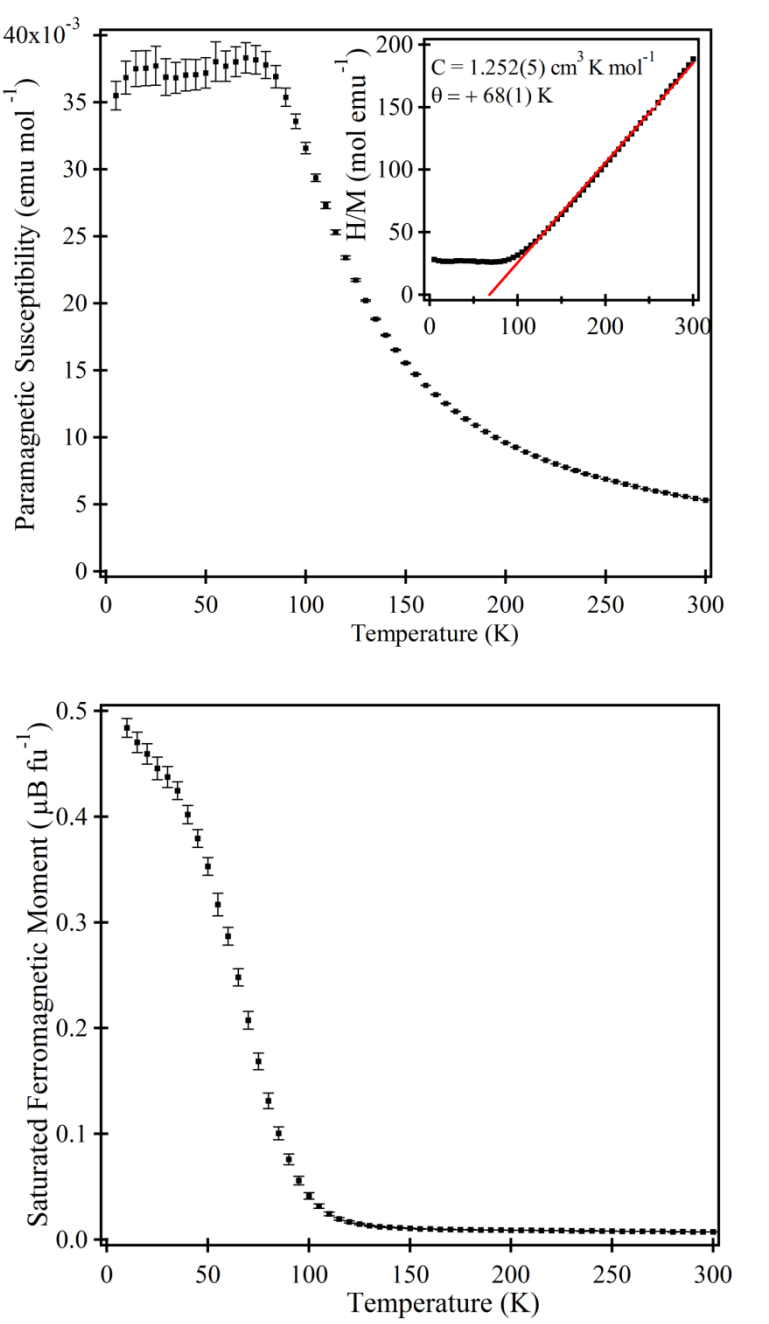


Figure 6.8. The paramagnetic susceptibility (top) and saturated ferromagnetic moment (bottom) of $LaSr_3NiRuO_6$ collected as a function of temperature. Inset: the fit to the Curie–Weiss law in the temperature range 100 < *T* / K < 300.

The observed Curie constant from this reduced oxide phase $LaSr_3NiRuO_6$ (contains a minority phase of $LaSr_3NiRuO_{7-x}$) yields a value of μ^2 to be 10.016 μ_B, which is approximately 91.05% of the expected μ^2 value 11 μ_B from a combination of a d^9, S = ½ Ni^{1+} centre and a d^6, Ru^{2+} centre with two unpaired electrons (S = 1), as previously observed in the reduced cation-ordered infinite layer phase $LaSrNiRuO_4$ formed in topochemical reduction of its parent double perovskite phase $LaSrNiRuO_6$ by using CaH_2 as a reducing agent.[10] Therefore an electronic configuration has been proposed for $LaSr_3NiRuO_6$ (Figure 6.9) based on the DFT calculation and resulting electronic configuration of infinite layer phase $LaSrNiRuO_4$.

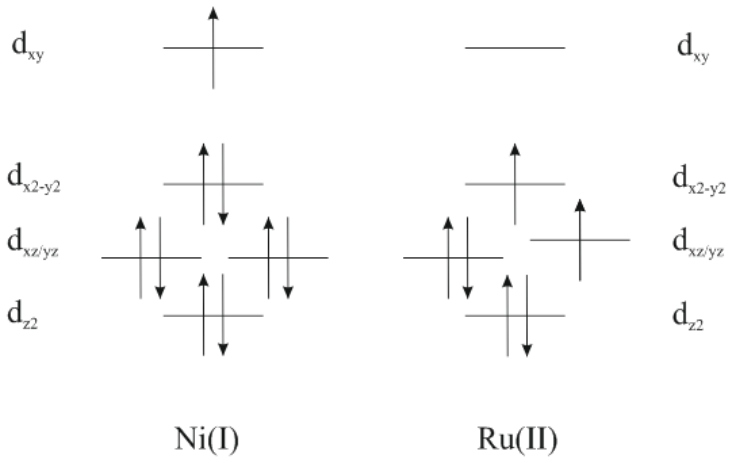


Figure 6.9. Proposed electronic configurations of $LaSr_3NiRuO_6$.

Although the reduced oxide phase $LaSr_3NiRuO_6$ undergoes the similar paramagnetic to ferromagnetic transition when the sample cools down, the transition temperature is below T = 80 K which is much lower than that of the equivalent infinite layer phase $LaSrNiRuO_4$ (T = 250 K). Also the maximum saturated ferromagnetic moment observed is roughly 0.5 μ_B per formulae unit for $LaSr_3NiRuO_6$ as showed in the bottom plot of Figure 6.8, which is only 50%

of the saturated ferromagnetic moment observed (~ 1.0 μ_B) for $LaSrNiRuO_4$.[10] The much lower net magnetic moment observed for $LaSr_3NiRuO_6$ might be explained by the absence of magnetic coupling between layers, despite Ni and Ru centres couple in a ferromagnetic way within each layer.

6.3.5 Low Temperature Neutron Powder Diffraction of $LaSr_3NiRuO_6$

The neutron powder diffraction measurement at low temperature was carried out at D2B diffractometer in ILL (Chapter 2 Section 2.5.2.2). The same body-centred orthorhombic unit cell (space group *Immm*) was used to refine the low temperature neutron data collected from $LaSr_3NiRuO_6$ and a two-phase model gives a much-improved refinement (Figure 6.10).

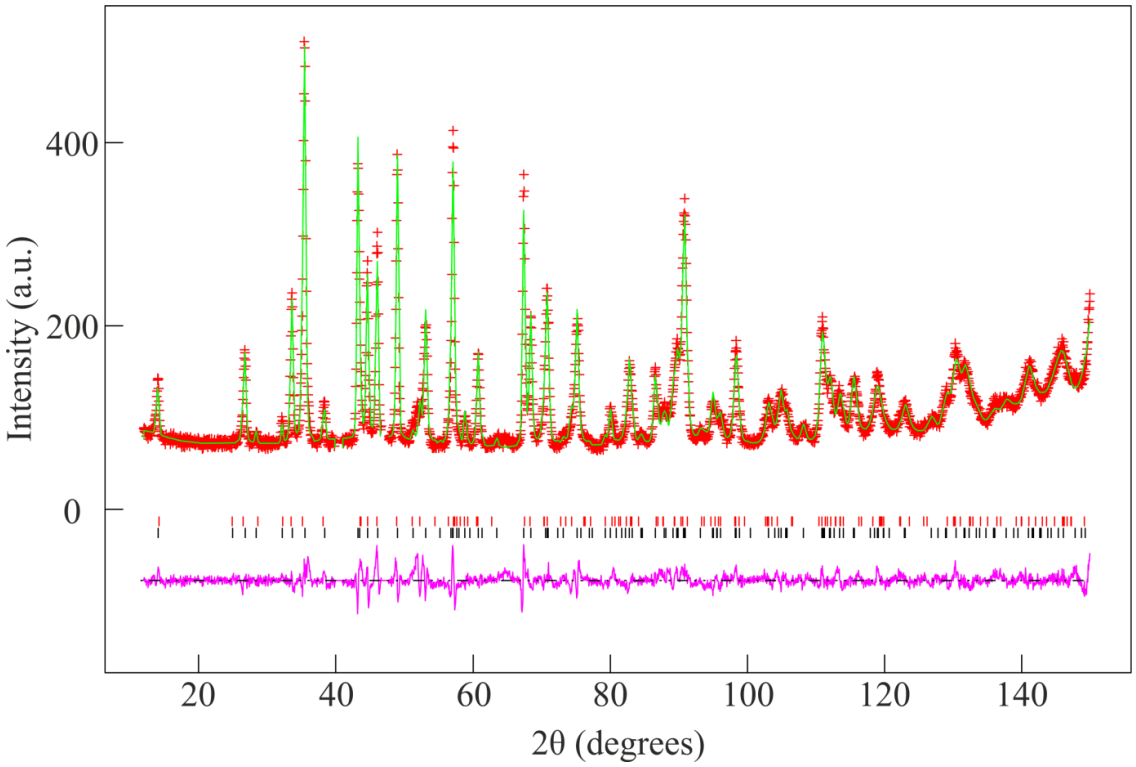


Figure 6.10. Observed, calculated and difference plots from the two-phase refinement of neutron powder diffraction data (space group *Immm*) collected from $LaSr_3NiRuO_6$ at 10 K. Lower tick marks indicate peak positions of the majority phase, upper tick marks $LaSr_3NiRuO_{7-x}$.

Full details of the structural parameters are given in Table 6.6, anisotropic displacement factors are given in Table 6.7 and selected bond lengths are given in Table 6.8.

Atom	**Wyckoff Position**	***x***	***y***	***z***	**Fraction**	**U_{iso} equiv. (Å^2)**
La/Sr(1)	4*i*	0	0	0.3544(1)	0.25/0.75	0.0032
Ni/Ru(1)	2*a*	0	0	0	0.5/0.5	0.0069
O(1)	4*i*	0	0	0.1633(2)	1	0.0070
O(2)	2*b*	0.5	0	0	1	0.0131
$LaSr_3NiRuO_6$ space group *Immm* (#71) Formula weight : 657.52 g mol^{-1}, Z = 2 Mass fraction: 81.9(2)% *a* = 3.8428(2) Å, *b* = 3.5657(2) Å, *c* = 12.9822(8) Å, Volume = 177.88(3) Å^3						
$LaSr_3NiRuO_{7-x}$ space group *Immm* (#71) Formula weight : 673.53 – δ g mol^{-1}, Z = 2 Mass fraction: 18.0(1)% *a* = 3.853(1) Å, *b* = 3.6178(8) Å, *c* = 12.895(3) Å, Volume = 179.79(7) Å^3						
Radiation source: Neutron Powder Diffraction, λ = 1.5943(2) Temperature: 10 K χ^2 = 3.463; *wRp* = 5.67%; *Rp* = 4.30%.						

Table 6.6. Structural parameters from the refinement of neutron powder diffraction data collected from $LaSr_3NiRuO_6$ at 10 K.

Atom	U_{11}	U_{22}	U_{33}
La/Sr(1)	0.0036(13)	0.0039(18)	0.0020(12)
Ni/Ru(1)	0.0034(18)	0.0155(21)	0.0016(16)
O(1)	0.0058(13)	0.0170(18)	0.0072(16)
O(2)	0.0049(23)	0.0293(37)	0.0049(25)

Table 6.7. Anisotropic displacement factors from the structural refinement of neutron powder diffraction data collected from $LaSr_3NiRuO_6$ at 10 K.

Cation	Anion	length (Å)
La/Sr(1)	O(1)	2.481(3) × 1
	O(1)	2.631(1) × 4
	O(2)	2.598(1) × 2
Ni/Ru(1)	O(1)	2.120(3) × 2
	O(2)	1.921(1) × 2

Table 6.8. Selected bond lengths from the low temperature refined structure of $LaSr_3NiRuO_6$.

The lattice parameters and bond lengths extracted from the structural refinement against low temperature neutron powder diffraction data are shorter compared to those extracted at room temperature, which is quite normal as the unit cell should undergo thermal expansion with elevated temperature.

Apart from information of crystallographic structure, low temperature neutron powder diffraction data lose paramagnetic scattering as reflected in the lowering background at low angles by comparing to the data collected at room temperature (Figure 6.11). However, it does not contain any extra peaks apart from those belong to the crystallographic structure. This is not surprising as the magnetisation data collected from SQUID magnetometer show strong evidence of a ferromagnetic ground state, therefore any additional magnetic diffraction features should appear under those crystallographic peaks. There are no obvious intensity mismatches between two patterns collected at 298 K and 10 K respectively. The differences in peak intensities attributed to magnetic scattering are too weak to determine the ferromagnetic unit cell of $LaSr_3NiRuO_6$ as they fit into the background.

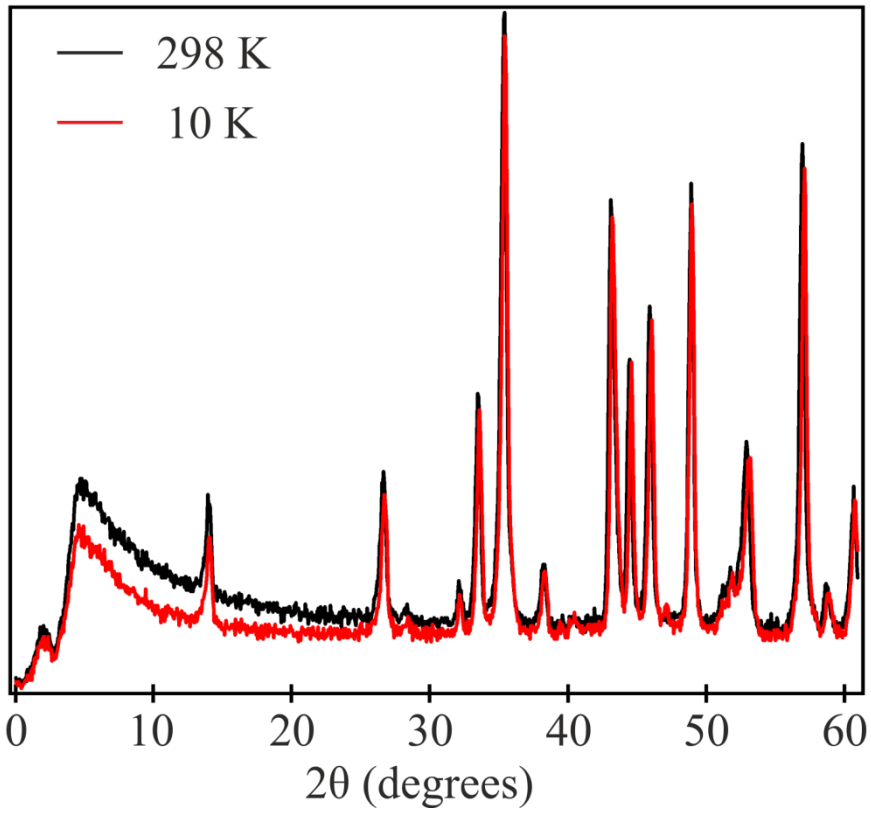


Figure 6.11. Comparing low-angle neutron powder diffraction data collected from $LaSr_3NiRuO_6$ at 298 K and 10 K.

In order to prove this situation, simulations of ferromagnetic unit cells of $LaSr_3NiRuO_6$ with moment (~ 0.5 μ_B, determined by SQUID magnetometer as mentioned in Section 6.3.4) pointing along *a*, *b* and *c* directions respectively were carried out. The same profiles of peak shapes used in the main phase were employed and a 100-times real scale factor was used to see reasonable reflections from simulated magnetic unit cell (Figure 6.12).

The peaks with highest intensities (between 10 to 20 degrees) in the plot (b) and (c) of Figure 6.12 are about 400 a.u., which approximately equal to 4 a.u. after dividing by 100, if the real scale factor is employed. In the neutron data collected from $LaSr_3NiRuO_6$ at 10 K, the error bar in the intensity of each data point within the range of 10 to 20 degrees is 3 or 4 a.u., therefore peak intensities contributed by the ferromagnetic unit cell (moment pointing along *a* and *b* directions) are approximately the same as the magnitude of error bars. In addition, the peak with the highest intensity (between 20 to 30 degrees) in the plot (d) of Figure 6.12 is about 150 a.u., which approximately equals to 1.5 a.u. after dividing by 100, if the real scale factor is employed. In the neutron data collected from $LaSr_3NiRuO_6$ at 10 K, the error bar in the intensity of each data point within the range of 20 to 30 degrees is 3 or 4 a.u., therefore peak intensities contributed by the ferromagnetic unit cell (moment pointing along *c* direction) is even smaller than the magnitude of error bars.

In conclusion, the absence of visible additional magnetic diffraction features is not surprising as none of the $LaSr_3NiRuO_xH_y$ compounds show them in low temperature neutron powder diffraction data. The saturated ferromagnetic moment (~ 0.5 μ_B) extracted from the magnetisation data collected from SQUID magnetometer is accompanied by a large applied field (5 T), so the subtle enhancement in the intensity of some reflections, as a consequence of ferromagnetic unit cell in low temperature neutron data set might be too weak to be observed under a zero-field circumstance.

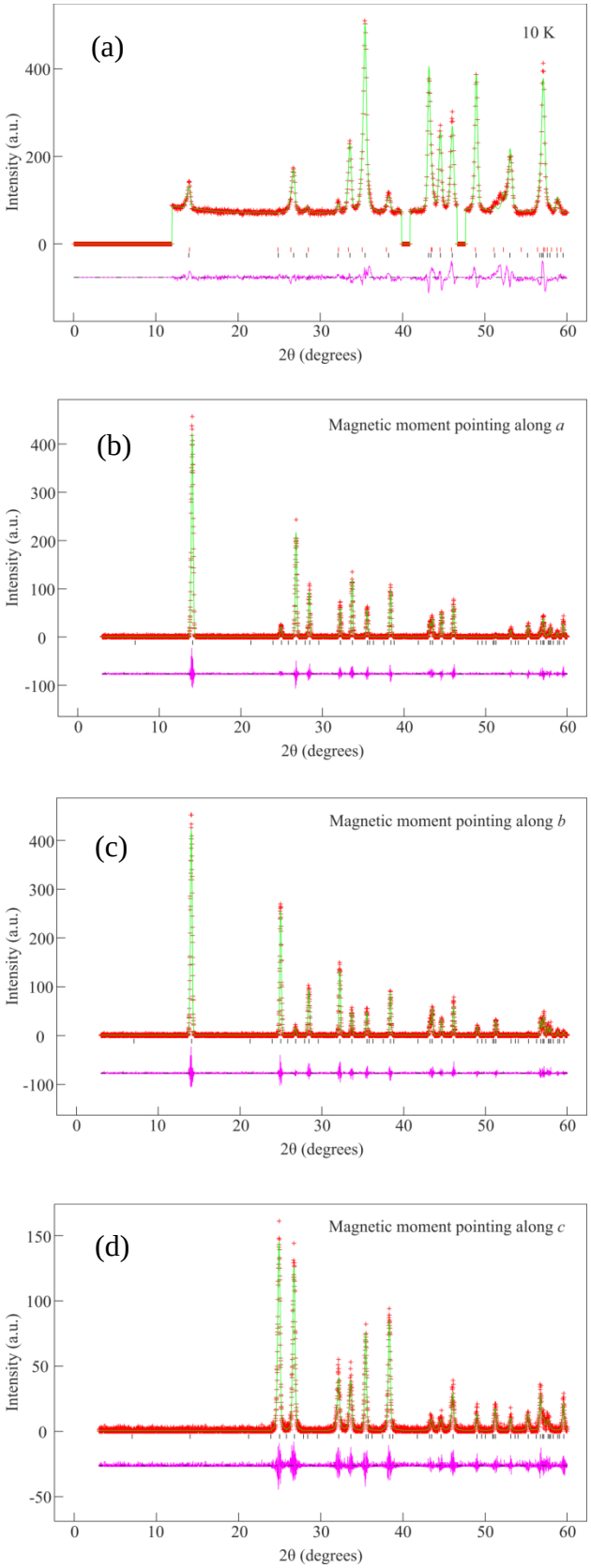


Figure 6.12. (a) Experimental neutron powder diffraction data collected from $LaSr_3NiRuO_6$ at 10 K; Simulations of ferromagnetic unit cells as moment pointing along (b) *a*; (c) *b* and (d) *c* directions by using a 100-times real scale factor.

6.4 Discussion

6.4.1 Crystallographic Structure of $LaSr_3NiRuO_6$

The topochemical reduction of n = 1 Ruddlesden-Popper phase $LaSr_3NiRuO_8$ with finely divided Zr powder getter eventually yields a reduced oxide phase $LaSr_3NiRuO_6$. The crystallographic structure of $LaSr_3NiRuO_6$ could be readily indexed using a body-centred orthorhombic unit cell with lattice parameters: a = 3.8433(4) Å, b = 3.5725(4) Å, c = 13.003(1) Å. The b lattice parameter is significantly shorter compared to its parent oxide phase as a result of ordered oxide vacancies forming along b-axis, which can be explained by the interesting structural selectivity in Ruddlesden-Popper phases as discussed in Chapter 4 Section 4.4.1.

Oxide ions in the parent n = 1 Ruddlesden-Popper phase $LaSr_3NiRuO_8$ are situated in different anion sites O(1) and O(2) as showed in Figure 6.13, that can be described as topologically distinct rather than simply crystallographically distinct.

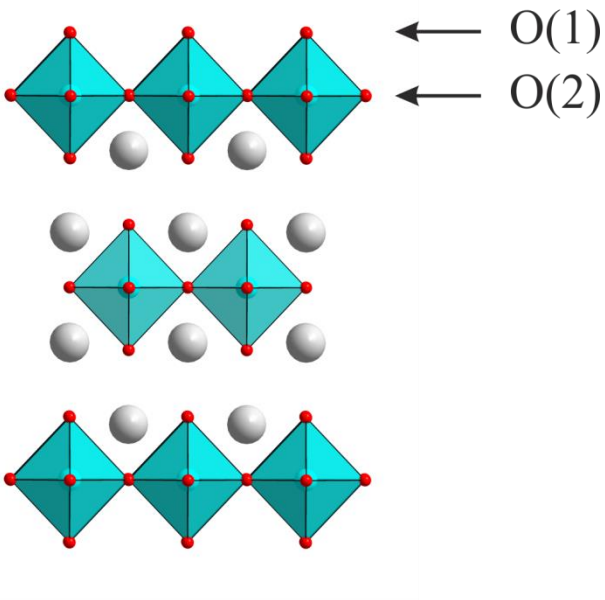


Figure 6.13. The topologically distinct anion sites in the n = 1 Ruddlesden-Popper phase $LaSr_3NiRuO_8$.

Anion	Anion BVS	$LaSr_3NiRuO_8$
O(1)	BVS A	1.172
	BVS B	1.013
	(BVS B) – (BVS A)	**- 0.159**
O(2)	BVS A	0.980
	BVS B	2.742
	(BVS B) – (BVS A)	**+ 1.762**

Table 6.9. The calculated anion bond valence sums of the *n* = 1 Ruddlesden-Popper phase $LaSr_3NiRuO_8$.

The coordination environment of O(1) is A_5B while that of O(2) is A_4B_2, both are six-coordinated, but O(2) has a greater impact on B-site cations as reflected in the more positive value of the term (BVS B) – (BVS A) in Table 6.9, simply because it is coordinated with one more B-site cation compared to O(1). Therefore in topochemical reactions of $LaSr_3NiRuO_8$ with Zr powder, oxide ions situated in O(2) sites are preferred to be deintercalated as the aim is to reduce Ni^{2+}/Ru^{5+} centres to Ni^{1+}/Ru^{2+} centres, hence it forms ordered oxide vacancies along *b*-axis, resulting in the final crystallographic structure of the reduced oxide phase $LaSr_3NiRuO_6$.

6.4.2 Zr Powder Getter versus CaH_2

The successful isolation of reduced oxide phase $LaSr_3NiRuO_6$ by using finely divided Zr powder as an oxygen getter provides us a clean and convenient way to deintercalate oxide ions from the lattice. This kind of set-up prevents the contamination of resulting reduced phase from by-products and unreacted reducing agents and protects the sample from further purification techniques. In addition, both chemical and structural characterisation techniques can be applied at any point of the reaction process which provides a better way to understand and monitor the reaction progress. However, this method is not as efficient as mixing binary metal hydrides together with the substrate, as the oxygen removed from the lattice need to pass through the gas phase and then reacts with metals which are in close proximity but not in contact with the substrate, slows down the reaction rate significantly and makes it even more difficult to prepare large-scale homogeneous samples.

The failure in isolation of the reduced oxide phase $LaSr_3NiRuO_6$ by using CaH_2 as a reducing agent no matter in sealed ampoules or in a venting apparatus suggest the preference of forming oxide-hydride phase $LaSr_3NiRuO_4H_4$ is so strong that even with tiny amount of H^- source presented in reaction vessels, the oxide-hydride phase will be formed, even at a slightly lower reaction temperature. It is quite rare as a lot of square planar Ru(II) have been observed in reduced oxide phases such as $LaSrNiRuO_4$[10], $Sr(Fe_{0.5}Ru_{0.5})O_2$[11], $Sr_2(Fe_{0.5}Ru_{0.5})O_{4-x}$[23] and $Sr_3(Fe_{0.5}Ru_{0.5})_2O_{7-x}$[23] by reacting their parent oxide phases with CaH_2 either in sealed ampoules or in a venting apparatus and none of above samples show similar preference of forming oxide-hydride phases. Therefore the driving force of forming the oxide-hydride phase $LaSr_3NiRuO_4H_4$ by reacting its parent oxide phase $LaSr_3NiRuO_8$ with CaH_2 needs to be investigated.

By switching the reducing agent from CaH_2 to Zr powder getter, the resulting reduced phase changes from $LaSr_3NiRuO_4H_4$ to $LaSr_3NiRuO_6$. Thus we have confirmed one essential and obvious criteria of forming oxide-hydride phase, the presence of H^- source in topochemical reactions. In order to investigate the relationship between transition-metal elements presented in complex oxides and the driving force of forming oxide-hydride phases, we have extended the chemistry to a Co-containing analogue $LaSr_3CoRuO_8$ and two Rh-containing n = 1 Ruddlesden-Popper phases $LaSr_3MnRhO_8$ and $La_2Sr_2CoRhO_8$ as well, which have been discussed in the following Chapter 7, 8 and 9.

6.4.3 Two-Phase Reduction Behaviour of $LaSr_3NiRuO_6$

A much improved fit to both synchrotron X-ray powder diffraction data and neutron powder diffraction data collected from the large-scale sample of the reduced oxide phase $LaSr_3NiRuO_6$ can be achieved by a two-phase refinement, consisting of the majority phase $LaSr_3NiRuO_6$ and the less reduced minority phase $LaSr_3NiRuO_{7-x}$ which agrees with the TGA result. This two-phase reduction behaviour has only been observed in the large-scale neutron sample and does not exist in the small scale test sample, which applies that it is due to incomplete reduction and inhomogeneous reaction conditions throughout the large-scale sample during reduction as the part of substrate gets less chance to be reduced if it is farther away from the Zr powder. The same phase separation on reduction has been observed in many other complex oxide phases. For example, the n = 1 Ruddlesden-Popper phase $LaSrCoO_4$ forms two phases on reduction with dilute hydrogen gas: $LaSrCoO_{3.43}$ and $LaSrCoO_{3.57}$ based on the same reason stated above.[19]

In contrast, the two-phase behaviour observed during the reduction of the $Y_2Ti_2O_7$ pyrochlore phase can be explained on the basis of the existence of a compositional ‘phase gap’

driven by the electronic structure of the material, such that materials with average compositions $Y_2Ti_2O_x$ ($5.90 \leq x \leq 6.50$) are two-phase mixtures of $Y_2Ti_2O_{5.90}$ and $Y_2Ti_2O_{6.50}$.[100]

In cases stated above, the reduction is still proceeding and single phases can be produced given enough time and good 'stirring' to make reaction conditions as homogeneous as possible throughout the sample during reductions. However, there is another example which behaves qualitatively different. The separation of both $Sr_2(Fe_{0.5}Ru_{0.5})O_4$ and $Sr_3(Fe_{0.5}Ru_{0.5})_2O_7$ into two phases on reduction does not arise from incomplete reduction or electronically-driven phase separation, but is a result of different portions of the sample reacting with CaH_2 to different extents, despite being subject to the same reaction conditions. The conclusion can be made that this behaviour is due to some inhomogeneous distribution of Fe and Ru over short-length scales in the starting material as it is supported by the observation that the ratios of the two phases produced is constant within any one batch of starting material, but different batches yield different ratios.[56]

In general, it is safe to conclude that the phase width with slight different oxygen contents can be minimized and the two-phase reduction behaviour will disappear, to eventually yield a large-scale pure sample that containing only the target reduced oxide phase $LaSr_3NiRuO_6$, if the system has been heating under a very homogeneous reaction conditions for sufficient amount of time.

6.5 Conclusion

A pure reduced oxide phase $LaSr_3NiRuO_6$ is quite difficult to be isolated from topochemical reactions of $LaSr_3NiRuO_8$ with CaH_2 by adjusting reaction conditions only, due to the simultaneous growth of strongly favoured oxide-hydride phase $LaSr_3NiRuO_4H_4$. However, by eliminating the H^- source during reactions, in other words, changing reducing agent from CaH_2 to Zr powder as an oxygen getter successfully isolates the reduced oxide phase $LaSr_3NiRuO_6$.

Both Synchrotron X-ray powder diffraction data and neutron powder diffraction data confirm that the crystal lattice of $LaSr_3NiRuO_6$ could be described by a body-centred orthorhombic cell (space group *Immm*) with lattice parameters a = 3.8474(2) Å, b = 3.5762(2) Å, c = 13.0168(9) Å. The reduction process only deintercalates oxide ions along b axis which makes b lattice parameter shorter than a, hence yields lowering the symmetry of the cell from tetragonal to orthorhombic after forming ordered oxide vacancies along b axis.

The low temperature neutron powder diffraction data collected from $LaSr_3NiRuO_6$ does not show any additional magnetic diffraction features in this phase, despite magnetisation data collected from SQUID show strong evidence of a ferromagnetic ground state consisting of a d^9, S = ½ Ni^{1+} centre and a d^6, Ru^{2+} centre with two unpaired electrons (S = 1). This can be explained by the relatively low ferromagnetic moment (~ 0.5 μ_B) of $LaSr_3NiRuO_6$, hence the subtle enhancement in the intensity of some reflections in low temperature neutron data set might be too weak to determine the ferromagnetic unit cell of $LaSr_3NiRuO_6$ as they fit into the background.

Chapter 7

$LaSr_3CoRuO_8$ and Its Topochemical Reductions

7.1 Introduction

As described in previous chapters, the topochemical reductions of $LaSr_3NiRuO_8$ by using solid-state reducing agents CaH_2 and Zr powder have been intensively studied. The successful isolation of those reduced oxide and oxide-hydride phase reveals that, with the sufficiently robust La-Sr-Ni-O lattice, pure Ru^{2+} centres can be obtained by topochemically reducing the parent n = 1 Ruddlesden-Popper phase.

Apart from Ni, Co is also a good candidate of providing sufficiently robust lattice to resist non-topochemical decomposition, and a number of topochemically reduced complex oxide and oxide-hydride phases containing Co have been successfully prepared.[15, 19, 20] Thus the La-Sr-Co-O network should also be able to stabilise low oxidation states of ruthenium, and therefore the n = 1 Ruddlesden-Popper phase $LaSr_3CoRuO_8$ was synthesized and its topochemical reduction behaviour towards both solid-state reducing agents CaH_2 and Zr powder was investigated.

Detailed synthesis and characterisations of the parent oxide phase $LaSr_3CoRuO_8$ and its topochemically reduced products are presented in this chapter.

7.2 Experimental

7.2.1 Synthesis of $LaSr_3CoRuO_8$

Samples of $LaSr_3CoRuO_8$ were prepared by a high-temperature ceramic method as described in Chapter 2 section 2.1.1. Suitable stoichiometric ratios of La_2O_3 (99.999%, dried at 900 °C), $SrCO_3$ (99.994%), RuO_2 (99.99%, dried at 800°C) and Co_3O_4 (99.9985%) were ground together using an agate mortar and pestle, transferred into an alumina crucible, and then heated at a rate of 1 ºC min^{-1} to 1000 °C in air to decompose the carbonate. The sample was reground, pressed into pellets and then heated for 3 periods of 48 hours at 1200°C in air, with grinding between heating periods. The reaction progress was monitored by laboratory X-ray diffractometer and the final pure phase achieved was examined by both synchrotron X-ray powder diffraction and neutron powder diffraction.

7.2.2 Synthesis of $LaSr_3CoRuO_4H_4$

As discussed in Chapter 4, the formation of the by-product, H_2 gas, during the CaH_2 reduction, acts as the source of H^- ions for hydride-for-oxide substitution, and also aids the formation of the pure oxide-hydride phase over other competing reduced phases.

A sample of $LaSr_3CoRuO_4H_4$ suitable for analysis by neutron powder diffraction was prepared by grinding together approximately 1.5 g of $LaSr_3CoRuO_8$ with 0.4 g of CaH_2 in an argon filled glovebox using an agate mortar and pestle. The resulting powders were sealed in a silica ampoule and heated at 460 °C for 3 periods of 7 days, with the sample being reground between heating periods. Once the reaction was deemed complete, the reaction mixture was washed, under nitrogen, with 8 × 25 ml of 0.1 M solution of NH_4Cl in methanol in order to remove the CaO formed as a by-product of the reaction and any unreacted CaH_2. This was then followed by washing with 5 × 25 ml of clean methanol to dissolve NH_4Cl residues. The sample was then dried under vacuum.

7.2.3 Synthesis of $LaSr_3CoRuO_6$

Analogous topochemical reduction chemistry has been extended to the $LaSr_3CoRuO_8$ case, where the reduced oxide phase $LaSr_3CoRuO_6$ can be observed, but never be purely isolated via CaH_2 reduction, due to the simultaneous formation of the strongly preferred oxide-hydride phase, e.g. $LaSr_3CoRuO_4H_4$, as a result of the formation of the by-product, H_2 gas, during the reaction. After switching the solid-state reducing agent to Zr powder, a pure phase of $LaSr_3CoRuO_6$ is successfully isolated by eliminating the possibility of forming the oxide-hydride phase as there is no H^- source in the whole apparatus.

A sample of $LaSr_3CoRuO_6$ suitable for analysis by neutron powder diffraction was prepared by putting approximately 1.5 g of $LaSr_3CoRuO_8$ in a smaller inner tube with 1.0 g of Zr powder in a larger outer tube to set up apparatus as described in Chapter 2 section 2.3 in an argon filled glovebox. The resulting reaction vessel was sealed under vacuum and heated at 550 °C for 5 periods of 7 days, with the substrate being reground, reacted Zr and ZrO_x being replaced by fresh Zr powder, and the reaction progress being monitored by laboratory X-ray diffractometer between heating periods. Since the substrate is not contaminated by any by-products or unreacted reducing agent, it does not require any further purification procedures.

7.3 Results

7.3.1 Structural Characterisation of $LaSr_3CoRuO_8$

7.3.1.1 Synchrotron X-Ray Powder Diffraction

Synchrotron X-ray powder diffraction data (Chapter 2 Section 2.5.1.2) was collected from a large neutron sample of $LaSr_3CoRuO_8$. The data could be readily indexed using a body-centred tetragonal unit cell (space group *I4/mmm*) with lattice parameters: a = 3.87658(3) Å and c = 12.6305(1) Å. A structural model was constructed, based on an n = 1, A_2BO_4 Ruddlesden-Popper phase with a 1 : 3 La : Sr solid-solution on the A-site and a 1 : 1 Co : Ru solid-solution on the B-site. This model was refined against the data to achieve a good statistical fit (χ^2 = 6.384; *wRp* = 3.39%; *Rp* = 1.93%). The observed, calculated, and difference plots are shown in Figure 7.1.

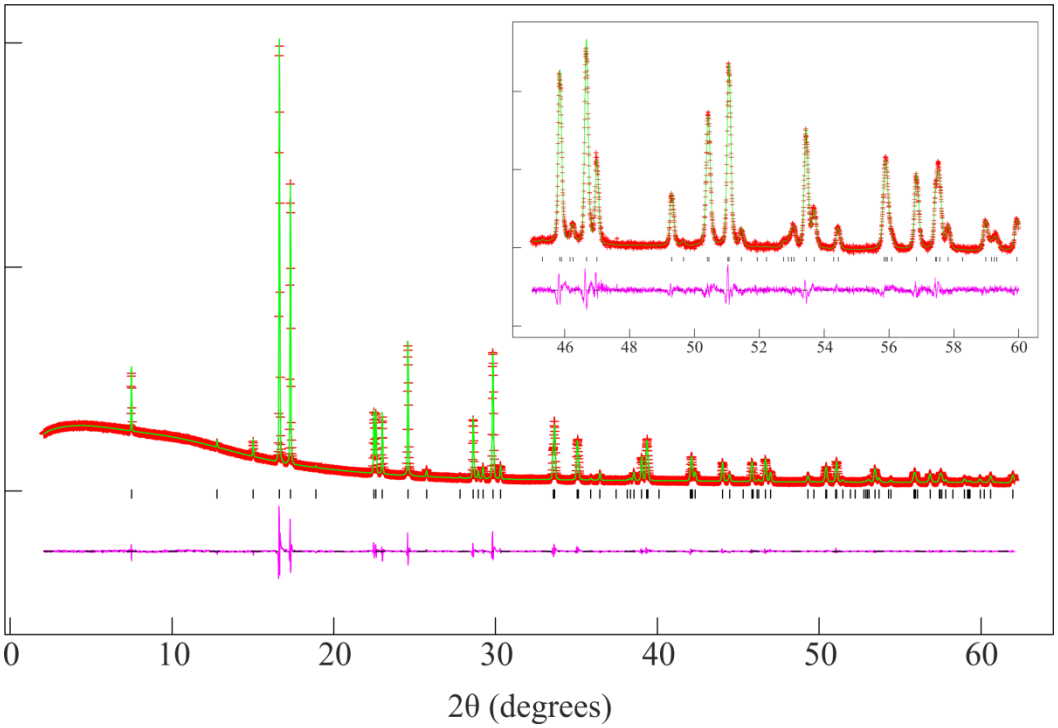


Figure 7.1: Rietveld refinement of synchrotron X-ray powder diffraction data collected from $LaSr_3CoRuO_8$ against *I4/mmm* model. Observed (red), calculated (green), and difference plots (pink) are shown.

7.3.1.2 Neutron Powder Diffraction

A neutron powder diffraction measurement at ambient temperature was carried out at D2B diffractometer in ILL (Chapter 2 Section 2.5.2.2). The body-centred tetragonal unit cell shown in Figure 7.2 (space group *I*4/*mmm*) was used to refine the data. The refinement converged readily to a give good statistical fit for ambient temperature data. The observed, calculated, and difference plots are shown in Figure 7.3. Full details of the structural parameters are given in Table 7.1, anisotropic displacement factors are given in Table 7.2 and selected bond lengths are given in Table 7.3.

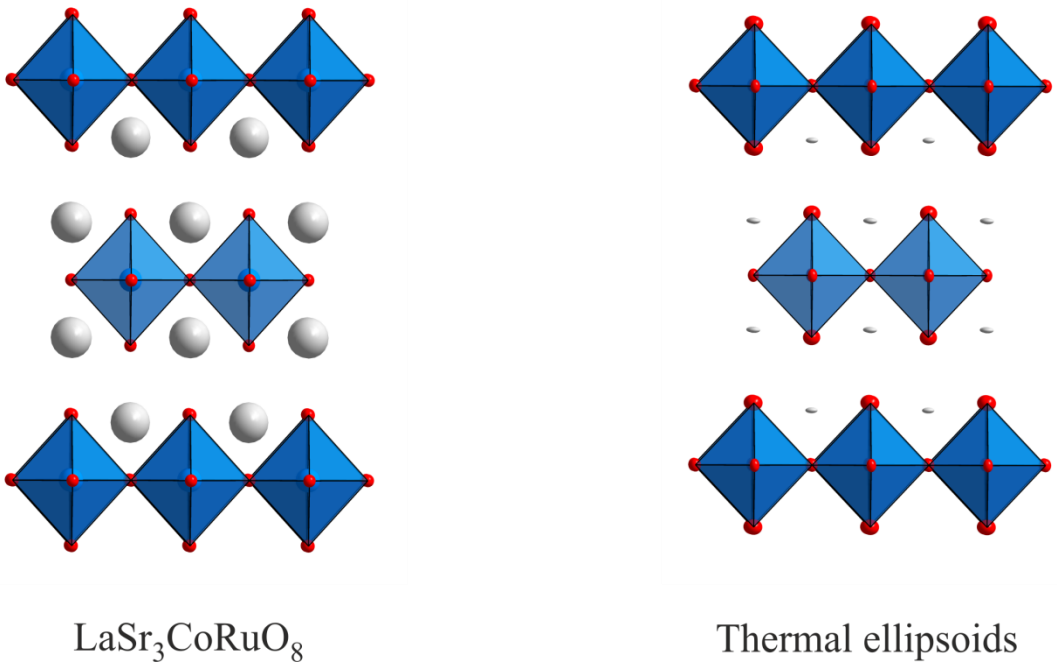
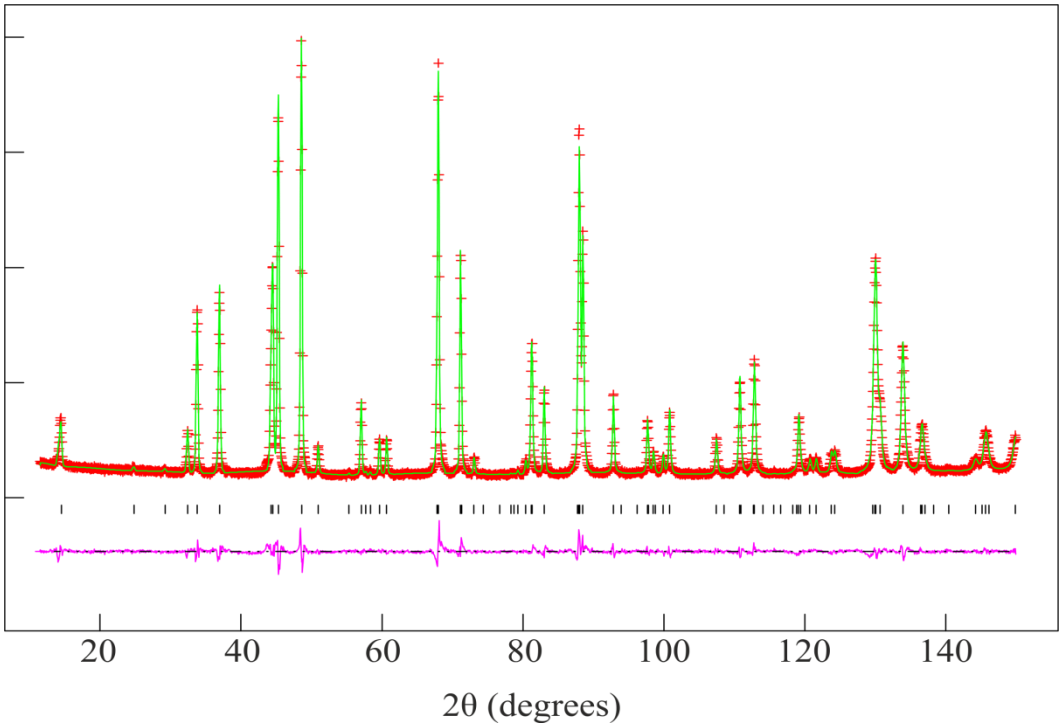


Figure 7.2. Crystal structure of $LaSr_3CoRuO_8$ (space group *I*4/*mmm*) with thermal ellipsoids displayed.



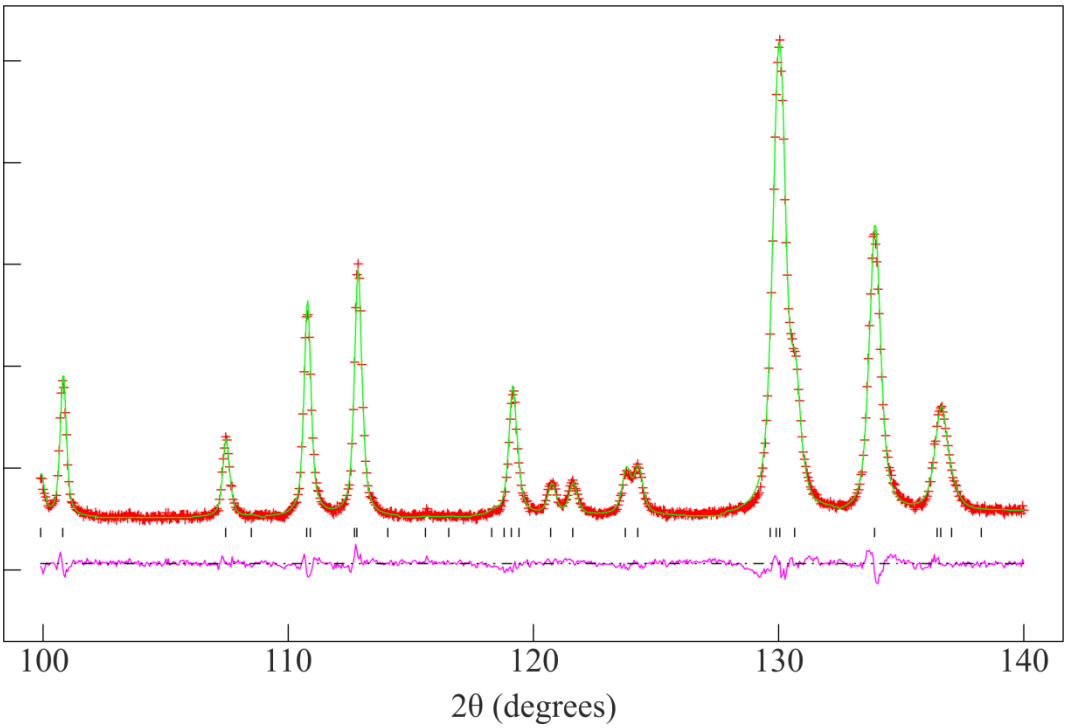


Figure 7.3. Observed, calculated and difference plots from the refinement of $LaSr_3CoRuO_8$ against neutron powder diffraction data collected at 298 K, full range (top) and high angles (bottom).

Atom	Wyckoff Position	*x*	*y*	*z*	Fraction	U_{iso} equiv. (Å^2)
La/Sr(1)	4*e*	0	0	0.3561(1)	0.25/0.75	0.0049
Co/Ru(1)	2*a*	0	0	0	0.5/0.5	0.0021
O(1)	4*e*	0	0	0.1636(1)	1	0.0124
O(2)	4*c*	0.5	0	0	1	0.0058
$LaSr_3CoRuO_8$ space group *I*4/*mmm* (#139) Formula weight : 689.76 g mol^{-1}, Z = 2 *a* = 3.87488(4) Å, *c* = 12.6258(1) Å, Volume = 189.574(7) Å^3						
Radiation source: Neutron Powder Diffraction, λ = 1.5943(2) Temperature: 298 K χ^2 = 4.132; *wRp* = 4.90%; *Rp* = 3.73%.						

Table 7.1. Structural parameters from the refinement of neutron powder diffraction data collected from $LaSr_3CoRuO_8$ at 298 K.

Atom	U_{11}	U_{22}	U_{33}
La/Sr(1)	0.00657(35)	0.00657(35)	0.00148(50)
Co/Ru(1)	0.00189(46)	0.00189(46)	0.00241(25)
O(1)	0.01318(42)	0.01318(42)	0.0107(11)
O(2)	0.00407(68)	0.00544(71)	0.00796(71)

Table 7.2. Anisotropic displacement factors from the structural refinement of neutron powder diffraction data collected from $LaSr_3CoRuO_8$ at 298 K.

Cation	Anion	length (Å)
La/Sr(1)	O(1)	2.430(2) × 1
	O(1)	2.751(1) × 4
	O(2)	2.656(1) × 4
Co/Ru(1)	O(1)	2.066(1) × 2
	O(2)	1.937(1) × 4

Table 7.3. Selected bond lengths from the refined structure of $LaSr_3CoRuO_8$.

7.3.2 Magnetic Characterisation of $LaSr_3CoRuO_8$

Zero-field-cooled and field-cooled magnetization data collected from $LaSr_3CoRuO_8$ as a function of temperature in an applied field of 100 Oe using a SQUID magnetometer (Chapter 2 Section 2.10), are shown in Figure 7.4 (top). Data in the range $135 < T / K < 300$ can be fitted to the Curie-Weiss law ($\chi = C/(T - \theta)$) to yield values of $C = 3.835(1)$ cm^3 K mol^{-1}, $\theta = +46(1)$ K, hence a value of $\mu^2 = 30.68$ μ_B can be calculated. The zero-field-cooled and field cooled data diverge below T = 85 K, consistent with the onset of canted antiferromagnetic order. Magnetization data collected at 300 K as a function of applied field is linear and passes through the origin. Analogous data collected at 5 K after cooling in an applied field of 5000 Oe exhibit hysteresis consistent with weak ferromagnetism (Figure 7.4 (bottom)).

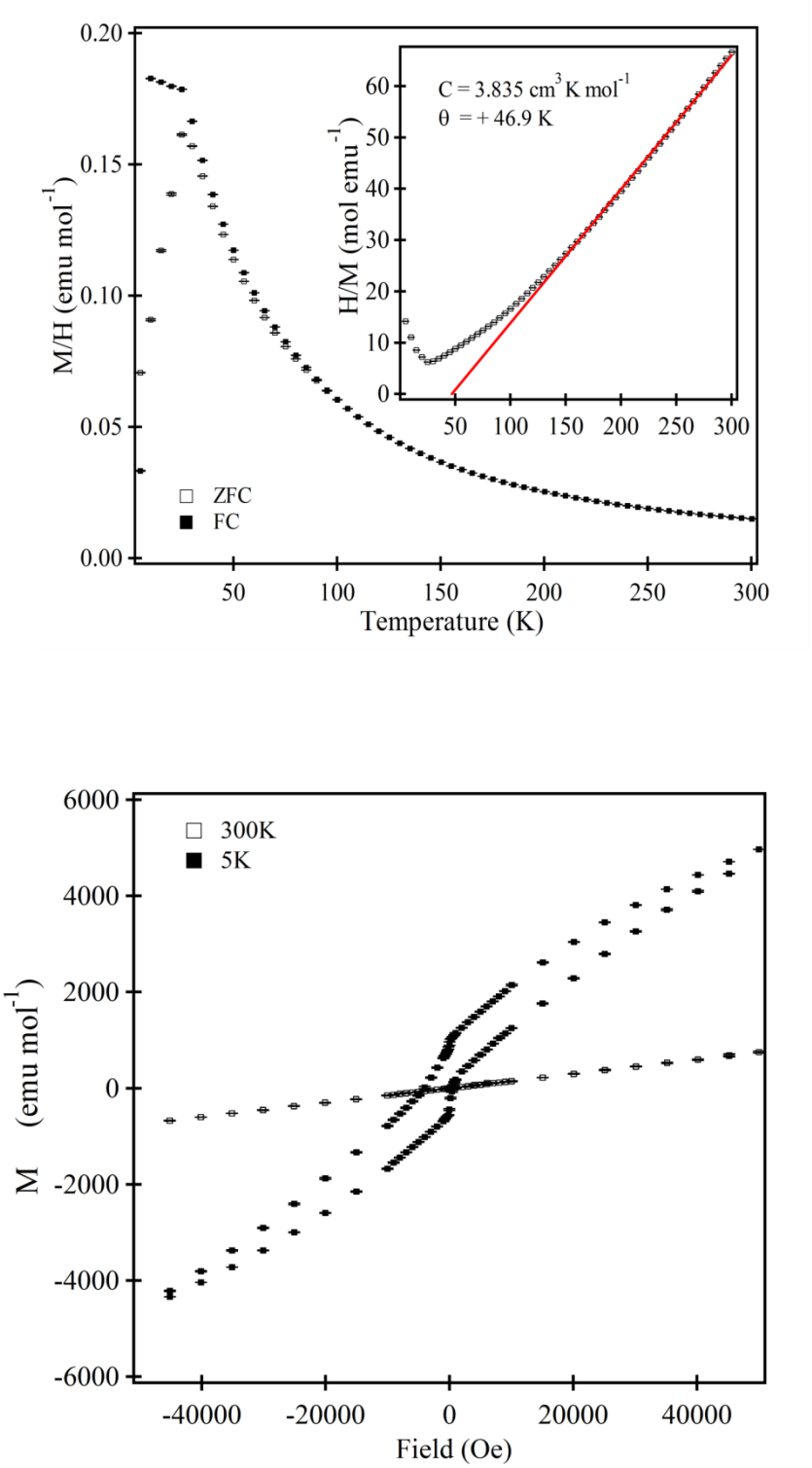


Figure 7.4. Zero-field-cooled and field-cooled magnetisation data collected in an applied field of 100 Oe. Inset shows fit to the Curie-Weiss law (top); Magnetisation data collected as a function of applied field (bottom) from $LaSr_3CoRuO_8$.

By considering the chemical formulation of $LaSr_3CoRuO_8$, it should consist of either Co^{2+} and Ru^{5+}, or Co^{3+} and Ru^{4+} if we assume electrons are localised for these B-site transition metal cations (Figure 7.5).

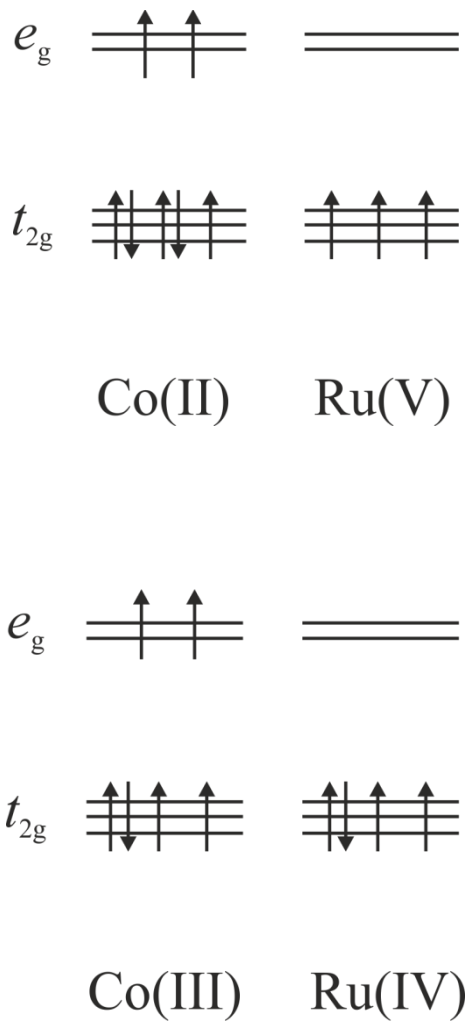


Figure 7.5. Predicted spin states of B-site transition metal cations in $LaSr_3CoRuO_8$.

In the first case which $LaSr_3CoRuO_8$ contains Co^{2+} and Ru^{5+} centres, with spin states of $S = {}^3/_2$ and $S = {}^3/_2$ respectively, the calculated value of $\mu^2 = 30.68\ \mu_B$ observed from

experimental data is approximately 102.3% of the expected value of $\mu^2 = 30\ \mu_B$ derived from spin-only formula, which agrees reasonably well. In the second case which $LaSr_3CoRuO_8$ contains Co^{3+} and Ru^{4+} centres, with spin states of $S = 2$ and $S = 1$ respectively, the value of the expected moment μ^2 derived from spin-only formula should be 32 μ_B, thus it is less closer to the observed moment compared to the first case. Therefore the combination of Co^{2+} and Ru^{5+} centres is preferred.

The magnetisation data show a low saturated magnetic moment consistent with canted antiferromagnetic interactions at low temperature, despite the Goodenough Kanamori rules[85] predicting strong ferromagnetic interactions between half-filled Co^{2+} e_g orbitals and empty Ru^{5+} e_g orbitals, which is similar to the Ni analogue discussed in Chapter 3. Therefore it could also have ferromagnetic ordering within each layer between Co and Ru centres, but with layers stacked antiferromagnetically to result in such a low saturated moment. Further Pair Distribution Function (PDF) analysis is required to investigate its detailed cation arrangement as it may adopt a paracrystalline order with rigorous Co/Ru order within each perovskite sheet, but no order between layers as they are not rigidly connected along *c* axis.

7.3.3 Thermogravimetric Analysis of $LaSr_3CoRuO_6$

The composition of the $LaSr_3CoRuO_{8-x}$ samples was determined from oxidative thermogravimetric analysis in a steady O_2 flow as described in Chapter 2 section 2.7. The oxidative TGA result predicts the oxygen content to be slightly higher than 6 (Figure 7.6), because there are some decomposition products presented in the sample, such as La_2O_3 and SrO, which are visible in both synchrotron X-ray powder diffraction data and neutron powder diffraction data. Data shown in Figure 7.6 are plots of mass gain against temperature and the final phase achieved was confirmed to be the original parent oxide phase $LaSr_3CoRuO_8$ by

laboratory X-ray diffractometer. Therefore the oxygen content in reduced phases can be calculated by the mass gain during the experiment as deintercalated oxide ions have been re-inserted into the crystal lattice to reoxidize back to the starting material $LaSr_3CoRuO_8$.

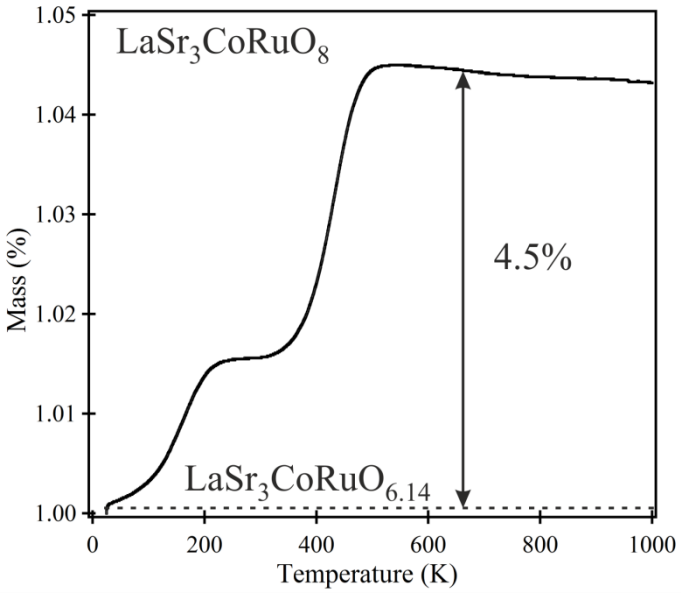


Figure 7.6. Plots of mass gain against temperature collected from the large-scale neutron sample of $LaSr_3CoRuO_6$.

The ratio between the main reduced oxide phase and other two impurities is approximately 93.4:6.6, as determined by the Rietveld refinement of ambient neutron powder diffraction data. Thus the mass gain should be:

$$4.5\% \div 93.4\% = 4.8\%$$

If the sample is assumed to be purely the reduced oxide phase, i.e. there are no decomposition products such as La_2O_3 and SrO. The mass gain of 4.8% is consistent with a composition of $LaSr_3CoRuO_{6.02(2)}$ for the reduced oxide phase.

7.3.4 Structural Characterisation of $LaSr_3CoRuO_6$

7.3.4.1 Synchrotron X-Ray Powder Diffraction

Synchrotron X-ray powder diffraction data (Chapter 2 Section 2.5.1.2) was collected from a large-scale neutron sample of $LaSr_3CoRuO_6$. The data were indexed using a body-centred orthorhombic unit cell with lattice parameters: a = 3.83769(7) Å, b = 3.64788(8) Å and c = 13.1014(2) Å. A structural model was constructed, based on an n = 1, A_2BO_4 Ruddlesden-Popper phase with a 1:3 La:Sr solid-solution on the A-site, a 1:1 Co:Ru solid-solution on the B-site and the two equatorial oxide ions deintercalated. This model was used to refine the synchrotron X-ray powder diffraction data collected at room temperature (Figure 7.7) and the refinement converged smoothly to give a good statistical fit (χ^2 = 57.25; wRp = 4.89%; Rp = 2.63%).

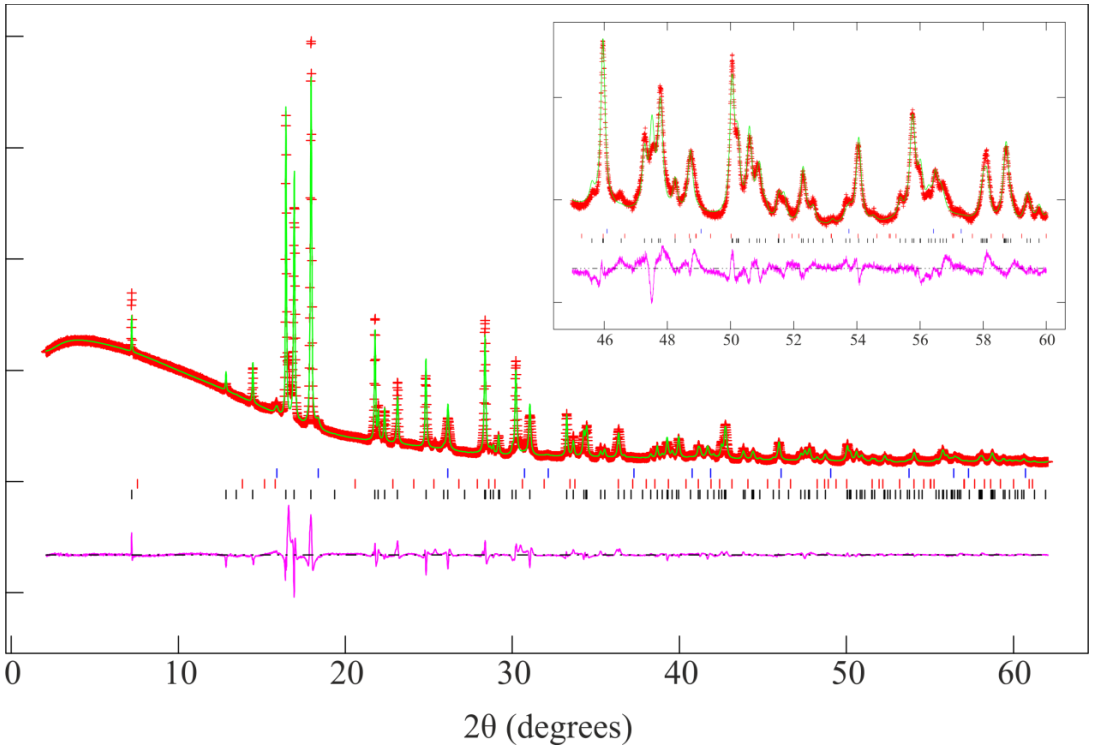


Figure 7.7. Observed, calculated and difference plots from the refinement of synchrotron X-ray powder diffraction data collected from $LaSr_3CoRuO_6$ (space group *Immm*) at 298 K. Tick marks indicate peak positions of the majority phase (black), La_2O_3 (red) and SrO (blue).

7.3.4.2 Neutron Powder Diffraction

The neutron powder diffraction measurements at ambient temperature and 5 K were carried out at D2B diffractometer in ILL (Chapter 2 Section 2.5.2.2). The body-centred orthorhombic unit cell previously described in Section 7.3.4.1 (Figure 7.8) was used to refine the neutron data collected from the reduced oxide phase $LaSr_3CoRuO_6$, formed in the topochemical reduction of its parent oxide phase $LaSr_3CoRuO_8$ by using Zr powder as an oxygen getter. Three-phase refinements of ambient and 5 K neutron data converged readily to give good statistical fit and visual fit (Figure 7.9), with the majority phase to be the reduced oxide phase $LaSr_3CoRuO_6$ (space group *Immm*) and two minority phases to be decomposition products La_2O_3 and SrO. Full details of the structural parameters are given in Table 7.4 & 7.5, anisotropic displacement factors are given in Table 7.6 and selected bond lengths are given in Table 7.7.

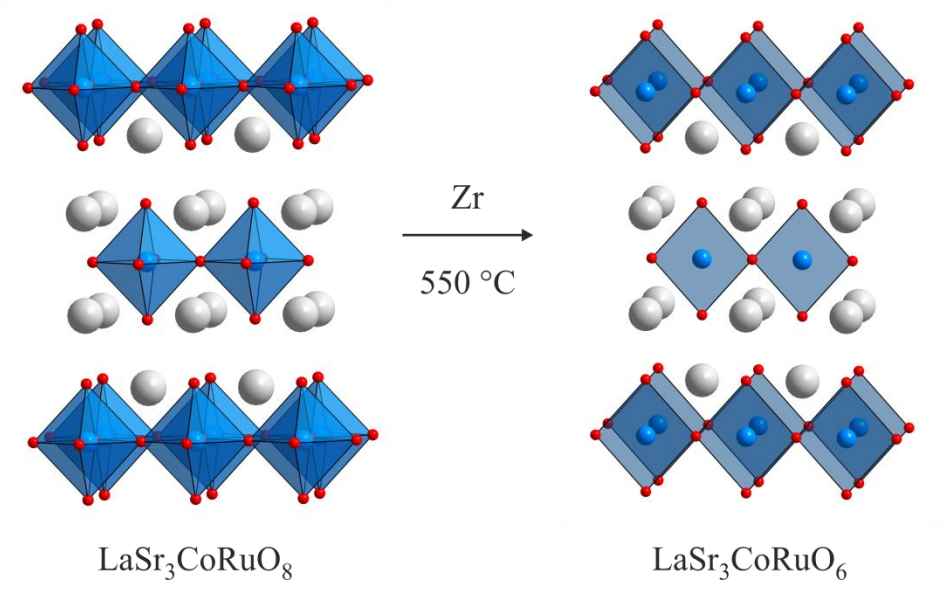


Figure 7.8. Topochemical reduction of $LaSr_3CoRuO_8$ with Zr powder to form reduced oxide phase $LaSr_3CoRuO_6$ with ordered oxide vacancies along *b*-axis.

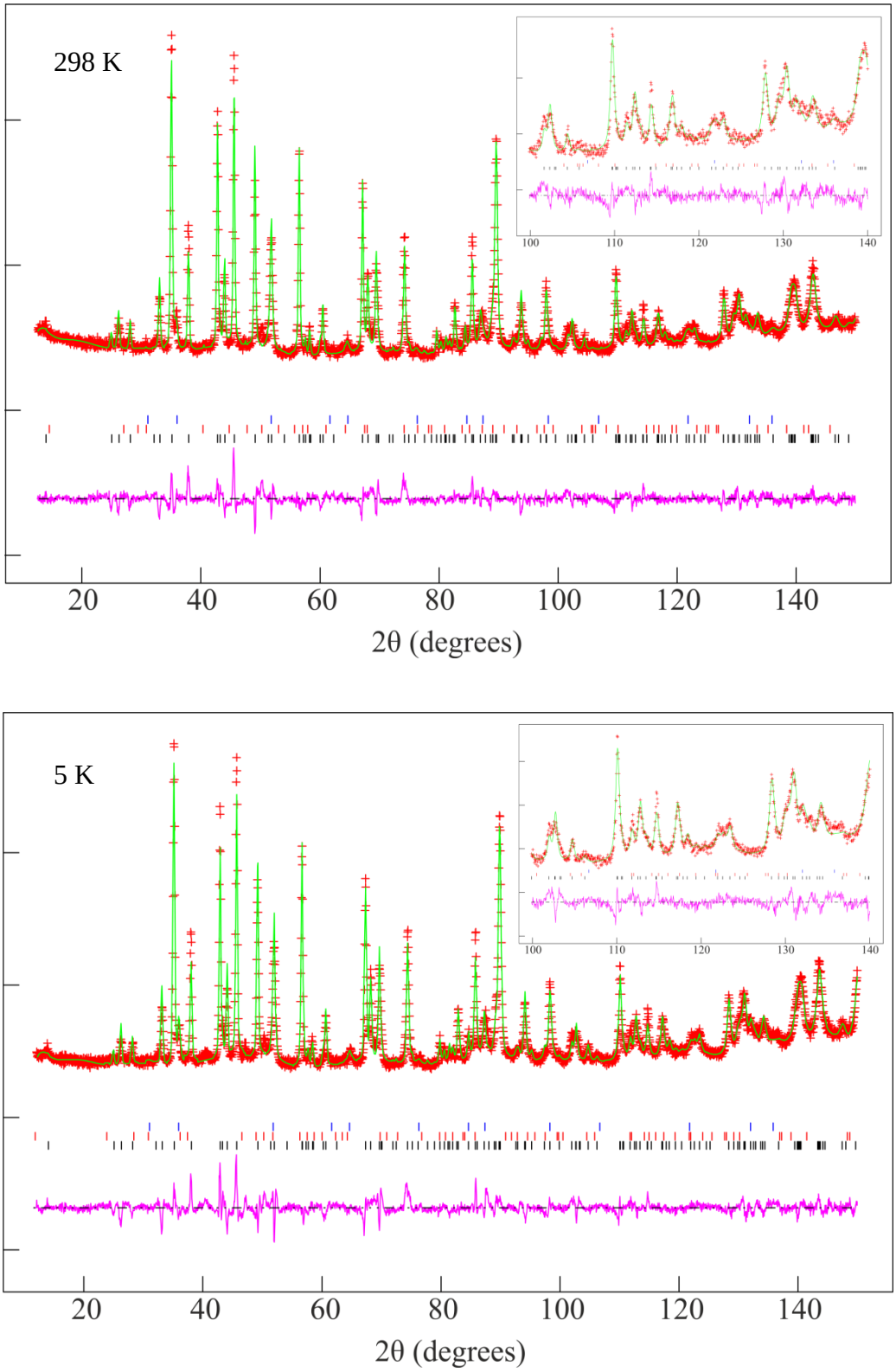


Figure 7.9. Observed, calculated and difference plots from the refinement of neutron powder diffraction data collected from $LaSr_3CoRuO_6$ (space group *Immm*) at 298 K (top) and 5 K (bottom). Tick marks indicate peak positions of the majority phase (black), La_2O_3 (red) and SrO (blue).

Atom	Wyckoff Position	*x*	*y*	*z*	Fraction	U_{iso} equiv. (Å^2)
La/Sr(1)	4*i*	0	0	0.3533(1)	0.25/0.75	0.0135
Co/Ru(1)	2*a*	0	0	0	0.5/0.5	0.0389
O(1)	4*i*	0	0	0.1633(2)	1	0.0100
O(2)	2*b*	0.5	0	0	1	0.0166
$LaSr_3CoRuO_6$ space group *Immm* (#71) Formula weight : 657.76 g mol^{-1}, Z = 2 Mass fraction: 93.4(2)% *a* = 3.8376(1) Å, *b* = 3.6458(2) Å, *c* = 13.0987(6) Å, Volume = 183.27(2) Å^3						
La_2O_3 space group $P\bar{3}m1$ (#164) Formula weight : 325.809 g mol^{-1}, Z = 1 Mass fraction: 0.3(1)% *a* = 3.960(1) Å, *c* = 6.224(4) Å, γ = 120°, Volume = 84.52(7) Å^3						
SrO space group $Fm\bar{3}m$ (#225) Formula weight : 414.476 g mol^{-1}, Z = 4 Mass fraction: 6.3(3)% *a* = 5.163(1) Å, Volume = 137.6(1) Å^3						
Radiation source: Neutron Powder Diffraction, λ = 1.5943(2) Temperature: 298 K χ^2 = 3.960; *wRp* = 5.84%; *Rp* = 4.43%.						

Table 7.4. Structural parameters from the refinement of neutron powder diffraction data collected from $LaSr_3CoRuO_6$ at 298 K.

Atom	Wyckoff Position	*x*	*y*	*z*	Fraction	U_{iso} equiv. (Å^2)
La/Sr(1)	4*i*	0	0	0.3532(1)	0.25/0.75	0.0100
Co/Ru(1)	2*a*	0	0	0	0.5/0.5	0.0329
O(1)	4*i*	0	0	0.1633(2)	1	0.0076
O(2)	2*b*	0.5	0	0	1	0.0211
$LaSr_3CoRuO_6$ space group *Immm* (#71) Formula weight : 657.76 g mol^{-1}, Z = 2 Mass fraction: 87.0(1)% *a* = 3.8284(1) Å, *b* = 3.6353(2) Å, *c* = 13.0719(5) Å, Volume = 181.93(2) Å^3						
La_2O_3 space group *P*-3*m*1 (#164) Formula weight : 325.809 g mol^{-1}, Z = 1 Mass fraction: 6.6(1)% *a* = 3.960(1) Å, *c* = 6.224(4) Å, γ = 120°, Volume = 84.52(7) Å^3						
SrO space group *Fm*-3*m* (#225) Formula weight : 414.476 g mol^{-1}, Z = 4 Mass fraction: 6.3(3)% *a* = 5.161(1) Å, Volume = 137.5(1) Å^3						
Radiation source: Neutron Powder Diffraction, λ = 1.5943(2) Temperature: 5 K χ^2 = 5.295; *wRp* = 6.64%; *Rp* = 5.00%.						

Table 7.5. Structural parameters from the refinement of neutron powder diffraction data collected from $LaSr_3CoRuO_6$ at 5 K.

Atom	U_{11}	U_{22}	U_{33}
La/Sr(1)	0.0065(14)	0.0308(27)	0.0032(12)
Co/Ru(1)	0.0194(33)	0.0847(62)	0.0126(24)
O(1)	0.0081(14)	0.0093(24)	0.0125(22)
O(2)	0.0070(20)	0.0424(39)	0.0037(21)
Temperature: 298 K			
Atom	U_{11}	U_{22}	U_{33}
La/Sr(1)	0.0032(12)	0.0243(24)	0.0053(12)
Co/Ru(1)	0.0162(32)	0.0641(55)	0.0184(21)
O(1)	0.0036(14)	0.0159(26)	0.0032(19)
O(2)	0.0134(18)	0.0454(38)	0.0042(19)
Temperature: 5 K			

Table 7.6. Anisotropic displacement factors from refinements of neutron powder diffraction data collected from $LaSr_3CoRuO_6$ at 298 K (top) and 5 K (bottom).

Temperature: 298 K			**Temperature: 5 K**		
Cation	**Anion**	**length (Å)**	**Cation**	**Anion**	**length (Å)**
La/Sr(1)	O(1)	2.489(3) × 1	**La/Sr(1)**	O(1)	2.482(3) × 1
	O(1)	2.656(1) × 4		O(1)	2.648(1) × 4
	O(2)	2.649(1) × 2		O(2)	2.643(1) × 2
Co/Ru(1)	O(1)	2.139(3) × 2	**Co/Ru(1)**	O(1)	2.135(3) × 2
	O(2)	1.919(1) × 2		O(2)	1.914(1) × 2

Table 7.7. Selected bond lengths from the refined structure of $LaSr_3CoRuO_6$ at 298 K (left) and 5 K (right).

7.3.5 Magnetic Characterisation of $LaSr_3CoRuO_6$

Magnetisation data were collected from the SQUID magnetometer by using a technique called ferromagnetic subtraction (Chapter 2 Section 2.10). Due to the inevitable presence of trace amount of ferromagnetic Co impurity in the sample prepared via topochemical reaction with Zr powder, a large field (3 T to 5 T) was applied to saturate elemental Co during the magnetic characterisation, so the ferromagnetic behaviour contributed by Co impurity would not mask the magnetic behaviour of the bulk phase. At 5 K temperature increments between 5 K and 300 K, magnetisation-field isotherms were collected over $3 \leq H / T \leq 5$ and the resultant magnetisation are plotted as a function of the applied field. For each 5 K step the gradient of the plot obtained shows the paramagnetic susceptibility and the intercept gives the saturated ferromagnetic moment from any impurities.

Unlike the Ni analogue ($LaSr_3NiRuO_6$) discussed in Chapter 6, which clearly undergoes a paramagnetic to ferromagnetic transition, this reduced oxide phase $LaSr_3CoRuO_6$ has a canted antiferromagnetic ground state with a much smaller magnetic moment (Figure 7.10 (bottom)). Combined the whole range temperature data, a field-cooled plot can be made. The plot of H/M against temperature is used to fit to the Curie-Weiss law ($\chi = C/(T - \theta)$), with the data in the temperature range $65 < T / K < 300$ yielding values of $C = 1.389(1)$ cm^3 K mol^{-1}, $\theta = -54.0(5)$ K (Figure 7.10 (top)). The negative value of Weiss temperature is consistent with the onset of canted antiferromagnetic order.

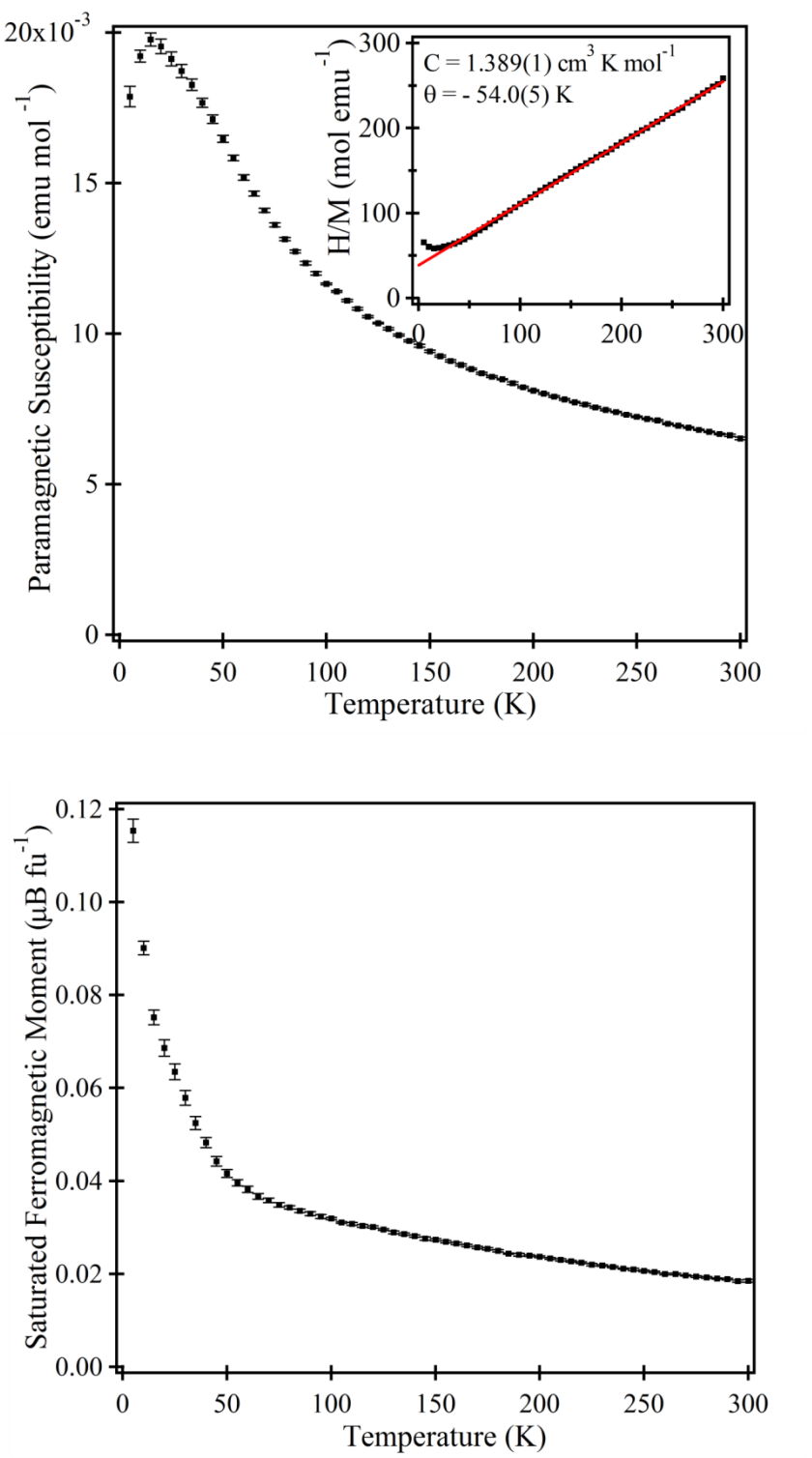


Figure 7.10. The paramagnetic susceptibility (top) and saturated ferromagnetic moment (bottom) of $LaSr_3CoRuO_6$ collected as a function of temperature. Inset: the fit to the Curie–Weiss law in the temperature range 65 < *T* / K < 300.

The observed Curie constant from this reduced oxide phase $LaSr_3CoRuO_6$ (contains two minority phases of La_2O_3 and SrO) yields a value of μ^2 to be 11.112 μ_B, which is much lower than expected for a spin-only combination of a square planar high spin d^8, $S = 1$ Co^{1+} centre and a d^6, $S = 1$ Ru^{2+} centre ($\mu^2_{expected} = 16$ μ_B) as shown in Figure 7.11, even accounting for the roughly 7.0% impurities in the sample.

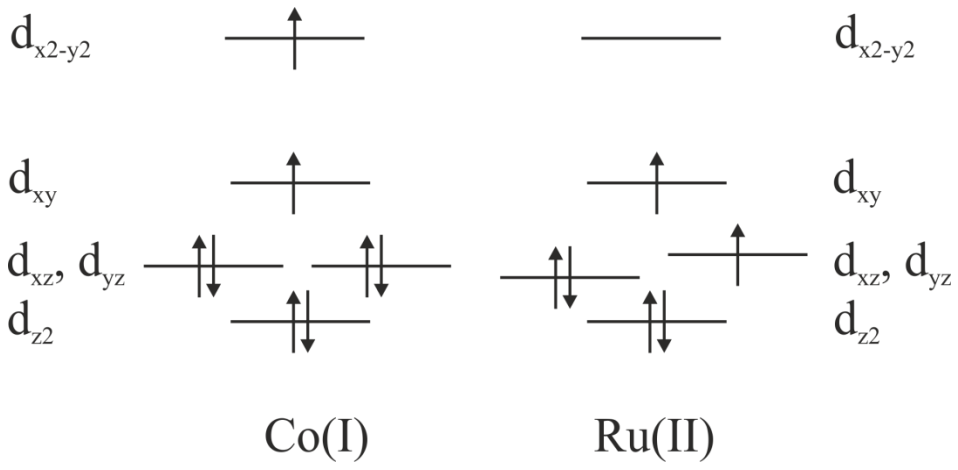


Figure 7.11. Proposed electronic configurations of $LaSr_3CoRuO_6$.

The lack of additional magnetic diffraction features in 5 K neutron data set suggest the absence of long-range magnetic ordering in the sample, which is a common feature found in all other Ru-containing phases in this thesis, despite the magnetisation data collected using a SQUID magnetometer show strong evidence for a canted antiferromagnetic ground state.

7.3.6 Structural Characterisation of $LaSr_3CoRuO_4H_4$

7.3.6.1 Neutron Powder Diffraction

Neutron powder diffraction measurements performed at ambient temperature and low temperature were carried out at WISH diffractometer, ISIS (Chapter 2 Section 2.5.2.1) and the ambient data collected was refined against a model based on the structure of its parent oxide phase $LaSr_3CoRuO_8$ (space group *I*4/*mmm*), but gave a poor fit until the occupancies of the anion sites were refined. It was observed that the 'equatorial' anion site occupancy rapidly refined to a negative value, indicating the presence of hydrogen at this position (H^1 neutron scattering length = -3.73 fm). Once the atom on this site had been changed to a hydride ion, the occupancy refined to unity, within error, confirming the stoichiometry of the phase as $LaSr_3CoRuO_4H_4$ (Figure 7.12). The refined plots are shown in Figure 7.13 with detailed structural parameters in Table 7.8, 7.9 and 7.10.

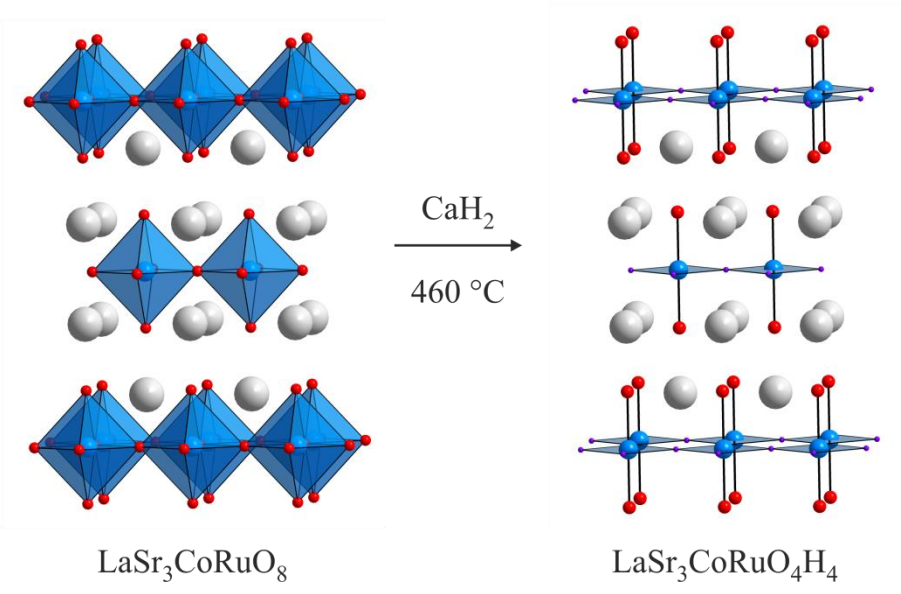


Figure 7.12. Topochemical reduction of $LaSr_3CoRuO_8$ with CaH_2 to form reduced oxide-hydride phase $LaSr_3CoRuO_4H_4$ with H^- substituted into equatorial positions.

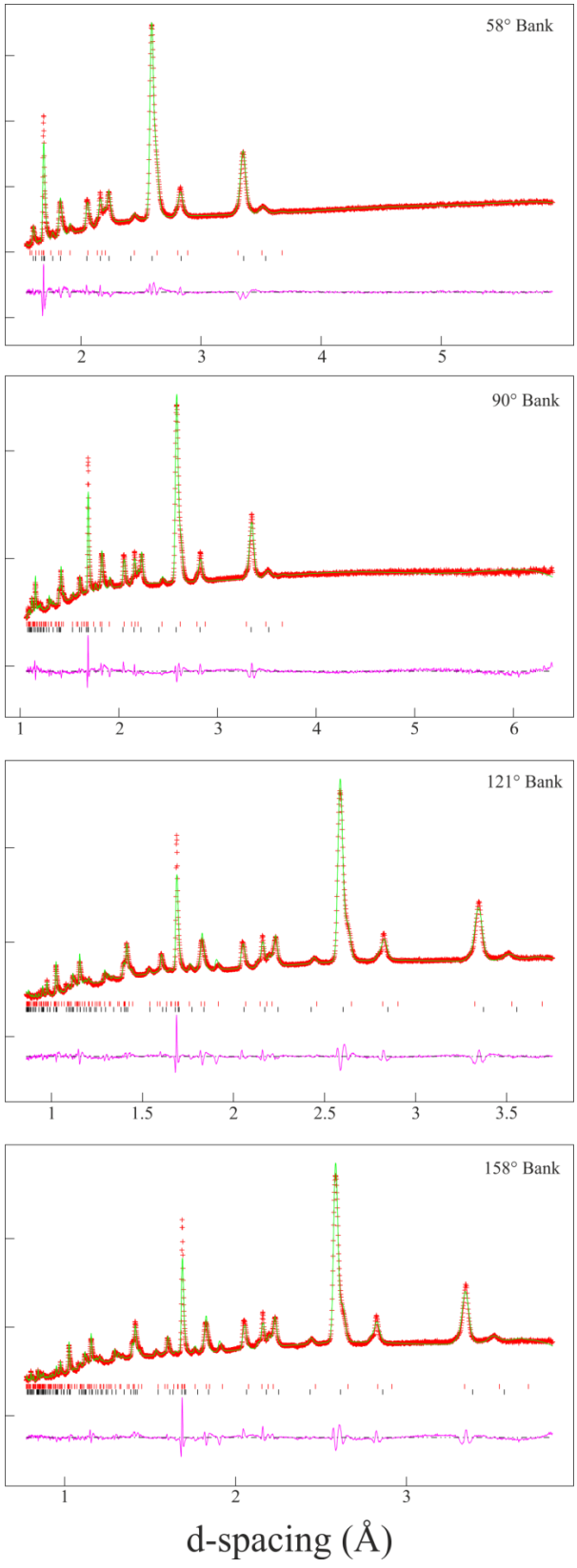


Figure 7.13. Observed, calculated and difference plots from the refinement of neutron powder diffraction data collected from $LaSr_3CoRuO_4H_4$ (space group *I*4/*mmm*) at 298 K. Tick marks indicate peak positions of the majority phase (black) and the minority phase $LaSr_3CoRuO_{6\pm x}$ (red).

Atom	Wyckoff Position	*x*	*y*	*z*	Fraction	U_{iso} equiv.(Å^2)
La/Sr(1)	4*e*	0	0	0.3513(1)	0.25/0.75	0.0174
Co/Ru(1)	2*a*	0	0	0	0.5/0.5	0.0250
O(1)	4*e*	0	0	0.1655(2)	1	0.0198
H(1)	4*c*	0.5	0	0	1	0.1379
$LaSr_3CoRuO_4H_4$ space group *I*4/*mmm* (#139) Formula weight : 629.80 g mol^{-1}, Z = 2 Mass fraction: 75.9(2)% *a* = 3.6484(3) Å, *c* = 13.353(1) Å, Volume = 177.75(4) Å^3						
$LaSr_3CoRuO_{6\pm x}$ space group *Immm* (#71) Formula weight : 657.76 ± δ g mol^{-1}, Z = 2 Mass fraction: 24.1(1)% *a* = 3.8071(6) Å, *b* = 3.6161(6) Å, *c* = 13.172(1) Å, Volume = 181.35(5) Å^3						
Radiation source: Neutron time of flight Temperature: 298 K χ^2 = 18.72; *wRp*= 2.96%; *Rp* = 1.76%.						

Table 7.8. Structural parameters from the refinement of neutron powder diffraction data collected from $LaSr_3CoRuO_4H_4$ at 298 K.

Both the visual fit and statistical fit of the refinement of neutron data collected from $LaSr_3CoRuO_4H_4$ were much worse compared to those of the Ni analogue, $LaSr_3NiRuO_4H_4$, suggesting that the Co oxide-hydride phase might deviate from the body-centred tetragonal system and have a lower symmetry unit cell due to potential tilting or twisting of octahedra.

Atom	U_{11}	U_{22}	U_{33}
La/Sr(1)	0.0192(11)	0.0192(11)	0.0136(22)
Co/Ru(1)	0.0276(27)	0.0276(27)	0.0196(34)
O(1)	0.0283(13)	0.0283(13)	0.0027(22)
H(1)	0.0880(62)	0.1902(75)	0.1354(50)

Table 7.9. Anisotropic displacement factors from the refinement of neutron powder diffraction data collected from $LaSr_3CoRuO_4H_4$ at 298 K.

Cation	Anion	length (Å)
La/Sr(1)	O(1)	2.481(3) × 1
	O(1)	2.590(1) × 4
	H(1)	2.696(1) × 4
Co/Ru(1)	O(1)	2.210(3) × 2
	H(1)	1.824(1) × 4

Table 7.10. Selected bond lengths from the refined structure of $LaSr_3CoRuO_4H_4$.

Low temperature neutron powder diffraction data were collected at 30 K, 20 K, 10 K and 2 K, but no additional features were observed which indicates the absence of long-range magnetic ordering.

7.3.6.2 Synchrotron X-Ray Powder Diffraction

Since the WISH diffractometer used above is primarily designed for neutron powder diffraction at long *d*-spacing in magnetic and large unit cell systems, its relatively low resolution at short *d*-spacing for small unit cell systems like $LaSr_3CoRuO_4H_4$, cannot fully confirm the tetragonal symmetry of the unit cell. Therefore synchrotron X-ray powder diffraction data were collected from this oxide-hydride phase as its extremely high resolution will reveal any extra peaks that do not belong to this high symmetry tetragonal unit cell and if the oxide-hydride phase requires a larger or distorted unit cell.

Synchrotron X-ray powder diffraction data (Chapter 2 Section 2.5.1.2) was collected from a large-scale neutron sample of $LaSr_3CoRuO_4H_4$. The data were indexed using a body-centred tetragonal unit cell (space group *I4/mmm*) with lattice parameters: a = 3.6458(1) Å and c = 13.3491(5) Å. A structural model was constructed, based on an n = 1, A_2BO_4 Ruddlesden-Popper phase with a 1:3 La:Sr solid-solution on the A-site, a 1:1 Co:Ru solid-solution on the B-site. This model was refined against the synchrotron X-ray powder diffraction data collected at room temperature and the refinement gives unsatisfactory visual fit (Figure 7.14) and statistical fit (χ^2 = 505.5; *wRp* = 9.70%; *Rp* = 5.53%), even with a secondary phase added to account for the part of sample which remains reduced oxide phase $LaSr_3CoRuO_{6\pm x}$, i.e. incomplete hydride-for-oxide substitution.

A close inspection of the two-phase refinement reveals that although peak positions are in place, some of the peaks are either too sharp or too broad than expected and these differences in peak shapes cannot be accounted for by simply applying *hkl* dependent broadening in peak profiles.

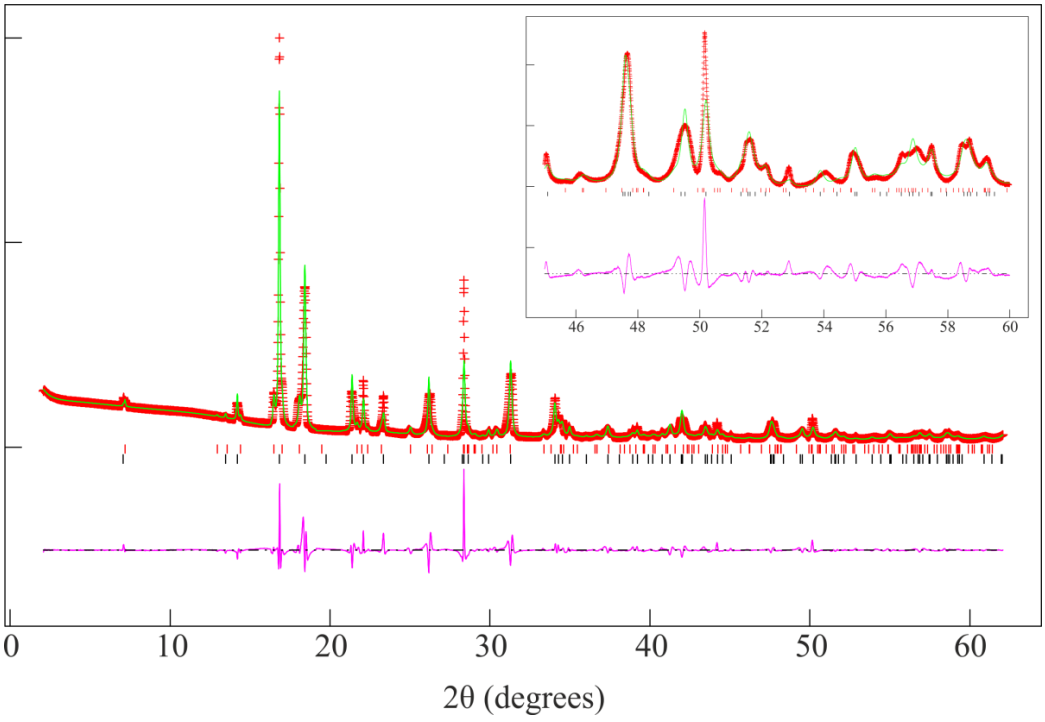


Figure 7.14. Observed, calculated and difference plots from the refinement of synchrotron X-ray powder diffraction data collected from $LaSr_3CoRuO_4H_4$ (space group *I*4/*mmm*) at 298 K. Tick marks indicate peak positions of the majority phase (black) and the minority phase $LaSr_3CoRuO_{6\pm x}$ (red).

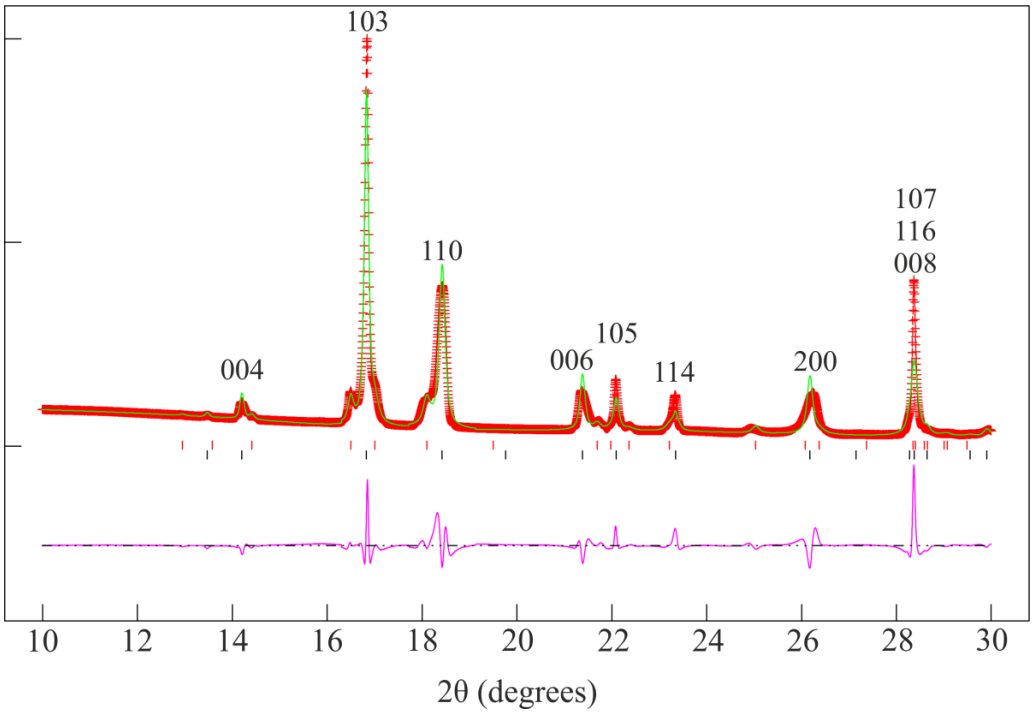


Figure 7.15. Observed, calculated and difference plots from the zoom-in area 10 ≤ 2θ/ ° ≤ 30 of the refinement of synchrotron X-ray powder diffraction data collected from $LaSr_3CoRuO_4H_4$ (space group *I*4/*mmm*) at 298 K.

For example, as shown in Figure 7.15 (the zoom-in area $10 \leq 2\theta/\,^{\circ} \leq 30$), peaks with *hkl* values of 103, 105, 114 are sharper than expected and those with *hkl* values of 004, 110, 006, 200 are broader than expected. The irregular pattern of mismatching in peak shapes in the powder diffraction data makes the determination of the crystallographic structure of $LaSr_3CoRuO_4H_4$ extremely challenging, as the important features, like additional peaks which indicate an orthorhombic distortion might be masked by the background. Therefore, Electron Diffraction (ED) patterns were acquired (Prof. Joke Hadermann from University of Antwerp) to reveal the real crystallographic structure of this oxide-hydride phase.

7.3.6.3 Transmission Electron Microscopy Study

Electron diffraction (ED) patterns were acquired on a FEI Tecnai transmission electron microscope operated at 200 kV. High angle annular dark field (HAADF) scanning transmission electron microscopy (STEM) images were acquired using a probe aberration corrected FEI Titan 80-300 "cubed" microscope operated at 300 kV. Samples for TEM analysis were prepared in the glove box filled with argon by grinding the material and dipping the copper TEM grid into the dry powder. The vacuum transfer holder was used to transfer the grids from the glove box to the microscope.

ED patterns were acquired from several crystals oriented along [100] and [110] directions. As can be seen in Figure 7.16, the ED patterns can be indexed in *I*4/*mmm* symmetry with the cell parameters $a \approx 3.6$ Å, $c \approx 13.0$ Å. There are no signs of superstructure reflections, so there is no indication for a need to expand the unit cell from ED. Therefore the simple body-centred tetragonal unit cell mentioned in both section 7.3.6.1 and 7.3.6.2 can be used to describe the real crystallographic structure of the oxide-hydride phase, $LaSr_3CoRuO_4H_4$.

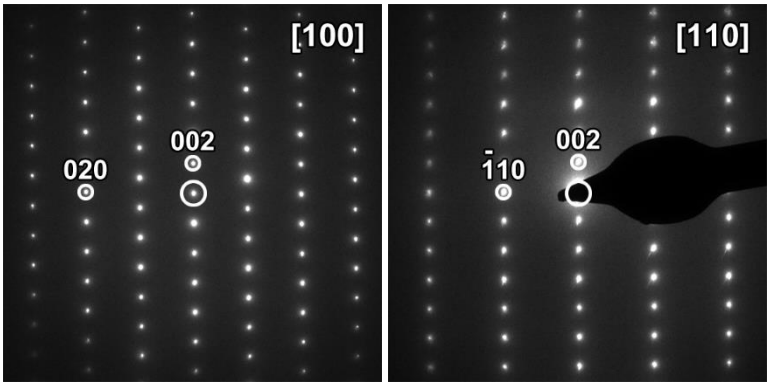


Figure 7.16. Electron diffraction (ED) patterns collected from $LaSr_3CoRuO_4H_4$, taken along [100] and [110] directions.

Although ED patterns do correspond to the simple body-centred tetragonal unit cell (space group *I4/mmm*), refinements of both neutron powder diffraction data and synchrotron X-ray powder diffraction data against this model were not satisfactory, with mismatching in peak shapes that cannot be neglected. Therefore the problem must lie at an even more local scale, which might be detectable by using high resolution imaging.

According to HAADF-STEM images, many crystals were covered with crystalline nanoparticles (Figure 7.17). Since the sample was not exposed to air and they were not formed during the electron beam exposure (some crystals were covered from the start of the experiment, whereas others are simply remained uncovered), these particles are intrinsic to the sample.

The more important outcome is that the HAADF-STEM images showed the presence of an $n = 2$ Ruddlesden-Popper (RP) phase. HAADF-STEM images from crystals oriented along the [100] direction are shown in Figure 7.18-7.20. Figures 7.18 and 7.19 show $n = 1$ RP, which constitutes most of the crystallites, Figure 7.20 shows crystals with $n = 2$ RP phase. The fact that most crystallites show $n = 1$ RP as main phase is derived from the absence of *n*

= 2 RP phase on the available electron diffraction patterns, which all show only *n* = 1 RP phase.

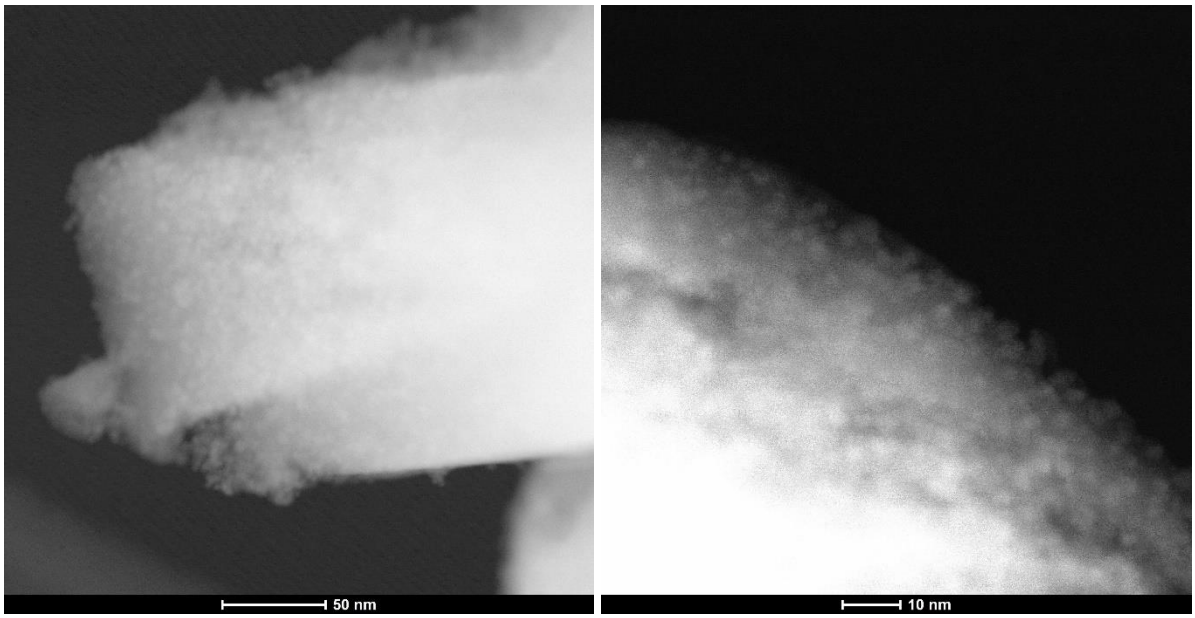


Figure 7.17. HAADF-STEM images of the crystals covered with nanoparticles.

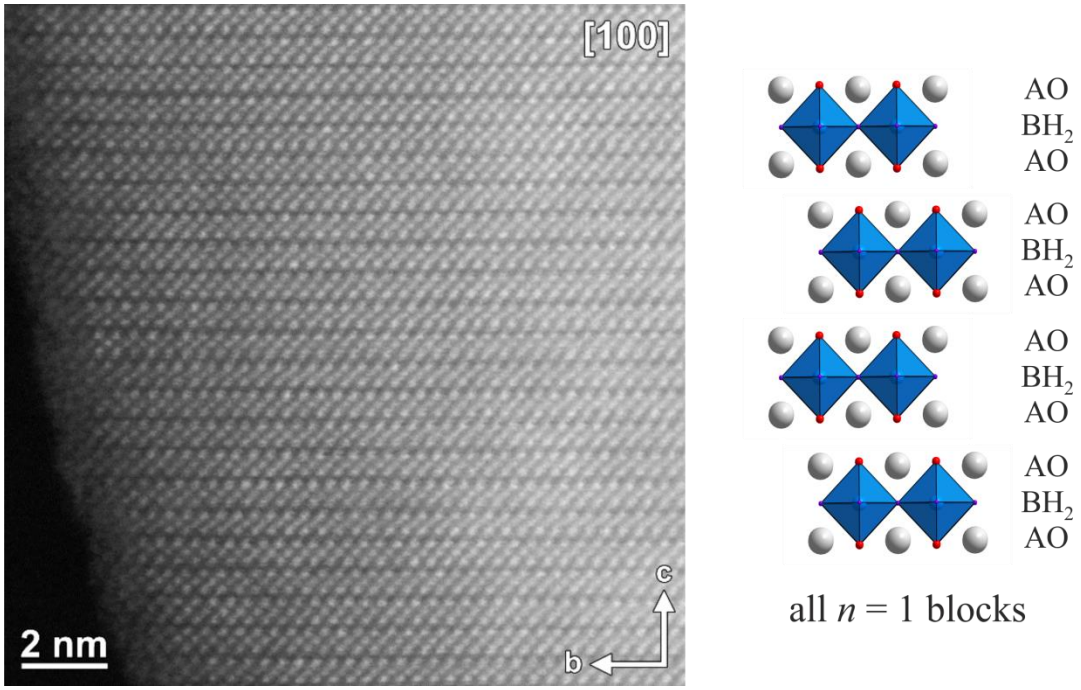


Figure 7.18. HAADF-STEM image from the perfect regions of *n* = 1 RP phase $LaSr_3CoRuO_4H_4$.

On the HAADF-STEM images, atomic columns of A cations are slightly brighter than of the B cations since Z_{La} = 57, Z_{Sr} = 38, Z_{Co} = 27 and Z_{Ru} = 44, and the brightness of the columns on such images scales with the average Z along a column. At the surface of the crystals, there is a thin amorphous layer with a thickness of 1-2 nm.

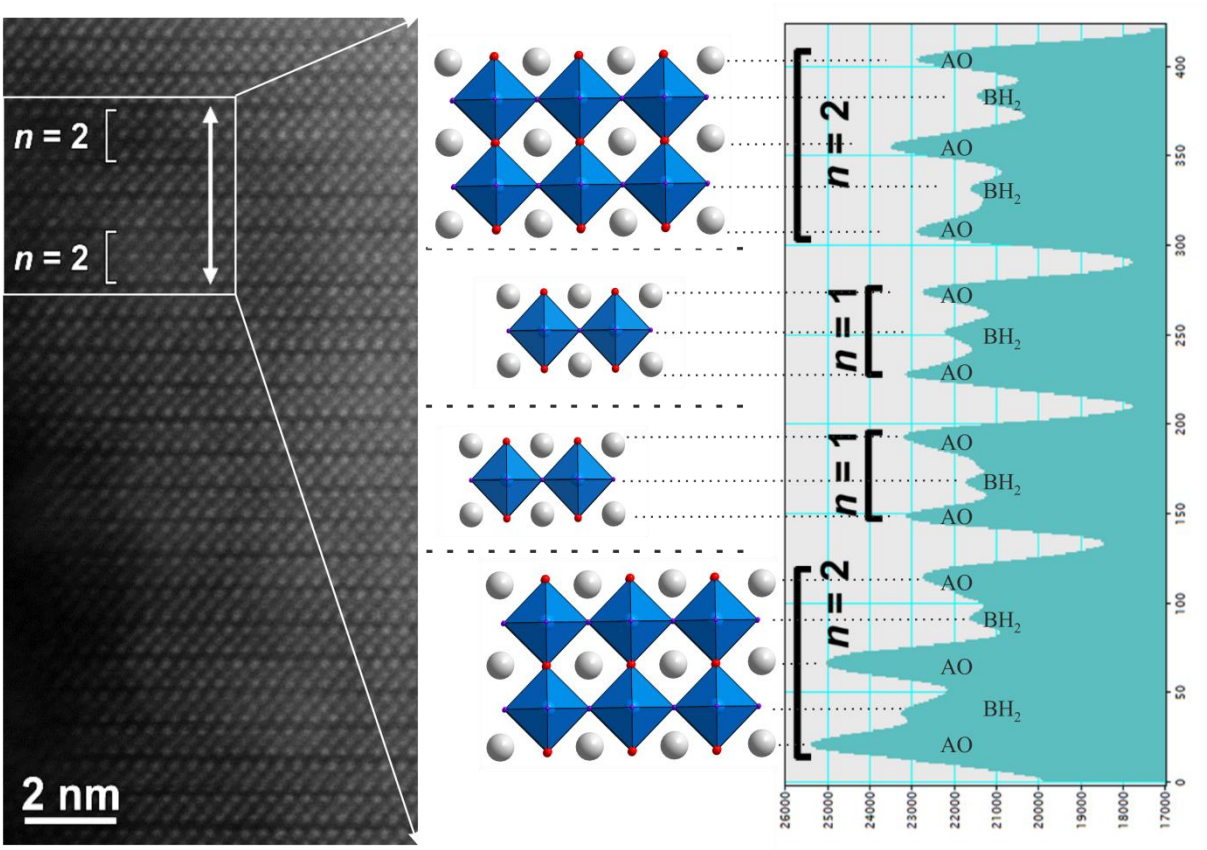


Figure 7.19. HAADF-STEM image from the *n* = 1 RP structure with inclusions of two *n* = 2 blocks. An intensity profile was measured along the arrow and corresponds to the intensity of 2-1-1-2 blocks (the signal is averaged along the b axis). Note that the A cation layers in the middle of the perovskite blocks of the *n* = 2 fragments are brighter than at the periphery and therefore they are most likely La-rich.

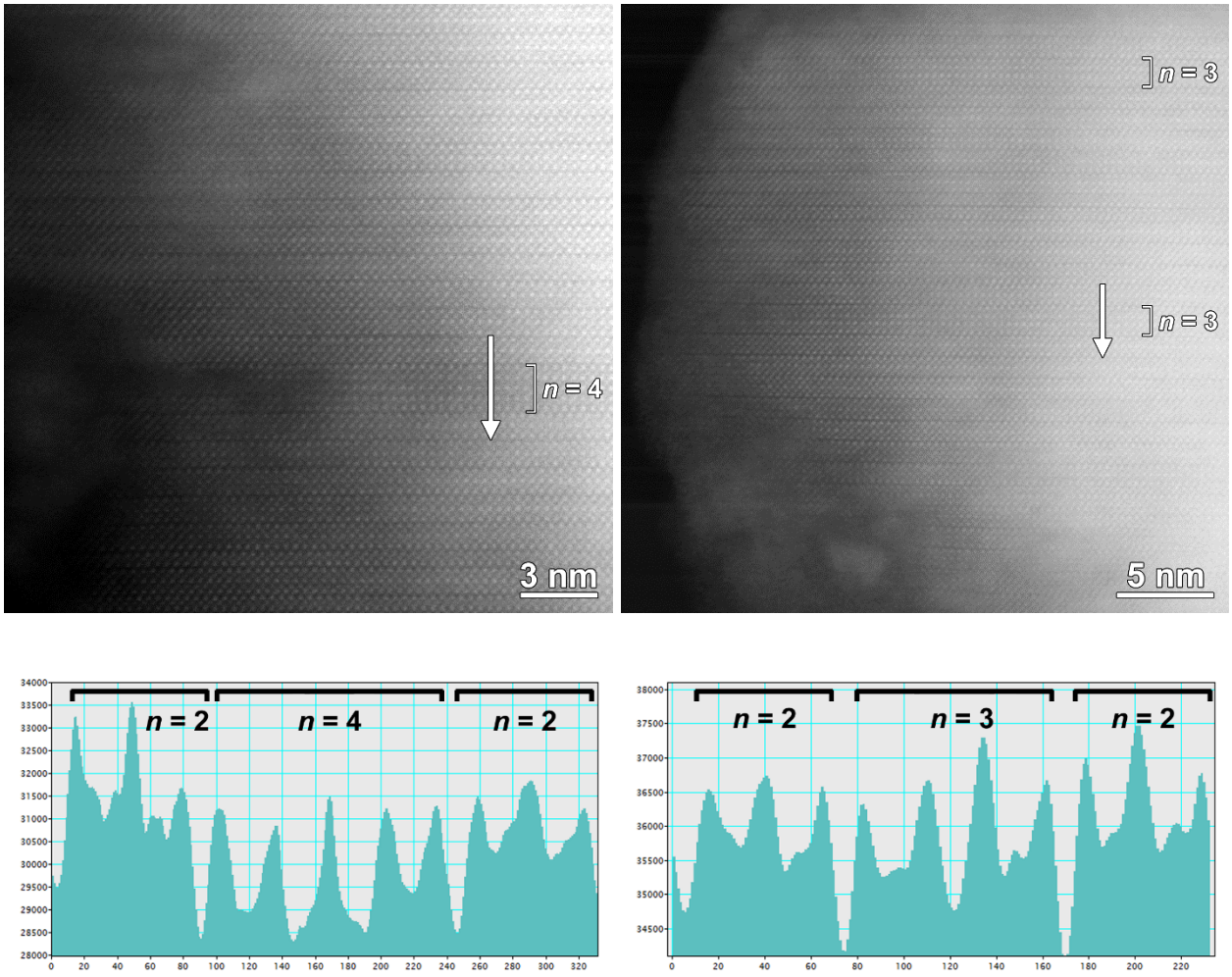


Figure 7.20. HAADF-STEM images of areas with *n* = 2 RP structure. On the left image there is a block of four perovskite unit cells and also one perovskite slab is present near the bottom of the image. On the right image, there are a few *n* = 3 and *n* = 1 blocks. The surface of the crystals is amorphous. Intensity profiles measured along the arrows are shown at the bottom of the images. Again, the central rows in the *n* = 2 RP are brighter and thus probably enriched with La. Also in these defects, the central A cation rows in the total perovskite blocks are brighter, most probably indicating La enrichment.

Figure 7.18 represents a typical crystal with an ideal n = 1 RP structure. Stacking faults were found in many crystals, which in the n = 1 RP phase are usually blocks with n = 2 RP structure, which could also be considered as just a slab of perovskite structure when it is just a single fault (Figures 7.19). The central A-site cation rows appear to be brighter, which would indicate a higher average Z along the projection direction for these rows. Indeed, according to the intensity profiles measured through these perovskite blocks (right-hand-side of Figure 7.19), the A cation layers in the middle of the perovskite blocks are brighter than at the periphery and therefore they are most likely La-rich.

Figure 7.20 shows areas that have n = 2 RP structure as the main phase. The stacking faults are present as well in this case, being blocks of the perovskite structure, 1, 3 or 4 unit cells high (if there were several next to each other, we could have referred to them as n = 3 or n = 4 RP). Again, the rows of A-site cations at the centre of the defects are brighter, indicating probable La-enrichment (intensity profiles in Figure 7.20).

Therefore, all the findings in TEM study suggest that any imperfections in fitting the neutron powder diffraction data and synchrotron X-ray powder diffraction data against the simple body-centred tetragonal unit cell (space group *I*4/*mmm*) might be due to the intergrowth of mainly the n = 2 RP phase and the separate perovskite blocks (of height up to 4 perovskite unit cells), scattered as defects throughout the crystals. In addition, all inclusions deviating from n = 1 RP phase appear to be La-enriched, which is not surprising, as n = 2 RP phase contains a higher La:Sr ratio (1:2) than n = 1 RP phase (1:3) according to their formula:

$$LaSr_2CoRuO_3H_4 + SrO \longleftrightarrow LaSr_3CoRuO_4H_4$$

7.3.6.4 Stacking Faults Study

As discussed in the previous section, TEM results confirm that the simple body-centred tetragonal unit cell (space group *I*4/*mmm*) does describe the average crystallographic structure of the oxide-hydride phase $LaSr_3CoRuO_4H_4$ and the imperfections found in fitting peak shapes of diffraction patterns arise from the intergrowth of n = 2 RP phase and the separate perovskite blocks throughout the main n = 1 RP phase as stacking faults. A study of these stacking faults, i.e. how the transition probability affects the peak shapes in powder diffraction patterns was carried out by FAULTS analysis (Chapter 2 Section 2.13).

According to TEM results, layer 1 in the input control file of FAULTS program is set to be the major n = 1 RP phase $LaSr_3CoRuO_4H_4$, and layer 2 is set to be the minor n = 2 RP phase $LaSr_2CoRuO_3H_4$. A map is plotted out (Figure 7.21) to show different combinations of transition probabilities between two kinds of layers.

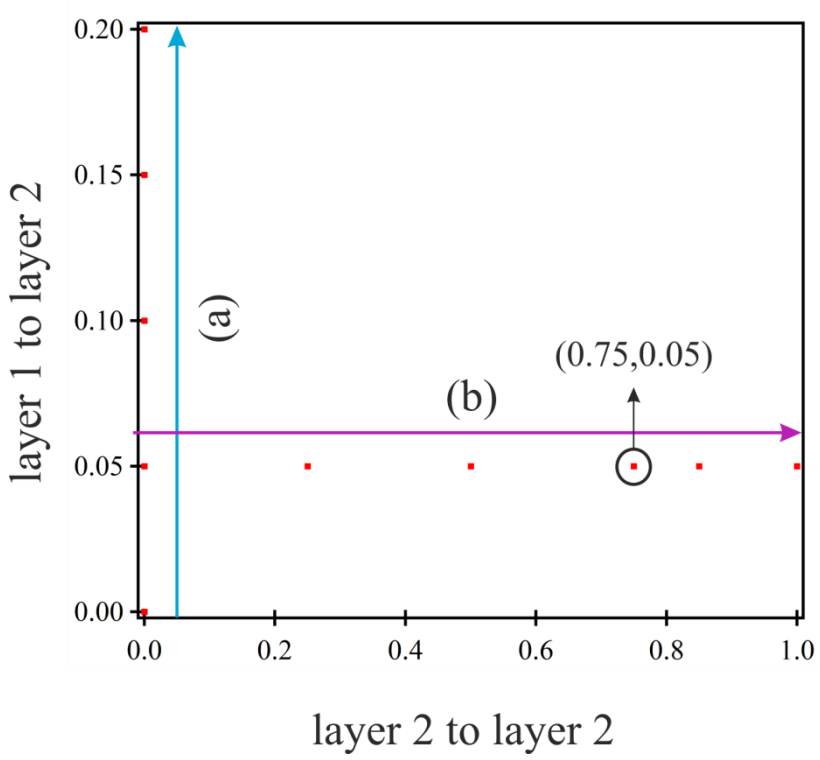


Figure 7.21. Transition probability of layer 1 to 2 plotted against that of layer 2 to 2.

Route (a) in Figure 7.21 investigates the relationship between the transition probability of layer 1 (n = 1) to layer 2 (n = 2) and peak profiles in X-ray powder diffraction data, by keeping the transition probability of layer 2 to layer 2 at zero, i.e. there are no clusters of defects in the lattice. The most diagnostic area of simulated patterns is shown in Figure 7.22.

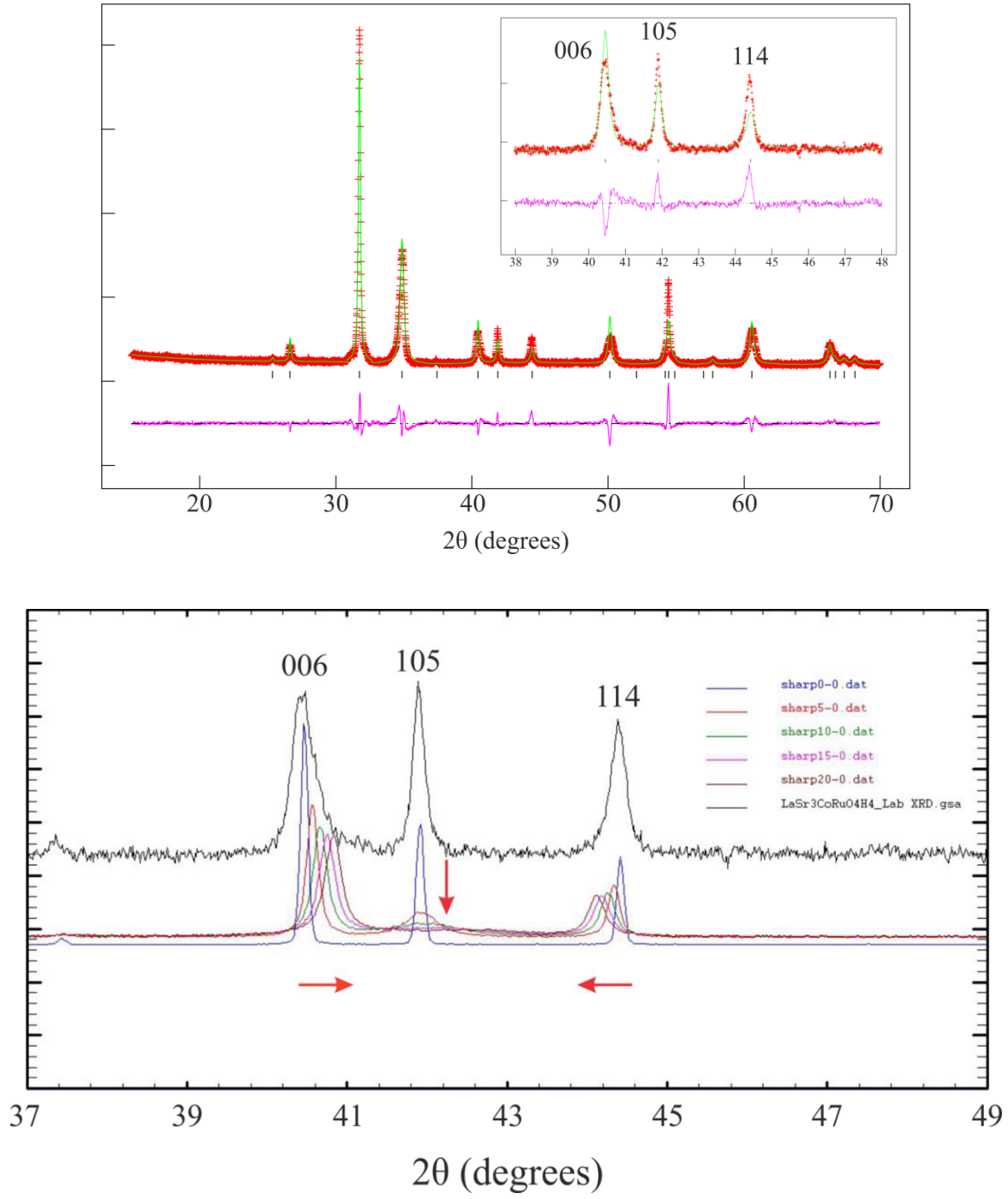


Figure 7.22. Rietveld refinement of laboratory X-ray powder diffraction data (top), and zoom-in area (37 ≤ 2θ/° ≤ 49) of simulated patterns for route (a) (bottom).

This area contains three diagnostic peaks with *hkl* values 006, 105 and 114 respectively. The first pattern (dark blue) is the simulated pattern of pure $n = 1$ RP phase $LaSr_3CoRuO_4H_4$, i.e. no defects in the lattice. It is clear that with the increase in the transition probability of layer 1 to layer 2 (the concentration of defects in the lattice), peak 006 shifts to the right and peak 114 shifts to the left in large steps, and also peak 105 becomes much broader (as represented by red arrows), which all contradict to the difference plot (pink) from the rietveld refinement of laboratory X-ray powder diffraction data (Figure 7.22 (top)).

In addition, a more subtle but important difference is that, in the experimental data, the 006 peak is asymmetric in right-hand-side and the 114 peak is asymmetric in left-hand-side, with respect to the calculated model (Figure 7.22 (top)), but in simulated patterns, these two peaks show their asymmetry in the opposite side respectively (Figure 7.22 (bottom)).

Therefore, the concentration of defects ($n = 2$ RP phase) should not be too high as peak positions are almost right in place, and these defects seem to distribute unevenly across the lattice.

The failed approach of route (a) suggests the possibility of having clusters of defects in the lattice, i.e. the transition probability of layer 2 ($n = 2$) to layer 2 ($n = 2$) is non-zero. Therefore simulated patterns of route (b) in Figure 7.21 show how the transition probability of layer 2 to layer 2 influences peak profiles in X-ray powder diffraction data, by keeping the transition probability of layer 1 to layer 2 (concentration of defects) at 5% (Figure 7.23)

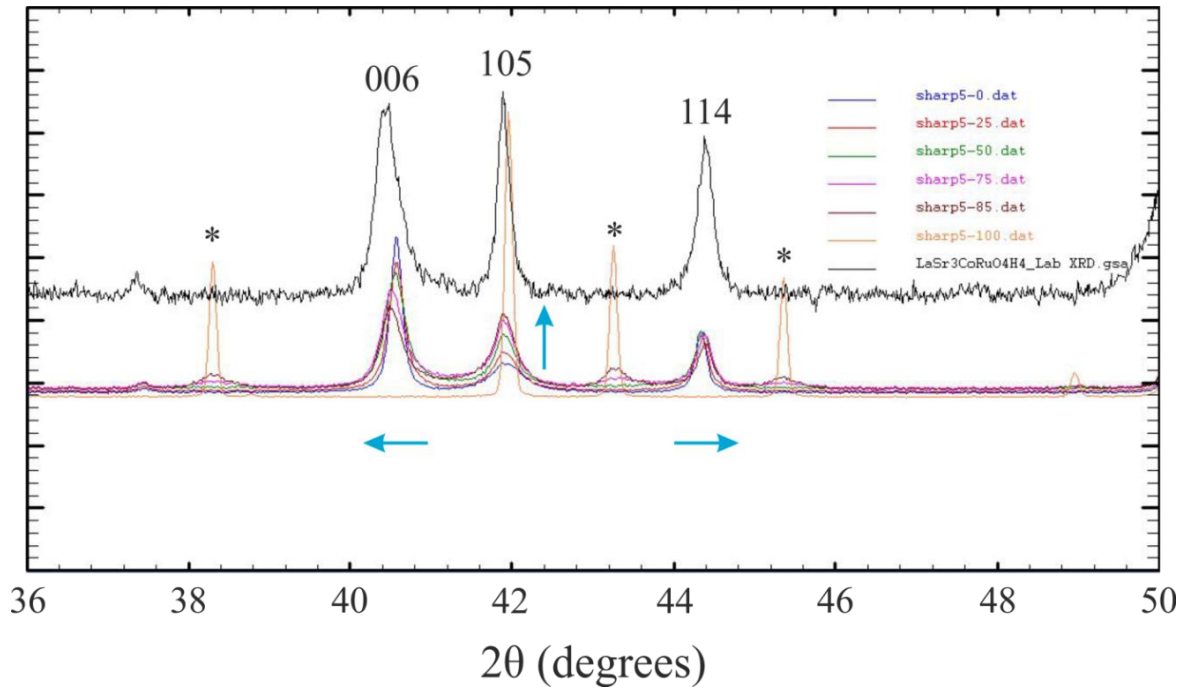


Figure 7.23. Zoom-in area (36 ≤ 2θ/° ≤ 50) of simulated patterns for route (b).

This area contains three diagnostic peaks with *hkl* values 006, 105 and 114 respectively. It is clear that with the increase in the transition probability of layer 2 to layer 2 (the expansion of clusters of defects), peak 006 shifts to the left and peak 114 shifts to the right only in tiny steps, and also peak 105 becomes more intense (as represented by blue arrows), which all agree with the difference plot (pink) from the rietveld refinement of laboratory X-ray powder diffraction data (Figure 7.22 (top)). Also, a more subtle but important observation is that the 006 peak and the 114 peak in simulated patterns (Figure 7.23) show their asymmetry in the same side (right-hand-side for 006 peak and left-hand-side for 114 peak) as expected from the rietveld refinement of the experimental data.

However, when the transition probability of layer 2 to layer 2 is too high, i.e. above 0.75, extra peaks (marked by * in Figure 7.23) attributed to large clusters of n = 2 RP phase cannot be neglected.

The formation of clusters of defects is totally reasonable, as the large-scale neutron sample cannot really be heated homogeneously during preparation. These $n > 1$ RP defects (2, 3 and 4 according to TEM), as a result of partial decomposition of the material, tend to be found in parts of the sample that get over-heated.

The stacking faults study by FAULTS program indicates that the concentration of defects ($n = 2$ RP phase) in the lattice is about 5%, and the probability of finding another $n = 2$ block next to an $n = 2$ block is approximately 75%, as highlighted in Figure 7.21, because the simulated pattern of this combination best matches the experimental data collected from a sample of $LaSr_3CoRuO_4H_4$ (Figure 7.24).

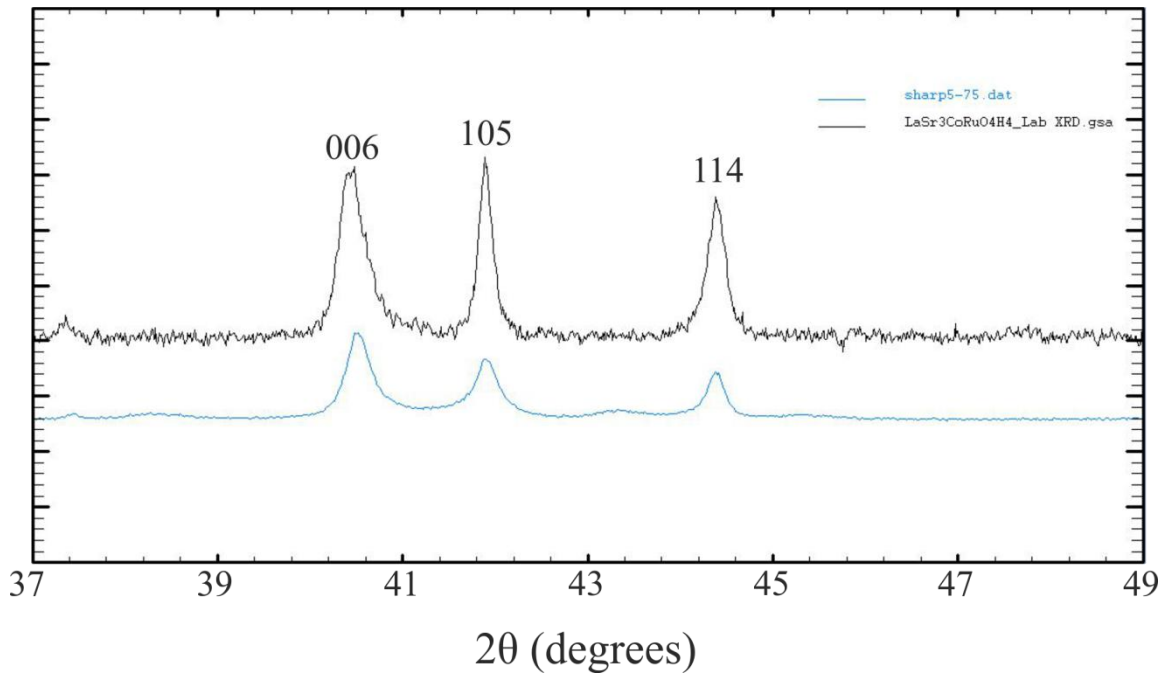


Figure 7.24. Zoom-in area ($37 \leq 2\theta/° \leq 49$) of the simulated pattern resulted from 5% of layer 1 to layer 2 transition and 75% of layer 2 to layer 2 transition, compared to the laboratory X-ray diffraction pattern.

Therefore, although these quantifications of transition probabilities are not quite accurate, FAULTS program does generally map out the low concentration and uneven distribution of defects (n = 2 RP phase) across the lattice of n = 1 RP phase $LaSr_3CoRuO_4H_4$, which agrees with all the findings in the TEM study.

The presence of small amount of defects (n = 2 RP phase) across the lattice of n = 1 RP phase $LaSr_3CoRuO_4H_4$, suggests that the n = 2 RP phase is more energetically stable than the n = 1 RP phase, and their activation energy barriers are not too different, i.e. ΔH_2 is only slightly larger than ΔH_1, which are both significantly larger than ΔH_3 (the activation energy barrier of non-topochemical decomposition products) (Figure 7.25).

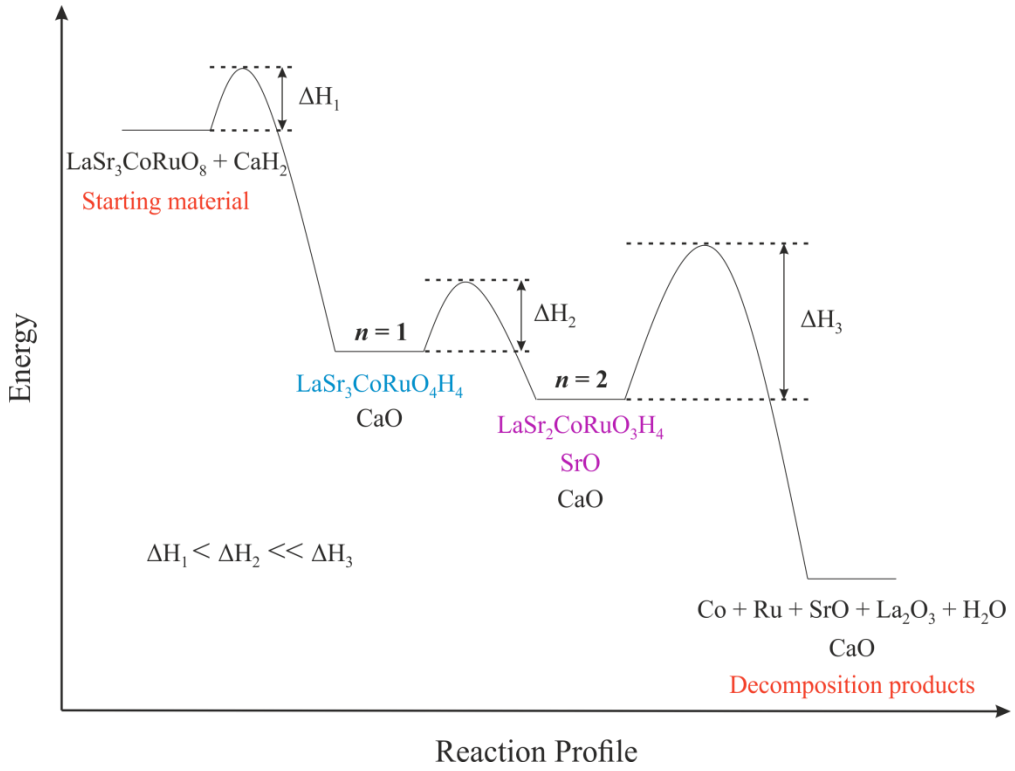


Figure 7.25. The proposed reaction profile for topochemical reduction of $LaSr_3CoRuO_8$ with CaH_2.

7.3.7 Magnetic Characterisation of $LaSr_3CoRuO_4H_4$

Magnetisation data were collected using a SQUID magnetometer by using a technique called ferronagnetic subtraction (Chapter 2 Section 2.10). Due to the inevitable presence of trace amount of ferromagnetic Co impurity in the sample prepared via topochemical reaction with CaH_2, a large field (3 T to 5 T) was applied to saturate elemental Co during the magnetic characterisation, so the ferromagnetic behaviour contributed by Co impurity would not mask the magnetic behaviour of the bulk phase. At 5 K increments between 5 K and 300 K, magnetisation-field isotherms were collected over the field range $3 \leq H / T \leq 5$ and the resultant magnetisation are plotted as a function of the applied field. For each 5 K step the gradient of the plot obtained shows the paramagnetic susceptibility and the intercept gives the saturated ferromagnetic moment. Combined the whole range temperature data, a field-cooled plot can be made. The plot of H/M against temperature is used to fit to the Curie-Weiss law ($\chi = C/(T - \theta)$), with the data in the temperature range $25 < T / K < 300$ yielding values of $C = 1.058(3)$ cm^3 K mol^{-1}, $\theta = - 39.4(4)$ K (Figure 7.27 (top)), and hence yields a value of μ^2 to be 8.464 μ_B which approximately corresponds to 2 unpaired electrons in total (Figure 7.26).

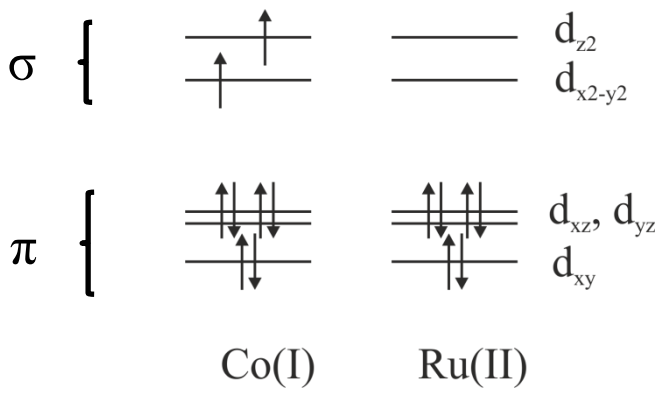


Figure 7.26. The O_2H_4 coordination of Co^+ and Ru^{2+} results in $S = 1$ and $S = 0$ spin states, respectively.

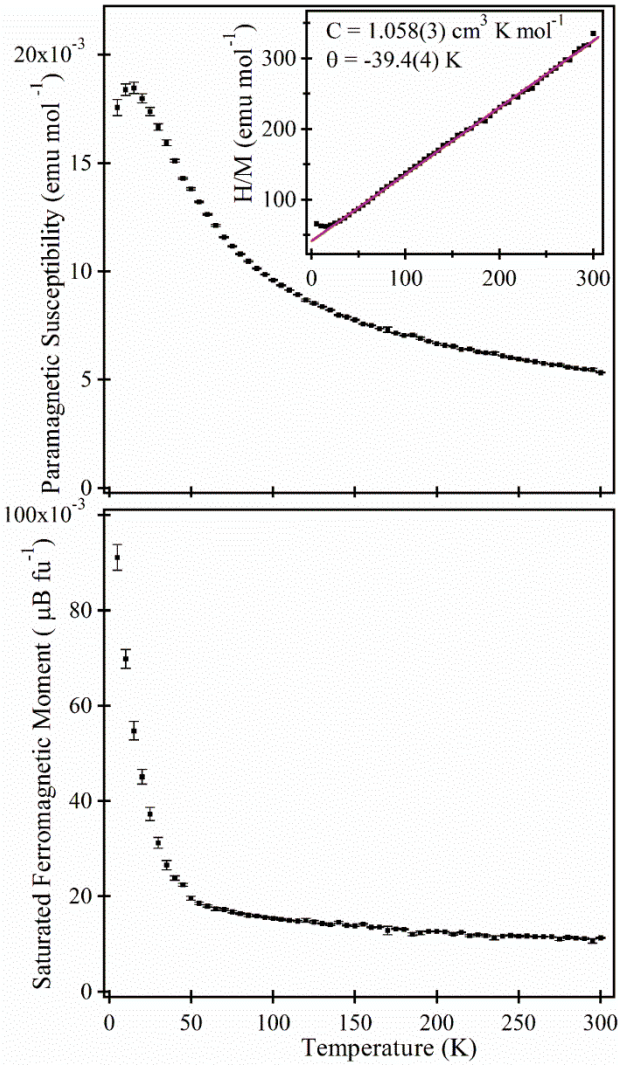


Figure 7.27. The paramagnetic susceptibility (top) and saturated ferromagnetic moment (bottom) of $LaSr_3CoRuO_4H_4$ collected as a function of temperature. Inset: the fit to the Curie–Weiss law in the temperature range 25 < *T* / K < 300.

The magnetisation data collected suggests B-site cations in the parent oxide phase have been reduced to Co^{1+} (high-spin d^8) with 2 unpaired electrons and diamagnetic Ru^{2+} (low-spin d^6). These states merit the closest predicted value to the experimental Curie constant. On cooling below T ~ 25 K the paramagnetic susceptibility of $LaSr_3CoRuO_4H_4$ goes through a local maximum and this is accompanied by an increase in the saturated ferromagnetic moment of the sample. These data in combination suggest the oxide-hydride phase should adopt an antiferromagnetic ground state.

7.3.8 μ^+SR data of $LaSr_3CoRuO_4H_4$

As a result of the conflict between low temperature neutron powder diffraction data and magnetisation data, we have collected μ^+SR data as an independent probe to investigate local magnetic ordering (μ^+SR data were collected at the Paul Scherrer Institute in Switzerland by Prof. Stephen J. Blundell, University of Oxford). Plots of the asymmetry of μ^+SR data collected from $LaSr_3CoRuO_4H_4$ at various temperatures are shown in Figure 7.28, and there is no indication of magnetic ordering down to a temperature of 1.9 K, which in agreement with the low temperature neutron powder diffraction data collected (2 K). However, this oxide-hydride phase behaves differently compared to the Ni analogue. The muon polarization simply relaxes with a rate which increases as the sample is cooled, consistent with fluctuations that slow down on cooling, but unlike the Ni analogue, the asymmetry plot starts to flatten out at low temperature. Although the asymmetry plot collected at 1.9 K has not started to oscillate, it is nearly approaching the point where a long range order is obtained. This suggests that $LaSr_3CoRuO_4H_4$ should adopt an antiferromagnetic ground state and the ordering temperature is just below 1.9 K.

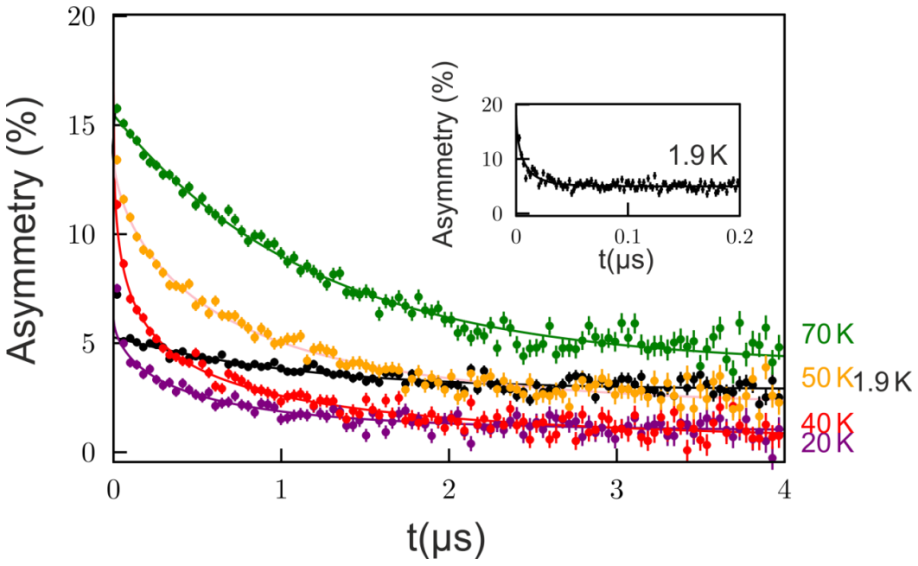


Figure 7.28. Plots of the asymmetry of μ^+SR data collected from $LaSr_3CoRuO_4H_4$ at various temperatures.

7.4 Discussion

7.4.1 Structural Peculiarity of $LaSr_3CoRuO_xH_y$ Phases

The topochemical reductions of n = 1 Ruddlesden-Popper phase $LaSr_3CoRuO_8$ with Zr powder oxygen getter and solid state binary metal hydride CaH_2 follow the same routine as the Ni analogue.

When the parent oxide phase is reduced by using Zr powder as an oxygen getter, to eliminate the source of H^-, ordered oxide vacancies are formed along *b*-axis, resulting in the changing of the coordination environment of Co and Ru from octahedra to square-planes. On the other hand, when the parent oxide phase is treated with CaH_2 in sealed ampoules, it eventually yields an anion-ordered oxide-hydride phase $LaSr_3CoRuO_4H_4$ with the Co and Ru cations located in a plane containing only hydride ligands and the coordination spheres of the corner-linked square-planar MH_4 units in this plane are completed by two axial oxide ions that link the planes to the neighbouring (La/Sr)O layers.

In both cases, the interesting structural selectivity of Ruddlesden-Popper phases is reflected by the preference of deintercalating oxide ions located in equatorial positions during reductions, as these anion sites are topologically distinct rather than simply crystallographically distinct compared to apical ones, because they are situated at different positions within the structural network and cannot be made equivalent by simply removing a symmetry-breaking tilting or twisting distortion.

Anions situated in topologically distinct coordination sites tend to exist in different chemical environments; therefore removal of them can exert different consequences on cations in one specific site. Hence in this case, which anions are moved or substituted during the topochemical reduction process of $LaSr_3CoRuO_8$, can be quantitatively analysed by

calculated anion bond valence sums (Table 7.11) of O(1) and O(2) shown in Figure 7.29, as these BVS values reflect the degree of influence exerted on the A-site cations (1:3 La/Sr, BVS A) and B-site cations (1:1 Co/Ru, BVS B) respectively by oxide ions in each 'topologically distinct' anion site.

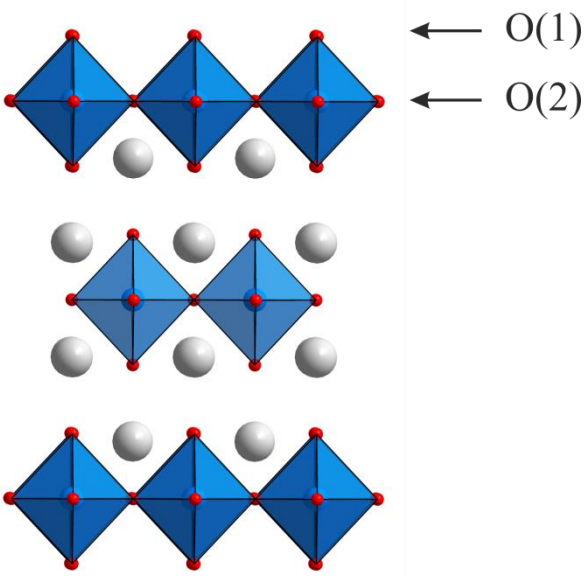


Figure 7.29. The topologically distinct anion sites in the *n* = 1 Ruddlesden-Popper phase $LaSr_3CoRuO_8$.

Anion	Anion BVS	$LaSr_3CoRuO_8$
O(1)	BVS A	1.209
	BVS B	1.002
	(BVS B) – (BVS A)	**- 0.207**
O(2)	BVS A	0.983
	BVS B	2.841
	(BVS B) – (BVS A)	**+ 1.858**

Table 7.11. The calculated anion bond valence sums of the *n* = 1 Ruddlesden-Popper phase $LaSr_3CoRuO_8$.

During topochemical reductions, B-site cations are reduced while the oxidation states of A-site cations remain unchanged. The best compromise between the two largely incompatible requirements of the two classes of cations is to deintercalate or substitute oxide ions which will lead to the greatest change in the bonding environment of B-cation with the smallest change in that of A-cation. The compromise can be quantified as the term (BVS B) – (BVS A) showed above in Table 7.11. The value of this term is more positive for O(2), the equatorial oxide ion, compared to that of O(1) which is the apical oxide ion, hence O(2) is the chosen one to be deintercalated or substituted during the modification of the anion lattice in $LaSr_3CoRuO_8$ if Co^{2+}/Ru^{5+} centres need to be reduced.

This outcome predicts oxide vacancies (in reduced oxide phase $LaSr_3CoRuO_6$), or hydride ions (in oxide-hydride phase $LaSr_3CoRuO_4H_4$) should prefer to reside in equatorial anion sites, O(2), which agrees with both synchrotron X-ray powder diffraction data and neutron powder diffraction data, as the coordination environment of O(1) is A_5B while that of O(2) is A_4B_2, both are six-coordinated, but O(2) has a greater impact on B-site cations, simply because it is coordinated with one more B-site cation compared to O(1).

7.4.2 Magnetic Characterisation of $LaSr_3CoRuO_xH_y$ Phases

A disordered Co/Ru lattice is expected to exhibit spin-glass behaviour, as observed for $Sr_{n+1}(Fe/Ru)_nO_{3n+1}$ phases. However, magnetisation data collected using a SQUID magnetometer indicates none of the $LaSr_3CoRuO_xH_y$ phases are spin-glasses at low temperature and showing strong evidence for an antiferromagnetic ground state. In contrast, low temperature neutron powder diffraction data show no additional magnetic diffraction features that would support the presence of a long-range magnetic ordered state and plots of asymmetry of μ^+SR data collected at 1.9 K is nearly approaching the point where a long

range order is obtained, i.e. it is just about to start oscillation, suggesting the ordering temperature is not far below 1.9 K.

One possible explanation is that these $LaSr_3CoRuO_xH_y$ phases adopt a paracrystalline order, just like the Ni series discussed in previous chapters, with rigorous Co/Ru order within each perovskite sheet, but no order between layers as they are not rigidly connected along *c* axis, hence low temperature neutron powder diffraction data do not show any indication of long-range magnetic ordering. Therefore further Pair Distribution Function (PDF) analysis is required to investigate the detailed cation arrangement in these phases.

7.4.3 Stacking Faults Found in $LaSr_3CoRuO_xH_y$ Phases

Although the chemistry of topochemical reductions of $n = 1$ Ruddlesden-Popper phase $LaSr_3NiRuO_8$, by using Zr powder oxygen getter and solid state binary metal hydride CaH_2, can be extended to $LaSr_3CoRuO_8$, yielding analogous reduced oxide phase $LaSr_3CoRuO_6$ and oxide-hydride phase $LaSr_3CoRuO_4H_4$, structural characterisation results of these reduced phases reveals some different features.

Both synchrotron X-ray powder diffraction data and neutron powder diffraction data were refined against the same model adopted by the corresponding Ni analogue, a body-centred orthorhombic unit cell (space group *Immm*) for the reduced oxide phase $LaSr_3CoRuO_6$, and a body-centred tetragonal unit cell (space group *I*4/*mmm*) for the oxide-hydride phase $LaSr_3CoRuO_4H_4$, but both visual fit and statistical fit became worse. A small sample of the oxide-hydride phase $LaSr_3CoRuO_4H_4$ was send out for collecting Electron Diffraction (ED) patterns and the results do correspond to the *I*4/*mmm* space group. Further Transmission Electron Microscopy (TEM) Study suggests that the unsatisfactory refinements

of powder diffraction data collected from Co analogues against these two simple undistorted models can be attributed to the intergrowth of mainly the n = 2 Ruddlesden-Popper phase and the separate perovskite blocks (of height up to 4 perovskite unit cells), scattered as defects throughout the crystals. These intergrowth defects do have significant influences on peak shapes of powder diffraction patterns.

The presence of mainly the n = 2 Ruddlesden-Popper phase (a few n = 3 and n = 4 blocks were found as well) as intergrowth defects indicates that the n = 1 Ruddlesden-Popper phase $LaSr_3CoRuO_8$ is probably less stable than the Ni analogue, because this phenomena was not observed in $LaSr_3NiRuO_8$ and its reduced phases.

7.5 Conclusion

The n = 1 Ruddlesden-Popper phase $LaSr_3CoRuO_8$ has been prepared via a traditional high-temperature ceramic synthetic route from binary metal oxides and metal carbonates. Both synchrotron X-ray powder diffraction data and ambient temperature neutron powder diffraction data could be readily indexed by a simple body-centred tetragonal unit cell (space group *I4/mmm*) with lattice parameters a = 3.87488(4) Å, c = 12.6258(1) Å. The magnetisation data collected using a SQUID magnetometer show strong evidence of a canted antiferromagnetic ground state consisting of Co^{2+} and Ru^{5+} centres, with both spin states being $S = {}^{3}/_{2}$. The detailed cation arrangement of $LaSr_3CoRuO_8$ (whether it is a paracrystalline material or not) needs to be confirmed by Pair Distribution Function (PDF) analysis.

The topochemical reductions of $LaSr_3CoRuO_8$ have been investigated as well. Just like the Ni analogue, it undergoes reductive deintercalation of oxide ions and eventually yields a reduced oxide phase $LaSr_3CoRuO_6$ (space group *Immm*) by using Zr powder as an oxygen getter, while it undergoes hydride-for-oxide substitution and forms an oxide-hydride phase $LaSr_3CoRuO_4H_4$ (space group *I*4/*mmm*) if it is treated with CaH_2 in sealed ampoules. Both reduced phases adopt the same simple undistorted structural model as their corresponding Ni analogues, but their refinements have worse visual fit and statistical fit due to the intergrowth of mainly the $n = 2$ Ruddlesden-Popper phase and the separate perovskite blocks (of height up to 4 perovskite unit cells), scattered as defects throughout the crystals, which have not been observed in $LaSr_3NiRuO_8$ and its reduced phases.

Low temperature neutron powder diffraction data collected for both the reduced oxide phase $LaSr_3CoRuO_6$ and the oxide-hydride phase $LaSr_3CoRuO_4H_4$ show no additional magnetic diffraction features, suggesting the lack of long-range magnetic ordering in these phases, despite the magnetisation data collected by using a SQUID magnetometer show strong evidence of antiferromagnetic ground states for both reduced phases.

Chapter 8

Synthesis and Characterisation of Rh-Containing Oxide Phases

8.1 Introduction

As described in previous chapters and other work,[10, 11, 23] Ru^{2+} has been extensively studied and found in many extended transition metal oxides while treating their parent complex oxide phases with solid-state reducing agents. During the discovery of these materials, the presence of 3*d* transition-metals is found to be necessary to prevent non-topochemical decomposition of materials, by stabilizing topochemical reductions with especially stable 3*d* transition-metal-oxide lattices.

Analogous chemistry has been extended to another 4*d* transition-metal, rhodium, and Mn-oxide and Co-oxide lattices are chosen to couple with these reductions to prevent complete reduction of the rhodium to the elemental metal state. Thus two $n = 1$ Ruddlesden-Popper phases $LaSr_3MnRhO_8$ and $La_2Sr_2CoRhO_8$ are prepared for detailed characterisation. Their reduction behaviour towards CaH_2 has also been investigated as well, which is presented in the following Chapter 9.

8.2 Experimental

8.2.1 Synthesis of $LaSr_3MnRhO_8$

Samples of $LaSr_3MnRhO_8$ were prepared by a high-temperature ceramic method. Suitable stoichiometric ratios of La_2O_3 (99.999%, dried at 900 °C), $SrCO_3$ (99.994%), Rh_2O_3 (99.99%, dried at 800 °C) and MnO_2 (99.997%) were ground together using an agate mortar and pestle, transferred into an alumina crucible, and then heated at a rate of 1 $^oC\ min^{-1}$ to

1000 °C in air to decompose the carbonate. The sample was reground, pressed into pellets and then heated for 3 periods of 48 hours at 1300 °C in air, with grinding between heating periods. The reaction progress was monitored by laboratory X-ray diffractometer and the final pure phase achieved was examined by both synchrotron X-ray powder diffraction and neutron powder diffraction.

8.2.2 Synthesis of $La_2Sr_2CoRhO_8$

Samples of $La_2Sr_2CoRhO_8$ were prepared by a high-temperature ceramic method. Suitable stoichiometric ratios of La_2O_3 (99.999%, dried at 900 °C), $SrCO_3$ (99.994%), Rh_2O_3 (99.99%, dried at 800 °C) and Co_3O_4 (99.9985%) were ground together using an agate mortar and pestle, transferred into an alumina crucible, and then heated at a rate of 1 $^oC\ min^{-1}$ to 1000 °C in air to decompose the carbonate. The sample was reground, pressed into pellets and then heated for 3 periods of 48 hours at 1300 °C in a steady pure O_2 flow, with grinding between heating periods. If the partial pressure of O_2 is not high enough, i.e. heating in air, $LaCoO_3$ were formed irreversibly as the secondary phase impurities, which results in the failure of isolating pure phase of $La_2Sr_2CoRhO_8$. The reaction progress was monitored by laboratory X-ray diffractometer and the final pure phase achieved was examined by both synchrotron X-ray powder diffraction and neutron powder diffraction.

8.3 Results

8.3.1 Structural Characterisation of $LaSr_3MnRhO_8$

8.3.1.1 Synchrotron X-ray Powder Diffraction

Synchrotron X-ray powder diffraction data (Chapter 2 Section 2.5.1.2) was collected from a large-scale neutron sample of $LaSr_3MnRhO_8$. The data was indexed using a body-centred tetragonal unit cell (space group *I*4/*mmm*) with lattice parameters: a = 3.87453(2) Å and c = 12.4887(1) Å. A structural model was constructed, based on an n = 1, A_2BO_4 Ruddlesden-Popper phase with a 1:3 La:Sr solid-solution on the A-site, a 1:1 Mn:Rh solid-solution on the B-site. This model was refined against the synchrotron X-ray powder diffraction data collected at room temperature and the single-phase refinement (Figure 8.1) converged smoothly to give a good statistical fit (χ^2 = 36.45; *wRp* = 7.68%; *Rp* = 4.17%).

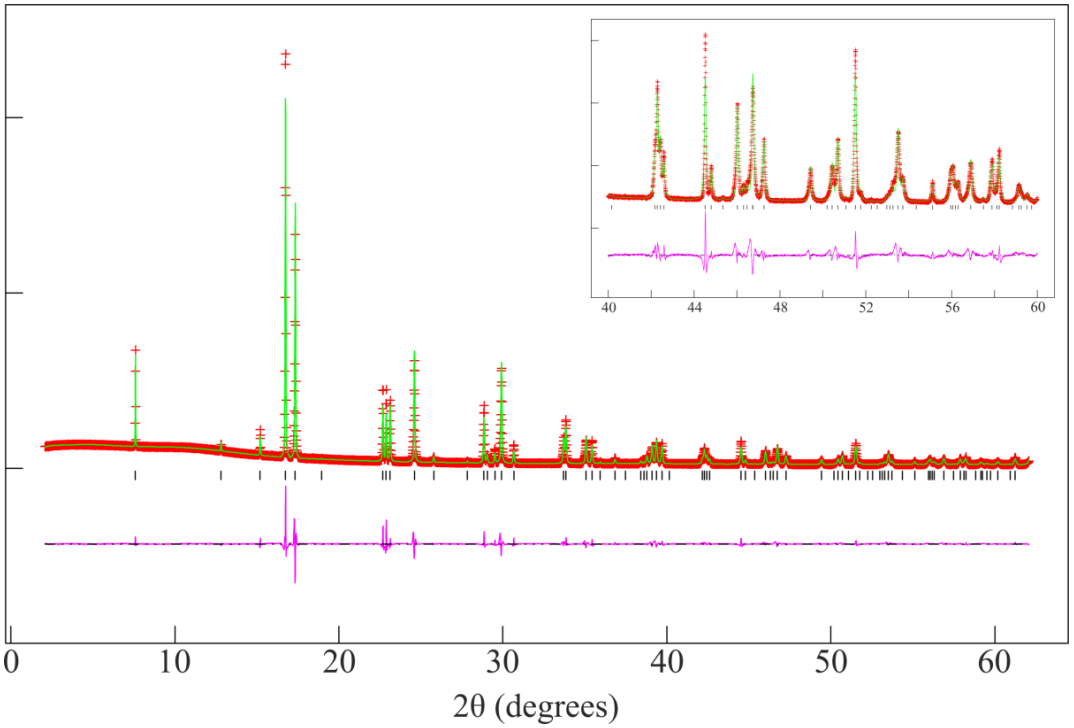


Figure 8.1. Observed, calculated and difference plots from the refinement of $LaSr_3MnRhO_8$ against synchrotron X-ray powder diffraction data collected at 298 K.

8.3.1.2 Neutron Powder Diffraction

Neutron powder diffraction measurements at ambient temperature and 5 K were carried out at D2B diffractometer in ILL (Chapter 2 Section 2.5.2.2). The body-centred tetragonal unit cell shown in Figure 8.2 (space group *I*4/*mmm*) was refined against the data. The refinements converged readily to give good statistical fits for both ambient temperature data and low temperature data. Observed, calculated, and difference plots are shown in Figure 8.3. Full details of the refined structural parameters are given in Table 8.1, anisotropic displacement factors are given in Table 8.2 and selected bond lengths are given in Table 8.3. There are no additional magnetic diffraction features at low temperature which indicates the absence of long-range magnetic ordering.

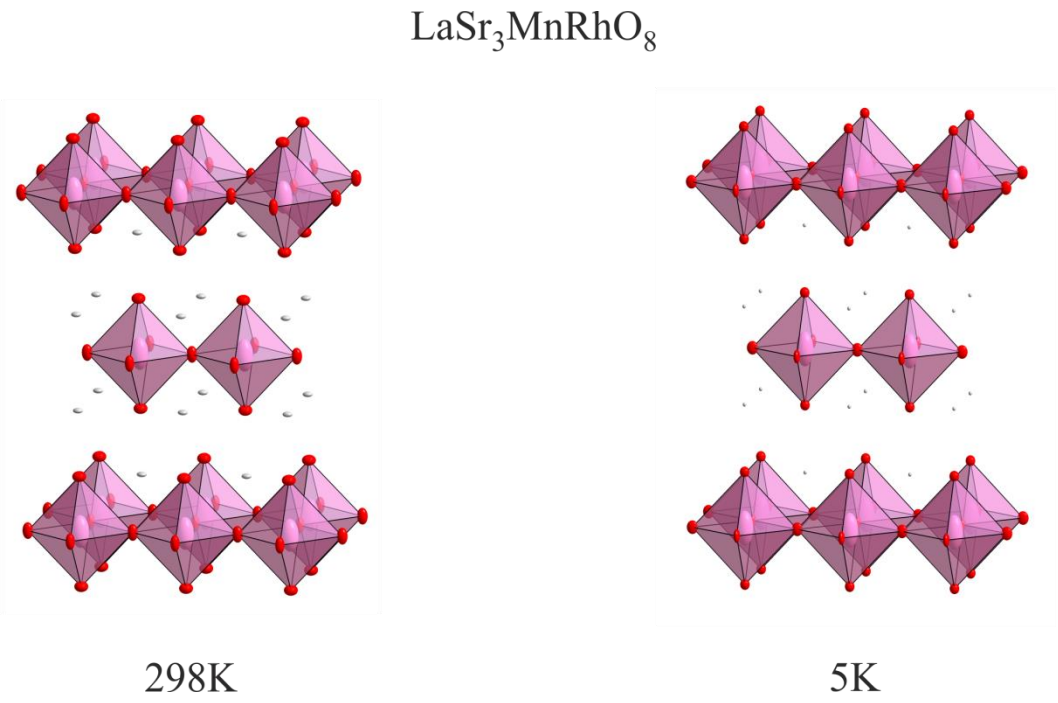


Figure 8.2. Crystal structures of $LaSr_3MnRhO_8$ with thermal ellipsoids displaced at 298K (left) and 5 K (right).

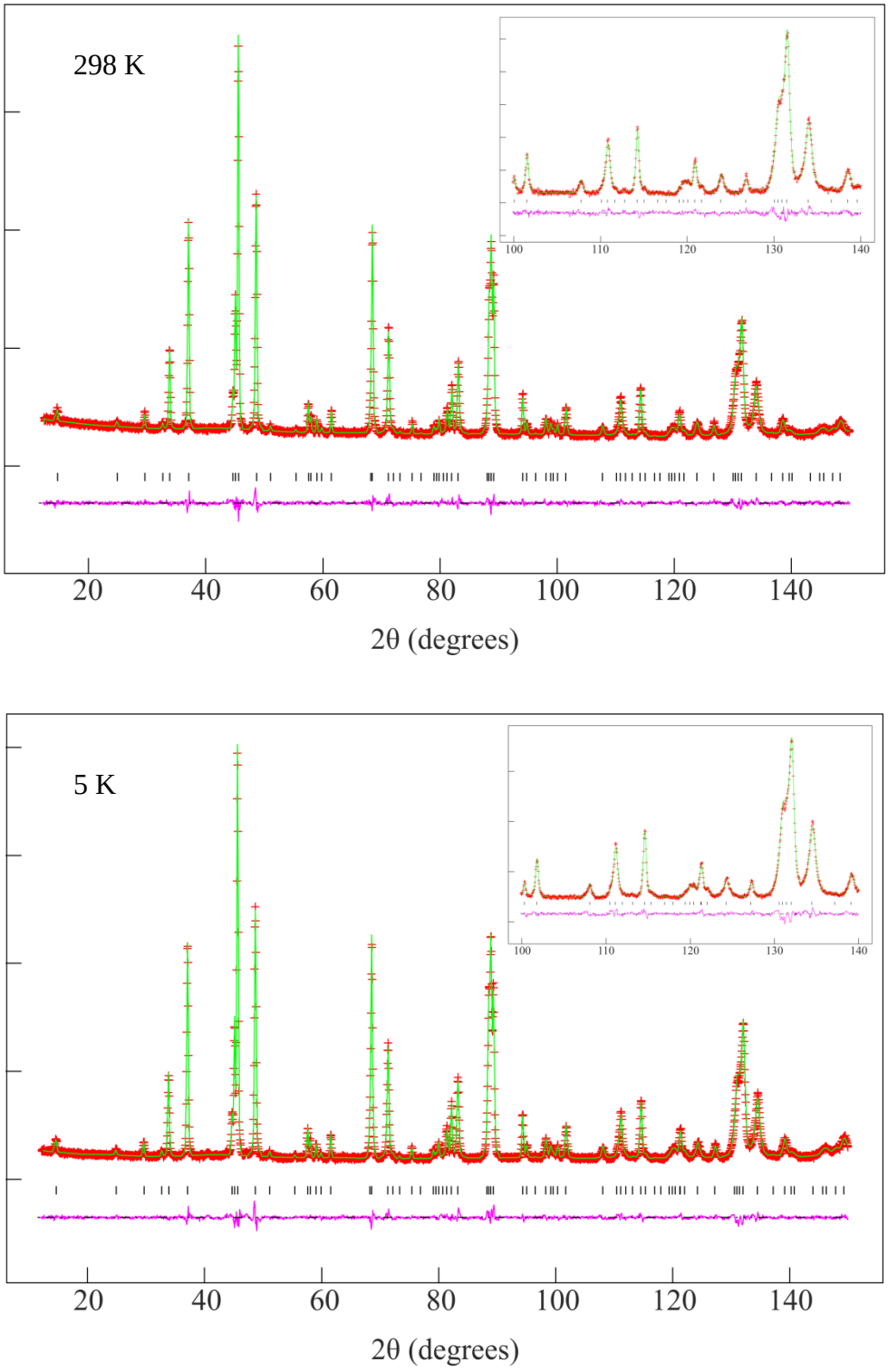


Figure 8.3. Observed, calculated and difference plots from the refinements of $LaSr_3MnRhO_8$ against neutron powder diffraction data collected at 298 K (top) and 5 K (bottom).

$LaSr_3MnRhO_8$ space group *I*4/*mmm* (#139) Formula weight : 687.62 g mol^{-1}, Z = 2 Radiation source: Neutron Powder Diffraction, λ = 1.5943(2)						
Atom	**Wyckoff Position**	***x***	***y***	***z***	**Fraction**	**U_{iso} equiv. ($Å^2$)**
La/Sr(1)	4*e*	0	0	0.35768(7)	0.25/0.75	0.0040
Mn/Rh(1)	2*a*	0	0	0	0.5/0.5	0.0280
O(1)	4*e*	0	0	0.16270(8)	1	0.0103
O(2)	4*c*	0.5	0	0	1	0.0102
Temperature: 298 K *a* = 3.87440(6) Å, *c* = 12.4868(2) Å, Volume = 187.440(9) $Å^3$ χ^2 = 1.949; *wRp* = 3.28%; *Rp* = 2.56%.						
Atom	**Wyckoff Position**	***x***	***y***	***z***	**Fraction**	**U_{iso} equiv. ($Å^2$)**
La/Sr(1)	4*e*	0	0	0.35789(6)	0.25/0.75	0.0007
Mn/Rh(1)	2*a*	0	0	0	0.5/0.5	0.0153
O(1)	4*e*	0	0	0.16259(8)	1	0.0072
O(2)	4*c*	0.5	0	0	1	0.0065
Temperature: 5 K *a* = 3.86609(7) Å, *c* = 12.4572(2) Å, Volume = 186.19(1) $Å^3$ χ^2 = 2.834; *wRp* = 4.21%; *Rp* = 3.28%.						

Table 8.1. Structural parameters from the refinements of $LaSr_3MnRhO_8$ against neutron powder diffraction data collected at 298 K (top) and 5 K (bottom).

Atom	U_{11}	U_{22}	U_{33}
La/Sr(1)	0.00451(40)	0.00451(40)	0.00284(45)
Mn/Rh(1)	0.01305(46)	0.01305(46)	0.05786(88)
O(1)	0.01172(54)	0.01172(54)	0.00741(75)
O(2)	0.01005(82)	0.00694(82)	0.01348(71)
Temperature: 298 K			
Atom	U_{11}	U_{22}	U_{33}
La/Sr(1)	0.00081(37)	0.00081(37)	0.00053(44)
Mn/Rh(1)	0.0040(27)	0.0040(27)	0.0376(59)
O(1)	0.00815(49)	0.00815(49)	0.00530(72)
O(2)	0.00542(76)	0.00491(74)	0.00919(68)
Temperature: 5 K			

Table 8.2. Anisotropic displacement factors from refinements of $LaSr_3MnRhO_8$ against neutron powder diffraction data collected at 298 K (top) and 5 K (bottom).

Temperature: 298 K			**Temperature: 5 K**		
Cation	**Anion**	**length (Å)**	**Cation**	**Anion**	**length (Å)**
La/Sr(1)	O(1)	2.435(1) × 1	**La/Sr(1)**	O(1)	2.433(1) × 1
	O(1)	2.751(1) × 4		O(1)	2.746(1) × 4
	O(2)	2.629(1) × 4		O(2)	2.621(1) × 4
Mn/Rh(1)	O(1)	2.032(1) × 2	**Mn/Rh(1)**	O(1)	2.025(1) × 2
	O(2)	1.937(1) × 4		O(2)	1.933(1) × 4

Table 8.3. Selected bond lengths from the refined structure of $LaSr_3MnRhO_8$ at 298 K (left) and 5 K (right).

8.3.2 Structural Characterisation of $La_2Sr_2CoRhO_8$

8.3.2.1 Synchrotron X-ray Powder Diffraction

Synchrotron X-ray powder diffraction data (Chapter 2 Section 2.5.1.2) was collected from a large-scale neutron sample of $La_2Sr_2CoRhO_8$. The data was indexed using a body-centred tetragonal unit cell (space group *I*4/*mmm*) with lattice parameters: a = 3.87948(1) Å and c = 12.51904(6) Å. A structural model was constructed, based on an n = 1, A_2BO_4 Ruddlesden-Popper phase with a 1:1 La:Sr solid-solution on the A-site, a 1:1 Co:Rh solid-solution on the B-site. This model was refined against the synchrotron X-ray powder diffraction data collected at room temperature and the single-phase refinement (Figure 8.4) converged smoothly to give a good statistical fit (χ^2 = 72.71; *wRp* = 5.32%; *Rp* = 2.88%).

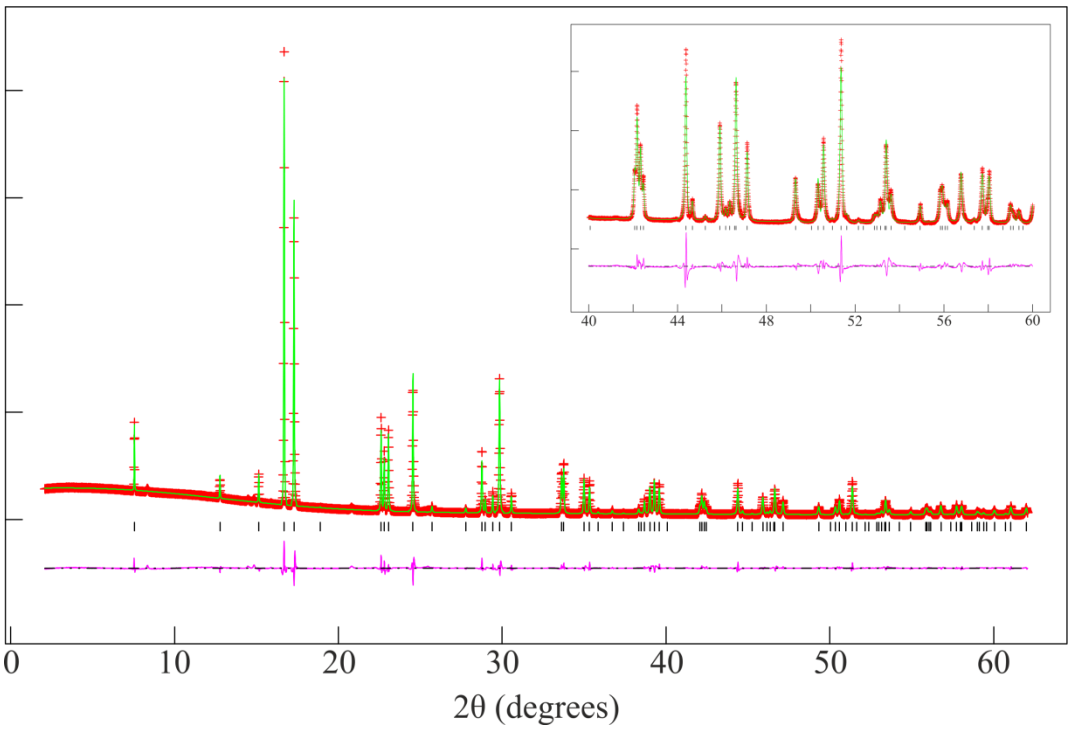


Figure 8.4. Observed, calculated and difference plots from the refinement of $La_2Sr_2CoRhO_8$ against synchrotron X-ray powder diffraction data collected at 298 K.

8.3.2.2 Neutron Powder Diffraction

Neutron powder diffraction measurements at ambient temperature and 5 K were carried out at D2B diffractometer in ILL (Chapter 2 Section 2.5.2.2). The body-centred tetragonal unit cell shown in Figure 8.5 (space group *I*4/*mmm*) was used to refine the data. The refinements converged readily to give good statistical fits for both ambient temperature data and low temperature data. The observed, calculated, and difference plots are shown in Figure 8.6. Full details of the refined structural parameters are given in Table 8.4, anisotropic displacement factors are given in Table 8.5 and selected bond lengths are given in Table 8.6. There are no additional magnetic diffraction features at low temperature which indicates the absence of long-range magnetic ordering.

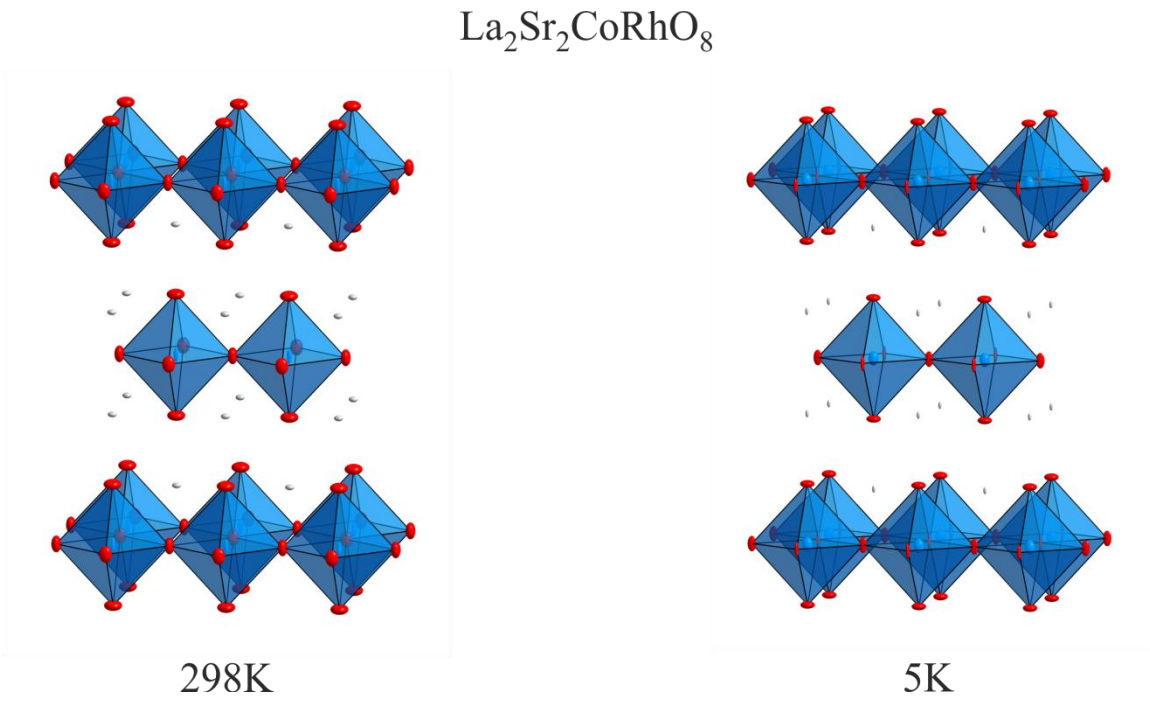


Figure 8.5. Crystal structures of $La_2Sr_2CoRhO_8$ with thermal ellipsoids displaced at 298 K (left) and 5 K (right).

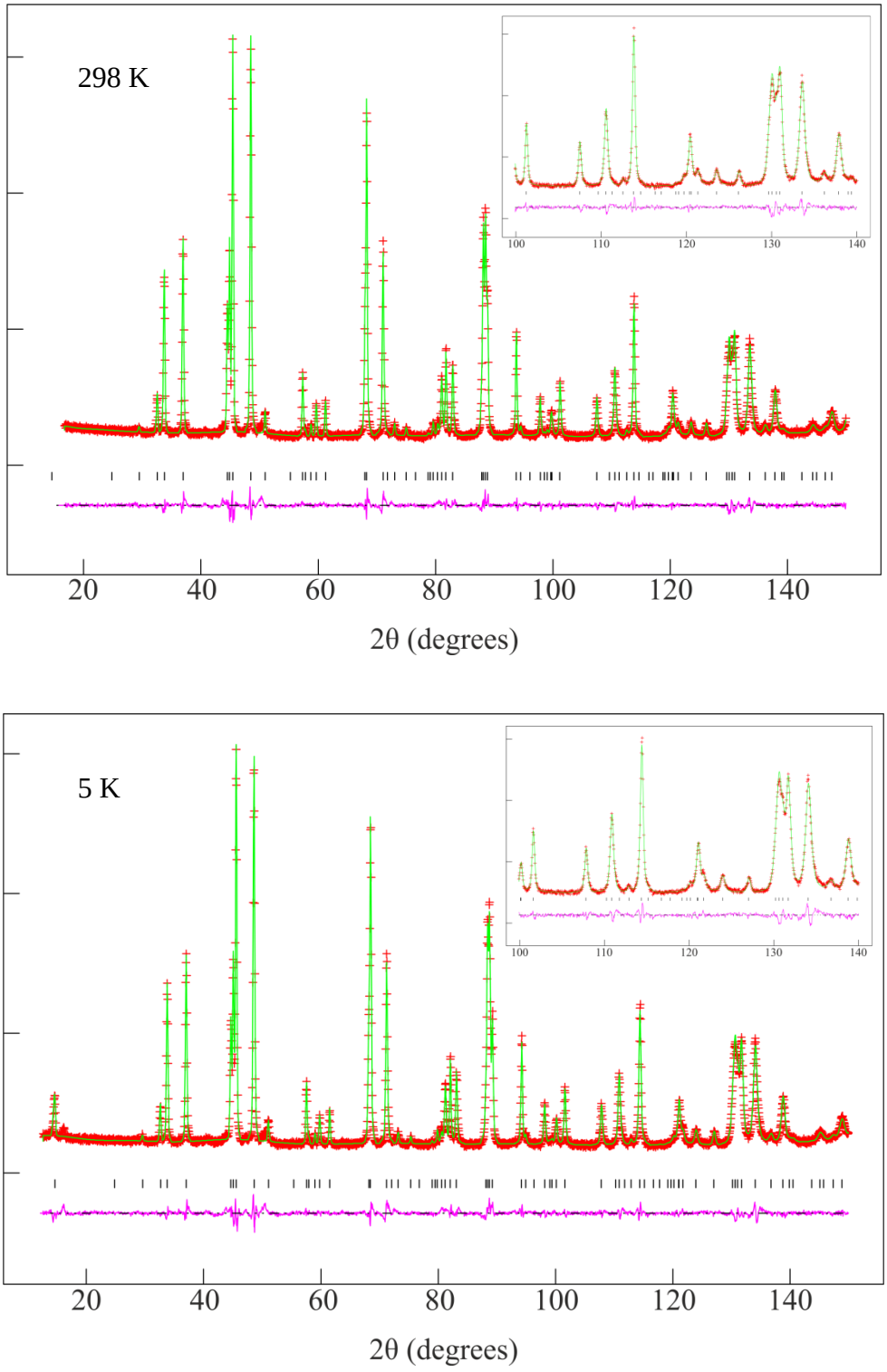


Figure 8.6. Observed, calculated and difference plots from the refinements of $La_2Sr_2CoRhO_8$ against neutron powder diffraction data collected at 298 K (top) and 5 K (bottom).

$La_2Sr_2CoRhO_8$ space group *I*4/*mmm* (#139) Formula weight : 742.90 g mol^{-1}, Z = 2 Radiation source: Neutron Powder Diffraction, λ = 1.5943(2)						
Atom	**Wyckoff Position**	***x***	***y***	***z***	**Fraction**	**U_{iso} equiv. ($Å^2$)**
La/Sr(1)	4*e*	0	0	0.35950(7)	0.5/0.5	0.0048
Co/Rh(1)	2*a*	0	0	0	0.5/0.5	0.0037
O(1)	4*e*	0	0	0.1668(1)	1	0.0134
O(2)	4*c*	0.5	0	0	1	0.0105
Temperature: 298 K *a* = 3.87942(6) Å, *c* = 12.5182(2) Å, Volume = 188.39(1) $Å^3$ χ^2 = 2.799; *wRp* = 4.15%; *Rp* = 3.21%.						
Atom	**Wyckoff Position**	***x***	***y***	***z***	**Fraction**	**U_{iso} equiv. ($Å^2$)**
La/Sr(1)	4*e*	0	0	0.35946(8)	0.5/0.5	0.0019
Co/Rh(1)	2*a*	0	0	0	0.5/0.5	0.0013
O(1)	4*e*	0	0	0.1665(1)	1	0.0090
O(2)	4*c*	0.5	0	0	1	0.0070
Temperature: 5 K *a* = 3.87204(6) Å, *c* = 12.4683(2) Å, Volume = 186.935(9) $Å^3$ χ^2 = 3.552; *wRp* = 4.68%; *Rp* = 3.65%.						

Table 8.4. Structural parameters from the refinements of $La_2Sr_2CoRhO_8$ against neutron powder diffraction data collected at 298 K (top) and 5 K (bottom).

Atom	U_{11}	U_{22}	U_{33}
La/Sr(1)	0.00584(33)	0.00584(33)	0.00260(41)
Co/Rh(1)	0.00077(13)	0.00077(13)	0.00964(20)
O(1)	0.01703(44)	0.01703(44)	0.00629(78)
O(2)	0.00916(68)	0.00730(67)	0.01496(85)
Temperature: 298 K			
Atom	U_{11}	U_{22}	U_{33}
La/Sr(1)	0.00248(38)	0.00248(38)	0.00086(48)
Co/Rh(1)	0.00015(89)	0.00015(89)	0.0037(14)
O(1)	0.001123(48)	0.001123(48)	0.00458(88)
O(2)	0.00377(79)	0.00588(75)	0.01141(91)
Temperature: 5 K			

Table 8.5. Anisotropic displacement factors from refinements of $La_2Sr_2CoRhO_8$ against neutron powder diffraction data collected at 298 K (top) and 5 K (bottom).

Temperature: 298 K			**Temperature: 5 K**		
Cation	**Anion**	**length (Å)**	**Cation**	**Anion**	**length (Å)**
La/Sr(1)	O(1)	2.412(2) × 1	**La/Sr(1)**	O(1)	2.406(2) × 1
	O(1)	2.763(1) × 4		O(1)	2.757(1) × 4
	O(2)	2.618(1) × 4		O(2)	2.611(1) × 4
Co/Rh(1)	O(1)	2.088(1) × 2	**Co/Rh(1)**	O(1)	2.076(1) × 2
	O(2)	1.940(1) × 4		O(2)	1.936(1) × 4

Table 8.6. Selected bond lengths from the refined structure of $La_2Sr_2CoRhO_8$ at 298 K (left) and 5 K (right).

8.3.3 Magnetic Characterisation of $LaSr_3MnRhO_8$

Zero-field-cooled and field-cooled magnetization data collected from $LaSr_3MnRhO_8$ as a function of temperature in an applied field of 100 Oe using a SQUID magnetometer (Chapter 2 Section 2.10), are shown in Figure 8.7 (top). Isothermal magnetisation data were also collected as a function of applied field for both T = 300 K and 5 K (Figure 8.7 (bottom)).

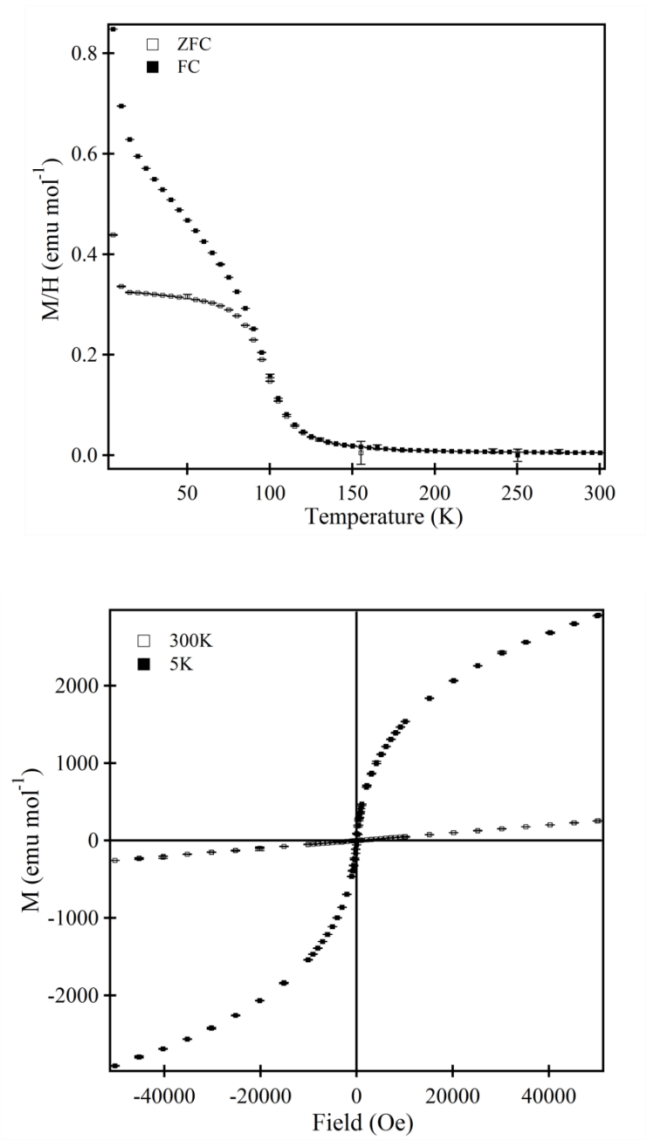


Figure 8.7. Zero-field-cooled and field-cooled magnetisation data (top); 300 K and 5 K magnetisation-field isotherms (bottom) of $La_{0.5}Sr_{1.5}Mn_{0.5}Rh_{0.5}O_4$.

Magnetization data collected at 300 K as a function of applied field is linear and passes through the origin. Analogous data collected at 5 K after cooling in an applied field of 5T

does not exhibit hysteresis. The zero-field-cooled and field-cooled data collected diverge below T = 120 K, consistent with the onset of canted antiferromagnetic order.

All the magnetisation data is scaled to the formula $La_{0.5}Sr_{1.5}Mn_{0.5}Rh_{0.5}O_4$ for further analysis. A plot of H/M against temperature (Figure 8.8) reveals two linear regions with ranges 125 < T / K < 200 and 210 < T / K < 300. Data in both regions are fitted to the Curie-Weiss law ($\chi = C/(T - \theta)$) independently (fitting statistics R = 0.99994 and 0.99968, respectively), with two values of the Curie constant, C, and Weiss temperature, θ, to be calculated, as shown in Figure 8.8 (top).

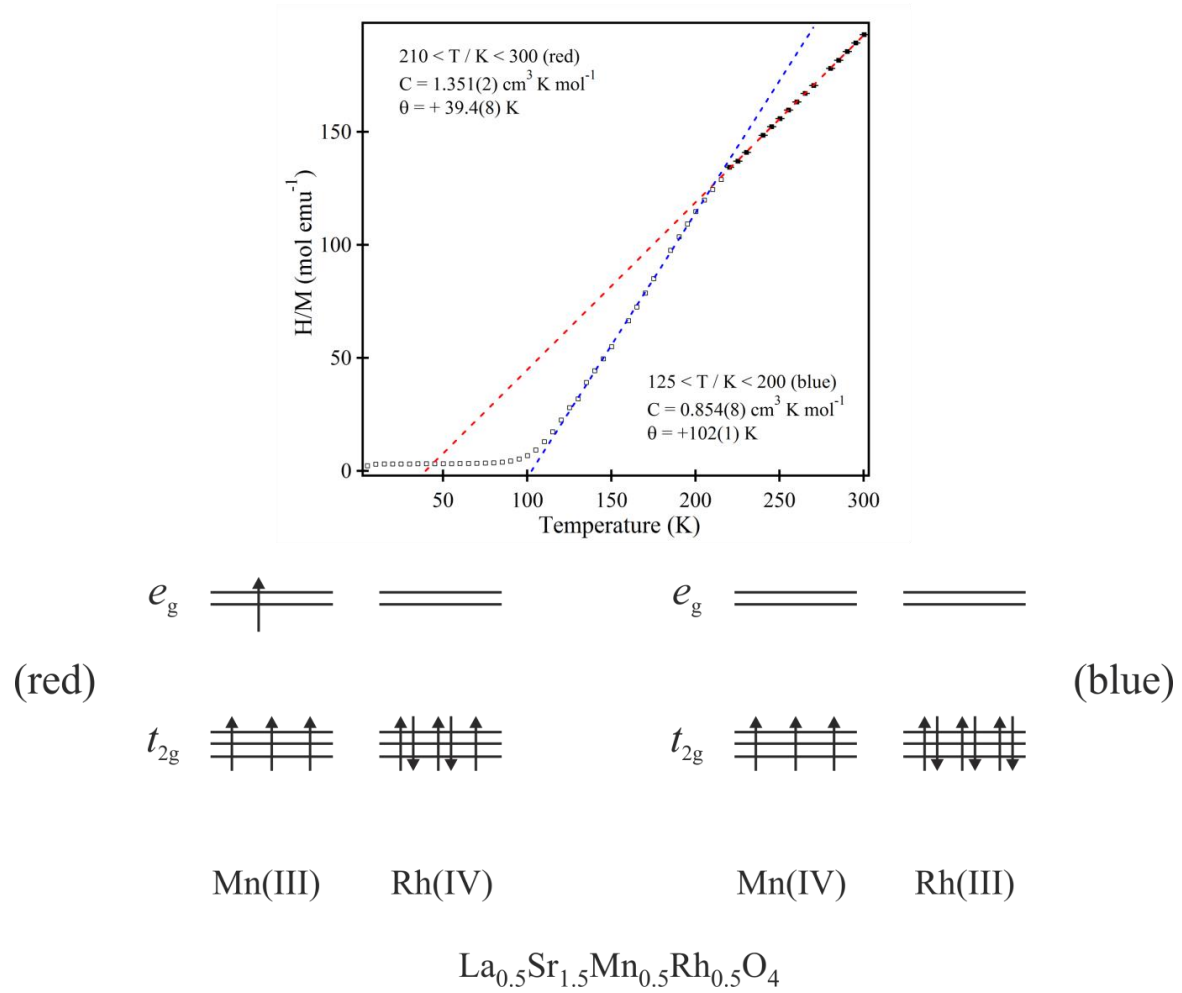


Figure 8.8. The plot of H/M against temperature with data in temperature ranges 210 < T / K < 300 and 125 < T / K < 200 fitted to the Curie-Weiss law ($\chi = C/(T - \theta)$) and proposed electronic configurations of $La_{0.5}Sr_{1.5}Mn_{0.5}Rh_{0.5}O_4$, respectively.

The data in the temperature range 125 < T / K < 200 can be fitted to the Curie-Weiss law ($\chi = C/(T - \theta)$) to yield values of C = 0.854(8) cm^3 K mol^{-1}, θ = + 102(1) K, hence a value of μ^2 to be 6.832 μ_B can be calculated. According to the proposed electronic configuration shown in Figure 8.8 (bottom right), the observed moment corresponds to approximately 91.1% of the expected moment for a half high-spin d^3 Mn^{4+} centre plus a half low-spin d^6 Rh^{3+} centre per formula unit ($\mu^2_{expected} = 7.5\ \mu_B$).

When the sample is warmed up above T = 200 K, i.e. after the valence transition, the gradient of the fitted straight line (red line in Figure 8.8) becomes smaller, which corresponds to an increase in the Curie constant (more unpaired electrons). A hypothesis is raised that one of the paired up electrons in the t_{2g} orbitals of Rh^{3+} has hopped into the empty e_g orbitals of Mn^{4+}, resulting a mixture of Mn^{3+}/ Rh^{4+} and Mn^{4+}/ Rh^{3+} centres. By doing this, the system is more stabilized as a consequence of gaining strain energy back, because Mn^{3+} is larger than Mn^{4+} and better match the size of the Rh centre it is mixed with. This hypothesis is supported by fitting the data in the temperature range 210 < T / K < 300 to the Curie-Weiss law ($\chi = C/(T - \theta)$) to yield values of C = 1.351(2) cm^3 K mol^{-1}, θ = + 39.4(8) K, hence a value of μ^2 to be 10.808 μ_B can be calculated. According to the proposed electronic configuration shown in Figure 8.8 (bottom left), the observed moment is clearly too small to be purely Mn^{4+}/ Rh^{3+} as it only equals to 80.1% of the expected moment for a half high-spin d^4 Mn^{3+} centre plus a half low-spin d^5 Rh^{4+} centre per formula unit ($\mu^2_{expected} = 13.5\ \mu_B$), but it could correspond to a mixture of Mn^{3+}/ Rh^{4+} and Mn^{4+}/ Rh^{3+} centres as the value of 10.808 μ_B falls into the range of $7.5 < \mu^2_{observed} / \mu_B < 13.5$.

Despite the magnetisation data collected using a SQUID magnetometer showing strong evidence for a canted antiferromagnetic ground state, the neutron data set collected at 5 K only shows the loss of paramagnetic scattering as reflected in the slight lowering background at low angles by comparing to the data set collected at ambient temperature (Figure 8.9). Apart from that, it does not contain any visible extra peaks, except those belong to the crystallographic structure.

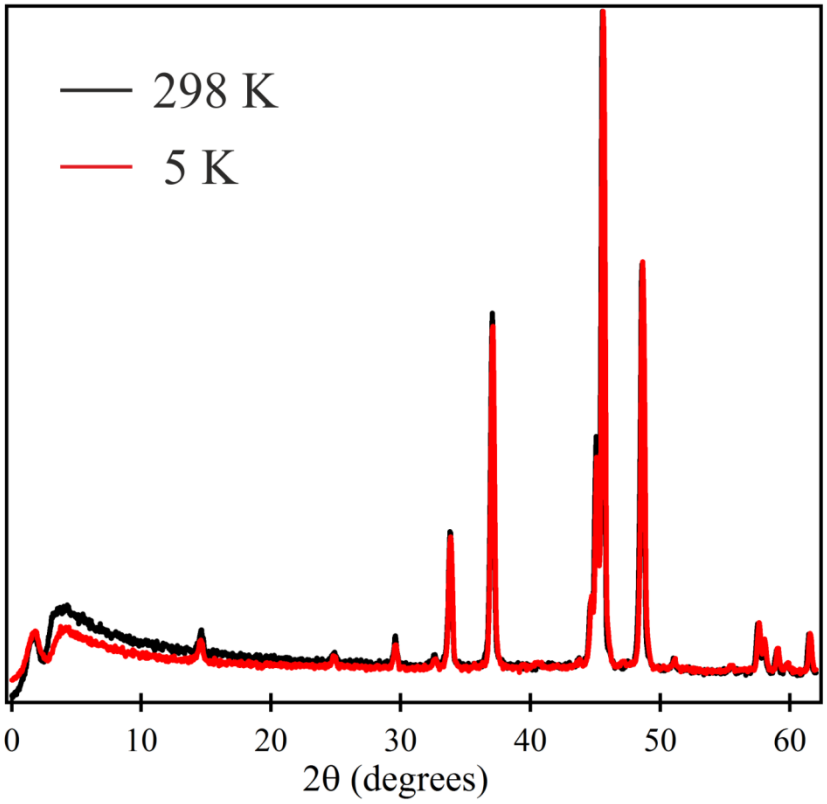


Figure 8.9. Comparing low-angle neutron powder diffraction data collected from $LaSr_3MnRhO_8$ at 298 K and 5 K.

8.3.4 Magnetic Characterisation of $La_2Sr_2CoRhO_8$

Zero-field-cooled and field-cooled magnetization data collected from $La_2Sr_2CoRhO_8$ as a function of temperature in an applied field of 100 Oe using a SQUID magnetometer (Chapter 2 Section 2.10), are shown in Figure 8.10 (top). Isothermal magnetisation data were also collected as a function of applied field for both T = 300K and 5K (Figure 8.10 (bottom)).

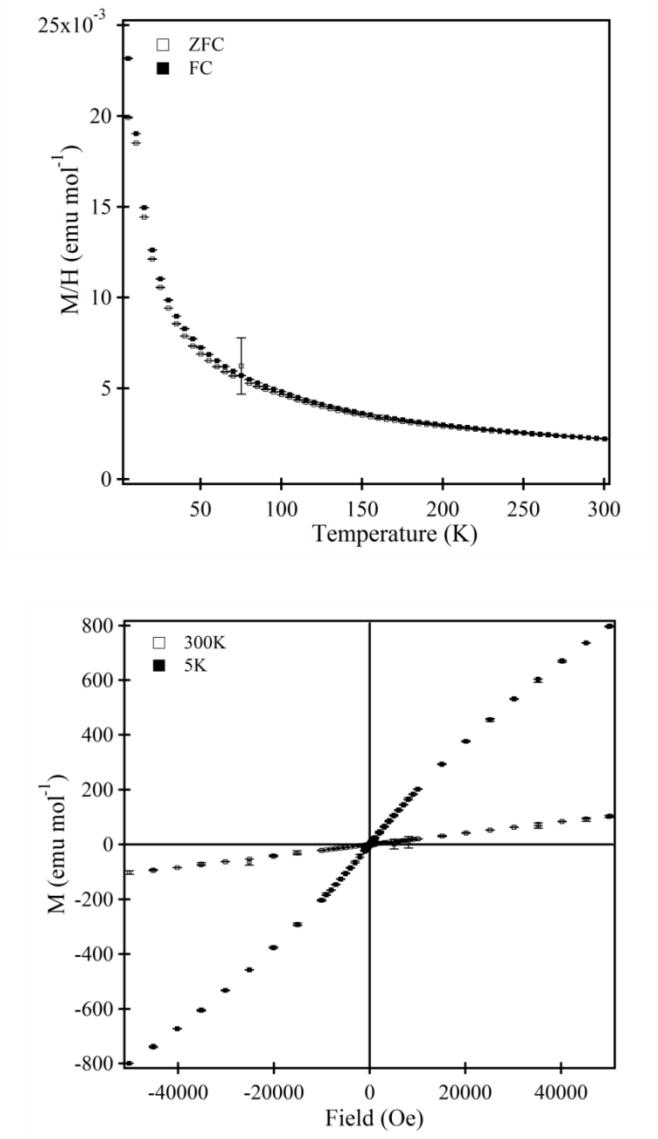


Figure 8.10. Zero-field-cooled and field-cooled magnetisation data (top); 300 K and 5 K magnetisation-field isotherms (bottom) of $LaSrCo_{0.5}Rh_{0.5}O_4$.

Magnetization data collected at 300 K as a function of applied field is linear and passes through the origin. Analogous data collected at 5 K after cooling in an applied field of 5T

does not exhibit hysteresis. The zero-field-cooled and field-cooled data collected diverge below T = 240 K, consistent with the onset of canted antiferromagnetic order.

All the magnetisation data is scaled to the formula $LaSrCo_{0.5}Rh_{0.5}O_4$ for further analysis. A plot of H/M against temperature (Figure 8.11) reveals two linear regions with ranges 65 < T / K < 185 and 200 < T / K < 300. Data in both regions are fitted to the Curie-Weiss law ($\chi = C/(T - \theta)$) independently (fitting statistics R = 0.99959 and 0.99970, respectively), with two values of the Curie constant, C, and Weiss temperature, θ, to be calculated, as shown in Figure 8.11 (top).

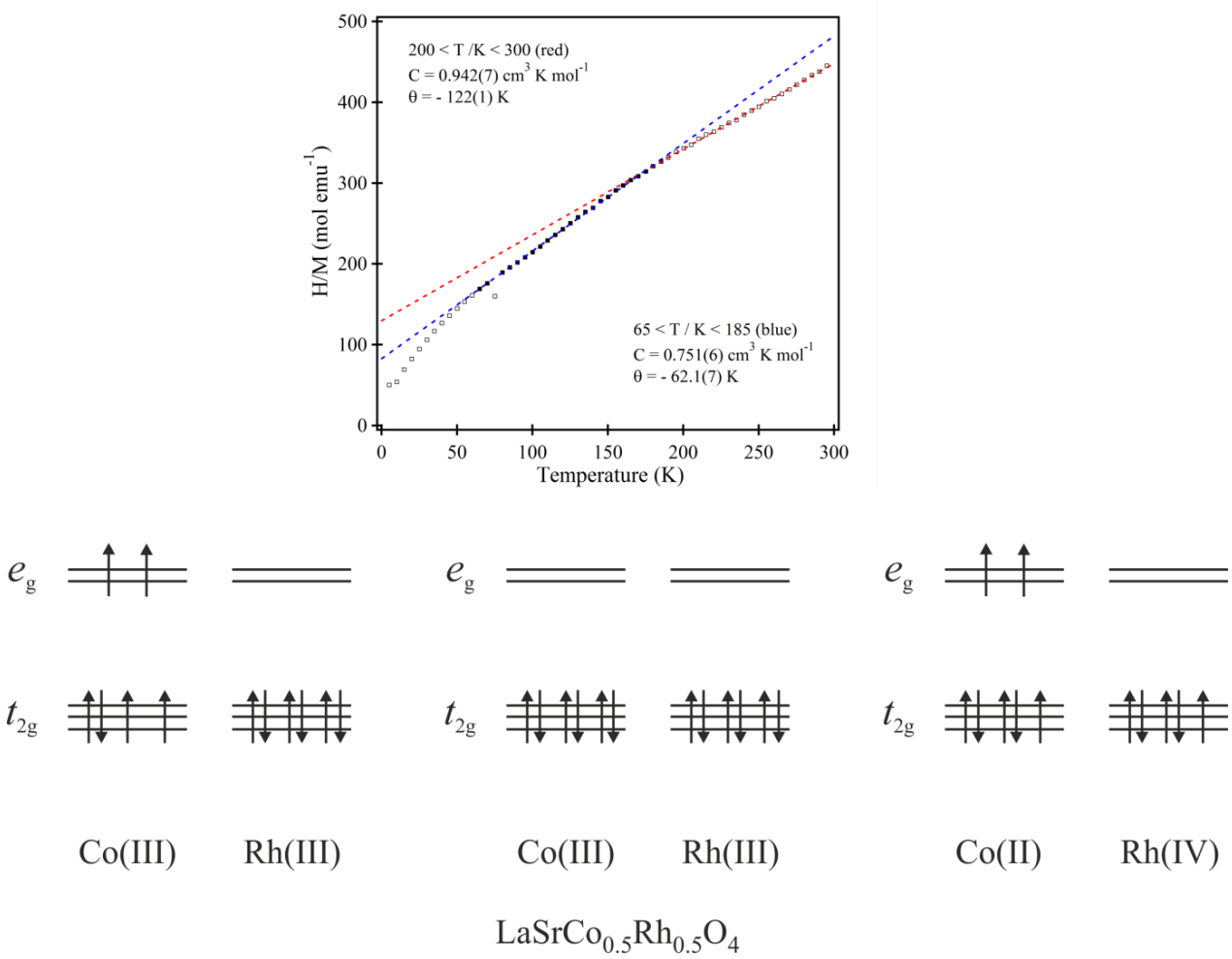


Figure 8.11. The plot of H/M against temperature with data in temperature ranges 200 < T / K < 300 and 65 < T / K < 185 fitted to the Curie-Weiss law ($\chi = C/(T - \theta)$) and proposed electronic configurations of $LaSrCo_{0.5}Rh_{0.5}O_4$, respectively.

The data in the temperature range 65 < T / K < 185 can be fitted to the Curie-Weiss law ($\chi = C/(T - \theta)$) to yield values of C = 0.751(6) cm^3 K mol^{-1}, θ = - 62.1(7) K, hence a value of μ^2 to be 6.008 μ_B can be calculated. According to the proposed electronic configurations shown in Figure 8.11, the first high-spin d^6 Co^{3+}/ low-spin d^6 Rh^{3+} combination yields a value of μ^2 to be 12.0 μ_B and the second low-spin d^6 Co^{3+}/Rh^{3+} yields a value of μ^2 to be 0.0 μ_B, therefore the observed moment (6.008 μ_B) could correspond to a 50:50 mixture of high-spin d^6 and low-spin d^6 Co^{3+} plus low-spin d^6 Rh^{3+} per formula unit ($\mu^2_{expected}$ = 6.0 μ_B). The mixing of high-spin and low-spin states of Co^{3+} with Rh^{3+} presented in the system has been reported before in perovskites as well.[101-103]

Although the changing in gradients of fitted straight lines is quite subtle in this case, the data in the temperature range 200 < T / K < 300 can still be fitted separately to the Curie-Weiss law ($\chi = C/(T - \theta)$), to yield different values of C = 0.942(7) cm^3 K mol^{-1}, θ = - 122(1) K, hence a value of μ^2 to be 7.536 μ_B can be calculated. Therefore a valence transition might occur here as well when the sample is warmed up, by hopping one of the paired up t_{2g} electrons of Rh^{3+} to the t_{2g} orbitals of high-spin Co^{3+}, hence resulting a mixture of Co^{3+}/Rh^{3+} and Co^{2+}/Rh^{4+} centres. A 'pure' combination of high-spin d^7 Co^{2+} and low-spin d^5 Rh^{4+}, as shown in the bottom right of Figure 8.11, should give an expected moment of 9.0 μ_B, therefore the observed moment (7.536 μ_B) supported the hypothesis as it falls into the range of $6.0 < \mu^2_{observed} / \mu_B < 9.0$.

Despite the magnetisation data collected using a SQUID magnetometer showing strong evidence for a canted antiferromagnetic ground state, the neutron data set collected at 5 K only shows the loss of paramagnetic scattering as reflected in the slight lowering background at low angles by comparing to the data set collected at ambient temperature (Figure 8.12). Apart from that, it does not contain any visible extra peaks, except those belong to the crystallographic structure.

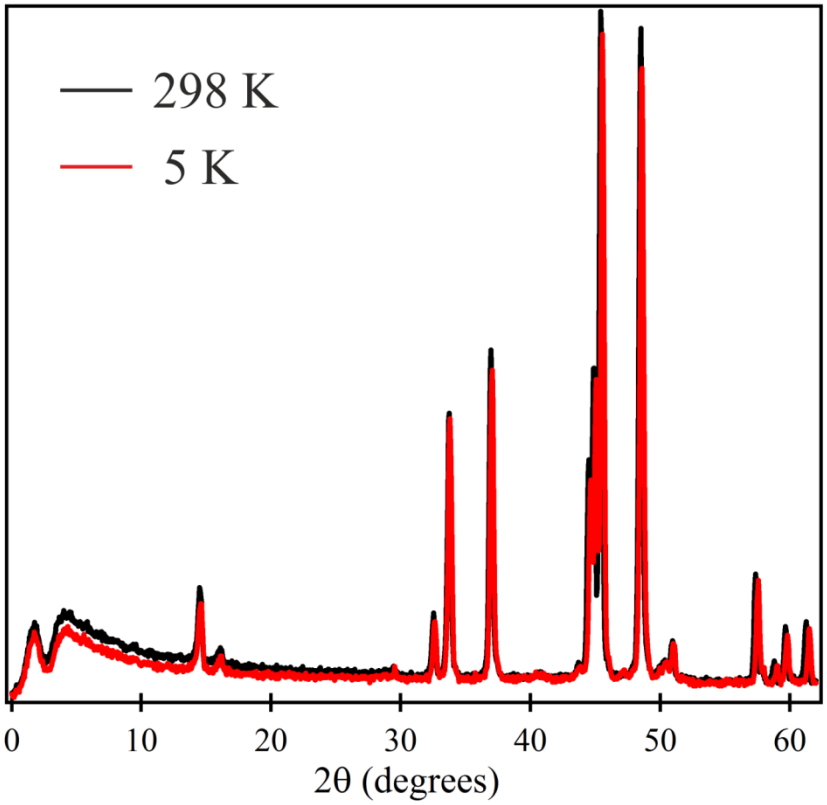


Figure 8.12. Comparing low-angle neutron powder diffraction data collected from $La_2Sr_2CoRhO_8$ at 298 K and 5 K.

8.4 Discussion

8.4.1 Cation Arrangement in Rh-containing *n* = 1 Ruddlesden-Popper Phases

Unlike Ru-containing *n* = 1 Ruddlesden-Popper Phases previously discussed in Chapter 3-7, which have great tendency to be B-site cation ordered as a result of the large charge difference between Ni/Co and Ru centres, in all the Rh-containing cases, these phases tend to be cation-disordered as the charge difference or size difference is too small.

From diffraction point of view (both synchrotron X-ray powder diffraction and neutron powder diffraction), there are no extra peaks which cannot be described by the simple body-centred tetragonal unit cell mentioned in Section 8.3.1 and 8.3.2, support the idea of cation-disordering in these phases. However, unlike the cation-disordered Fe/Ru series, $Sr(Fe_{0.5}Ru_{0.5})O_3$, $Sr_2(Fe_{0.5}Ru_{0.5})O_4$ and $Sr_3(Fe_{0.5}Ru_{0.5})_2O_7$, all showing indications for magnetic frustration or spin-glass behaviour, which are quite common with high levels of chemical and structural disorder, as a result of wide range of competing magnetic interactions, neither $LaSr_3MnRhO_8$ nor $La_2Sr_2CoRhO_8$ have obvious displacement around the origin observed in the isothermal magnetisation data collected using a SQUID magnetometer.

There are a series of perovskites $A_nB_nO_{3n}$ and Ruddlesden-Popper Phases $A_{n+1}B_nO_{3n+1}$ reported in literature, where six-coordinated B sites are occupied by a disordered distribution of first-row transition metals (Cr, Mn, Fe, Co, Ni and Cu) and rhodium cations.[101, 104-108] Therefore it is not surprising that for both Rh-containing *n* = 1 Ruddlesden-Popper Phases discussed in this chapter, $LaSr_3MnRhO_8$ and $La_2Sr_2CoRhO_8$, Mn/Co and Rh cations are disordered over the six-coordinated B sites within the perovskite layers of the structure.

The disordered distribution of Mn/Co and Rh cations across the lattice may be the reason to cause the absence of long-range magnetic ordering in these phases, as reflected by the lack of additional magnetic diffraction peaks in the neutron data set collected at 5 K.

8.4.2 Valence Transitions in Rh-containing *n* = 1 Ruddlesden-Popper Phases

The oxidation states remain ambiguous for the first-row transition metals M (Cr, Mn, Fe, Co, Ni and Cu) and rhodium cations in reported Rh-containing complex metal oxide phases as many phases show μ_{eff} value which sit in between M^{3+}/Rh^{3+} and M^{2+}/Rh^{4+} as summarized in A.E. Smith *et al.* [105]. Therefore the low-spin d^6 Rh^{3+} is not as non-negotiable as we think, as proved by Nakamura *et al*. that even though Rh^{3+} takes up the 'closed shell' configuration, the susceptibility of $LaRhO_3$ is not quite zero.[109]

In the $LaSr_3MnRhO_8$ case, the changing in gradients of fitted straight lines is quite sharp and obvious when two regions of data ($125 < T / K < 200$ and $210 < T / K < 300$) are fitted to the Curie-Weiss law ($\chi = C/(T - \theta)$) respectively. The observed moments extracted from these two separate fittings reveal that there might be a valence transition happening around the transition temperature T = 200 K, where a 'pure' combination of Mn^{4+}/ Rh^{3+} centres is converted into a mixture of Mn^{3+}/ Rh^{4+} and Mn^{4+}/ Rh^{3+} centres as a result of part of Mn^{4+} cations are reduced to Mn^{3+} by Rh cations. This assumption is supported by the observed magnetic moments μ^2 since they nearly agree with the derived values from the spin-only formula of these combinations. The coexistence of Mn^{3+}/ Rh^{4+} and Mn^{4+}/ Rh^{3+} centres has been reported before in $LaMn_{1-x}Rh_xO_3$ solid solution by Md. Tahidul Haque *et al.*[106] so it is not surprising that it occurs in the equivalent *n* = 1 Ruddlesden-Popper Phase $LaSr_3MnRhO_8$ as well.

The changing in gradients of fitted straight lines is much more subtle in the $La_2Sr_2CoRhO_8$ case, compared to the Mn analogue, but the situation is much more complicated as it involves not only mixed valences, but also mixed spin states for Co and Rh centres. At lower temperature regime, i.e. 65 < T / K < 185, the observed moment extracted from experimental data suggest a 50:50 mixture of high-spin d^6 and low-spin d^6 Co^{3+} plus low-spin d^6 Rh^{3+} per formula unit. The mixing of high-spin d^6 and low-spin d^6 Co^{3+} in the presence of Rh cations has been reported before in $LaCo_{1-x}Rh_xO_3$ solid solution by H. Guo *et al.*[103], therefore it is not surprising that it occurs in the equivalent n = 1 Ruddlesden-Popper Phase $La_2Sr_2CoRhO_8$ as well. When the sample is warmed up, i.e. 200 < T / K < 300, a different value of observed moment is extracted from experimental data, which nearly agree with the derived values from the spin-only formula, if half of the Co^{3+}/ Rh^{3+} centres is converted into Co^{2+}/ Rh^{4+} centres. The valence transition ('redox reaction') between Co^{3+}/ Rh^{3+} centres and Co^{2+}/ Rh^{4+} centres has been previously proposed and examined by Sergey V Streltsov *et al.* by carrying out unbiased *ab initio* calculations of the system and they suggest that this valence transition could reasonably explain the observed behaviour of the magnetic susceptibility of $LaCo_{1-x}Rh_xO_3$.[110] Therefore, in the equivalent n = 1 Ruddlesden-Popper Phase $La_2Sr_2CoRhO_8$, the complexity of explaining the magnetisation data collected could be attributed to mixed valences and spin states for Co and Rh centres as well.

8.5 Conclusion

Two n = 1 Ruddlesden-Popper phases $LaSr_3MnRhO_8$ and $La_2Sr_2CoRhO_8$ have been prepared via a traditional high-temperature ceramic synthetic route from binary metal oxides and metal carbonates. Both synchrotron X-ray powder diffraction data and ambient temperature neutron powder diffraction data could be readily indexed by simple body-centred tetragonal unit cells (space group *I*4/*mmm*) with lattice parameters a = 3.87440(6) Å, c = 12.4868(2) Å ($LaSr_3MnRhO_8$) and a = 3.87942(6) Å, c = 12.5182(2) Å ($La_2Sr_2CoRhO_8$), respectively. There are no phase transitions or cation-ordering within the temperature range we have explored so far, BO_6 octahedra remain undistorted and the high symmetry unit cell can be used to index patterns throughout the whole temperature range.

The magnetisation data collected using a SQUID magnetometer for both phases show strong evidence of a canted antiferromagnetic ground state. Magnetization data collected at 300 K as a function of applied field is linear and passes through the origin. Analogous data collected at 5 K after cooling in an applied field of 5T does not exhibit hysteresis. The difficulty of fitting the whole range of data before magnetic ordering occurs, to the Curie-Weiss law ($\chi = C/(T - \theta)$), might be the reason to cause suspicious disagreements between observed moments and expected moments derived from spin-only formula. A close inspection of H/M plots reveals that there might be valence transitions occurring for both $LaSr_3MnRhO_8$ and $La_2Sr_2CoRhO_8$ phases. In addition, for the Co analogue, the situation is more complicated as it might contain mixed spin states for Co^{3+} as well.

The topochemical reactions of these two n = 1 Ruddlesden-Popper phases $LaSr_3MnRhO_8$ and $La_2Sr_2CoRhO_8$ have been investigated as well and details are presented in the following Chapter 9.

Chapter 9

Synthesis and Characterisation of Rh-Containing Oxide-Hydride Phases

9.1 Introduction

Building upon the work of the successful synthesis of two anion-ordered, Ru-containing oxide-hydride phases, $LaSr_3NiRuO_4H_4$ and $LaSr_3CoRuO_4H_4$, the hypothesis of forming covalently-stabilised oxide-hydride phases which contains late 4*d* transition metals has been validated. In order to explore other potential candidates, analogous reduction chemistry has been extended to another late 4*d* transition metal, rhodium. The Mn-oxide and Co-oxide lattices are chosen to couple with these CaH_2 reductions to prevent complete reduction of the rhodium to the elemental metal state, and reactions are suggested to occur as follows:

$$LaSr_3MnRhO_8 + 2\ CaH_2 \longrightarrow LaSr_3MnRhO_6H_2 + 2\ CaO + H_2 \qquad [1]$$

$$La_2Sr_2CoRhO_8 + 2\ CaH_2 \longrightarrow La_2Sr_2CoRhO_6H_2 + 2\ CaO + H_2 \qquad [2]$$

Detailed characterisations of these two oxide-hydride phases will be described in this chapter.

9.2 Experimental

In order to assess the reactivity of $LaSr_3MnRhO_8$ and $La_2Sr_2CoRhO_8$ with CaH_2, small samples of the oxides (~ 300 mg) were ground together with a 4 mole-equivalents of CaH_2 in an argon filled glove box using an agate mortar and pestle. These mixtures were then sealed

under vacuum in silica ampoules and reaction profiles were mapped by heating for periods of 48 h at 25 ºC intervals in temperature range 350 < T/°C < 450. Since reactions with CaH_2 generate H_2 gas, measures must be taken to avoid excessive pressure building up inside sealed apparatus.

X-ray powder diffraction data collected from the products of reaction between CaH_2 and $La_2Sr_2CoRhO_8$ (Figure 9.1 (a)) show no evidence for reaction below 400 ºC. In the temperature range 400 < T/ºC < 450, $La_2Sr_2CoRhO_8$ is transformed into a second tetragonal phase (a = 3.75 Å, c = 13.09 Å) with concomitant conversion of CaH_2 to CaO. Diffraction data collected after heating at 400 ºC and 425 ºC (Figure 9.1 (a)) provide some evidence for an orthorhombic intermediate phase (a = 3.87 Å, b = 3.70 Å, c = 13.15 Å), however it was not possible to isolate this phase by varying the reaction conditions or reaction time. Raising the reaction temperature above 450 ºC led to decomposition of samples into elemental Co, Rh and a number of binary oxides.

The reaction between $LaSr_3MnRhO_8$ and CaH_2 followed a similar pattern to the cobalt phase (Figure 9.1 (b)). Below 400 ºC there was no observable reaction. In the temperature range 400 < T/ºC < 450, $LaSr_3MnRhO_8$ is transformed into a second tetragonal phase (a = 3.73 Å, c = 13.14 Å), again with concomitant conversion of CaH_2 to CaO. Data collected after heating at 400 ºC and 425 ºC (Figure 9.1 (b)) provide some evidence for a tetragonal intermediate phase (a = 3.82 Å, c = 12.89 Å), again however it was not possible to isolate this phase. Raising the reaction temperature above 450 ºC led to decomposition of samples into elemental Rh, MnO and a number of other binary oxides.

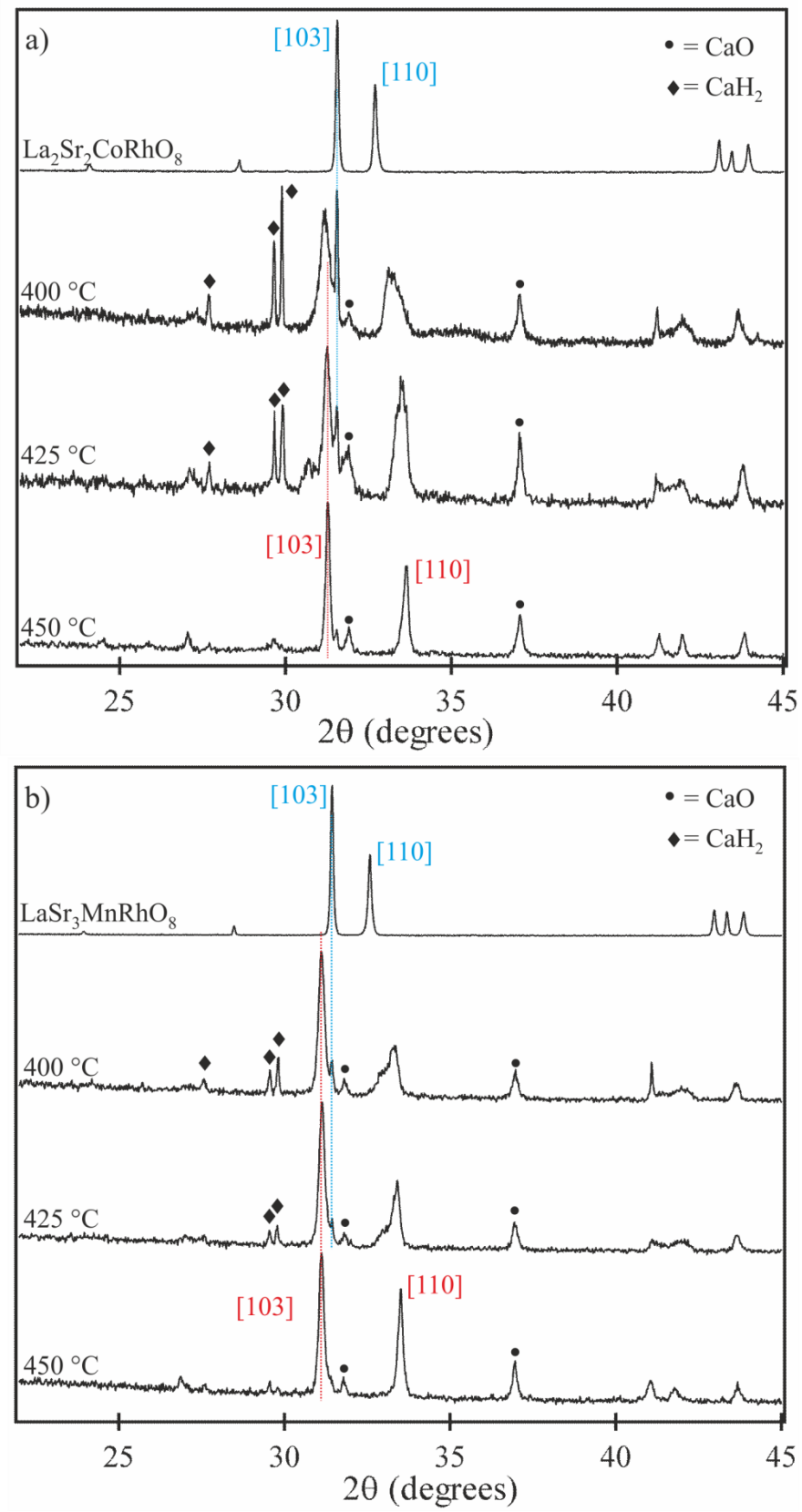


Figure 9.1. X-ray powder diffraction patterns collected from the products of reaction between CaH_2 and a) $La_2Sr_2CoRhO_8$ or b) $LaSr_3MnRhO_8$ as a function of reaction temperature.

After this initial screening for reactivity, large-scale samples of $LaSr_3MnRhO_6H_2$ and $La_2Sr_2CoRhO_6H_2$ suitable for analysis by neutron powder diffraction were prepared by grinding together approximately 0.4 g of CaH_2 with 1.5 g of $LaSr_3MnRhO_8$ and $La_2Sr_2CoRhO_8$ respectively in an argon-filled glove box using an agate mortar and pestle. The resulting powders were sealed in silica ampoules and heated at 450 °C for 3 periods of 7 days, with the samples being reground between heating periods. Once the reaction was deemed complete, the reaction mixture was washed, under nitrogen, with 8 × 25 ml of 0.1 M solution of NH_4Cl in methanol in order to remove the CaO formed as a by-product of the reaction and any unreacted CaH_2. This was then followed by washing with 5 × 25 ml of clean methanol to dissolve NH_4Cl residues. The sample was then dried under vacuum.

9.3 Results

9.3.1 Thermogravimetric Analysis of $LaSr_3MnRhO_6H_2$ and $La_2Sr_2CoRhO_6H_2$

The compositions of two oxide-hydride phases were determined from oxidative thermogravimetric analysis in a steady O_2 flow as described in Chapter 2 section 2.7. The oxygen contents of two oxide-hydride phases formed at 450 °C were both confirmed to be approximately A_2MRhO_6 and the presence of hydride ions was later confirmed by neutron powder diffraction.

Thermogravimetric data (Figure 9.2) collected during the reoxidation of the tetragonal phase, which was the ultimate product of the reduction of $LaSr_3MnRhO_8$ (after removal of CaO/CaH_2), revealed a mass gain of 5.40% indicating a composition of $LaSr_3MnRhO_{5.68}$ if the sample was only considered as an anion-deficient oxide.

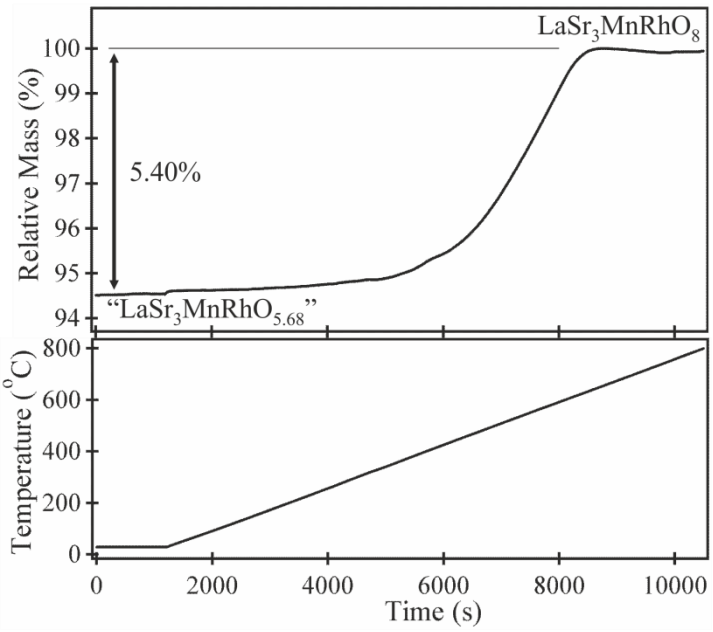


Figure 9.2. Thermogravimetric data collected during the oxidation of $LaSr_3MnRhO_6H_2$.

Thermogravimetric data (Figure 9.3) collected during the reoxidation of the tetragonal phase, which was the ultimate product of the reduction of $La_2Sr_2CoRhO_8$ (after removal of CaO/CaH_2), revealed a mass gain of 4.35% indicating a composition of $La_2Sr_2CoRhO_6$ if the sample was only considered as an anion-deficient oxide.

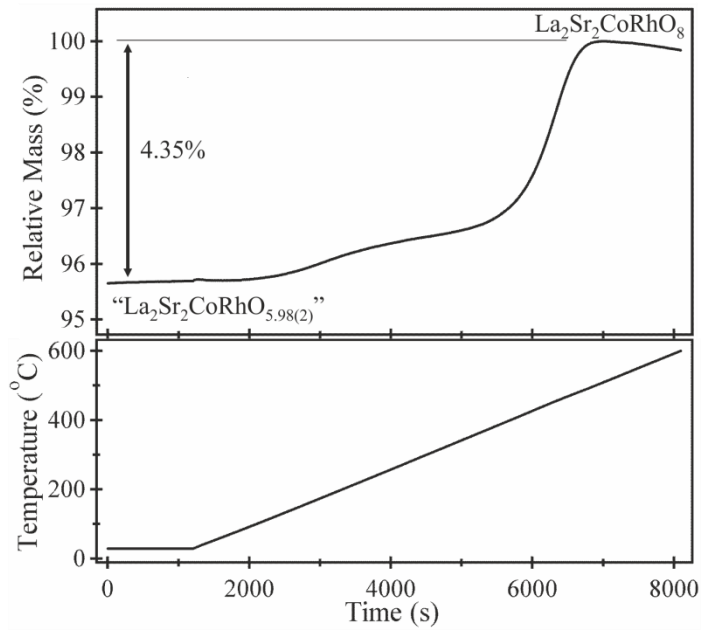


Figure 9.3. Thermogravimetric data collected during the oxidation of $La_2Sr_2CoRhO_6H_2$.

9.3.2 Structural Characterisation of $LaSr_3MnRhO_6H_2$

9.3.2.1 Neutron Powder Diffraction

Neutron powder diffraction measurements performed at ambient temperature and low temperature were carried out at WISH diffractometer, ISIS (Chapter 2 Section 2.5.2.1) and data collected was refined against a model based on the structure of its parent $LaSr_3MnRhO_8$ oxide phase (space group *I*4/*mmm*) with lattice parameters determined by synchrotron X-ray powder diffraction data collected from the oxide-hydride phase (a = 3.73141(8) Å, c = 13.1344(2) Å), but gave a poor fit until the occupancies of the equatorial anion sites were refined. Once atoms on this site had been changed to a 50 : 50 mixture of oxide ion and hydride ion, the occupancy refined, within error, confirming the stoichiometry of the phase as $LaSr_3MnRhO_6H_2$ (Figure 9.4). The refined plots are shown in Figure 9.5 (298 K) and Figure 9.6 (2 K) with detailed structural parameters in Table 9.1, 9.2 and 9.3. There are no additional magnetic diffraction features at low temperature which indicates the absence of long-range magnetic ordering.

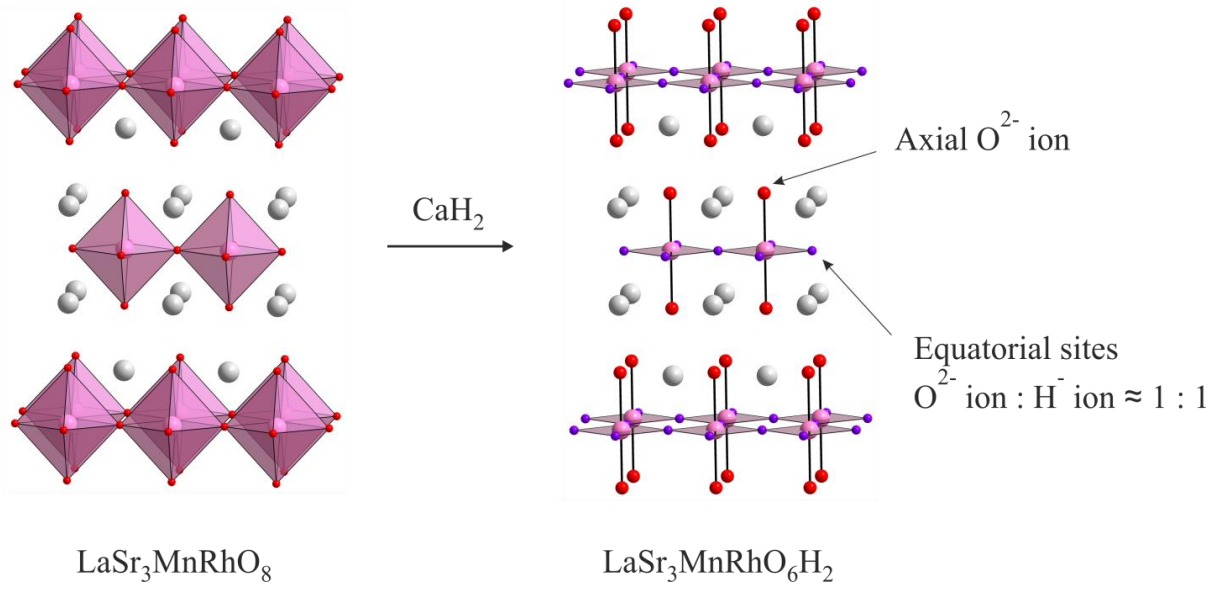


Figure 9.4. Topochemical reduction of $LaSr_3MnRhO_8$ with CaH_2 to form reduced oxide-hydride phase $LaSr_3MnRhO_6H_2$.

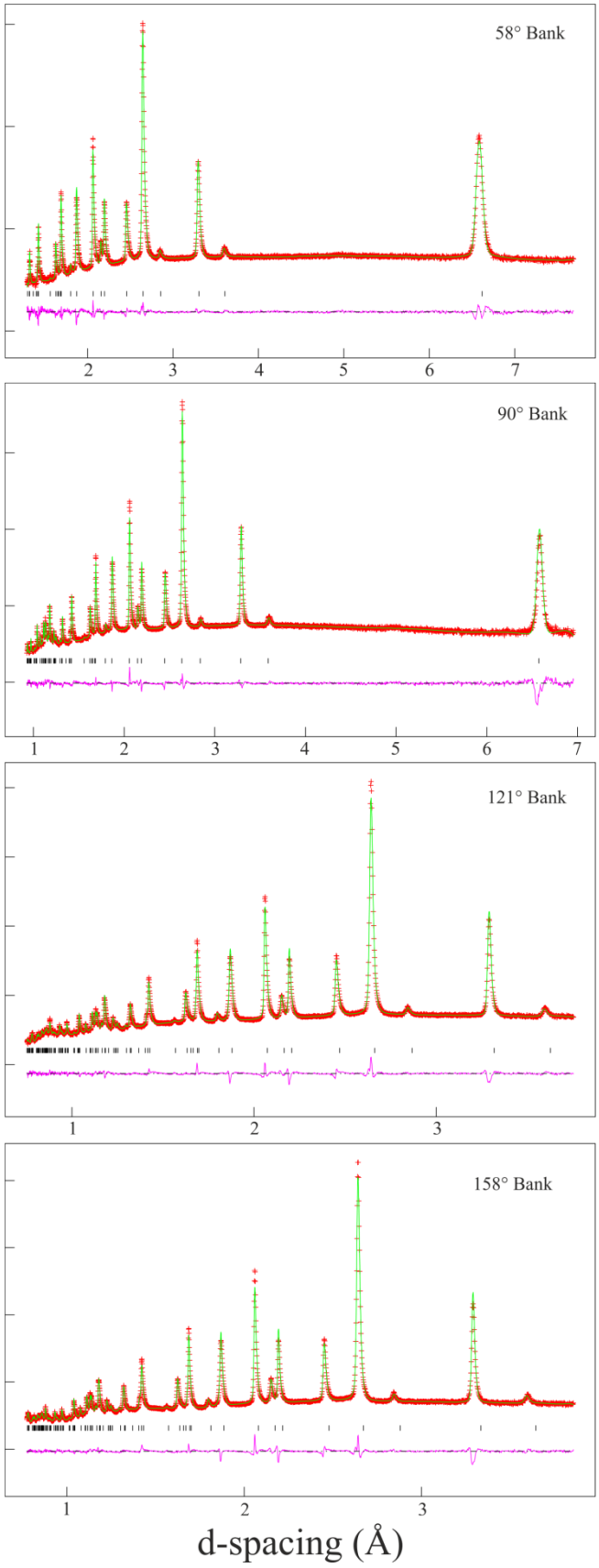


Figure 9.5. Observed, calculated and difference plots from the structural refinement of $LaSr_3MnRhO_6H_2$ against neutron powder diffraction data collected at 298 K.

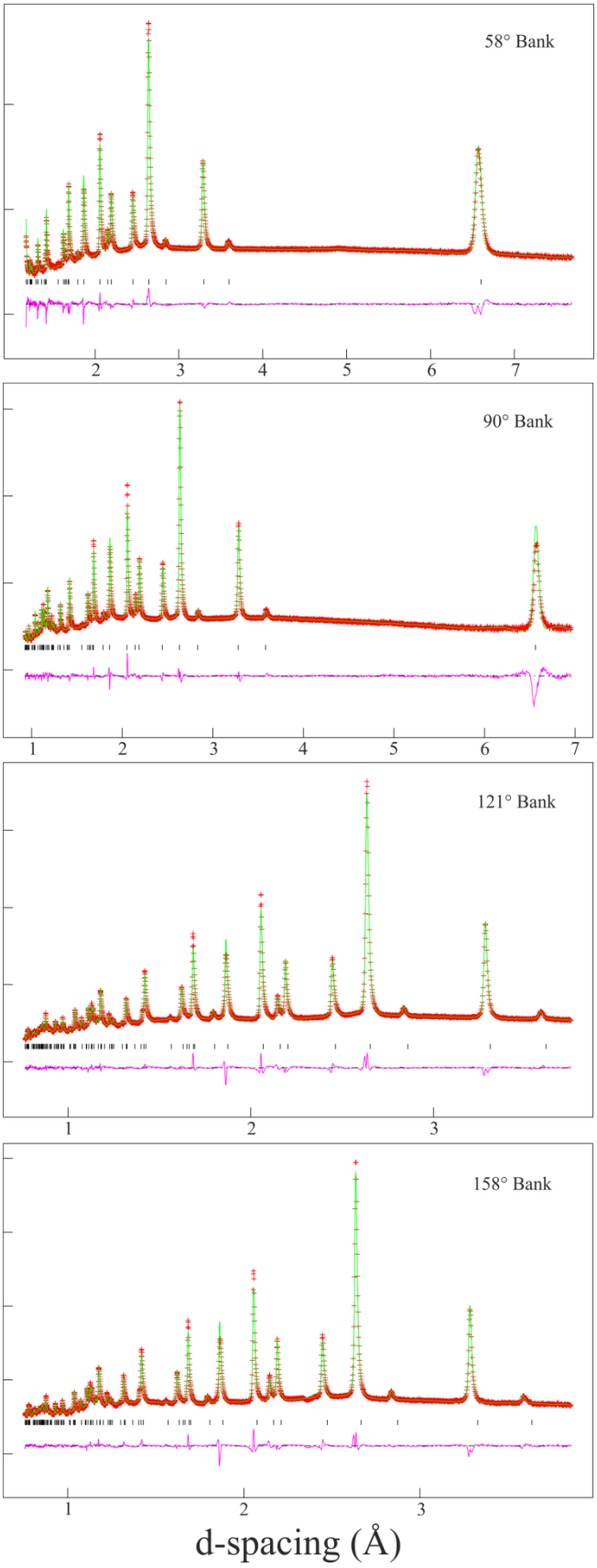


Figure 9.6. Observed, calculated and difference plots from the structural refinement of $LaSr_3MnRhO_6H_2$ against neutron powder diffraction data collected at 2 K.

$LaSr_3MnRhO_6H_2$ space group *I*4/*mmm* (#139) Formula weight: 657.64 g mol^{-1}, Z = 2 Radiation source: Neutron time of flight						
Atom	**Wyckoff Position**	***x***	***y***	***z***	**Fraction**	**U_{iso} equiv. ($Å^2$)**
La/Sr(1)	4*e*	0	0	0.35409(4)	0.25/0.75	0.0183
Mn/Rh(1)	2*a*	0	0	0	0.5/0.5	0.057
O(1)	4*e*	0	0	0.16591(7)	1	0.0217
O(2)/H(1)	4*c*	0.5	0	0	0.51(1)/0.49(1)	0.055
Temperature: 298 K *a* = 3.7302(1) Å, *c* = 13.1425(4) Å, Volume = 182.87(1) $Å^3$ χ^2 = 4.951; *wRp* = 2.28%; *Rp* = 1.66%.						
Atom	**Wyckoff Position**	***x***	***y***	***z***	**Fraction**	**U_{iso} equiv. ($Å^2$)**
La/Sr(1)	4*e*	0	0	0.35383(4)	0.25/0.75	0.0132
Mn/Rh(1)	2*a*	0	0	0	0.5/0.5	0.056
O(1)	4*e*	0	0	0.16503(7)	1	0.0157
O(2)/H(1)	4*c*	0.5	0	0	0.51(1)/0.49(1)	0.0215
Temperature: 2 K *a* = 3.7207(1) Å, *c* = 13.1158(5) Å, Volume = 181.57(2) $Å^3$ χ^2 = 11.30; *wRp* = 2.62%; *Rp* = 1.82%.						

Table 9.1. Structural parameters from the structural refinements of $LaSr_3MnRhO_6H_2$ against neutron powder diffraction data collected at 298 K (top) and 2 K (bottom).

Atom	U_{11}	U_{22}	U_{33}
La/Sr(1)	0.02662(58)	0.02662(58)	0.02011(62)
Mn/Rh(1)	0.0431(36)	0.0431(36)	0.0360(26)
O(1)	0.02193(70)	0.02193(70)	0.0371(11)
O(2)/H(1)	0.0820(10)	0.0082(30)	0.0323(42)
Temperature: 298 K			
Atom	U_{11}	U_{22}	U_{33}
La/Sr(1)	0.01948(63)	0.01948(63)	0.00389(64)
Mn/Rh(1)	0.0843(49)	0.0843(49)	0.0121(63)
O(1)	0.01777(77)	0.01777(77)	0.0123(10)
O(2)/H(1)	0.02153(10)	0.02153(10)	0.02153(10)
Temperature: 2 K			

Table 9.2. Anisotropic displacement factors from refinements of $LaSr_3MnRhO_6H_2$ against neutron powder diffraction data collected at 298 K (top) and 2 K (bottom).

Temperature: 298 K			**Temperature: 2 K**		
Cation	**Anion**	**length (Å)**	**Cation**	**Anion**	**length (Å)**
La/Sr(1)	O(1)	2.473(1) × 1	**La/Sr(1)**	O(1)	2.476(1) × 1
	O(1)	2.651(1) × 4		O(1)	2.643(1) × 4
	O(2)/H(1)	2.675(1) × 4		O(2)/H(1)	2.671(1) × 4
Mn/Rh(1)	O(1)	2.180(1) × 2	**Mn/Rh(1)**	O(1)	2.165(1) × 2
	O(2)/H(1)	1.865(1) × 4		O(2)/H(1)	1.860(1) × 4

Table 9.3. Selected bond lengths from the refined structure of $LaSr_3MnRhO_6H_2$ at 298 K (left) and 2 K (right).

9.3.2.2 Synchrotron X-ray Powder Diffraction

Since the WISH diffractometer used above is primarily designed for neutron powder diffraction at long *d*-spacing in magnetic and large unit cell systems, its relatively low resolution at short *d*-spacing for small unit cell systems like $LaSr_3MnRhO_6H_2$, cannot fully confirm the tetragonal symmetry of the unit cell. Therefore, synchrotron X-ray powder diffraction data were collected from this oxide-hydride phase as its extremely high resolution will reveal any extra peaks that do not belong to this high symmetry tetragonal unit cell and if the oxide-hydride phase requires a larger or distorted unit cell.

Synchrotron X-ray powder diffraction data (Chapter 2 Section 2.5.1.2) were collected from a large-scale neutron sample of $LaSr_3MnRhO_6H_2$. The data could be readily indexed using a body-centred tetragonal unit cell (space group *I*4/*mmm*) with lattice parameters: a = 3.73141(8) Å, c = 13.1344(2) Å, as described in Section 9.3.2.1. The equatorial anion sites were set to be half-occupied by oxide ions, as hydride ion is too 'light' to be observed in synchrotron X-ray powder diffraction data and contributes nearly nothing to the pattern. This model was refined against the data to achieve a good statistical fit (χ^2 = 115.7; *wRp* = 6.22%; *Rp* = 3.73%.).

Observed, calculated and difference plots from the Rietveld refinement of $LaSr_3MnRhO_6H_2$ (space group *I*4/*mmm*) against synchrotron X-ray powder diffraction data are shown in Figure 9.7. There are no extra peaks which cannot be indexed by this high symmetry model and fittings to peak shapes are quite satisfied, even for peaks at high angles as showed in the embeded plot for zoom-in area $46 \leq 2\theta/^\circ \leq 60$, suggest BO_2H_4 octahedra in this phase remain undistorted.

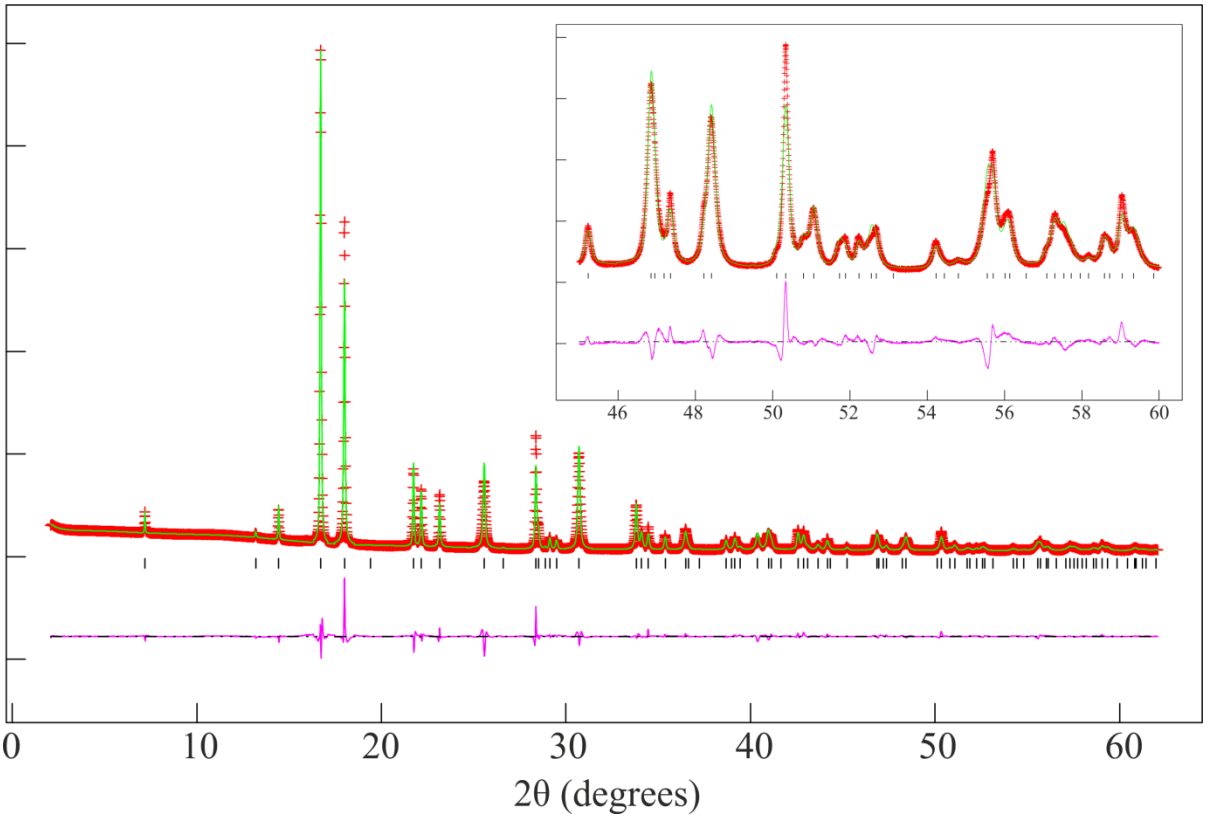


Figure 9.7. Observed, calculated and difference plots from the refinement of $LaSr_3MnRhO_6H_2$ (space group *I*4/*mmm*) against synchrotron X-ray powder diffraction data collected at 298 K.

The good fit of synchrotron X-ray powder diffraction data by a simple body-centred tetragonal unit cell (space group *I*4/*mmm*) confirms that the oxide-hydride phase $LaSr_3MnRhO_6H_2$ adopts the same crystallographic structure as its parent $LaSr_3MnRhO_8$ oxide phase, with a significant contraction in *a*-*b* plane due to the exchange of 50% equatorial oxide ions to hydride ions, which has already been confirmed by the neutron powder diffraction data collected from WISH diffractometer, ISIS.

9.3.3 Structural Characterisation of $La_2Sr_2CoRhO_6H_2$

9.3.3.1 Neutron Powder Diffraction

Neutron powder diffraction measurements performed at ambient temperature and low temperature were carried out at D2B diffractometer, ILL (Chapter 2 Section 2.5.2.2) and data collected was refined against a model based on the structure of its parent $La_2Sr_2CoRhO_8$ oxide phase (space group *I*4/*mmm*) with lattice parameters determined by synchrotron X-ray powder diffraction data collected from the oxide-hydride phase (a = 3.71745(7) Å, c = 13.0928(3) Å), but gave a poor fit until the occupancies of the equatorial anion sites were refined. Once atoms on this site had been changed to a 50 : 50 mixture of oxide ion and hydride ion, the occupancy refined, within error, confirming the stoichiometry of the phase as $La_2Sr_2CoRhO_6H_2$ (Figure 9.8). The refined plots are shown in Figure 9.9 with detailed structural parameters in Table 9.4, 9.5 and 9.6. There are no additional magnetic diffraction features at low temperature which indicates the absence of long-range magnetic ordering.

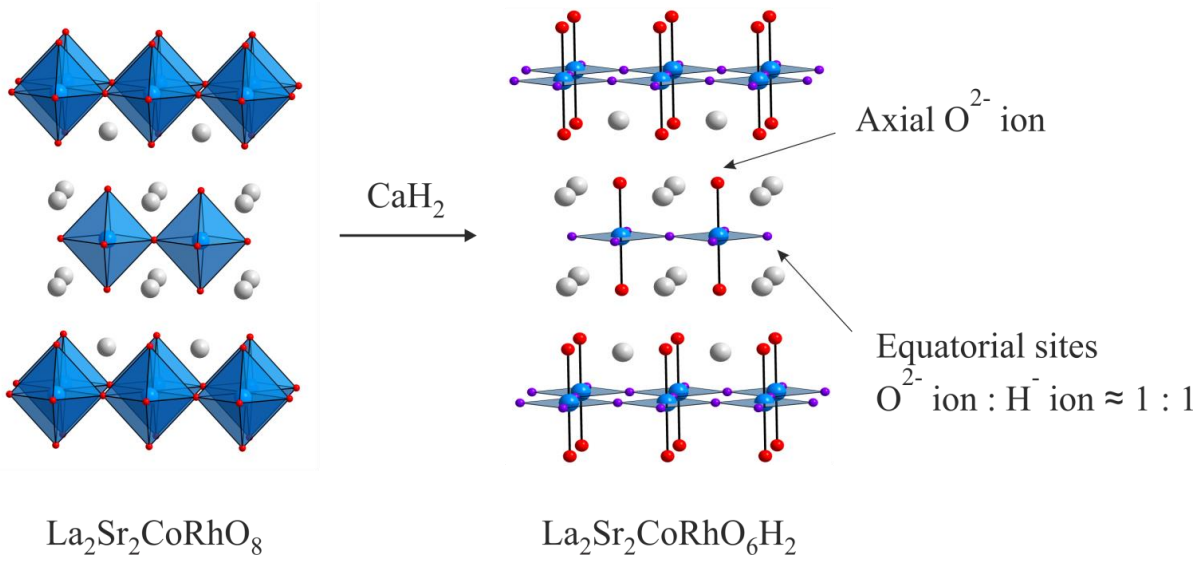


Figure 9.8. Topochemical reduction of $La_2Sr_2CoRhO_8$ with CaH_2 to form reduced oxide-hydride phase $La_2Sr_2CoRhO_6H_2$.

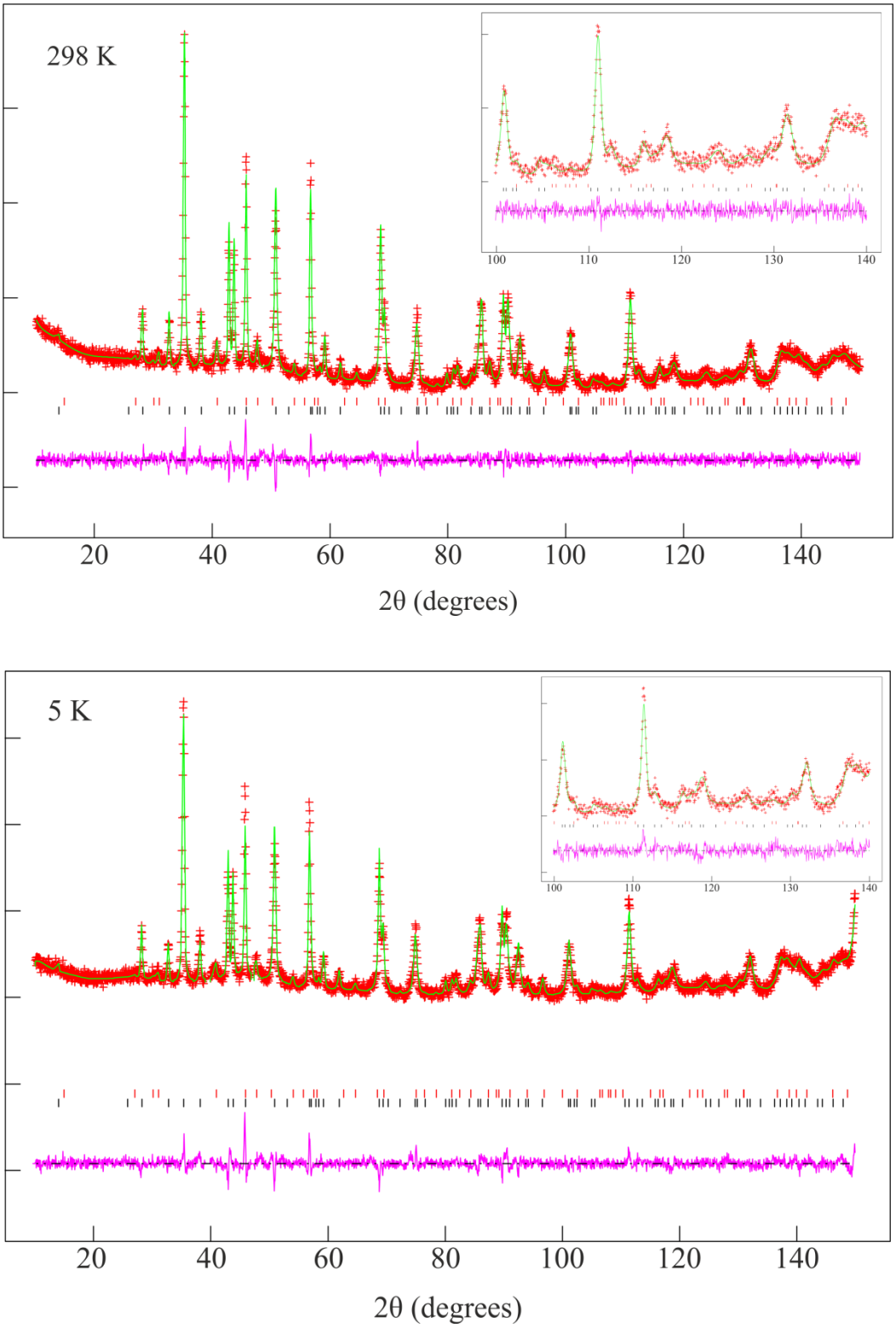


Figure 9.9. Observed, calculated and difference plots from the refinements of $La_2Sr_2CoRhO_6H_2$ (space group *I*4/*mmm*) against neutron powder diffraction data collected at 298 K (top) and 5 K (bottom); Lower tick marks indicate peak positions of the majority phase, upper tick marks La_2O_3.

Majority phase: $La_2Sr_2CoRhO_6H_2$ space group *I*4/*mmm* (#139)

Formula weight: 712.92 g mol^{-1}, Z = 2

Radiation source: Neutron Powder Diffraction, λ = 1.5943(2)

Atom	Wyckoff Position	*x*	*y*	*z*	Fraction	U_{iso} eqv. ($Å^2$)
La/Sr(1)	4*e*	0	0	0.3568(1)	0.5/0.5	0.0113
Co/Rh(1)	2*a*	0	0	0	0.5/0.5	0.0238
O(1)	4*e*	0	0	0.1683(2)	1	0.0176
O(2)/H(1)	4*c*	0.5	0	0	0.50(1)/0.50(1)	0.0220

Temperature: 298 K

a = 3.7175(2) Å, *c* = 13.0926(8) Å, Volume = 180.94(3) $Å^3$

Mass fraction: 95.5(1)%, χ^2 = 1.452; *wRp* = 3.25%; *Rp* = 2.54%.

Atom	Wyckoff Position	*x*	*y*	*z*	Fraction	U_{iso} eqv. ($Å^2$)
La/Sr(1)	4*e*	0	0	0.3568(1)	0.5/0.5	0.0061
Co/Rh(1)	2*a*	0	0	0	0.5/0.5	0.0206
O(1)	4*e*	0	0	0.1682(2)	1	0.0130
O(2)/H(1)	4*c*	0.5	0	0	0.50(1)/0.50(1)	0.0126

Temperature: 5 K

a = 3.7095(2) Å, *c* = 13.0556(7) Å, Volume = 179.65(3) $Å^3$

Mass fraction: 94.3(1)%, χ^2 = 1.913; *wRp* = 3.75%; *Rp* = 2.98%.

Minority phase: La_2O_3 space group *P*-3*m*1 (#164)

Formula weight: 325.82 g mol^{-1}, Z = 4, Mass fraction: 4.5(1)% for 298K and 5.7(1)% for 5K.

Table 9.4. Structural parameters from the structural refinements of $La_2Sr_2CoRhO_6H_2$ against neutron powder diffraction data collected at 298 K (top) and 5 K (bottom).

Atom	U_{11}	U_{22}	U_{33}
La/Sr(1)	0.01323(11)	0.01323(11)	0.0073(12)
Co/Rh(1)	0.0240(20)	0.0240(20)	0.02129(46)
O(1)	0.01860(12)	0.01860(12)	0.01572(21)
O(2)/H(1)	0.0430(83)	0.0120(48)	0.0110(12)
Temperature: 298 K			
Atom	U_{11}	U_{22}	U_{33}
La/Sr(1)	0.0078(10)	0.0078(10)	0.0025(10)
Co/Rh(1)	0.0223(26)	0.0223(26)	0.0170(39)
O(1)	0.0158(13)	0.0158(13)	0.0072(18)
O(2)/H(1)	0.0069(81)	0.0244(58)	0.0063(60)
Temperature: 5 K			

Table 9.5. Anisotropic displacement factors from refinements of $La_2Sr_2CoRhO_6H_2$ against neutron powder diffraction data collected at 298 K (top) and 5 K (bottom).

Temperature: 298 K			**Temperature: 5 K**		
Cation	**Anion**	**length (Å)**	**Cation**	**Anion**	**length (Å)**
La/Sr(1)	O(1)	2.468(3) × 1	**La/Sr(1)**	O(1)	2.462(3) × 1
	O(1)	2.649(1) × 4		O(1)	2.643(1) × 4
	O(2)/H(1)	2.650(1) × 4		O(2)/H(1)	2.634(1) × 4
Co/Rh(1)	O(1)	2.203(3) × 2	**Co/Rh(1)**	O(1)	2.196(3) × 2
	O(2)/H(1)	1.859(1) × 4		O(2)/H(1)	1.855(1) × 4

Table 9.6. Selected bond lengths from the refined structure of $La_2Sr_2CoRhO_6H_2$ at 298 K (left) and 5 K (right).

9.3.3.2 Synchrotron X-ray Powder Diffraction

Synchrotron X-ray powder diffraction data (Chapter 2 Section 2.5.1.2) were collected from a large-scale neutron sample of $La_2Sr_2CoRhO_6H_2$, as its extremely high resolution will reveal any extra peaks that do not belong to this high symmetry tetragonal unit cell and if the oxide-hydride phase requires a larger or distorted unit cell. The data could be readily indexed using a body-centred tetragonal unit cell (space group *I*4/*mmm*) with lattice parameters: a = 3.71745(7) Å, c = 13.0928(3) Å, as described in Section 9.3.3.1. The equatorial anion sites were set to be half-occupied by oxide ions, as hydride ion is too 'light' to be observed in synchrotron X-ray powder diffraction data and contributes nearly nothing to the pattern. This model was refined against the data to achieve a good statistical fit (χ^2 = 23.87; *wRp* = 3.51%; *Rp* = 1.88%.).

Observed, calculated and difference plots from the Rietveld refinement of $La_2Sr_2CoRhO_6H_2$ (space group *I*4/*mmm*) against synchrotron X-ray powder diffraction data are shown in Figure 9.10. There are no extra peaks which cannot be indexed by this high symmetry model and fittings to peak shapes are quite satisfied, even for peaks at high angles as showed in the embeded plot for zoom-in area $46 \leq 2\theta/^\circ \leq 60$, suggest BO_2H_4 octahedra in this phase remain undistorted.

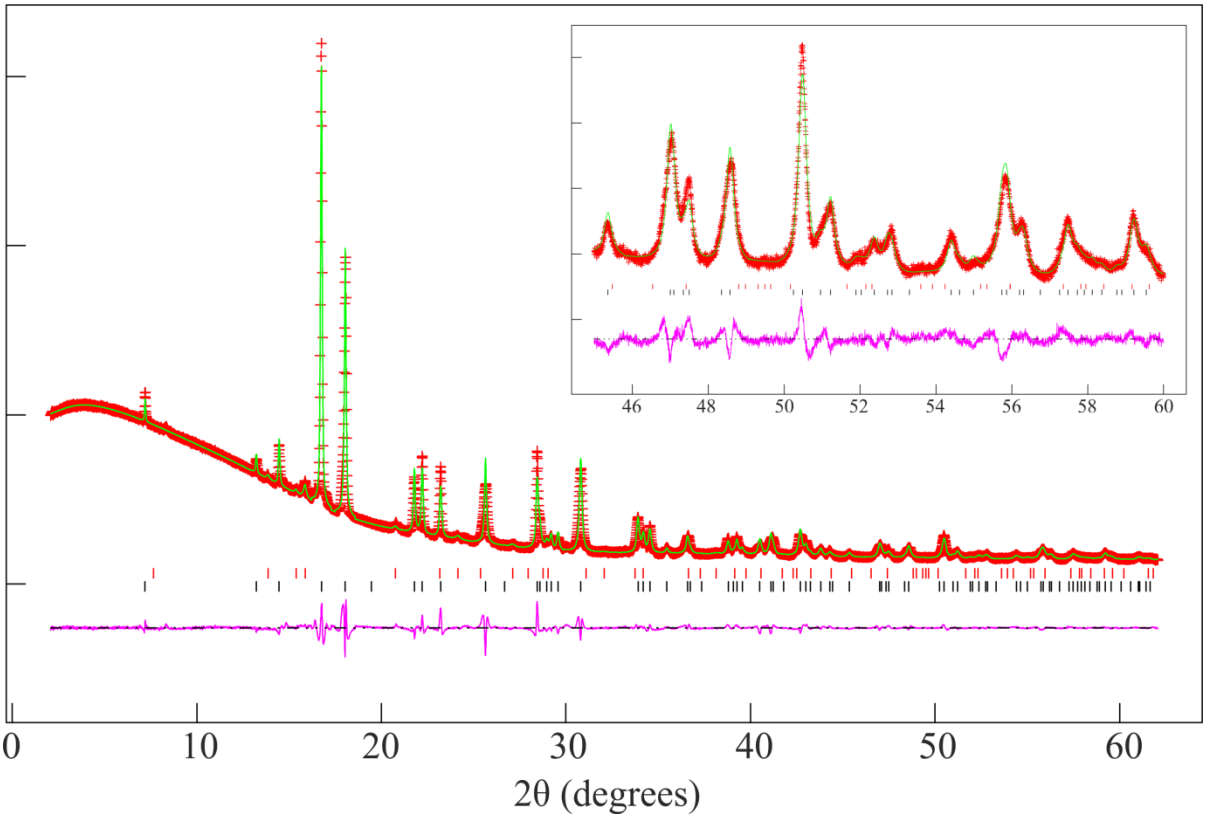


Figure 9.10. Observed, calculated and difference plots from the refinements of $La_2Sr_2CoRhO_6H_2$ (space group *I*4/*mmm*) against synchrotron X-ray powder diffraction data collected at 298 K; Lower tick marks indicate peak positions of the majority phase, upper tick marks La_2O_3.

The good fit of synchrotron X-ray powder diffraction data by a simple body-centred tetragonal unit cell (space group *I*4/*mmm*) confirms that the oxide-hydride phase $La_2Sr_2CoRhO_6H_2$ adopts the same crystallographic structure as its parent $La_2Sr_2CoRhO_8$ oxide phase, with a significant contraction in *a*-*b* plane due to the exchange of 50% equatorial oxide ions to hydride ions, which has already been confirmed by the neutron powder diffraction data collected from D2B diffractometer, ILL.

9.3.4 Magnetic Characterisation of $LaSr_3MnRhO_6H_2$

Initial magnetisation data collected from $LaSr_3MnRhO_6H_2$ using a SQUID magnetometer (Chapter 2 Section 2.10) indicated the sample was contaminated by a low concentration of ferromagnetic impurities, most likely a $La_{1-x}Sr_xMnO_3$ perovskite phase in the $LaSr_3MnRhO_6H_2$ sample. The concentration of the ferromagnetic impurities was too low to be observed by diffraction methods. As a result, magnetization data were collected using a 'ferromagnetic subtraction' technique (Chapter 2 Section 2.10.2). The magnetization of $LaSr_3MnRhO_6H_2$ is observed to become linear with respect to the applied magnetic field in fields greater than 2 T (as shown in Figure 9.11) indicating that the magnetisation of the ferromagnetic impurity phases has saturated for H > 2T. Therefore, a large field (3T to 5T) was applied to saturate the ferromagnetic impurities during the magnetic characterisation, thus the paramagnetic susceptibility of a bulk sample can be measured. At 5K temperature increments between 5K and 300K, magnetisation-field isotherms were collected over $3T \leq H \leq 5T$ and the resultant magnetisation are plotted as a function of the applied field. For each 5K step the gradient of the plot obtained shows the paramagnetic susceptibility and the intercept gives the saturated ferromagnetic moment from any impurities (Figure 9.12).

These magnetisation data (scaled to the formula $La_{0.5}Sr_{1.5}Mn_{0.5}Rh_{0.5}O_3H$) can be fit to the Curie-Weiss law ($\chi = C/(T-\theta)$) in the temperature range $185 < T/K < 300$ to yield values of C = 2.034(2) cm^3 K mol^{-1} and θ = -227(2) K, consistent with S = $^5/_2$, Mn^{2+} and S = 0, Rh^{3+} (C_{calc} = 2.18 cm^3 K mol^{-1}) (Figure 9.13). On cooling below T ~ 50 K the paramagnetic susceptibility shows a positive deviation from the Curie-Weiss expectation and the saturated ferromagnetic moment of the sample rises sharply, suggesting the onset of magnetic order. However, neutron powder diffraction data collected from $La_{0.5}Sr_{1.5}Mn_{0.5}Rh_{0.5}O_3H$ at 2 K show no additional features compared to the analogous 300 K data set, and thus provide no evidence for a long-range-ordered magnetic state.

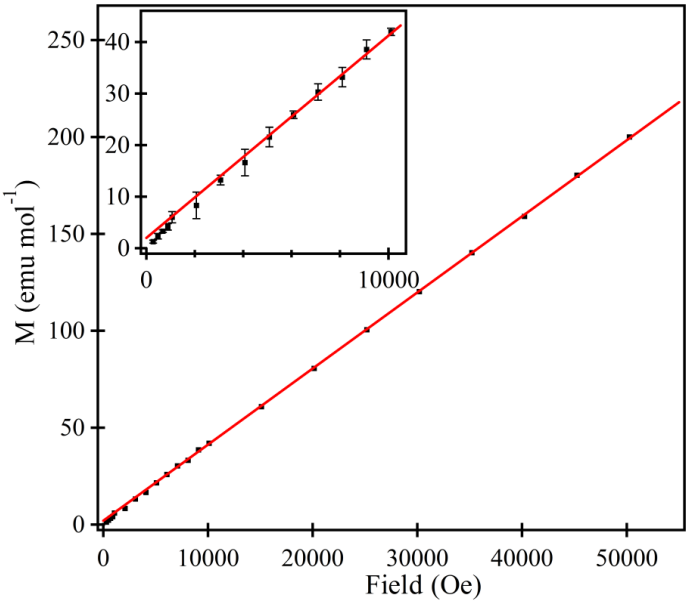


Figure 9.11. A linear fit to the high-field region (H > 30000 Oe) of magnetisation data collected from $LaSr_3MnRhO_6H_2$, measured as a function of applied field at 300 K.

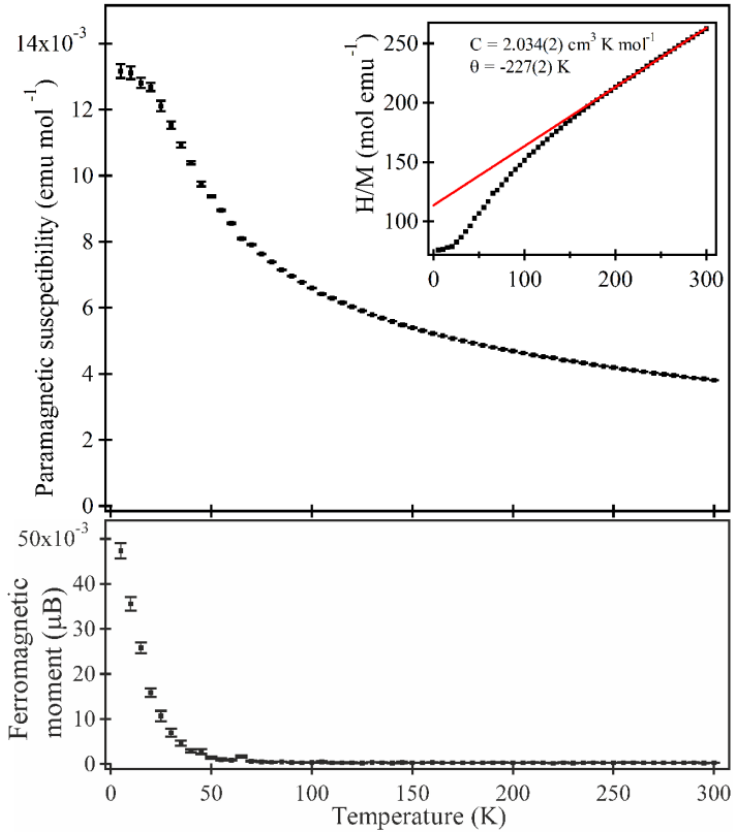


Figure 9.12. The paramagnetic susceptibility (top) and saturated ferromagnetic moment (bottom) of $LaSr_3MnRhO_6H_2$ collected as a function of temperature.

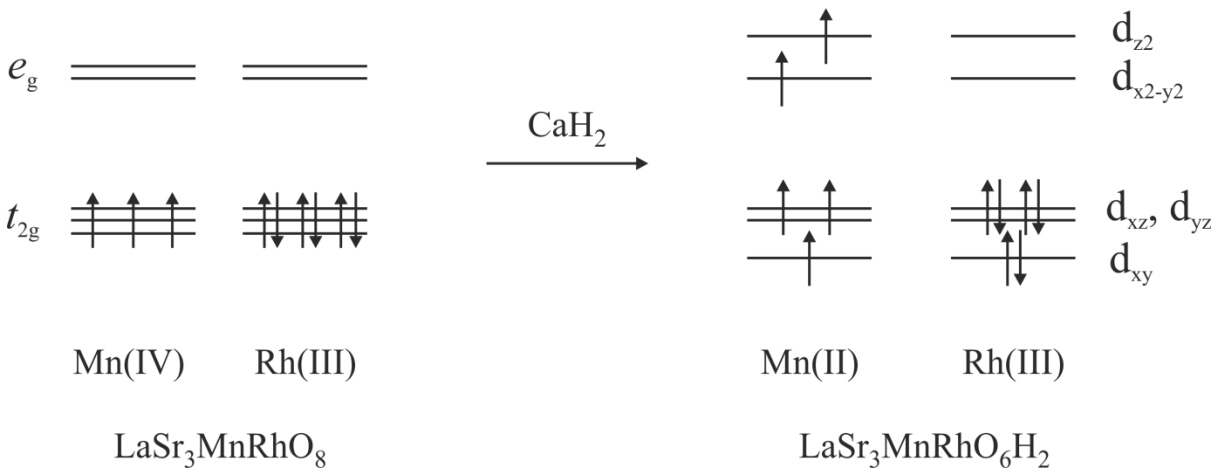


Figure 9.13. Proposed electronic configurations of $LaSr_3MnRhO_8$ and $LaSr_3MnRhO_6H_2$.

9.3.5 Magnetic Characterisation of $La_2Sr_2CoRhO_6H_2$

Initial magnetisation data collected from $La_2Sr_2CoRhO_6H_2$ using a SQUID magnetometer (Chapter 2 Section 2.10) indicated the sample was contaminated by a low concentration of ferromagnetic impurities, most likely elemental Co in the $La_2Sr_2CoRhO_6H_2$ sample. The concentration of the ferromagnetic impurities was too low to be observed by diffraction methods. As a result, magnetization data were collected using a 'ferromagnetic subtraction' technique, described in Chapter 2 Section 2.10.2. The magnetization of $La_2Sr_2CoRhO_6H_2$ is observed to become linear with respect to the applied magnetic field in fields greater than 2 T (as shown in Figure 9.14) indicating that the magnetisation of the ferromagnetic impurity phases has saturated for H > 2T. Therefore, a large field (3T to 5T) was applied to saturate the ferromagnetic impurities during the magnetic characterisation, thus the paramagnetic susceptibility of a bulk sample can be measured. At 5K temperature increments between 5K and 300K, magnetisation-field isotherms were collected over $3T \leq H \leq 5T$ and the resultant magnetisation are plotted as a function of the applied field. For each 5K step the gradient of the plot obtained shows the paramagnetic susceptibility and the intercept gives the saturated ferromagnetic moment from any impurities (Figure 9.15).

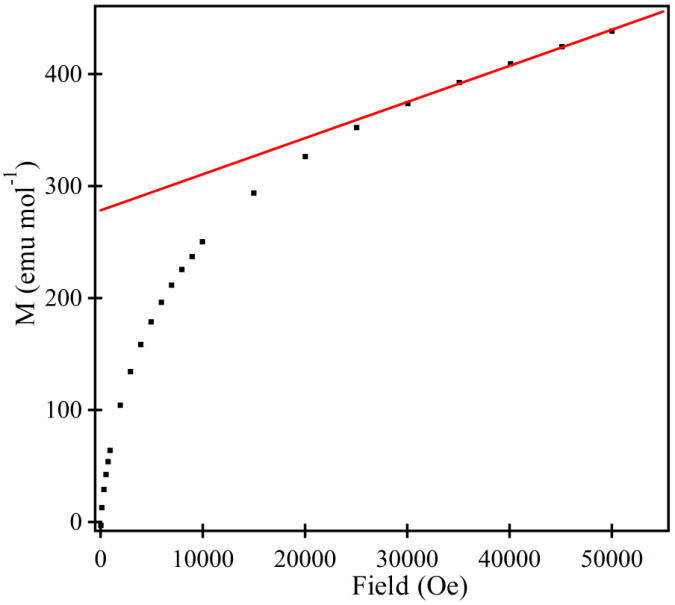


Figure 9.14. A linear fit to the high-field region (H > 30000 Oe) of magnetisation data collected from $La_2Sr_2CoRhO_6H_2$, measured as a function of applied field at 300 K.

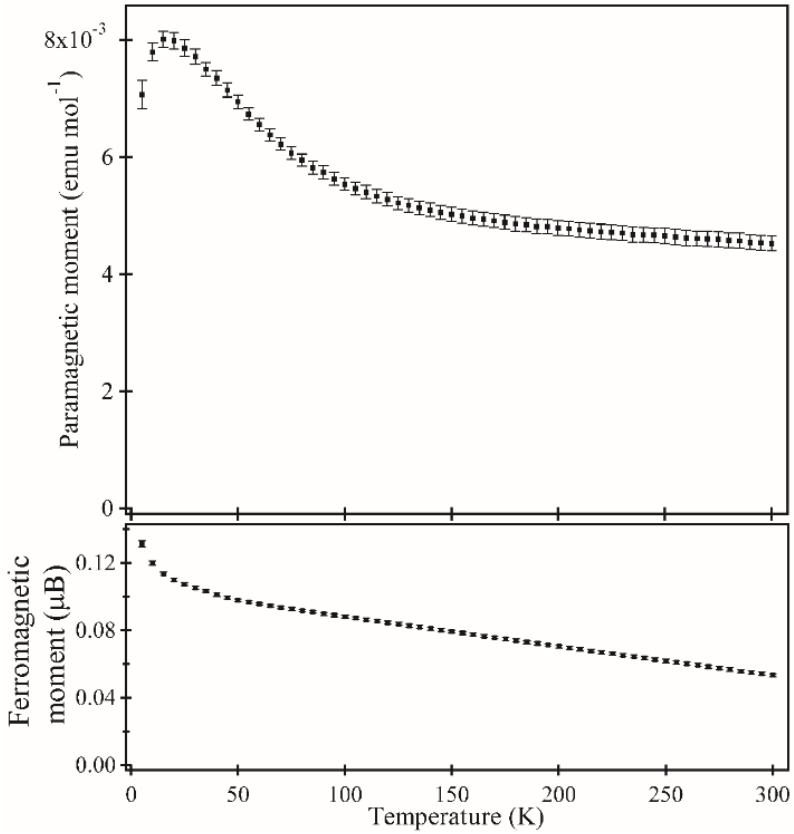


Figure 9.15. The paramagnetic susceptibility (top) and saturated ferromagnetic moment (bottom) of $La_2Sr_2CoRhO_6H_2$ collected as a function of temperature.

These magnetisation data (scaled to the formula $LaSrCo_{0.5}Rh_{0.5}O_3H$) (Figure 9.15) could not be fitted to the Curie-Weiss law over any significant temperature range, indicating strong spin-spin coupling. Such strong magnetic exchange has been observed previously in a number of oxide-hydrides resulting in high-temperature magnetic order. The local maximum in the data at T ~ 15 K suggests the onset of (antiferro)magnetic order, however close inspection of neutron powder diffraction data collected at 5 K show no additional features compared to analogous data collected at 300 K, and thus provide no evidence for a long-range-ordered magnetic state. Resistivity measurements performed on cold-pressed powder samples yielded values greater than 3 MΩcm, consistent with insulating behaviour.

Although the paramagnetic susceptibility data could not be fitted to the Curie-Weiss law, electronic configurations have been proposed for both $La_2Sr_2CoRhO_8$ and $La_2Sr_2CoRhO_6H_2$ based on their basic chemistry and experiences from analogue samples (Figure 9.16).

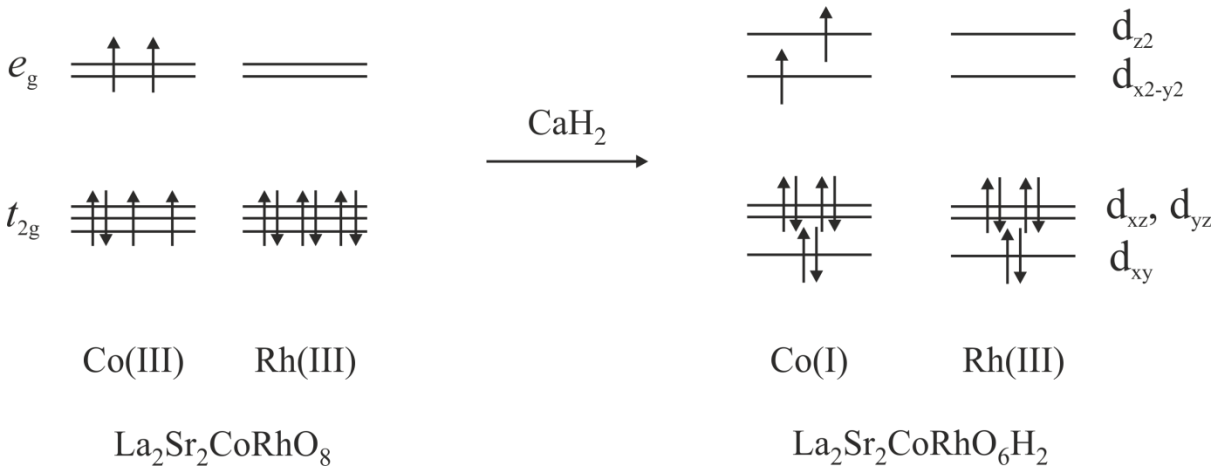


Figure 9.16. Proposed electronic configurations of $La_2Sr_2CoRhO_8$ and $La_2Sr_2CoRhO_6H_2$.

9.4 Discussion

9.4.1 The Role of Rhodium in Stabilizing Oxide-hydride Phases

The substitution of hydride anions for oxide anions, to form transition-metal oxide-hydride phases, offers an opportunity to exploit these concepts due to the strongly contrasting features of the two anions.[111] However only a handful of examples are currently known. This is principally because all transition-metal oxide-hydrides are unstable with respect to decomposition to the elemental metal and water ($AMO_xH_y \rightarrow AO + M + H_2O$) at ambient pressure. As a result, the only oxide hydrides observed are those in which the M-H bonding is strong enough to provide some kinetic stability to the oxide-hydride lattice.

The kinetic stability of 'early' transition metal oxide-hydrides can be attributed to strong ionic interactions between the hydride anions and elements such as scandium, titanium, vanadium and chromium. Here the low electronegativities of the metals help resist reduction and the relatively high metal cation charges lead to strong coulombic interactions with the H^- anions, which in combination provide a kinetic barrier to the decomposition of these phases. In contrast, 'late' transition metals such as cobalt exhibit strong Co_{3d}-H_{1s}-O_{2p} covalent interactions[45] in oxide-hydrides which account from the kinetic stability of these compounds. This strong covalency is directly analogous to the strong M-H σ-bonding observed in the molecular hydrides of 4d and 5d transition metals, suggesting that the inclusion of these elements should enable a wide range of new oxide-hydrides to be prepared.

As discussed in Chapter 4 and 7, the synthesis of two Ru-containing oxide-hydride phases, $LaSr_3NiRuO_4H_4$ and $LaSr_3CoRuO_4H_4$, validates the hypothesis stated above, and hence the chemistry has been extended to rhodium. The successful synthesis of these two Rh-containing oxide-hydride phases, $LaSr_3MnRhO_6H_2$ and $La_2Sr_2CoRhO_6H_2$, clearly demonstrates the ability of rhodium, a late 4d transition metal, to kinetically stabilize oxide-

hydride lattices, reinforcing the paradigm of covalent stabilization of transition-metal oxide-hydride phases.

For example, the reaction between $LaSr_3MnRhO_8$ and CaH_2 to form the oxide-hydride phase $LaSr_3MnRhO_6H_2$ is significantly different from the reactivity observed for the all-manganese phases, $LaSrMnO_4$ and Sr_2MnO_4, which react with CaH_2 to form the anion-deficient oxides $LaSrMnO_{3.5}$ and $Sr_2MnO_{3.63}$ respectively[112, 113], with no indication of oxide-hydride formation in either case. The formation of $LaSr_3MnRhO_6H_2$ is therefore consistent with the idea that strong Rh-H σ-type bonding is responsible for stabilizing this oxide-hydride phase. It should be noted that it is possible to prepare an all-manganese oxide-hydride phase $LaSrMnO_{3.3}H_{0.7}$ by combination of La_2O_3, SrO, SrH_2, MnO and Mn_2O_3 at 1000 ºC under an applied pressure of 5 GPa[114], suggesting that in the absence of the strong Rh-H σ-type bonding, the strength of the Mn-H bonding is close to the threshold required to stabilize an oxide-hydride phase, but not sufficient at ambient pressure.

9.4.2 The Anion-disorder in Rh-containing Oxide-hydride Phases

The two Ru-containing oxide-hydride phases, $LaSr_3NiRuO_4H_4$ and $LaSr_3CoRuO_4H_4$, previously discussed in Chapter 4 and 7 are anion-ordered. However, a combination of neutron powder diffraction and thermogravimetric analysis data collected from these Rh-containing oxide-hydride phases revealed $La_2Sr_2CoRhO_8$ and $LaSr_3MnRhO_8$ had been converted into $La_2Sr_2CoRhO_6H_2$ and $LaSr_3MnRhO_6H_2$ respectively, in which 50% of the oxide ions in the 'equatorial' anion sites have been exchanged for hydride anions, converting the –AO–BO_2–AO– stacking sequence of the oxides into an –AO–$B(O_{0.5}H_{0.5})_2$–AO– sequence in the oxide-hydrides, with the oxide and hydride anions adopting a disordered configuration within the $B(O_{0.5}H_{0.5})_2$ sheets.

The conversion of $La_2Sr_2CoRhO_8$ into $La_2Sr_2CoRhO_6H_2$ can be considered analogous to the previously observed conversion of $LaSrCoO_4$ to $LaSrCoO_3H_{0.7}$.[15] In this latter case $LaSrCoO_4$ is first reduced via anion deintercalation to $LaSrCoO_{3.35}$ before subsequent hydride-for-oxide anion-exchange/insertion leading to the formation of $LaSrCoO_3H_{0.7}$ in a redox-neutral process.[19, 45] The observation of an orthorhombic intermediate during the conversion of $La_2Sr_2CoRhO_8$ into $La_2Sr_2CoRhO_6H_2$ suggests a similar mechanism is followed: reduction to form an anion-deficient $La_2Sr_2CoRhO_{8-x}$ ($x \sim 1.0$) phase and then anion-exchange to form the oxide-hydride phase.

Although $LaSrCoO_3H_{0.7}$ and $La_2Sr_2CoRhO_6H_2$ appear to be formed by similar routes, they show contrasting degrees of anion order, with the all-cobalt phase adopting rigorous oxide/hydride order[15], while the Co/Rh phase has a disordered array of O^{2-} and H^- anions in the Co-Rh-O-H plane. This difference can be rationalized by considering effect of d-electron count on the relative stabilities of the *cis*- and *trans*- configurations of the MO_4H_2 units which make up these phases. As noted previously the strong trans influence of the hydride anion generally disfavours configurations in which the hydride ions are mutually trans – principally this is because only a single d-orbital can contribute to M-H bonding in this arrangement.[96] Thus, in general *cis*-MO_4H_2 configurations are favoured. However particular d-electron counts – notably d^2 and high-spin d^7 – can overcome this effect and stabilize *trans*-MO_4H_2 configurations by optimizing the π-bonding interactions, as observed for the *trans*-VO_4H_2 units in $SrVO_2H$.[14] In the context of $LaSrCoO_3H_{0.7}$ and $La_2Sr_2CoRhO_6H_2$ we can see that the anion order in the former phase can be attributed to the favourability of the *trans*-$Co^{II}O_4H_2$ configuration conveyed by the d^7 electron count of the Co^{2+} centres, while the anion-disorder in $La_2Sr_2CoRhO_6H_2$ implies that the electronic configurations of the cobalt and rhodium cations in this phase (presumably d^8, S = 1, Co^{1+} and d^6, S = 0, Rh^{3+} as showed above in

Figure 9.16) provide no such stability for the trans arrangement and thus adopt a *cis*-(Co/Rh)O_4H_2 configuration resulting in anion disorder within the $Co_{0.5}Rh_{0.5}(O_{0.5}H_{0.5})_2$ planes.

In addition, the anion disorder observed in $LaSr_3MnRhO_6H_2$ can again be rationalized on the basis that d^5, S = $^5/_2$, Mn^{2+} and d^6, S = 0, Rh^{3+} centres (as showed above in Figure 9.13) will not stabilize a *trans*-(Mn/Rh)O_4H_2 local configuration in a direct analogy to the argument presented for $La_2Sr_2CoRhO_6H_2$ above.

9.5 Conclusion

The two anion-disordered Rh-containing oxide-hydride phases, $La_2Sr_2CoRhO_6H_2$ and $LaSr_3MnRhO_6H_2$, can be prepared by treating their corresponding parent oxide phases, $La_2Sr_2CoRhO_8$ and $LaSr_3MnRhO_8$, with CaH_2 in sealed silica ampoules. The oxygen contents in these reduced phases were confirmed to be approximately A_2MRhO_6 by TGA results and the presence of hydride ions was later confirmed by neutron powder diffraction. These two oxide-hydride phases both adopt the structure of their parent oxide phases, the simple body-centred tetragonal unit cell (space group *I*4/*mmm*), with 50% of the oxide ions in the 'equatorial' anion sites being exchanged for hydride anions to form a *cis*-(M/Rh)O_4H_2 configuration, thus results in the contraction in *a*-*b* plane and elongation in *c*-axis.

Although the magnetisation data collected from both reduced phases suggest the onset of (antiferro)magnetic order, neutron powder diffraction data collected at low temperature show no additional features compared to the analogous room temperature data set, and thus provide no evidence for a long-range-ordered magnetic state in these two oxide-hydride phases.

The successful conversion of $La_2Sr_2CoRhO_8$ and $LaSr_3MnRhO_8$ into $La_2Sr_2CoRhO_6H_2$ and $LaSr_3MnRhO_6H_2$ respectively, proves the ability of the strong Rh-H σ-type bonding to kinetically stabilise oxide-hydride phases from decomposition to the elemental metal and water ($AMO_xH_y \rightarrow AO + M + H_2O$) at ambient pressure, reinforcing the paradigm of covalent stabilization of transition-metal oxide-hydride phases.

Chapter 10

Conclusions

In this thesis, topochemical reactions of Ru-containing and Rh-containing complex transition-metal oxides by using CaH_2 as a reducing agent or Zr powder as an oxygen getter were thoroughly studied and a wide range of kinetically-controlled metastable phases have been prepared for the first time.

One of the key findings is that the presence of the by-product H_2 gas in CaH_2 reductions strongly favours the formation of oxide-hydride phases. If the reaction mixture is sealed and heated in a silica ampoule, the H_2 gas formed during the reaction has no options but to accumulate inside the reaction vessel and thus can act as a source of hydride ions, leading to the subsequent hydride-for-oxide substitution. Several distinct anion-deficient reduced oxide phases have been observed at low reaction temperatures during the initial screening for the reactivity of complex oxides such as $LaSr_3NiRuO_8$ or $LaSr_3CoRuO_8$, but these phases can never be successfully isolated from the CaH_2 reduction due to the simultaneous formation of the competing oxide-hydride phase. After switching to a venting apparatus, with a steady Ar flow purging the system all the time to drive away the H_2 gas, the isolation of these anion-deficient reduced oxide phases still fails, which suggests that the preference for the oxide-hydride phase is so strong that even with small amount of hydrogen left in the system, the formation of the oxide-hydride phase is inevitable.

The successful synthesis of the first 4*d* transition metal oxide-hydride phases, $LaSr_3NiRuO_4H_4$ and $LaSr_3CoRuO_4H_4$, validates the hypothesis that it should be possible to prepare covalently stabilized oxide-hydride phases of late 4d transition metals, paralleling the strong σ-bonds observed in molecular hydride systems of late 4d transition metals. In

addition these two anion-ordered oxide-hydride phases have a 1:1 ratio of hydride to oxide ions, which is the highest yet reported, and the presence of a plane that contains only hydride ligands is a unique feature in the oxide–hydride chemistry.

This CaH_2 reduction chemistry has been extended to another 4d transition metal, rhodium. The Mn-oxide and Co-oxide lattices are chosen to couple with these reductions to prevent complete reduction of the rhodium to the elemental metal state, hence the first rhodium-containing oxide-hydride phases, $La_2Sr_2CoRhO_6H_2$ and $LaSr_3MnRhO_6H_2$, have been prepared from the corresponding A_4MRhO_8 oxide phases via topochemical anion exchange. The successful synthesis of these two oxide-hydride phases clearly demonstrates that the strong Rh-H σ-type bonding is able to kinetically stabilize oxide-hydride lattices, reinforcing the paradigm of covalent stabilization of transition-metal oxide-hydride phases.

Although the formation of oxide-hydride phases offers many attractive opportunities to modify the electronic properties of parent oxide phases due to the strongly contrasting features of the two anions, the anion-deficient reduced oxide phases which have been observed during the initial screening for the reactivity, are still worthy to study. Since the presence of the by-product H_2 gas makes the CaH_2 reduction a 'dead' approach in this case, alternative reduction methods need to be employed. Finely divided Zr powder, as an oxygen getter, has a similar reaction temperature regime as CaH_2, but does not generate any source of hydride ions, and thus provides an elegant solution to the problem mentioned above. Two reduced oxide phases, $LaSr_3NiRuO_6$ and $LaSr_3CoRuO_6$, have been successfully synthesized by treating their parent oxides with a Zr powder getter, which again proves that the accumulation of H_2 gas during the reaction is the key to form oxide-hydride phases, but it is something which needs to be avoided if reduced oxide phases are the target products. Although the formation of corresponding Rh-containing reduced oxide phases is less experimentally obvious when treating their parent oxide phases with CaH_2, it is still an open

and worthwhile possibility for future research, since if they follow the same reaction pathway as their Ru-containing analogues, the first Rh(I) or Rh(II) centres in extended solids can be prepared.

In addition, the cation doping of $LaSr_3NiRuO_8$ and $LaSr_3NiRuO_4H_4$ was studied with the intention of inducing metallic behaviour into these insulating phases. However, despite the large change in magnetic behaviour observed on doping these phases, which suggests that electrons of the B-site cations are no longer localised once the ratio between La and Sr deviates from 1:3, their electronic conductivity has not changed qualitatively compared to the undoped compounds. This suggests the electronic bands are too narrow for these n = 1 Ruddlesden-popper phases and electrons in the e_g band of $La_xSr_{4-x}NiRuO_8$ are still localised by strong on-site repulsion. In addition, upon hydride-for-oxide substitution, the degeneracy of the e_g band is broken chemically and splits into a d_{x2-y2} band and a d_{z2} band in the oxide-hydride phase, $La_xSr_{4-x}NiRuO_4H_4$. As a result, it makes the already narrow e_g band even narrower, which is not helpful for delocalising electrons. Therefore, switching to an n = 2 Ruddlesden-popper phase (wider bands) is another open and worthwhile possibility for future research, as it might induce the expected insulator-to-metal transition.

The idea of investigating n = 2 Ruddlesden-popper phases in the future is also derived from the presence of small amount of defects (n = 2 RP phase) within the framework of the n = 1 RP phase $LaSr_3CoRuO_4H_4$, which suggests that the anion-exchanged n = 2 RP phase is more energetically stable than the n = 1 RP phase in the Co/Ru case, and the activation energy barrier of forming the n = 2 RP exchanged phase is only slightly larger than that of forming the n = 1 RP exchanged phase, hence the reduction chemistry should not be too different.

Overall the work presented in this thesis shows that Ru-containing and Rh-containing complex transition-metal oxides have a rich reduction chemistry that has allowed for the isolation of both oxide-hydride phases and reduced oxide phases, depending on which reducing agent is used. The properties of these compounds are intimately linked to their structure and as such reinforce the integral link between the structure of a compound and the properties it exhibits, as discussed in Chapter 1. This thesis represents a significant amount of work but is by no means exhaustive, contrarily, the general direction of related areas of research indicate that there are still many open and worthwhile possibilities. The three clearest directions that can build on this work are the isolation of Rh-containing reduced oxide phases by using Zr powder getter to form the first Rh(I) or Rh(II) centres in extended solids, switching from $n = 1$ Ruddlesden-popper phases to $n = 2$ Ruddlesden-popper phases to see whether semi-conductors or even metallic compounds can be made as $n = 2$ systems have wider bands, and finally a deeper investigation of the doping chemistry of all possible candidates.

Appendix 1 Table of Figures

Figure 1.1. Topochemical reduction of $LaNiO_3$ with NaH to form the reduced oxide phase $LaNiO_2$ containing Ni^+ in square planes.[18] 4

Figure 1.2. Topochemical reduction of $Sr_3Fe_2O_5Cl_2$ with LiH to form the reduced oxide-halide phase $Sr_3Fe_2O_4Cl_2$ containing square planar Fe^{2+}.[22] 5

Figure 1.3. The reduction of (a) $SrFe_{0.5}Ru_{0.5}O_3$ and (b) $LaSrNiRuO_6$ via topochemical anion deintercalation using CaH_2.[10, 11] 6

Figure 1.4. Topochemical reduction of $SrVO_3$ with CaH_2 to form the reduced oxide-hydride phase $SrVO_2H$ with H^- substituted into axial positions [14] 7

Figure 1.5. Topochemical reduction of $LaSr_3NiRuO_8$ with CaH_2 to form reduced oxide-hydride phase $LaSr_3NiRuO_4H_4$ with H^- substituted into equatorial positions [13]. 8

Figure 1.6. Topochemical reduction of $LaCoO_3$ with Zr getter to form the anion-deficient perovskite $La_2Co_2O_5$.[27] 10

Figure 1.7. Topochemical reduction of $CaMnO_3$ with H_2 gas to form the anion-deficient perovskite $CaMnO_{2.5}$.[29] 11

Figure 1.8. The ABO_3 perovskite type structure of (a) $SrTiO_3$ (*Pm*-3*m*) and (b) $CaTiO_3$ (*Pbnm*).[32, 33] 13

Figure 1.9. The structure of the hexagonal variant perovskite $BaNiO_3$ ($P6_3/mmc$).[36] 14

Figure 1.10. The Ruddlesden-Popper phases with n = 1, 2 and 3, along with coordination environments of two different A-sites. 16

Figure 1.11. Orbital of a) an atom; b) a small molecule; c) a large molecule; becoming d) the band with the density of states in extended solids.[48] 19

Figure 1.12. The hopping (t) and energy (U) terms in the Hubbard model.[48] 20

Figure 1.13. Hubbard sub-bands as a function of the band width W. On energy axis E, $-I$ represents the ionisation energy and $-A$ the electron affinity.[49] 21

Figure 1.14. Structures of Sr_2RuO_4 (left), Ca_2RuO_4 (middle) and Sr_2IrO_4 (right).[56] 23

Figure 2.1. The schematic representation of the venting apparatus. 29

Figure 2.2. The schematic representation of the zirconium getter ampoule. 31

Figure 2.3. The schematic representation of an air-sensitive X-ray sample holder. 32

Figure 2.4. Bragg's construction for diffraction of monochromatic radiation by a set of parallel lattice planes. 33

Figure 2.5. Engineering layout of the Wish diffractometer. The two pictures show the instrument in the TS2 experimental hall (right) and the large ^3He detector array inside the blockhouse (left).[68] 39

Figure 2.6. D2B diffractometer at ILL, Grenoble, France.[69] 40

Figure 2.7. Schematic representation of the principal component in a SQUID magnetometer.[75] 44

Figure 2.8. Schematic representation of a magnetisation-field isotherm of a sample consisting of a paramagnetic phase and a ferromagnetic impurity phase. The dotted line indicates the region used for a ferrosubtraction experiment. 46

Figure 2.9. A schematic representation of super-exchange interactions of M-O-M in 180° (left) and 90° (right) arrangements. 49

Figure 2.10. A schematic representation of two types of layers and four different stacking situations. 52

Figure 3.1: Rietveld refinement of $LaSr_3NiRuO_8$ using *I* 4/*m m m* model against synchrotron X-ray powder diffraction data. Observed (red), calculated (green), and difference plots (pink) are shown. 55

Figure 3.2. Crystal structure of $LaSr_3NiRuO_8$ (space group *I*4/*mmm*) with thermal ellipsoids displayed. 57

Figure 3.3. Observed, calculated and difference plots from the refinement of $LaSr_3NiRuO_8$ against neutron powder diffraction data collected at 298 K, full range (top) and high angles (bottom) 58

Figure 3.4. Zero-field-cooled and field-cooled magnetisation data collected in an applied field of 100 Oe. Inset shows fit to the Curie-Weiss law (top); Magnetisation data collected as a function of applied field (bottom) from $LaSr_3NiRuO_8$. 61

Figure 3.5. Predicted spin states of B-site transition metal cations in $LaSr_3NiRuO_8$. 62

Figure 3.6. Crystallographic structures of (a) cation-disordered simple perovskite $SrFe_{0.5}Ru_{0.5}O_3$ and (b) cation-ordered double perovskite $LaSrNiRuO_6$ [10, 11]. 65

Figure 4.1. Topochemical reduction profile of $LaSr_3NiRuO_8$ with CaH_2 to form a range composition of $LaSr_3NiRuO_{8-x}$. 72

Figure 4.2. Topochemical reduction of $LaSr_3NiRuO_8$ with CaH_2 to form reduced oxide-hydride phase $LaSr_3NiRuO_4H_4$ with H^- substituted into equatorial positions. 75

Figure 4.3. Observed, calculated and difference plots from the refinement of $LaSr_3NiRuO_4H_4$ against neutron powder diffraction data collected at 298 K. Lower tick marks indicate peak positions of the majority phase, upper tick marks CaO. 76

Figure 4.4. Observed, calculated and difference plots from the refinement of $LaSr_3NiRuO_4H_4$ (space group *I*4/*mmm*) against synchrotron X-ray powder diffraction data collected at 298 K. Lower tick marks indicate peak positions of the majority phase, upper tick marks CaO. 80

Figure 4.5. The O_2H_4 coordination of Ni^+ and Ru^{2+} results in $S = ½$ and $S = 0$ spin states, respectively. 81

Figure 4.6. The paramagnetic susceptibility (top) and saturated ferromagnetic moment (bottom) of $LaSr_3NiRuO_4H_4$ collected as a function of temperature. Inset: the fit to the Curie–Weiss law in the temperature range $10 < T / K < 300$. 82

Figure 4.7. 2√2 x 2√2 x 1 expanded unit cell used in the computational model. Grey: La; Brown: Sr; Green: Ni; Yellow: Ru; Red: O; Purple: H. 84

Figure 4.8. Spin-polarized projected density of states (Ni and Ru) for $LaSr_3NiRuO_4H_4$ (U_{eff}(Ni)=6.0 eV, U_{eff}(Ru)=3.0 eV). The Ni^+ ions are coupled ferromagnetically within the $NiRuH_2$ layers, but coupling between adjacent layers is antiferromagnetic. 84

Figure 4.9. Plots of the asymmetry of μ^+SR data collected from $LaSr_3NiRuO_4H_4$ at various temperatures. 86

Figure 4.10. The topologically distinct anion sites in the n = 1 Ruddlesden-Popper phase $LaSr_3NiRuO_8$ 88

Figure 4.11. The schematic electronic band structure of the oxide-hydride phase $LaSr_3NiRuO_4H_4$. 91

Figure 4.12. Orbital overlapping through a linear Ni-H-Ru-H-Ni superexchange pathway in $LaSr_3NiRuO_4H_4$. 93

Figure 5.1. Rietveld refinement of synchrotron X-ray powder diffraction data collected from $La_{1.4}Sr_{2.6}NiRuO_8$ against *I4/mmm* model. Observed (red), calculated (green), and difference plots (pink) are shown. 98

Figure 5.2. Plot (a) *a*; (b) *c*; (c) *a/c*; and (d) volume against x in $La_xSr_{4-x}NiRuO_8$ ($0.5 \leq x \leq 1.5$) series of compounds. 99

Figure 5.3. Zero-field-cooled and field-cooled magnetisation data collected in an applied field of 100 Oe. Inset shows fit to the Curie-Weiss law (left); Magnetisation data collected as a function of applied field (right) from $La_{0.6}Sr_{3.4}NiRuO_8$. 102

Figure 5.4. Plot of (a) Curie Constant; and (b) Weiss Temperature against x in $La_xSr_{4-x}NiRuO_8$ ($0.5 \leq x \leq 1.5$) series of compounds. 103

Figure 5.5. Predicted spin states of B-site transition metal cations in $La_xSr_{4-x}NiRuO_8$ ($0.5 \leq x \leq 1.5$) series of compounds. 104

Figure 5.6. Magnetisation data collected as a function of applied field from (a) $LaSr_3NiRuO_8$ and (b) $La_{1.5}Sr_{2.5}NiRuO_8$ 106

Figure 5.7. Rietveld refinement of synchrotron X-ray powder diffraction data collected from $La_{1.3}Sr_{2.7}NiRuO_4H_4$ against *I4/mmm* model. Observed (red), calculated (green), and difference plots (pink) are shown. 107

Figure 5.8. Plot (a) *a*; (b) *c*; (c) *a/c*; and (d) volume against x in $La_xSr_{4-x}NiRuO_4H_4$ ($0.5 \leq x \leq 1.5$) series of compounds. 108

Figure 5.9. The paramagnetic susceptibility (left) and saturated ferromagnetic moment (right) of $La_{0.8}Sr_{3.2}NiRuO_4H_4$ collected as a function of temperature. Inset: the fit to the Curie–Weiss law in the temperature range $115 < T / K < 300$. 110

Figure 5.10. Plot of (a) Curie Constant; and (b) Weiss Temperature against x in $La_xSr_{4-x}NiRuO_4H_4$ ($0.5 \leq x \leq 1.5$) series of compounds 112

Figure 5.11. Predicted spin states of B-site transition metal cations in $La_xSr_{4-x}NiRuO_4H_4$ ($0.5 \leq x \leq 1.5$) series of compounds. 113

Figure 5.12. Orbital overlapping through a linear Ni-H-Ru-H-Ni superexchange pathway in $LaSr_3NiRuO_4H_4$. 114

Figure 6.1. Observed, calculated and difference plots from the refinement of synchrotron X-ray powder diffraction data (*Immm*) collected from $LaSr_3NiRuO_6$ (formed at 425 °C in CaH_2 reduction). 122

Figure 6.2. Observed, calculated and difference plots from the refinement of synchrotron X-ray powder diffraction data (*Immm*) collected from $LaSr_3NiRuO_6$ (formed at 500 - 510 °C in Zr powder reduction). 126

Figure 6.3. Plots of mass gain against temperature collected from (a) small sample and (b) neutron sample of $LaSr_3NiRuO_6$. 128

Figure 6.4. Observed, calculated and difference plots from the (a) single-phase and (b) two-phase refinement of synchrotron X-ray powder diffraction data (space group *Immm*) collected from $LaSr_3NiRuO_6$ at 298 K. Lower tick marks indicate peak positions of the majority phase, upper tick marks minority phase $LaSr_3NiRuO_{7-x}$. 131

Figure 6.5. Topochemical reduction of $LaSr_3NiRuO_8$ with Zr powder to form reduced oxide phase $LaSr_3NiRuO_6$ with ordered oxide vacancies along *b*-axis. 132

Figure 6.6. Observed, calculated and difference plots from the (a) single-phase and (b) two-phase refinement of neutron powder diffraction data (space group *Immm*) collected from $LaSr_3NiRuO_6$ at 298 K. Lower tick marks indicate peak positions of the majority phase, upper tick marks minority phase $LaSr_3NiRuO_{7-x}$. 133

Figure 6.7. Observed, calculated and difference plots from the single-phase refinement of neutron powder diffraction data (space group *C*2/*c*) collected from $LaSr_3NiRuO_6$ at 298 K. 137

Figure 6.8. The paramagnetic susceptibility (top) and saturated ferromagnetic moment (bottom) of $LaSr_3NiRuO_6$ collected as a function of temperature. Inset: the fit to the Curie–Weiss law in the temperature range $100 < T / K < 300$. 139

Figure 6.9. Proposed electronic configurations of $LaSr_3NiRuO_6$. 140

Figure 6.10. Observed, calculated and difference plots from the two-phase refinement of neutron powder diffraction data (space group *Immm*) collected from $LaSr_3NiRuO_6$ at 10 K. Lower tick marks indicate peak positions of the majority phase, upper tick marks $LaSr_3NiRuO_{7-x}$. 141

Figure 6.11. Comparing low-angle neutron powder diffraction data collected from $LaSr_3NiRuO_6$ at 298 K and 10 K. 144

Figure 6.12. (a) Experimental neutron powder diffraction data collected from $LaSr_3NiRuO_6$ at 10 K; Simulations of ferromagnetic unit cells as moment pointing along (b) *a*; (c) *b* and (d) *c* directions by using a 100-times real scale factor. 146

Figure 6.13. The topologically distinct anion sites in the n = 1 Ruddlesden-Popper phase $LaSr_3NiRuO_8$.....147

Figure 7.1: Rietveld refinement of synchrotron X-ray powder diffraction data collected from $LaSr_3CoRuO_8$ against *I4/mmm* model. Observed (red), calculated (green), and difference plots (pink) are shown.....156

Figure 7.2. Crystal structure of $LaSr_3CoRuO_8$ (space group *I*4/*mmm*) with thermal ellipsoids displayed. 157

Figure 7.3. Observed, calculated and difference plots from the refinement of $LaSr_3CoRuO_8$ against neutron powder diffraction data collected at 298 K, full range (top) and high angles (bottom).....158

Figure 7.4. Zero-field-cooled and field-cooled magnetisation data collected in an applied field of 100 Oe. Inset shows fit to the Curie-Weiss law (top); Magnetisation data collected as a function of applied field (bottom) from $LaSr_3CoRuO_8$. 161

Figure 7.5. Predicted spin states of B-site transition metal cations in $LaSr_3CoRuO_8$. 162

Figure 7.6. Plots of mass gain against temperature collected from the large-scale neutron sample of $LaSr_3CoRuO_6$. 164

Figure 7.7. Observed, calculated and difference plots from the refinement of synchrotron X-ray powder diffraction data collected from $LaSr_3CoRuO_6$ (space group *Immm*) at 298 K. Tick marks indicate peak positions of the majority phase (black), La_2O_3 (red) and SrO (blue)....165

Figure 7.8. Topochemical reduction of $LaSr_3CoRuO_8$ with Zr powder to form reduced oxide phase $LaSr_3CoRuO_6$ with ordered oxide vacancies along *b*-axis 166

Figure 7.9. Observed, calculated and difference plots from the refinement of neutron powder diffraction data collected from $LaSr_3CoRuO_6$ (space group *Immm*) at 298 K (top) and 5 K (bottom). Tick marks indicate peak positions of the majority phase (black), La_2O_3 (red) and SrO (blue).....167

Figure 7.10. The paramagnetic susceptibility (top) and saturated ferromagnetic moment (bottom) of $LaSr_3CoRuO_6$ collected as a function of temperature. Inset: the fit to the Curie–Weiss law in the temperature range $65 < T / K < 300$. 172

Figure 7.11. Proposed electronic configurations of $LaSr_3CoRuO_6$. 173

Figure 7.12. Topochemical reduction of $LaSr_3CoRuO_8$ with CaH_2 to form reduced oxide-hydride phase $LaSr_3CoRuO_4H_4$ with H^- substituted into equatorial positions. 174

Figure 7.13. Observed, calculated and difference plots from the refinement of neutron powder diffraction data collected from $LaSr_3CoRuO_4H_4$ (space group *I*4/*mmm*) at 298 K. Tick marks indicate peak positions of the majority phase (black) and the minority phase $LaSr_3CoRuO_{6\pm x}$ (red).....175

Figure 7.14. Observed, calculated and difference plots from the refinement of synchrotron X-ray powder diffraction data collected from $LaSr_3CoRuO_4H_4$ (space group *I*4/*mmm*) at 298 K. Tick marks indicate peak positions of the majority phase (black) and the minority phase $LaSr_3CoRuO_{6\pm x}$ (red). 179

Figure 7.15. Observed, calculated and difference plots from the zoom-in area $10 \leq 2\theta/^\circ \leq 30$ of the refinement of synchrotron X-ray powder diffraction data collected from $LaSr_3CoRuO_4H_4$ (space group *I*4/*mmm*) at 298 K. 179

Figure 7.16. Electron diffraction (ED) patterns collected from $LaSr_3CoRuO_4H_4$, taken along [100] and [110] directions. 181

Figure 7.17. HAADF-STEM images of the crystals covered with nanoparticles. 182

Figure 7.18. HAADF-STEM image from the perfect regions of *n* = 1 RP phase $LaSr_3CoRuO_4H_4$. 182

Figure 7.19. HAADF-STEM image from the *n* = 1 RP structure with inclusions of two *n* = 2 blocks. An intensity profile was measured along the arrow and corresponds to the intensity of 2-1-1-2 blocks (the signal is averaged along the b axis). Note that the A cation layers in the middle of the perovskite blocks of the *n* = 2 fragments are brighter than at the periphery and therefore they are most likely La-rich. 183

Figure 7.20. HAADF-STEM images of areas with *n* = 2 RP structure. On the left image there is a block of four perovskite unit cells and also one perovskite slab is present near the bottom of the image. On the right image, there are a few *n* = 3 and *n* = 1 blocks. The surface of the crystals is amorphous. Intensity profiles measured along the arrows are shown at the bottom of the images. Again, the central rows in the *n* = 2 RP are brighter and thus probably enriched with La. Also in these defects, the central A cation rows in the total perovskite blocks are brighter, most probably indicating La enrichment. 184

Figure 7.21. Transition probability of layer 1 to 2 plotted against that of layer 2 to 2. 186

Figure 7.22. Rietveld refinement of laboratory X-ray powder diffraction data (top), and zoom-in area ($37 \leq 2\theta/^\circ \leq 49$) of simulated patterns for route (a) (bottom). 187

Figure 7.23. Zoom-in area ($36 \leq 2\theta/^\circ \leq 50$) of simulated patterns for route (b). 189

Figure 7.24. Zoom-in area ($37 \leq 2\theta/^\circ \leq 49$) of the simulated pattern resulted from 5% of layer 1 to layer 2 transition and 75% of layer 2 to layer 2 transition, compared to the laboratory X-ray diffraction pattern. 190

Figure 7.25. The proposed reaction profile for topochemical reduction of $LaSr_3CoRuO_8$ with CaH_2. 191

Figure 7.26. The O_2H_4 coordination of Co^+ and Ru^{2+} results in *S* = 1 and *S* = 0 spin states, respectively. 192

Figure 7.27. The paramagnetic susceptibility (top) and saturated ferromagnetic moment (bottom) of $LaSr_3CoRuO_4H_4$ collected as a function of temperature. Inset: the fit to the Curie–Weiss law in the temperature range $25 < T / K < 300$. 193

Figure 7.28. Plots of the asymmetry of μ^+SR data collected from $LaSr_3CoRuO_4H_4$ at various temperatures. 194

Figure 7.29. The topologically distinct anion sites in the *n* = 1 Ruddlesden-Popper phase $LaSr_3CoRuO_8$. 196

Figure 8.1. Observed, calculated and difference plots from the refinement of $LaSr_3MnRhO_8$ against synchrotron X-ray powder diffraction data collected at 298 K. 203

Figure 8.2. Crystal structures of $LaSr_3MnRhO_8$ with thermal ellipsoids displaced at 298K (left) and 5 K (right).....204

Figure 8.3. Observed, calculated and difference plots from the refinements of $LaSr_3MnRhO_8$ against neutron powder diffraction data collected at 298 K (top) and 5 K (bottom).....205

Figure 8.4. Observed, calculated and difference plots from the refinement of $La_2Sr_2CoRhO_8$ against synchrotron X-ray powder diffraction data collected at 298 K. 208

Figure 8.5. Crystal structures of $La_2Sr_2CoRhO_8$ with thermal ellipsoids displaced at 298 K (left) and 5 K (right).....209

Figure 8.6. Observed, calculated and difference plots from the refinements of $La_2Sr_2CoRhO_8$ against neutron powder diffraction data collected at 298 K (top) and 5 K (bottom).....210

Figure 8.7. Zero-field-cooled and field-cooled magnetisation data (top); 300 K and 5 K magnetisation-field isotherms (bottom) of $La_{0.5}Sr_{1.5}Mn_{0.5}Rh_{0.5}O_4$. 213

Figure 8.8. The plot of H/M against temperature with data in temperature ranges $210 < T / K < 300$ and $125 < T / K < 200$ fitted to the Curie-Weiss law ($\chi = C/(T - \theta)$) and proposed electronic configurations of $La_{0.5}Sr_{1.5}Mn_{0.5}Rh_{0.5}O_4$, respectively. 214

Figure 8.9. Comparing low-angle neutron powder diffraction data collected from $LaSr_3MnRhO_8$ at 298 K and 5 K.....216

Figure 8.10. Zero-field-cooled and field-cooled magnetisation data (top); 300 K and 5 K magnetisation-field isotherms (bottom) of $LaSrCo_{0.5}Rh_{0.5}O_4$.....217

Figure 8.11. The plot of H/M against temperature with data in temperature ranges $200 < T / K < 300$ and $65 < T / K < 185$ fitted to the Curie-Weiss law ($\chi = C/(T - \theta)$) and proposed electronic configurations of $LaSrCo_{0.5}Rh_{0.5}O_4$, respectively. 218

Figure 8.12. Comparing low-angle neutron powder diffraction data collected from $La_2Sr_2CoRhO_8$ at 298 K and 5 K. 220

Figure 9.1. X-ray powder diffraction patterns collected from the products of reaction between CaH_2 and a) $La_2Sr_2CoRhO_8$ or b) $LaSr_3MnRhO_8$ as a function of reaction temperature. 227

Figure 9.2. Thermogravimetric data collected during the oxidation of $LaSr_3MnRhO_6H_2$. ...229

Figure 9.3. Thermogravimetric data collected during the oxidation of $La_2Sr_2CoRhO_6H_2$. ...229

Figure 9.4. Topochemical reduction of $LaSr_3MnRhO_8$ with CaH_2 to form reduced oxide-hydride phase $LaSr_3MnRhO_6H_2$. 230

Figure 9.5. Observed, calculated and difference plots from the structural refinement of $LaSr_3MnRhO_6H_2$ against neutron powder diffraction data collected at 298 K. 231

Figure 9.6. Observed, calculated and difference plots from the structural refinement of $LaSr_3MnRhO_6H_2$ against neutron powder diffraction data collected at 2 K. 232

Figure 9.7. Observed, calculated and difference plots from the refinement of $LaSr_3MnRhO_6H_2$ (space group *I*4/*mmm*) against synchrotron X-ray powder diffraction data collected at 298 K. 236

Figure 9.8. Topochemical reduction of $La_2Sr_2CoRhO_8$ with CaH_2 to form reduced oxide-hydride phase $La_2Sr_2CoRhO_6H_2$. 237

Figure 9.9. Observed, calculated and difference plots from the refinements of $La_2Sr_2CoRhO_6H_2$ (space group *I*4/*mmm*) against neutron powder diffraction data collected at 298 K (top) and 5 K (bottom); Lower tick marks indicate peak positions of the majority phase, upper tick marks La_2O_3. 238

Figure 9.10. Observed, calculated and difference plots from the refinements of $La_2Sr_2CoRhO_6H_2$ (space group *I*4/*mmm*) against synchrotron X-ray powder diffraction data collected at 298 K; Lower tick marks indicate peak positions of the majority phase, upper tick marks La_2O_3. 242

Figure 9.11. A linear fit to the high-field region (H > 30000 Oe) of magnetisation data collected from $LaSr_3MnRhO_6H_2$, measured as a function of applied field at 300 K.....244

Figure 9.12. The paramagnetic susceptibility (top) and saturated ferromagnetic moment (bottom) of $LaSr_3MnRhO_6H_2$ collected as a function of temperature. 244

Figure 9.13. Proposed electronic configurations of $LaSr_3MnRhO_8$ and $LaSr_3MnRhO_6H_2$...245

Figure 9.14. A linear fit to the high-field region (H > 30000 Oe) of magnetisation data collected from $La_2Sr_2CoRhO_6H_2$, measured as a function of applied field at 300 K. 246

Figure 9.15. The paramagnetic susceptibility (top) and saturated ferromagnetic moment (bottom) of $La_2Sr_2CoRhO_6H_2$ collected as a function of temperature.....246

Figure 9.16. Proposed electronic configurations of $La_2Sr_2CoRhO_8$ and $La_2Sr_2CoRhO_6H_2$..247

Appendix 2 Additional Data for Chapter 5

Appendix 2.1 Synchrotron X-ray diffraction data of $La_xSr_{4-x}NiRuO_8$ ($0.5 \leq x \leq 1.5$)

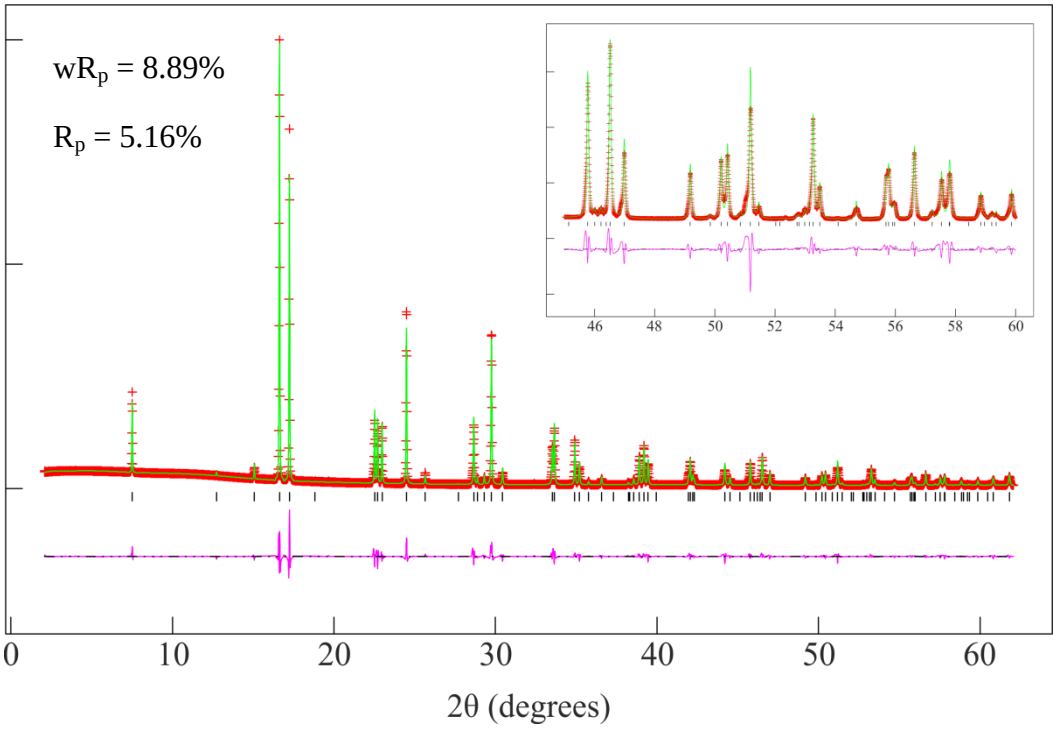


Figure 2.1. Rietveld refinement of synchrotron X-ray powder diffraction data collected from $La_{0.5}Sr_{3.5}NiRuO_8$ against *I4/mmm* model. Observed (red), calculated (green), and difference plots (pink) are shown.

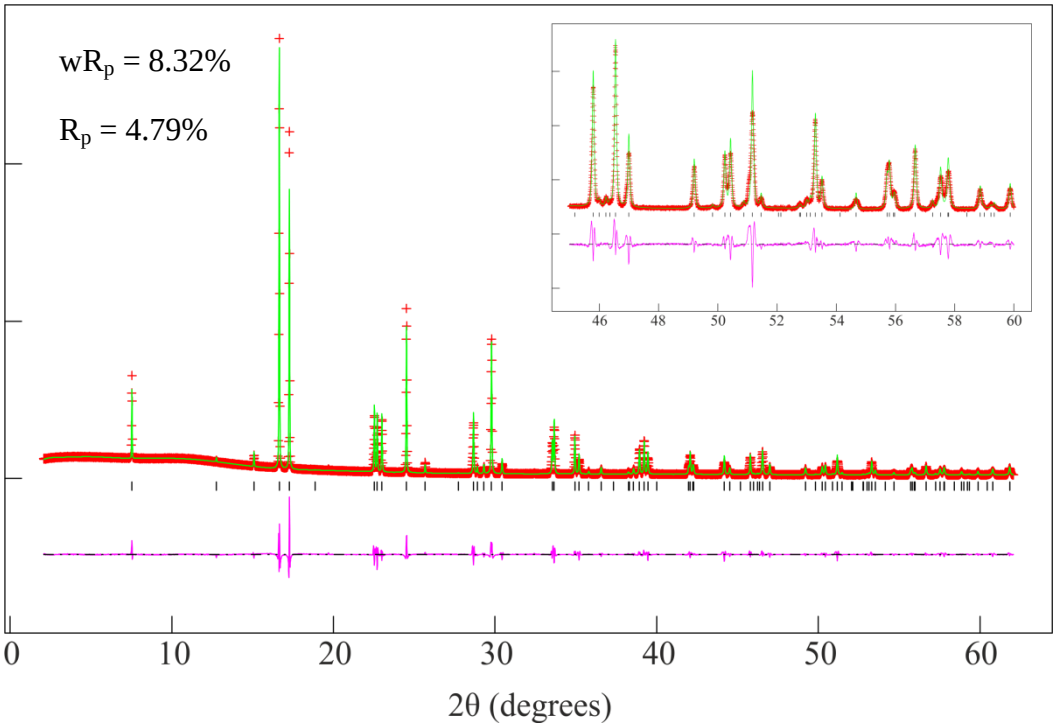


Figure 2.2. Rietveld refinement of synchrotron X-ray powder diffraction data collected from $La_{0.6}Sr_{3.4}NiRuO_8$ against *I4/mmm* model. Observed (red), calculated (green), and difference plots (pink) are shown.

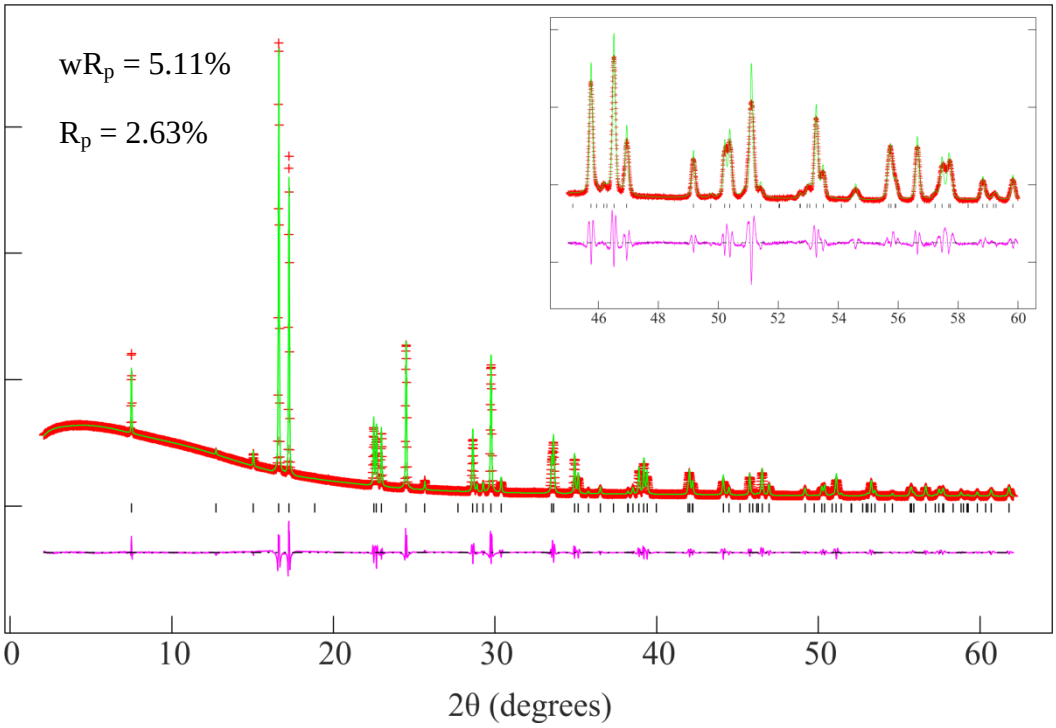


Figure 2.3. Rietveld refinement of synchrotron X-ray powder diffraction data collected from $La_{0.7}Sr_{3.3}NiRuO_8$ against *I4/mmm* model. Observed (red), calculated (green), and difference plots (pink) are shown.

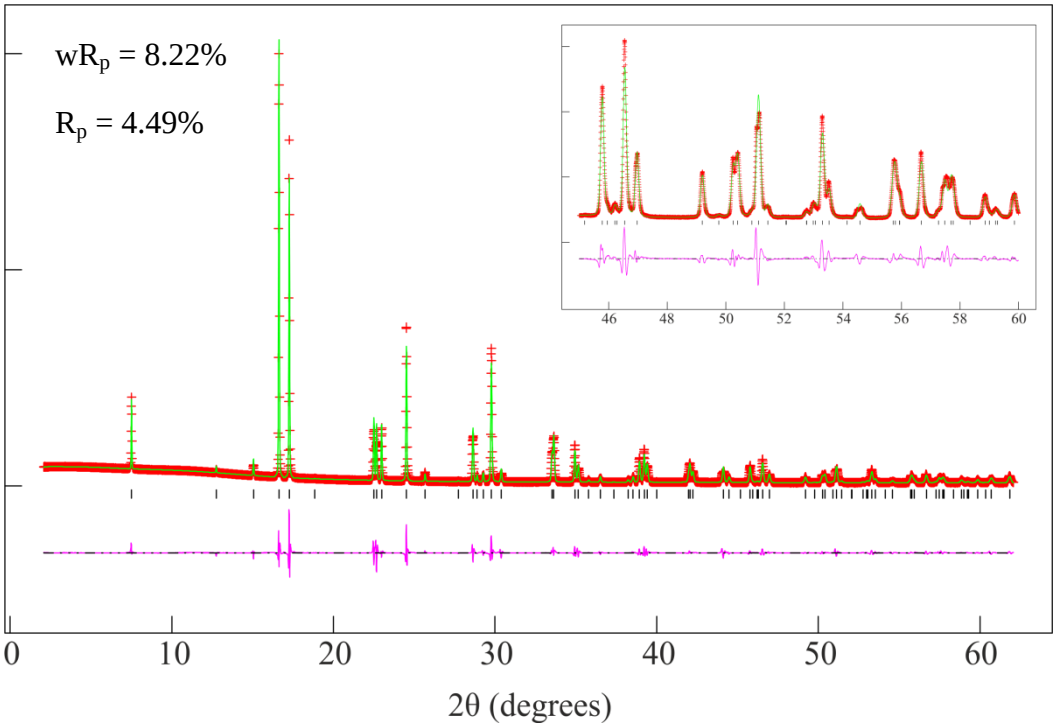


Figure 2.4. Rietveld refinement of synchrotron X-ray powder diffraction data collected from $La_{0.8}Sr_{3.2}NiRuO_8$ against *I4/mmm* model. Observed (red), calculated (green), and difference plots (pink) are shown.

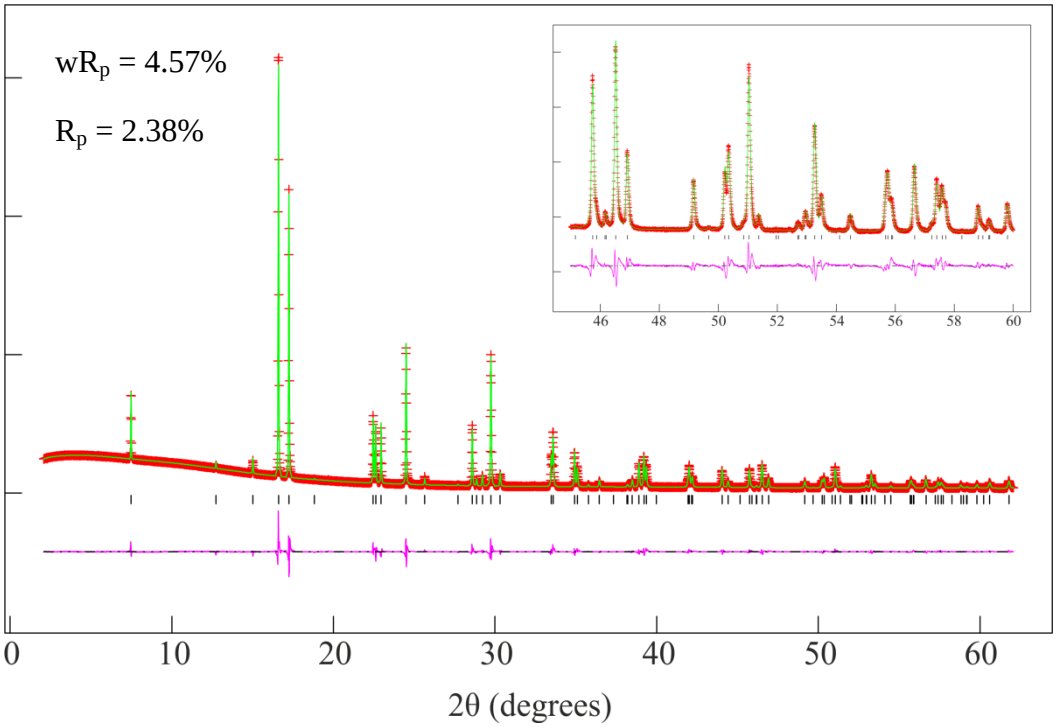


Figure 2.5. Rietveld refinement of synchrotron X-ray powder diffraction data collected from $La_{0.9}Sr_{3.1}NiRuO_8$ against *I4/mmm* model. Observed (red), calculated (green), and difference plots (pink) are shown.

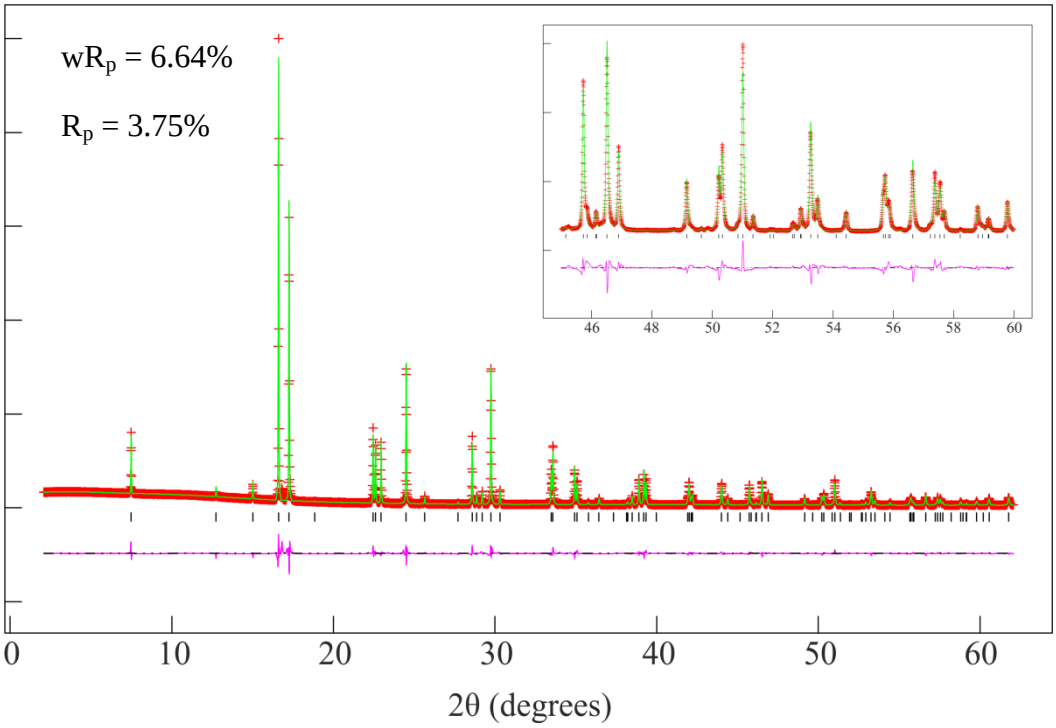


Figure 2.6. Rietveld refinement of synchrotron X-ray powder diffraction data collected from $La_{1.1}Sr_{2.9}NiRuO_8$ against *I4/mmm* model. Observed (red), calculated (green), and difference plots (pink) are shown.

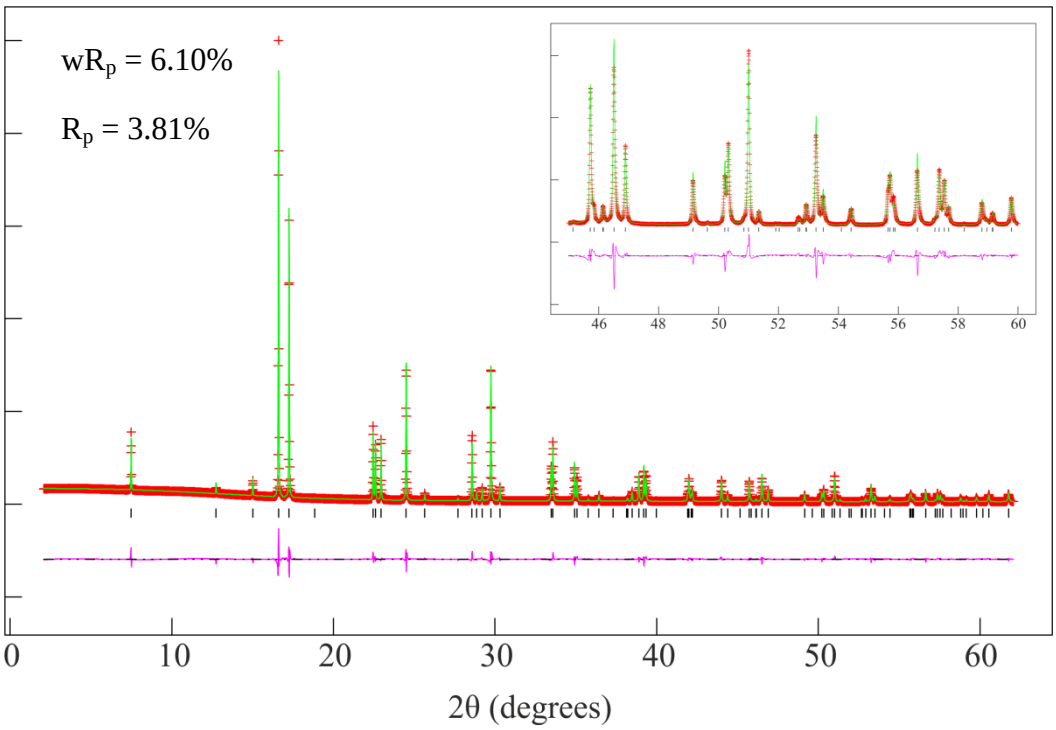


Figure 2.7. Rietveld refinement of synchrotron X-ray powder diffraction data collected from $La_{1.2}Sr_{2.8}NiRuO_8$ against *I4/mmm* model. Observed (red), calculated (green), and difference plots (pink) are shown.

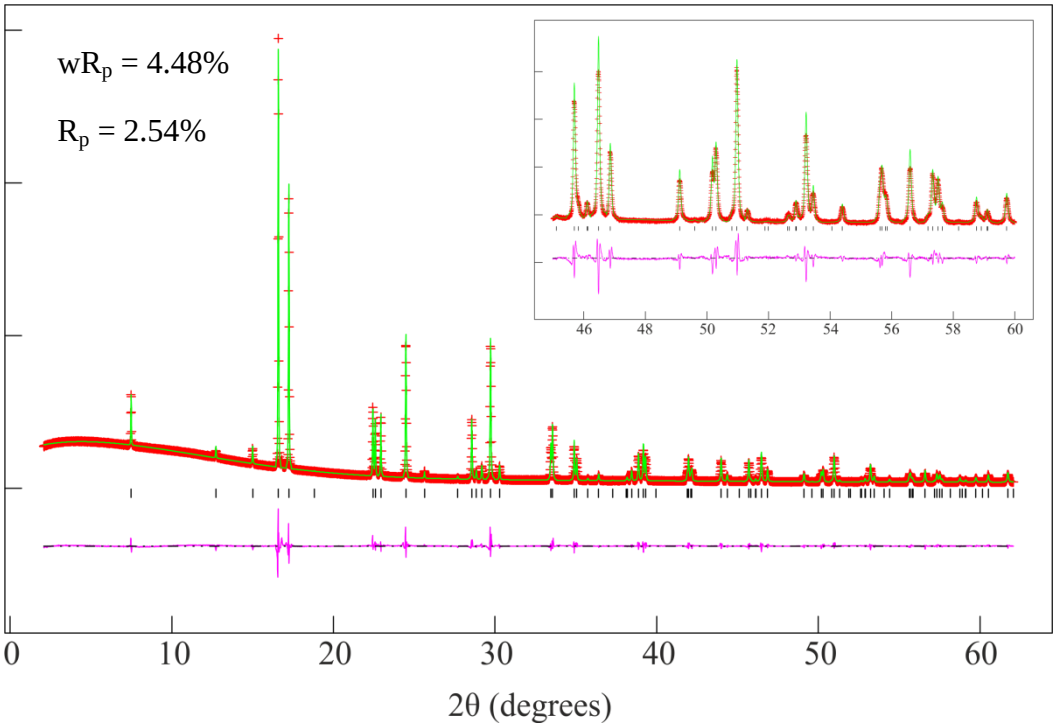


Figure 2.8. Rietveld refinement of synchrotron X-ray powder diffraction data collected from $La_{1.3}Sr_{2.7}NiRuO_8$ against *I4/mmm* model. Observed (red), calculated (green), and difference plots (pink) are shown.

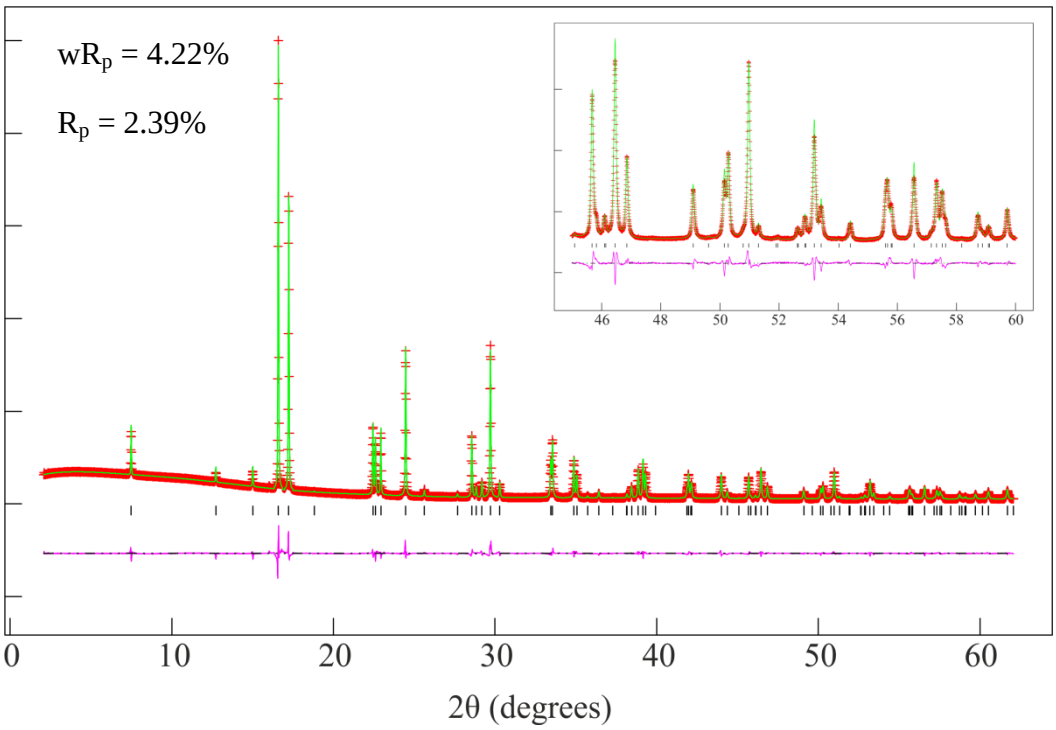


Figure 2.9. Rietveld refinement of synchrotron X-ray powder diffraction data collected from $La_{1.5}Sr_{2.5}NiRuO_8$ against *I4/mmm* model. Observed (red), calculated (green), and difference plots (pink) are shown.

Appendix 2.2 Magnetisation data of $La_xSr_{4-x}NiRuO_8$ ($0.5 \leq x \leq 1.5$)

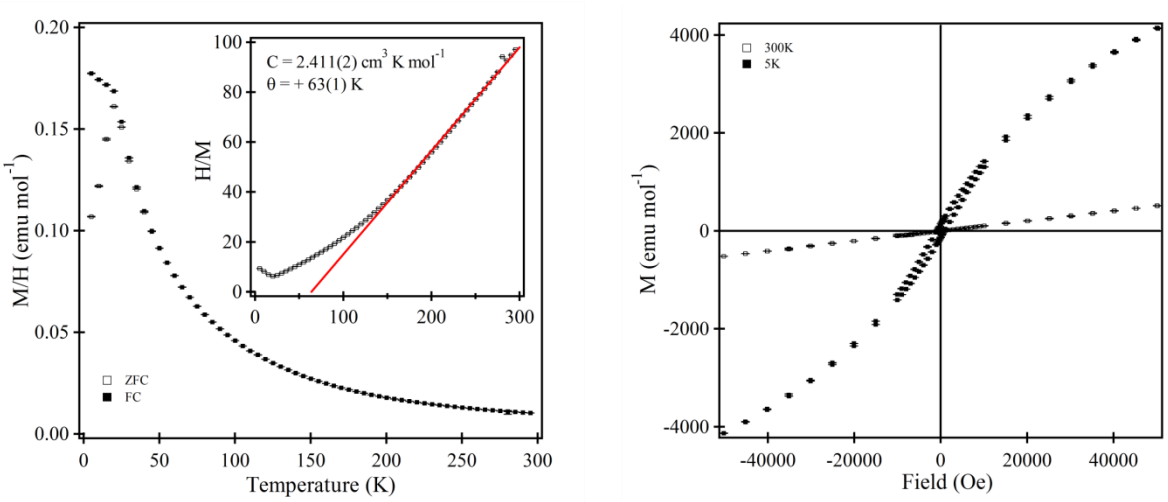


Figure 2.10. Zero-field-cooled and field-cooled magnetisation data collected in an applied field of 100 Oe. Inset shows fit to the Curie-Weiss law (left); Magnetisation data collected as a function of applied field (right) from $La_{0.5}Sr_{3.5}NiRuO_8$.

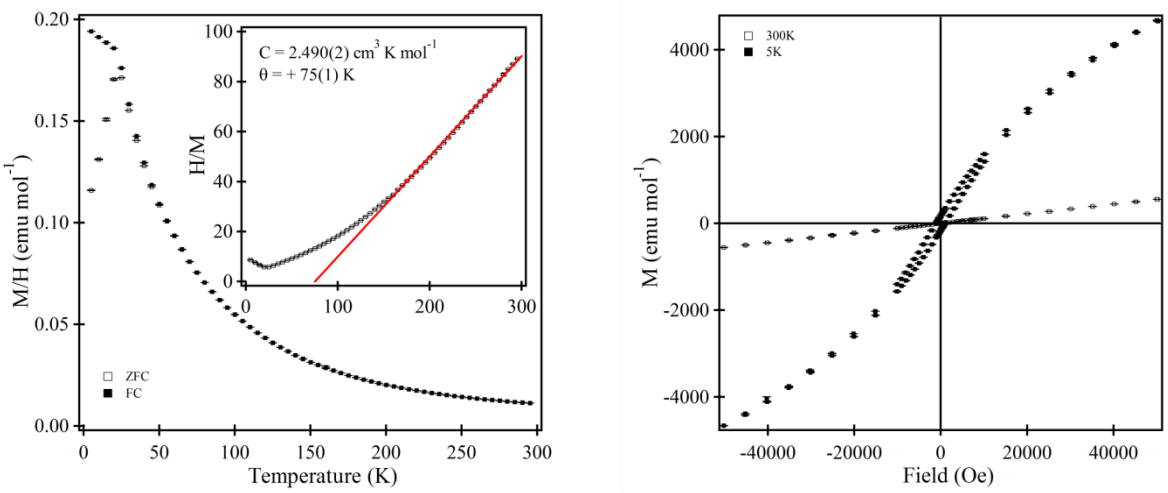


Figure 2.11. Zero-field-cooled and field-cooled magnetisation data collected in an applied field of 100 Oe. Inset shows fit to the Curie-Weiss law (left); Magnetisation data collected as a function of applied field (right) from $La_{0.6}Sr_{3.4}NiRuO_8$.

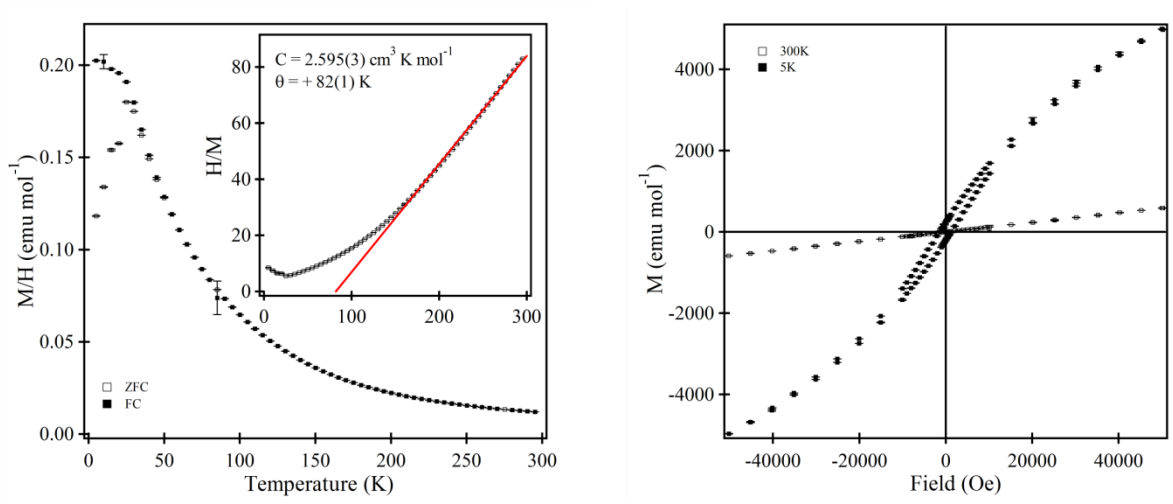


Figure 2.12. Zero-field-cooled and field-cooled magnetisation data collected in an applied field of 100 Oe. Inset shows fit to the Curie-Weiss law (left); Magnetisation data collected as a function of applied field (right) from $La_{0.7}Sr_{3.3}NiRuO_8$.

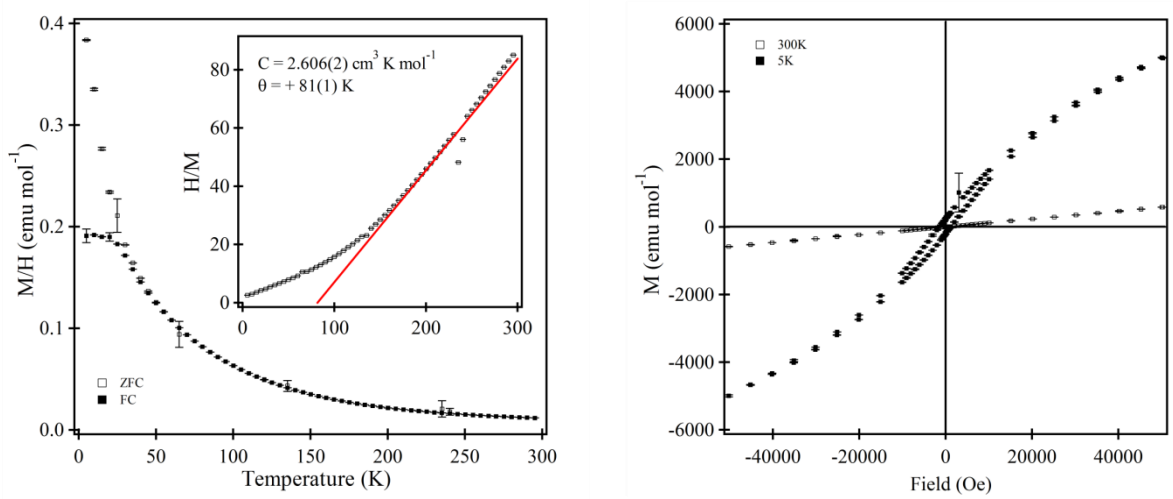


Figure 2.13. Zero-field-cooled and field-cooled magnetisation data collected in an applied field of 100 Oe. Inset shows fit to the Curie-Weiss law (left); Magnetisation data collected as a function of applied field (right) from $La_{0.8}Sr_{3.2}NiRuO_8$.

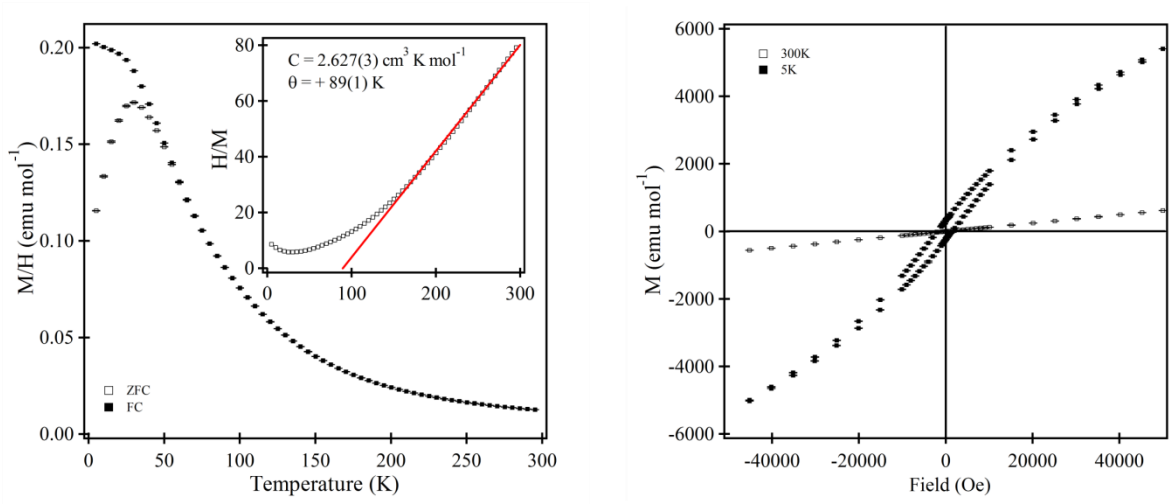


Figure 2.14. Zero-field-cooled and field-cooled magnetisation data collected in an applied field of 100 Oe. Inset shows fit to the Curie-Weiss law (left); Magnetisation data collected as a function of applied field (right) from $La_{0.9}Sr_{3.1}NiRuO_8$.

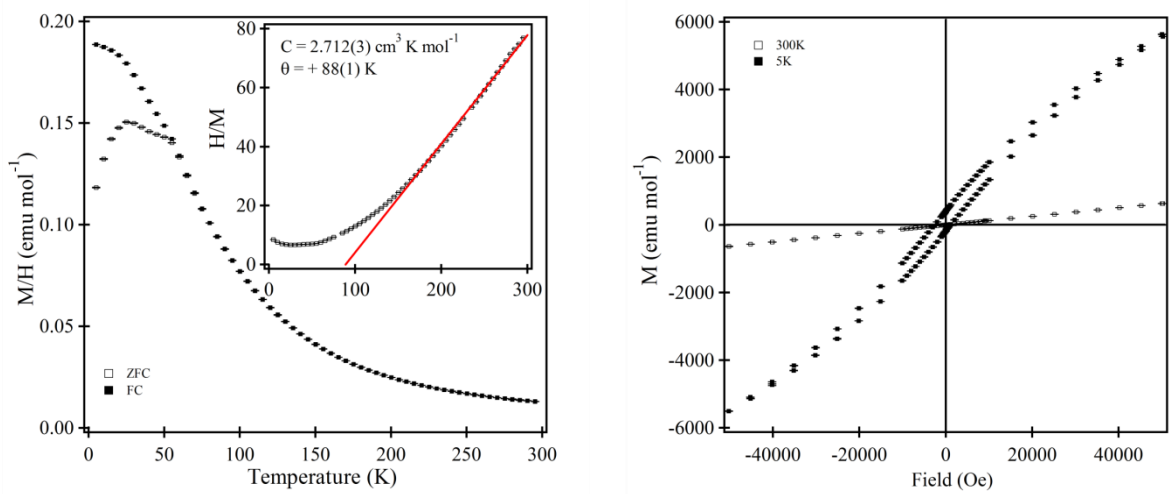


Figure 2.15. Zero-field-cooled and field-cooled magnetisation data collected in an applied field of 100 Oe. Inset shows fit to the Curie-Weiss law (left); Magnetisation data collected as a function of applied field (right) from $La_{1.1}Sr_{2.9}NiRuO_8$.

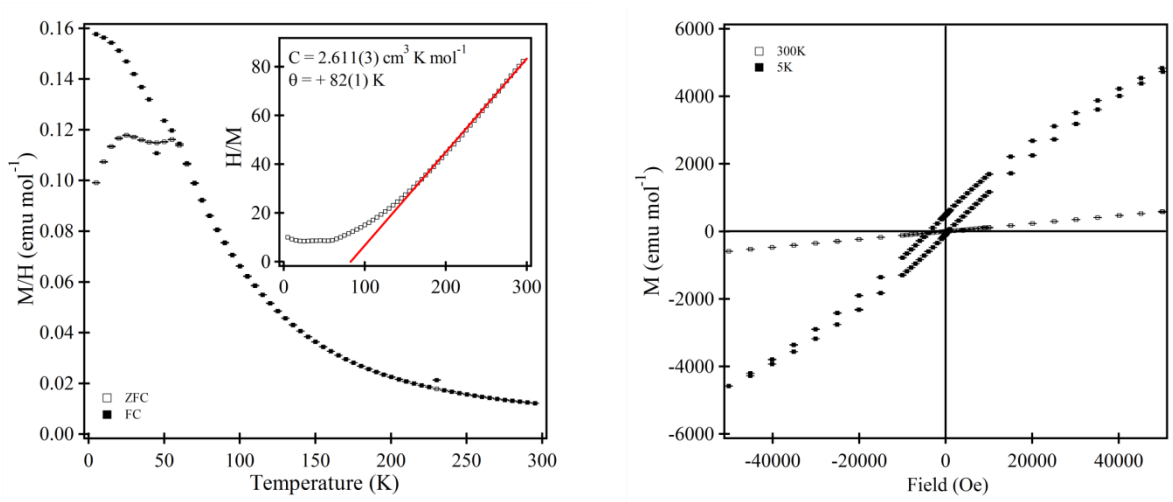


Figure 2.16. Zero-field-cooled and field-cooled magnetisation data collected in an applied field of 100 Oe. Inset shows fit to the Curie-Weiss law (left); Magnetisation data collected as a function of applied field (right) from $La_{1.2}Sr_{2.8}NiRuO_8$.

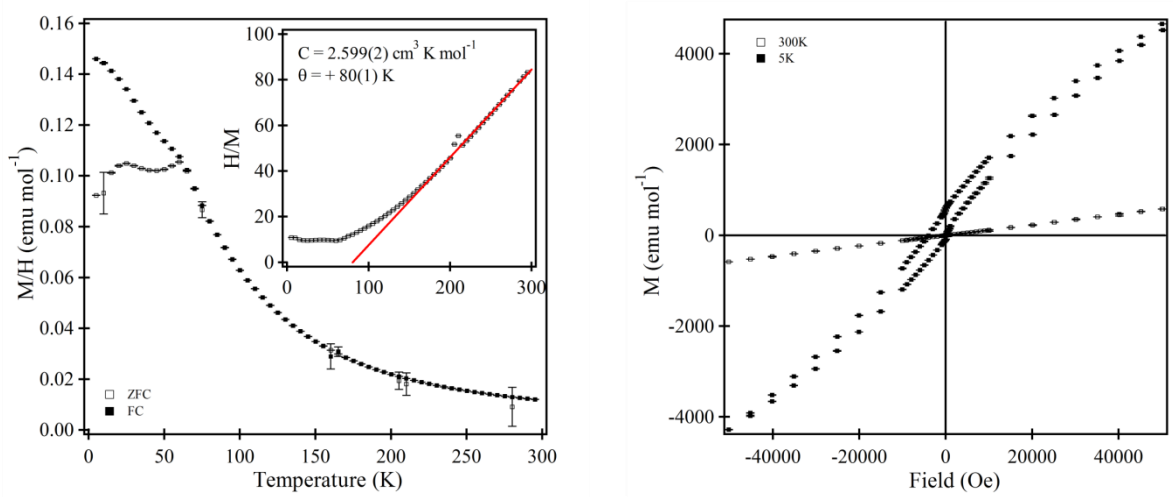


Figure 2.17. Zero-field-cooled and field-cooled magnetisation data collected in an applied field of 100 Oe. Inset shows fit to the Curie-Weiss law (left); Magnetisation data collected as a function of applied field (right) from $La_{1.3}Sr_{2.7}NiRuO_8$.

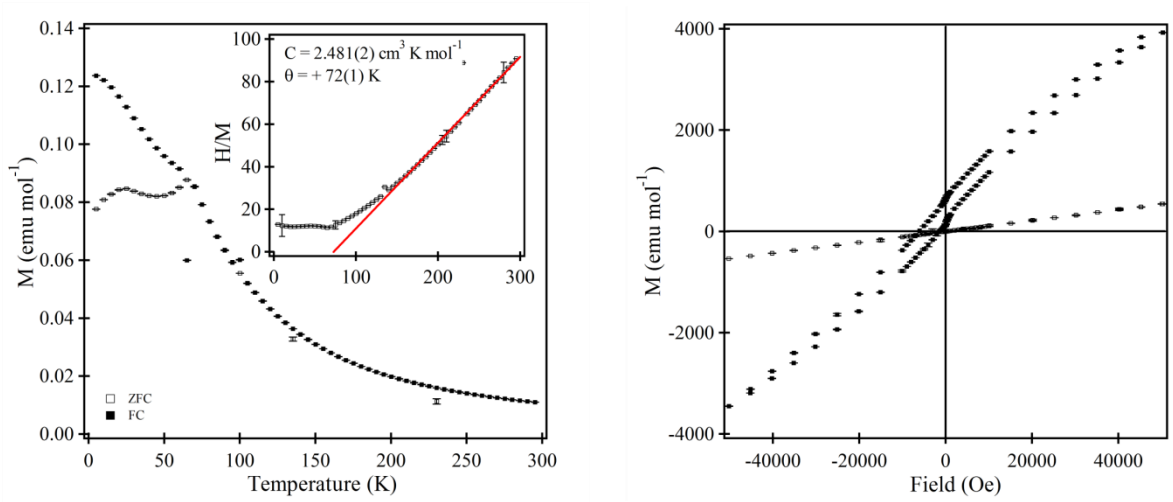


Figure 2.18. Zero-field-cooled and field-cooled magnetisation data collected in an applied field of 100 Oe. Inset shows fit to the Curie-Weiss law (left); Magnetisation data collected as a function of applied field (right) from $La_{1.4}Sr_{2.6}NiRuO_8$.

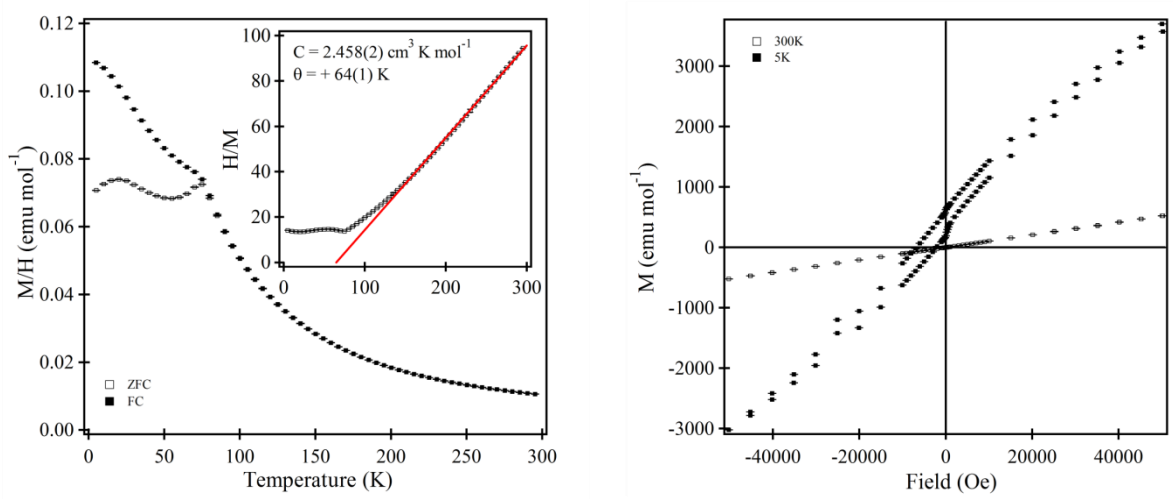


Figure 2.19. Zero-field-cooled and field-cooled magnetisation data collected in an applied field of 100 Oe. Inset shows fit to the Curie-Weiss law (left); Magnetisation data collected as a function of applied field (right) from $La_{1.5}Sr_{2.5}NiRuO_8$.

Appendix 2.3 Synchrotron X-ray diffraction data of $La_xSr_{4-x}NiRuO_4H_4$ ($0.5 \leq x \leq 1.5$)

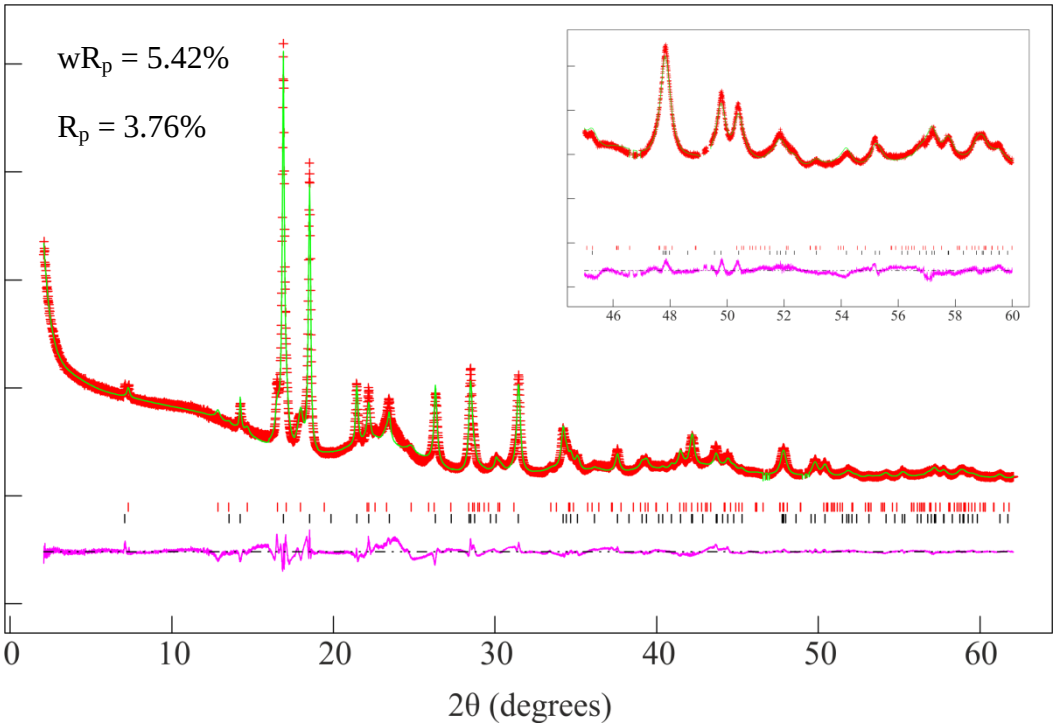


Figure 2.20. Rietveld refinement of synchrotron X-ray powder diffraction data collected from $La_{0.5}Sr_{3.5}NiRuO_4H_4$ against *I4/mmm* model. Observed (red), calculated (green), and difference plots (pink) are shown.

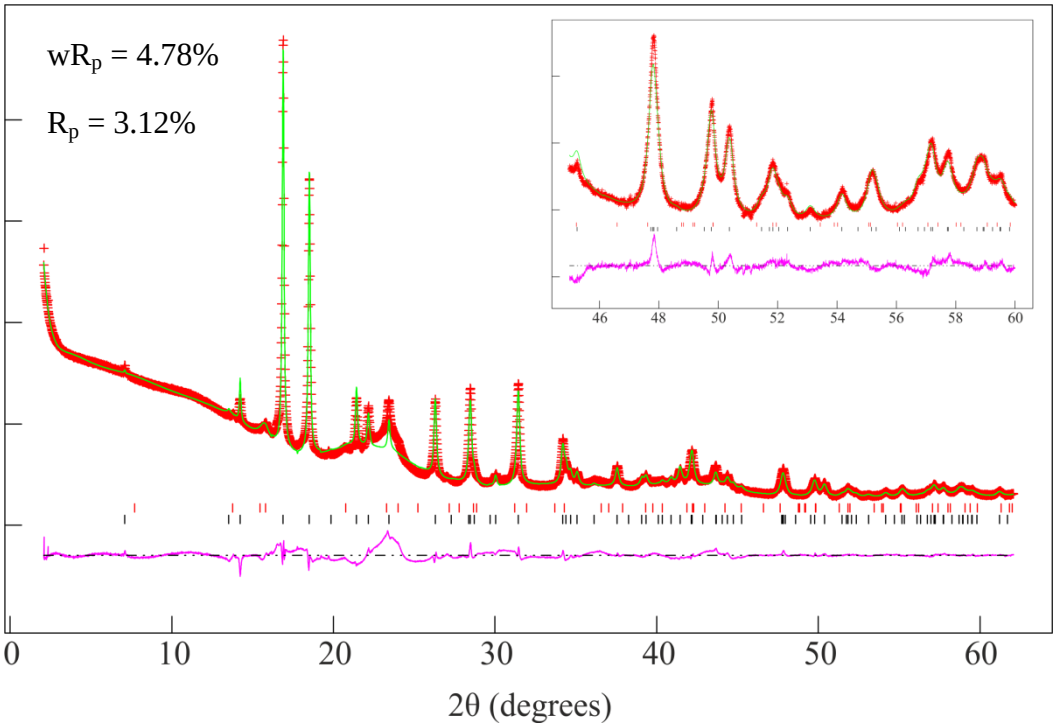


Figure 2.21. Rietveld refinement of synchrotron X-ray powder diffraction data collected from $La_{0.6}Sr_{3.4}NiRuO_4H_4$ against *I4/mmm* model. Observed (red), calculated (green), and difference plots (pink) are shown.

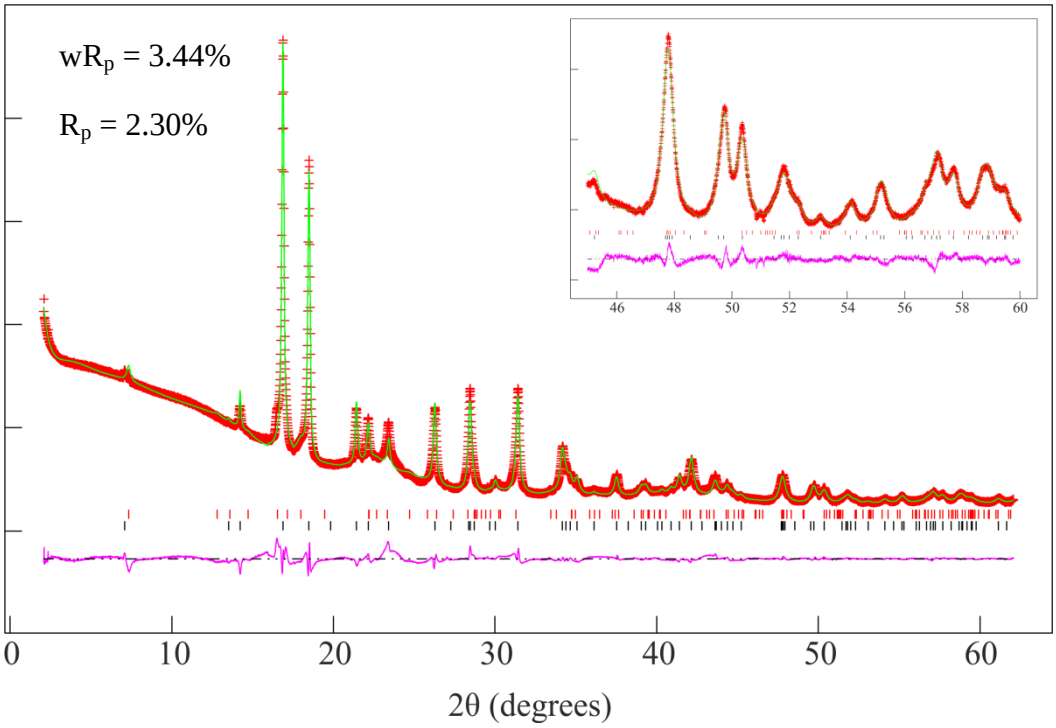


Figure 2.22. Rietveld refinement of synchrotron X-ray powder diffraction data collected from $La_{0.7}Sr_{3.3}NiRuO_4H_4$ against *I4/mmm* model. Observed (red), calculated (green), and difference plots (pink) are shown.

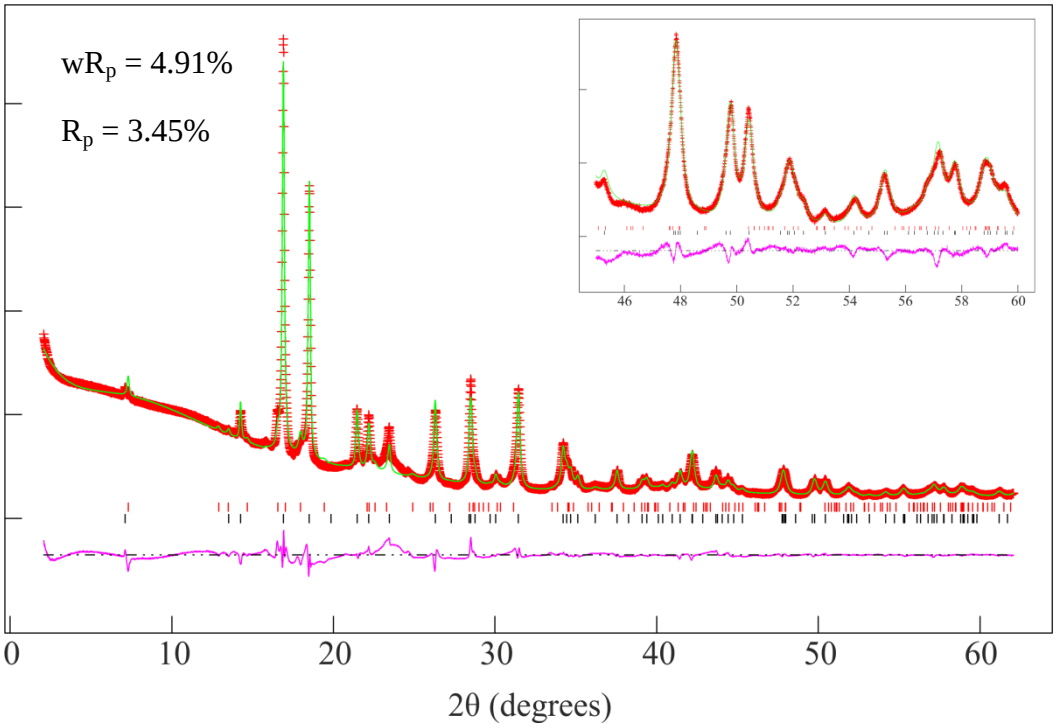


Figure 2.23. Rietveld refinement of synchrotron X-ray powder diffraction data collected from $La_{0.8}Sr_{3.2}NiRuO_4H_4$ against *I4/mmm* model. Observed (red), calculated (green), and difference plots (pink) are shown.

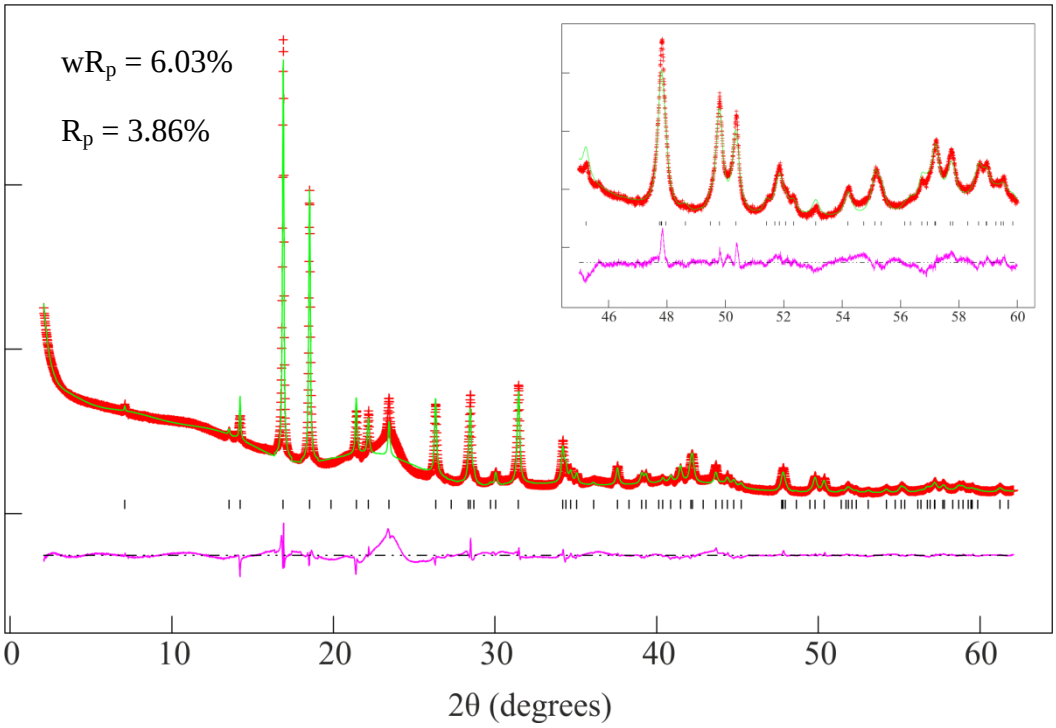


Figure 2.24. Rietveld refinement of synchrotron X-ray powder diffraction data collected from $La_{0.9}Sr_{3.1}NiRuO_4H_4$ against *I4/mmm* model. Observed (red), calculated (green), and difference plots (pink) are shown.

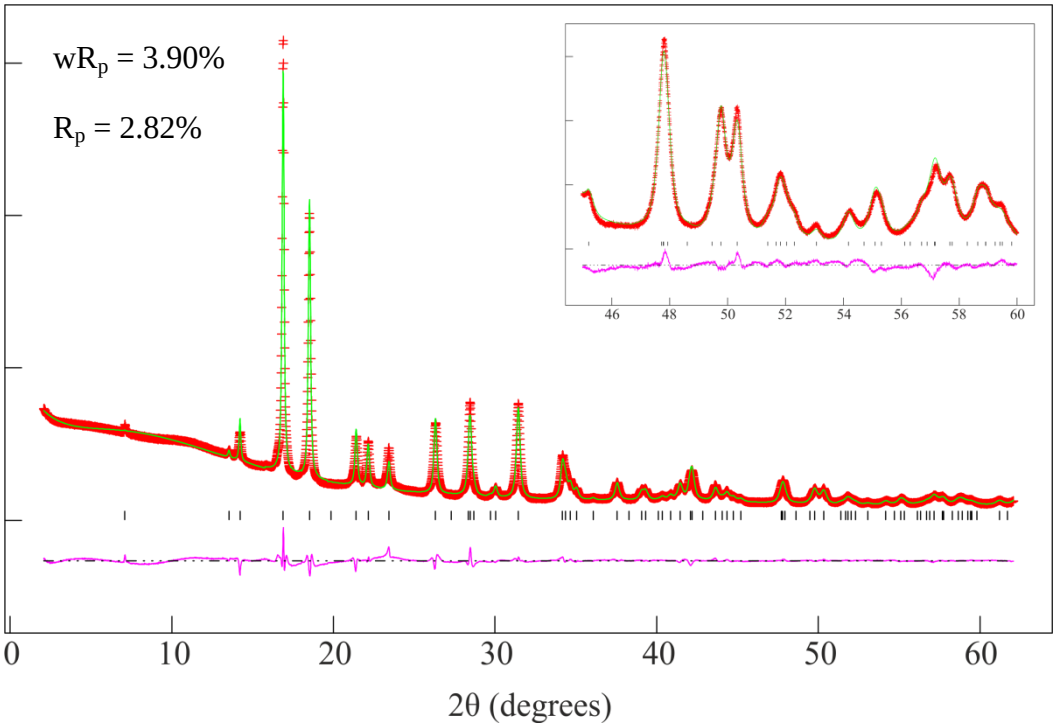


Figure 2.25. Rietveld refinement of synchrotron X-ray powder diffraction data collected from $La_{1.1}Sr_{2.9}NiRuO_4H_4$ against *I4/mmm* model. Observed (red), calculated (green), and difference plots (pink) are shown.

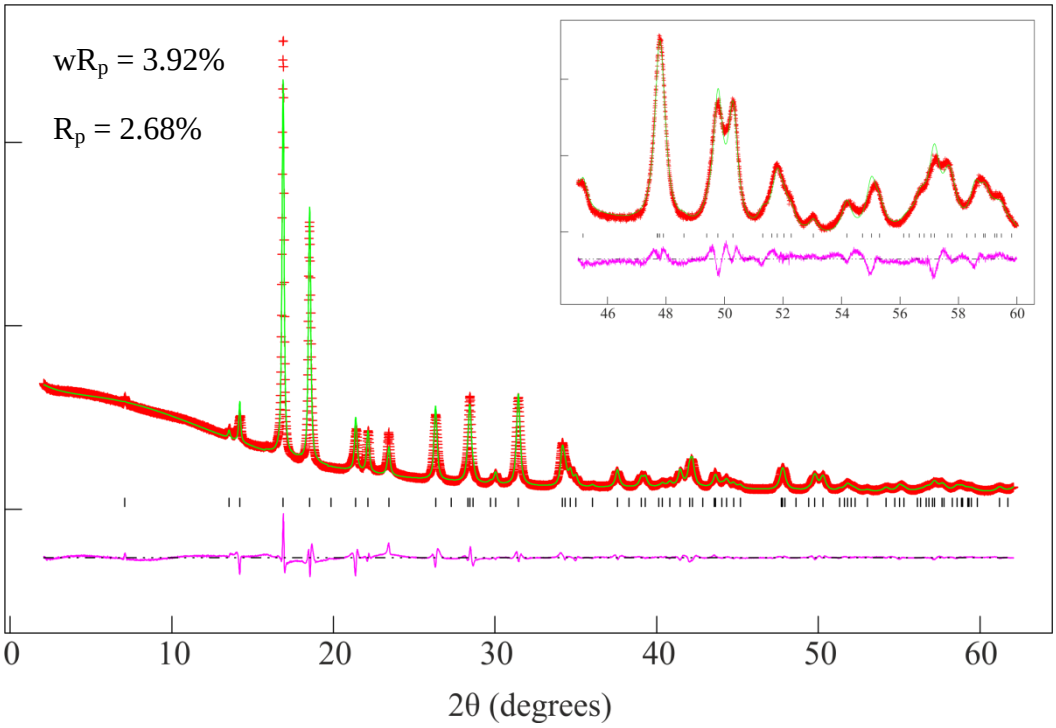


Figure 2.26. Rietveld refinement of synchrotron X-ray powder diffraction data collected from $La_{1.2}Sr_{2.8}NiRuO_4H_4$ against *I4/mmm* model. Observed (red), calculated (green), and difference plots (pink) are shown.

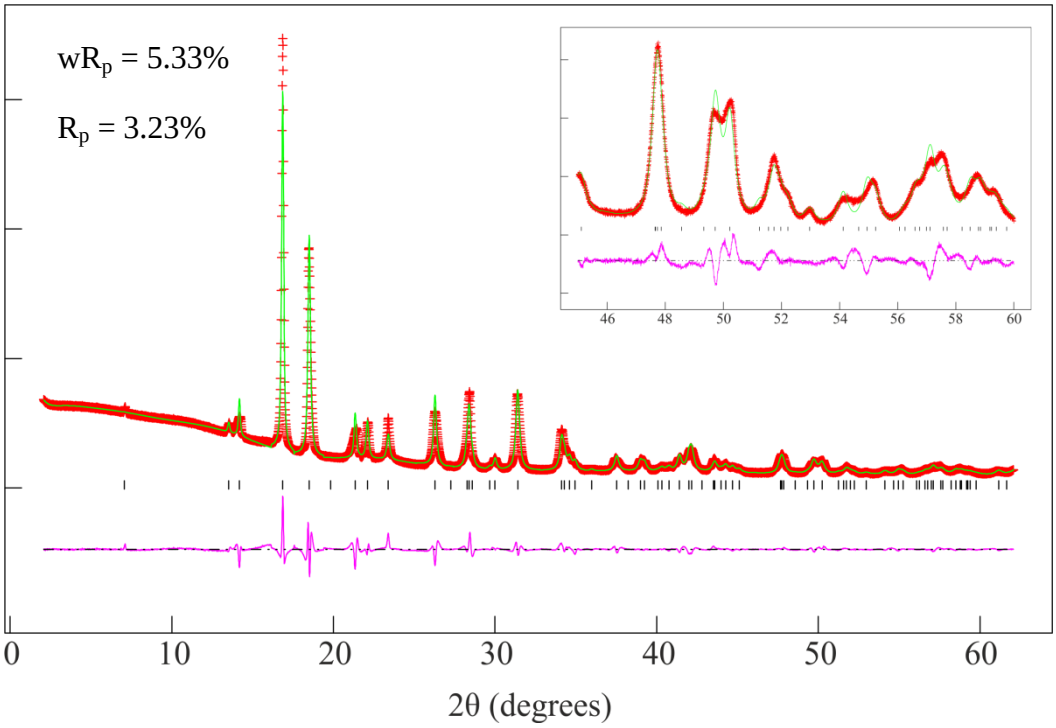


Figure 2.27. Rietveld refinement of synchrotron X-ray powder diffraction data collected from $La_{1.4}Sr_{2.6}NiRuO_4H_4$ against *I4/mmm* model. Observed (red), calculated (green), and difference plots (pink) are shown.

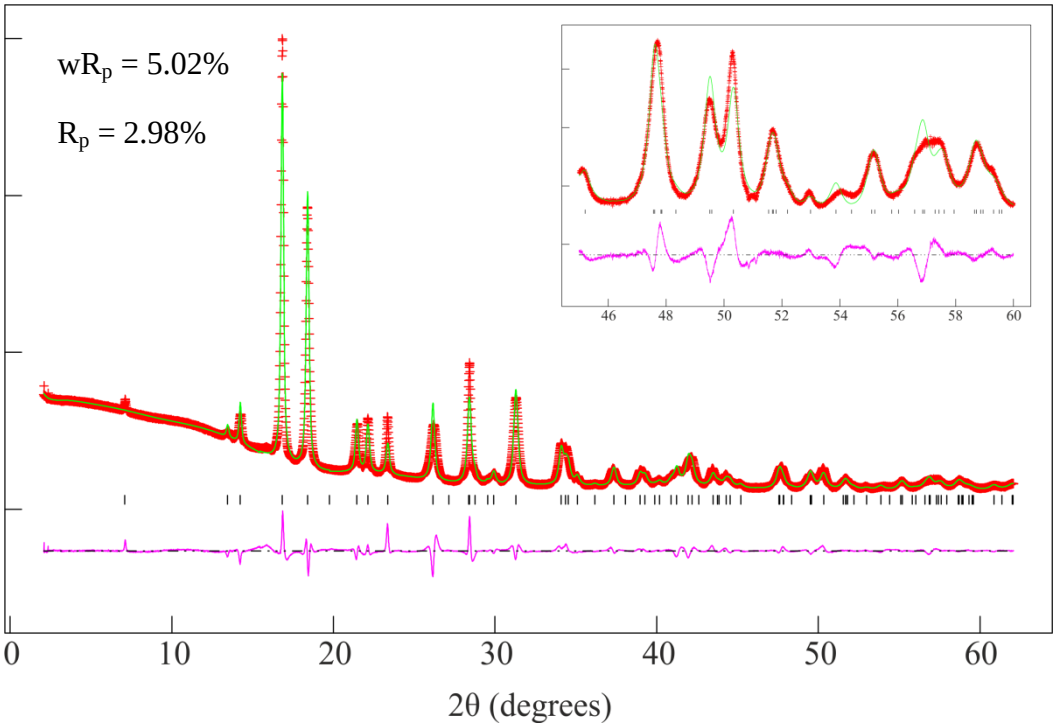


Figure 2.28. Rietveld refinement of synchrotron X-ray powder diffraction data collected from $La_{1.5}Sr_{2.5}NiRuO_4H_4$ against *I4/mmm* model. Observed (red), calculated (green), and difference plots (pink) are shown.

Appendix 2.4 Magnetisation data of $La_xSr_{4-x}NiRuO_4H_4$ ($0.5 \leq x \leq 1.5$)

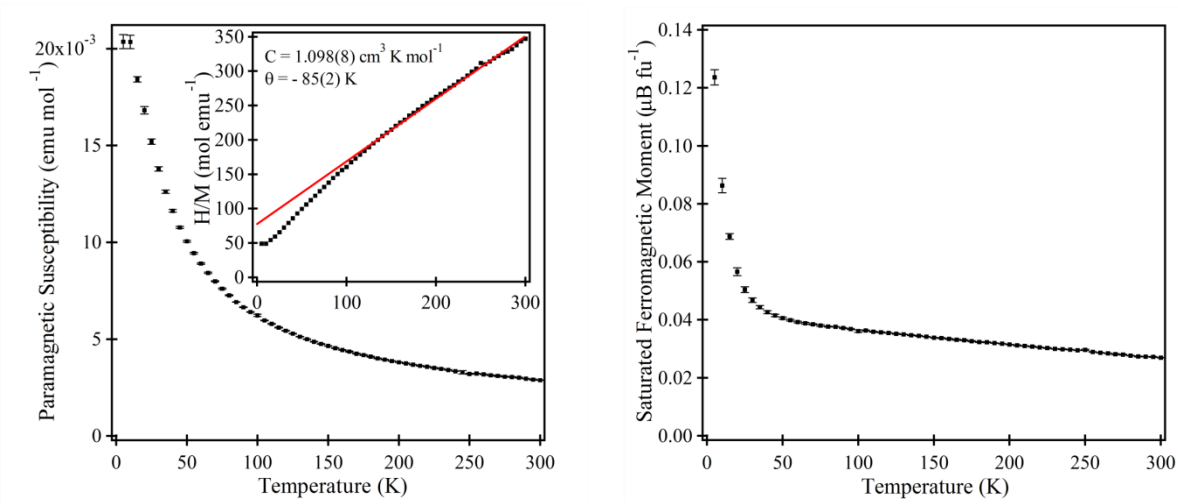


Figure 2.29. The paramagnetic susceptibility (left) and saturated ferromagnetic moment (right) of $La_{0.5}Sr_{3.5}NiRuO_4H_4$ collected as a function of temperature. Inset: the fit to the Curie–Weiss law in the temperature range $105 < T / K < 300$.

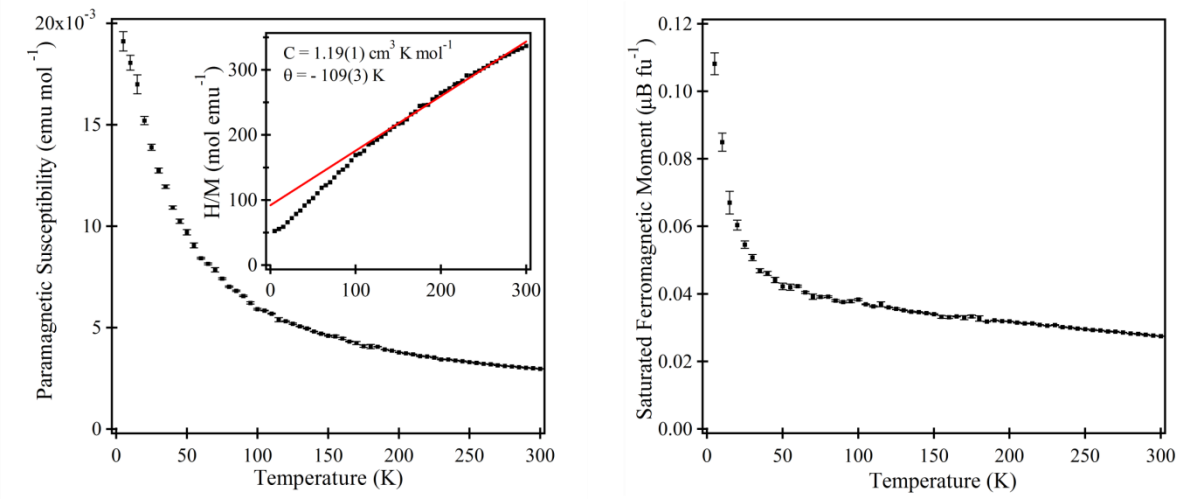


Figure 2.30. The paramagnetic susceptibility (left) and saturated ferromagnetic moment (right) of $La_{0.6}Sr_{3.4}NiRuO_4H_4$ collected as a function of temperature. Inset: the fit to the Curie–Weiss law in the temperature range $115 < T / K < 300$.

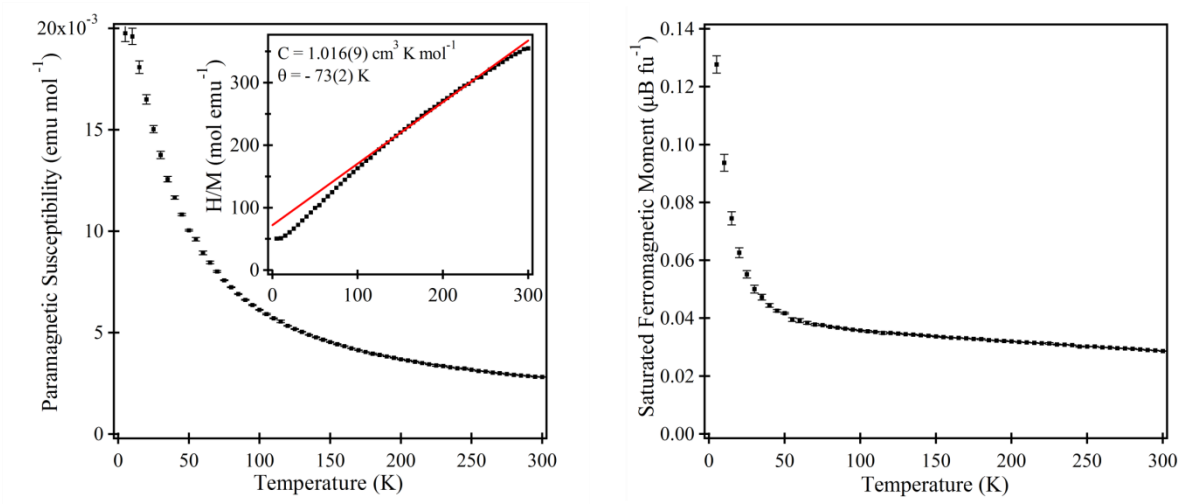


Figure 2.31. The paramagnetic susceptibility (left) and saturated ferromagnetic moment (right) of $La_{0.7}Sr_{3.3}NiRuO_4H_4$ collected as a function of temperature. Inset: the fit to the Curie–Weiss law in the temperature range 115 < *T* / K < 260.

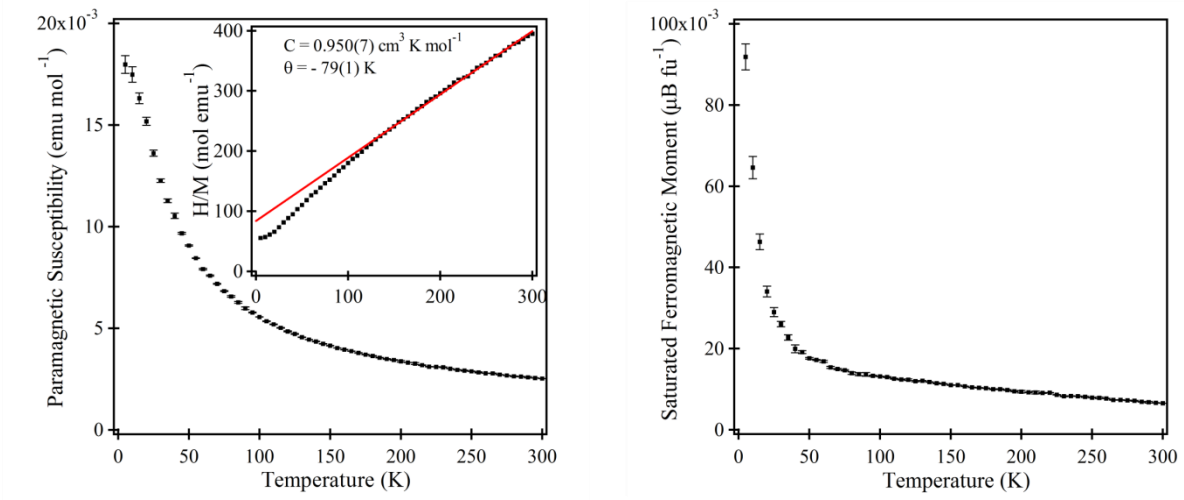


Figure 2.32. The paramagnetic susceptibility (left) and saturated ferromagnetic moment (right) of $La_{0.8}Sr_{3.2}NiRuO_4H_4$ collected as a function of temperature. Inset: the fit to the Curie–Weiss law in the temperature range 115 < *T* / K < 300.

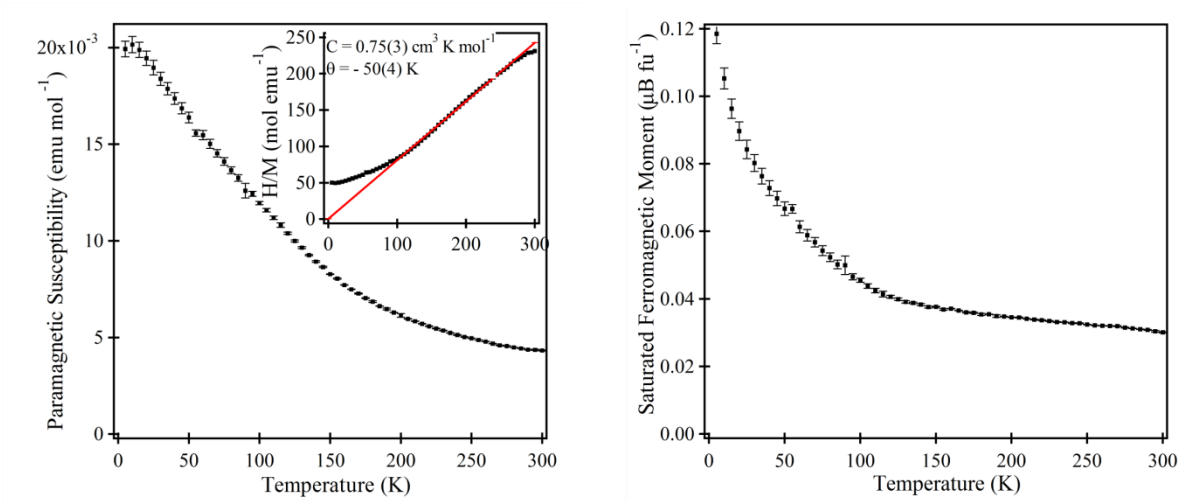


Figure 2.33. The paramagnetic susceptibility (left) and saturated ferromagnetic moment (right) of $La_{0.9}Sr_{3.1}NiRuO_4H_4$ collected as a function of temperature. Inset: the fit to the Curie–Weiss law in the temperature range 95 < *T* / K < 270.

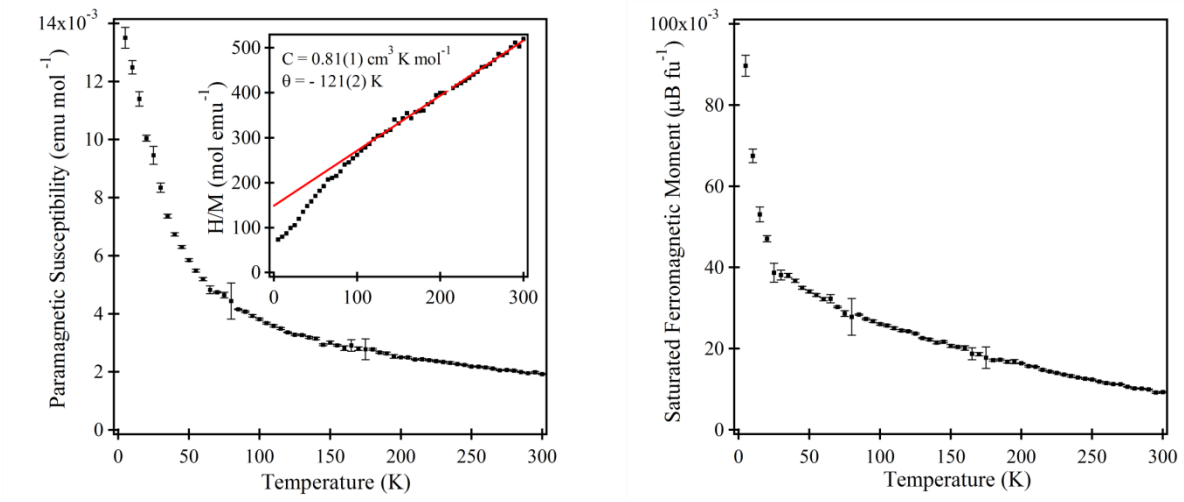


Figure 2.34. The paramagnetic susceptibility (left) and saturated ferromagnetic moment (right) of $La_{1.1}Sr_{2.9}NiRuO_4H_4$ collected as a function of temperature. Inset: the fit to the Curie–Weiss law in the temperature range 110 < *T* / K < 300.

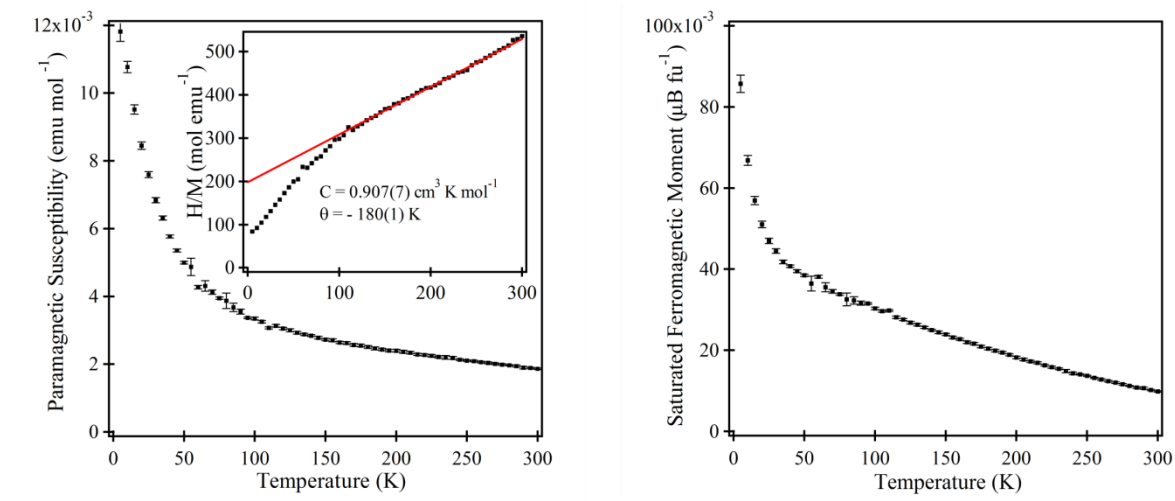


Figure 2.35. The paramagnetic susceptibility (left) and saturated ferromagnetic moment (right) of $La_{1.2}Sr_{2.8}NiRuO_4H_4$ collected as a function of temperature. Inset: the fit to the Curie–Weiss law in the temperature range 120 < *T* / K < 285.

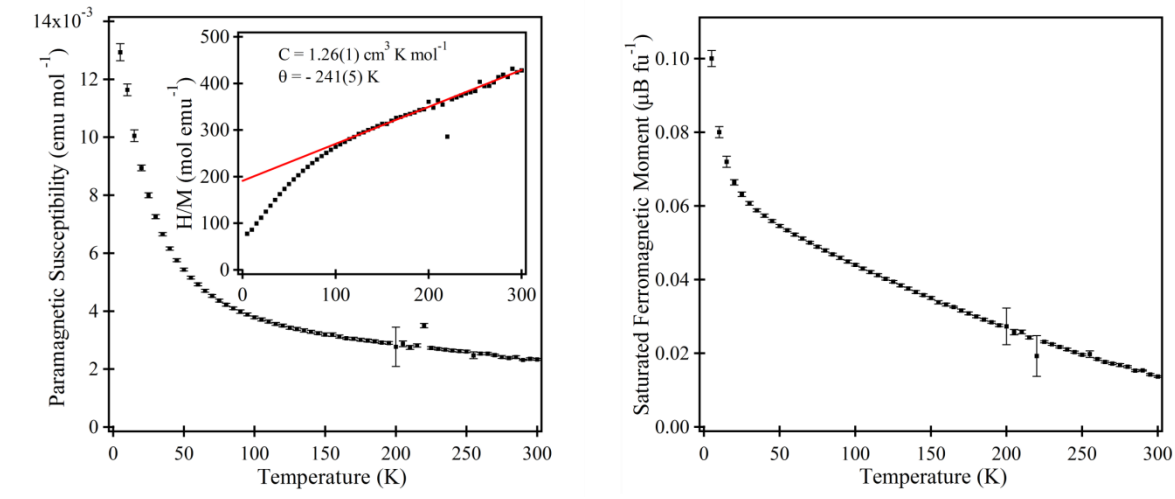


Figure 2.36. The paramagnetic susceptibility (left) and saturated ferromagnetic moment (right) of $La_{1.3}Sr_{2.7}NiRuO_4H_4$ collected as a function of temperature. Inset: the fit to the Curie–Weiss law in the temperature range 105 < *T* / K < 300.

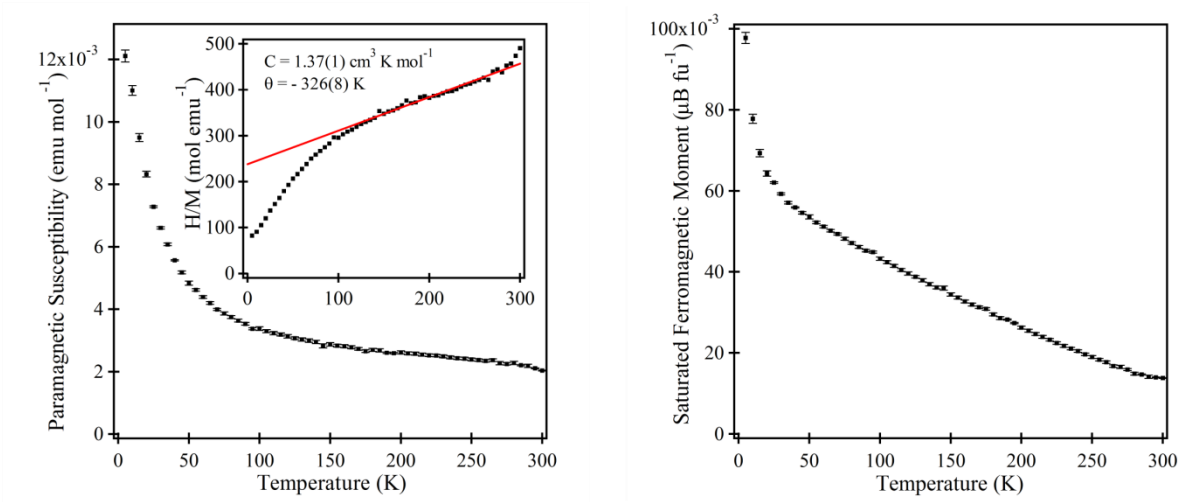


Figure 2.37. The paramagnetic susceptibility (left) and saturated ferromagnetic moment (right) of $La_{1.4}Sr_{2.6}NiRuO_4H_4$ collected as a function of temperature. Inset: the fit to the Curie–Weiss law in the temperature range 120 < *T* / K < 290.

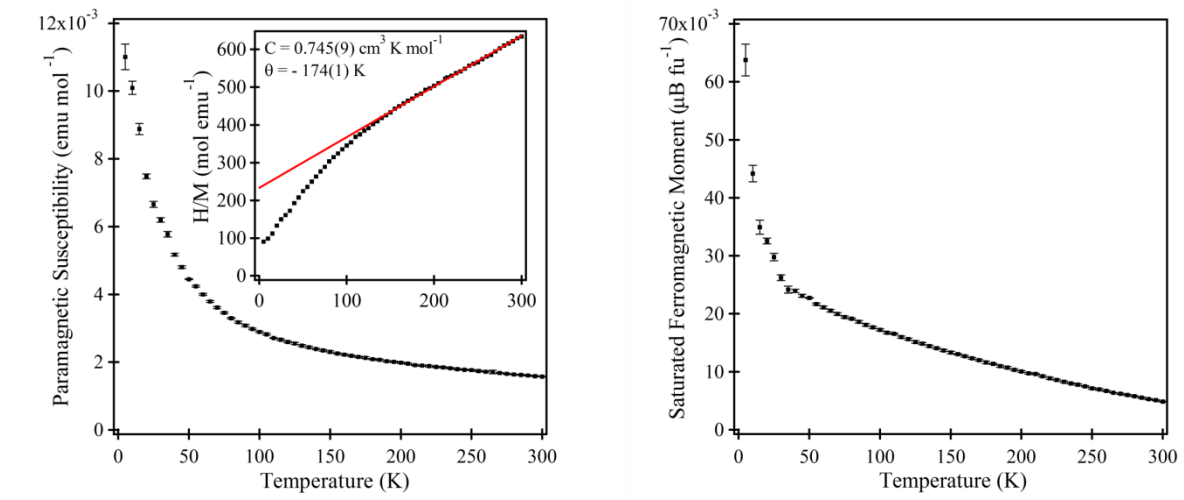


Figure 2.38. The paramagnetic susceptibility (left) and saturated ferromagnetic moment (right) of $La_{1.5}Sr_{2.5}NiRuO_4H_4$ collected as a function of temperature. Inset: the fit to the Curie–Weiss law in the temperature range 130 < *T* / K < 300.

Appendix 3 Bibliography

1. P. Schiffer, A. P. Ramirez, W. Bao and S. W. Cheong, *Physical Review Letters*, 1995, **75**, 3336-3339.
2. P. Lacorre, F. Goutenoire, O. Bohnke, R. Retoux and Y. Laligant, *Nature*, 2000, **404**, 856.
3. R. E. Cohen, *Nature*, 1992, **358**, 136.
4. J. G. Bednorz and K. A. Müller, *Zeitschrift für Physik B Condensed Matter*, 1986, **64**, 189-193.
5. R. Asahi, T. Morikawa, T. Ohwaki, K. Aoki and Y. Taga, *Science*, 2001, **293**, 269.
6. T. Ishihara, *Perovskite Oxide for Solid Oxide Fuel Cells*; Springer London, Limited, 2009.
7. M. Dawber, K. M. Rabe and J. F. Scott, *Reviews of Modern Physics*, 2005, **77**, 1083-1130.
8. M. A. Peña and J. L. G. Fierro, *Chemical Reviews*, 2001, **101**, 1981-2018.
9. J. E. Page, H. W. T. Morgan, D. Zeng, P. Manuel, J. E. McGrady and M. A. Hayward, *Inorganic Chemistry*, 2018, **57**, 13577-13585.
10. M. A. Patino, D. Zeng, R. Bower, J. E. McGrady and M. A. Hayward, *Inorganic Chemistry*, 2016, **55**, 9012-9016.
11. F. D. Romero, S. J. Burr, J. E. McGrady, D. Gianolio, G. Cibin and M. A. Hayward, *Journal of the American Chemical Society*, 2013, **135**, 1838-1844.
12. H. Yamashita, T. Broux, Y. Kobayashi, F. Takeiri, H. Ubukata, T. Zhu, M. A. Hayward, K. Fujii, M. Yashima, K. Shitara, A. Kuwabara, T. Murakami and H. Kageyama, *Journal of the American Chemical Society*, 2018, **140**, 11170-11173.
13. L. Jin, M. Lane, D. Zeng, F. K. K. Kirschner, F. Lang, P. Manuel, S. J. Blundell, J. E. McGrady and M. A. Hayward, *Angewandte Chemie International Edition*, 2018, **57**, 5025-5028.
14. F. D. Romero, A. Leach, J. S. Moller, F. Foronda, S. J. Blundell and M. A. Hayward, *Angewandte Chemie International Edition*, 2014, **53**, 7556-7559.
15. M. A. Hayward, E. J. Cussen, J. B. Claridge, M. Bieringer, M. J. Rosseinsky, C. J. Kiely, S. J. Blundell, I. M. Marshall, F. L. Pratt, *Science*, 2002, **295**, 1882-1884.
16. R. Zhang, G. Read, F. Lang, T. Lancaster, S. J. Blundell and M. A. Hayward, *Inorganic Chemistry*, 2016, **55**, 3169-3174.
17. H. Kageyama, K. Hayashi, K. Maeda, J. P. Attfield, Z. Hiroi, J. M. Rondinelli and K. R. Poeppelmeier, *Nature Communications*, 2018, **9**, 772.
18. M. A. Hayward, M. A. Green, M. J. Rosseinsky and J. Sloan, *Journal of the American Chemical Society*, 1999, **121**, 8843-8854.
19. M. A. Hayward and M. J. Rosseinsky, *Chemistry of Materials*, 2000, **12**, 2182-2195.
20. J. Seddon, E. Suard and M. A. Hayward, *Journal of the American Chemical Society*, 2010, **132**, 2802-2810.
21. E. Dixon, J. Hadermann, S. Ramos, A. L. Goodwin and M. A. Hayward, *Journal of the American Chemical Society*, 2011, **133**, 18397-18405.
22. E. Dixon and M. A. Hayward, *Inorganic Chemistry*, 2010, **49**, 9649-9654.

23. F. D. Romero, D. Gianolio, G. Cibin, P. A. Bingham, J. C. d'Hollander, S. D. Forder and M. A. Hayward, *Inorganic Chemistry*, 2013, **52**, 10920-10928.
24. J. A. Alonso and M. J. Martínez-Lope, *Dalton Transactions*, 1995, **17**, 2819-2824.
25. N. Hasanli, N. Gauquelin, J. Verbeeck, J. Hadermann and M. A. Hayward, *Dalton Transactions*, 2018, **47**, 15783-15790.
26. A. Perejon and M. A. Hayward, *Dalton Transactions*, 2015, **44**, 10636-10643.
27. O. H. Hansteen, H. Fjellvåg and B. C. Hauback, *Journal of Materials Chemistry*, 1998, **8**, 2081-2088.
28. T. Moriga, O. Usaka, I. Nakabayashi, T. Kinouchi, S. Kikkawa and F. Kanamaru, *Solid State Ionics*, 1995, **79**, 252-255.
29. C. C. K. Chiang and K. R. Poeppelmeier, *Materials Letters*, 1991, **12**, 102-108.
30. J. B. Goodenough and J. S. Zhou, *Chemistry of Materials*, 1998, **10**, 2980-2993.
31. V. M. Goldschmidt, *Naturwissenschaften*, 1926, **14**, 477-485.
32. Y. A. Abramov, V. G. Tsirelson, V. E. Zavodnik, S. A. Ivanov and I. D. Brown, *Acta Crystallographica Section B*, 1995, **51**, 942-951.
33. R. H. Buttner and E. N. Maslen, *Acta Crystallographica Section B*, 1992, **48**, 644-649.
34. H. D. Megaw and C. N. W. Darlington, *Acta Crystallographica Section A*, 1975, **31**, 161-173.
35. B. Morosin, R. J. Baughman, D. S. Ginley and M. A. Butler, *Journal of Applied Crystallography*, 1978, **11**, 121-124.
36. Y. Takeda, F. Kanamura, M. Shimada and M. Koizumi, *Acta Crystallographica Section B*, 1976, **32**, 2464-2466.
37. P. D. Battle, J. E. Millburn, M. J. Rosseinsky, L. E. Spring, J. F. Vente and P. G. Radaelli, *Chemistry of Materials*, 1997, **9**, 3136-3143.
38. J. Meng, H. Satoh, M. Ishida and N. Kamegashira, *Journal of Alloys and Compounds*, 2006, **408-412**, 1182-1186.
39. G. Bouilly, T. Yajima, T. Terashima, W. Yoshimune, K. Nakano, C. Tassel, Y. Kususe, K. Fujita, K. Tanaka, T. Yamamoto, Y. Kobayashi and H. Kageyama, *Chemistry of Materials*, 2015, **27**, 6354-6359.
40. T. Yajima, A. Kitada, Y. Kobayashi, T. Sakaguchi, G. Bouilly, S. Kasahara, T. Terashima, M. Takano and H. Kageyama, *Journal of the American Chemical Society*, 2012, **134**, 8782-8785.
41. C. Tassel, Y. Goto, Y. Kuno, J. Hester, M. Green, Y. Kobayashi and H. Kageyama, *Angewandte Chemie International Edition*, 2014, **53**, 10377-10380.
42. T. Yamamoto, D. Zeng, T. Kawakami, V. Arcisauskaite, K. Yata, M. A. Patino, N. Izumo, J. E. McGrady, H. Kageyama and M. A. Hayward, *Nature Communications*, 2017, **8**, 1217.
43. Y. Kobayashi, O. J. Hernandez, T. Sakaguchi, T. Yajima, T. Roisnel, Y. Tsujimoto, M. Morita, Y. Noda, Y. Mogami, A. Kitada, M. Ohkura, S. Hosokawa, Z. Li, K. Hayashi, Y. Kusano, J. Kim, N. Tsuji, A. Fujiwara, Y. Matsushita, K. Yoshimura, K. Takegoshi, M. Inoue, M. Takano and H. Kageyama, *Nature Materials*, 2012, **11**, 507-511.
44. R. M. Helps, N. H. Rees and M. A. Hayward, *Inorganic Chemistry*, 2010, **49**, 11062-11068.

45. C. A. Bridges, G. R. Darling, M. A. Hayward and M. J. Rosseinsky, *Journal of the American Chemical Society*, 2005, **127**, 5996-6011.
46. Y. Liu, D. Duan, F. Tian, C. Wang, Y. Ma, D. Li, X. Huang, B. Liu and T. Cui, *Physical Chemistry Chemical Physics*, 2016, **18**, 1516-1520.
47. B. Li, Y. Ding, D. Y. Kim, R. Ahuja, G. Zou and H.-K. Mao, *Proceedings of the National Academy of Sciences*, 2011, **108**, 18618.
48. P. A. Cox, *The Electronic Structure and Chemistry of Solids*, Oxford University Press, 1987.
49. P. A. Cox, *Transition Metal Oxides: An Introduction to Their Electronic Structure and Properties*, Oxford University Press, 2010.
50. R. J. Cava, *Dalton Transactions*, 2004, **19**, 2979-2987.
51. Y. Maeno, T. M. Rice and M. Sigrist, *Physics Today*, 2001, **54**, 42-47.
52. Q. Huang, J. L. Soubeyroux, O. Chmaissem, I. N. Sora, A. Santoro, R. J. Cava, J. J. Krajewski and W. F. Peck, *Journal of Solid State Chemistry*, 1994, **112**, 355-361.
53. S. Nakatsuji and Y. Maeno, *Physical Review Letters*, 2000, **84**, 2666-2669.
54. G. Cao, J. Bolivar, S. McCall, J. E. Crow and R. P. Guertin, *Physical Review B*, 1998, **57**, R11039-R11042.
55. R. J. Cava, B. Batlogg, K. Kiyono, H. Takagi, J. J. Krajewski, W. F. Peck, L. W. Rupp and C. H. Chen, *Physical Review B*, 1994, **49**, 11890-11894.
56. F. D. Romero, *Topochemical Synthesis of Novel Electronic Materials*, DPhil thesis, 2013.
57. M. P. Pechini, *US Patent*, 1967.
58. J. J. Adkin and M. A. Hayward, *Inorganic Chemistry*, 2008, **47**, 10959-10964.
59. M. O'Malley, M. A. Lockett and M. A. Hayward, *Journal of Solid State Chemistry*, 2007, **180**, 2851-2858.
60. A. J. Blake, J. Evans and W. Clegg, *Crystal Structure Analysis: Principles and Practice*, Oxford Science Publications, 2001.
61. E. J. W. Whittaker, *Crystallography*, Pergamon, 1981.
62. S. P. Thompson, J. E. Parker, J. Potter, T. P. Hill, A. Birt, T. M. Cobb, F. Yuan and C. C. Tang, *Review of Scientific Instruments*, 2009, **80**, 075107.
63. V. F. Sears, *Neutron News*, 1992, **3**, 26-37.
64. H. Ekstein, *Physical Review*, 1950, **78**, 731-732.
65. J. Rodríguez-Carvajal, *Physica B: Condensed Matter*, 1993, **192**, 55-69.
66. *https://wwwilleu/about/what-is-the-ill/*.
67. *http://wwwisisstfcacuk/about/aboutisishtml*.
68. L. C. Chapon, P. Manuel, P. G. Radaelli, C. Benson, L. Perrott, S. Ansell, N. J. Rhodes, D. Raspino, D. Duxbury, E. Spill and J. Norris, *Neutron News*, 2011, **22**, 22-25.
69. D. Bagayoko and J. Callaway, *Physical Review B*, 1983, **28**, 5419-5422.
70. A. C. Larson and R. B. Von Dreele, *General Structure Analysis System*, Los Alamos National Laboratory Report LAUR 86-748 (2004).
71. H. Rietveld, *Journal of Applied Crystallography*, 1969, **2**, 65-71.
72. N. E. Brese and M. O'Keeffe, *Acta Crystallographica Section B*, 1991, **47**, 192-197.
73. I. D. Brown and D. Altermatt, *Acta Crystallographica Section B*, 1985, **41**, 244-247.

74. *https://wwwpsich/science/facilities-and-instruments*.
75. J. Clarke, *Scientific American*, 1994, **271**.
76. J. Bardeen, L. N. Cooper and J. R. Schrieffer, *Physical Review*, 1957, **108**, 1175-1204.
77. J. B. Goodenough, *Magnetism and the chemical bond*, Wiley, 1963.
78. P. W. Anderson, *Physical Review*, 1950, **79**, 350-356.
79. M. M. J. Treacy, J. M. Newsam and M. W. Deem, *Proceedings of the Royal Society of London. Series A: Mathematical and Physical Sciences*, 1991, **433**, 499-520.
80. *http://www.public.asu.edu/~mtreacy/DIFFaX.html*.
81. http://www.iucr.org/iucr-top/comm/ccom/newsletters/.
82. *http://forge.epn-campus.eu/projects/crysfml/repository/*.
83. M. Casas-Cabanas, M. Reynaud, J. Rikarte, P. Horbach and J. Rodriguez-Carvajal, *Journal of Applied Crystallography*, 2016, **49**, 2259-2269.
84. C. N. R. Rao, B. Raveau, *Transition Metal Oxides: Structure, Properties, and Synthesis of Ceramic Oxides, 2nd Edition*, Wiley, 1998.
85. J. Kanamori, *Journal of Physics and Chemistry of Solids*, 1959, **10**, 87-98.
86. R. Bower, *Reduction of Some Ruthenium Containing Mixed Perovskites*, Part II thesis, 2014.
87. G. King and P. M. Woodward, *Journal of Materials Chemistry*, 2010, **20**, 5785-5796.
88. M. Lane, *The Anion Chemistry of Some Ruthenium Containing Ruddlesden-Popper Oxide Phases*, Part II thesis, 2016.
89. M. A. Hayward, *Semiconductor Science and Technology*, 2014, **29**, 064010.
90. J. Zaanen, G. A. Sawatzky and J. W. Allen, *Physical Review Letters*, 1985, **55**, 418-421.
91. S. W. Cheong, J. D. Thompson and Z. Fisk, *Physica C: Superconductivity*, 1989, **158**, 109-126.
92. H. Romberg, M. Alexander, N. Nücker, P. Adelmann and J. Fink, *Physical Review B*, 1990, **42**, 8768-8771.
93. A. S. Group, *http://abulafia.mt.ic.ac.uk/shannon/ptable.php*.
94. F. Green, *The influence of doping on the chemistry and properties of $LaSrNiRuO_4$*, Part II thesis, 2017.
95. T. Yamamoto, H. Ohkubo, C. Tassel, N. Hayashi, S. Kawasaki, T. Okada, T. Yagi, J. Hester, M. Avdeev, Y. Kobayashi and H. Kageyama, *Inorganic Chemistry*, 2016, **55**, 12093-12099.
96. M. Amano Patino, D. Zeng, S. J. Blundell, J. E. McGrady and M. A. Hayward, *Inorganic Chemistry*, 2018, **57**, 2890-2898.
97. E. O. Wollan and W. C. Koehler, *Physical Review*, 1955, **100**, 545-563.
98. K. R. Poeppelmeier, M. E. Leonowicz and J. M. Longo, *Journal of Solid State Chemistry*, 1982, **44**, 89-98.
99. Y. Tokura, *Colossal Magnetoresistive Oxides*, Gordon and Breach Science Publishers, 2000.
100. M. A. Hayward, *Chemistry of Materials*, 2005, **17**, 670-675.
101. J. Li, A. E. Smith, K.-S. Kwong, C. Powell, A. W. Sleight and M. A. Subramanian, *Journal of Solid State Chemistry*, 2010, **183**, 1388-1393.

102. K. Knížek, J. Hejtmánek, M. Maryško, Z. Jirák and J. Buršík, *Physical Review B*, 2012, **85**, 134401.
103. H. Guo, K. Manna, H. Luetkens, M. Hoelzel and A. C. Komarek, *Physical Review B*, 2016, **94**, 205128.
104. D. J. Gallon, P. D. Battle, S. J. Blundell, A. I. Coldea, M. J. Rosseinsky and C. Steer, *Journal of Materials Chemistry*, 2003, **13**, 1166-1172.
105. A. E. Smith, A. W. Sleight and M. A. Subramanian, *Materials Research Bulletin*, 2010, **45**, 460-463.
106. M. T. Haque, H. Satoh and N. Kamegashira, *Journal of Alloys and Compounds*, 2005, **390**, 115-121.
107. S. Asai, N. Furuta, Y. Yasui and I. Terasaki, *Journal of the Physical Society of Japan*, 2011, **80**, 104705.
108. L. Awin, B. J. Kennedy and M. Avdeev, *Ceramics International*, 2013, **39**, S233-S237.
109. M. Nakamura, Y. Krockenberger, J. Fujioka, M. Kawasaki and Y. Tokura, *Applied Physics Letters*, 2015, **106**, 072103.
110. S. V. Streltsov, V. V. Gapontsev and D. I. Khomskii, *Journal of Physics Condensed Matter*, 2016, **28**, 086005-086010.
111. Y. Kobayashi, O. Hernandez, C. Tassel and H. Kageyama, *Science and Technology of Advanced Materials*, 2017, **18**, 905-918.
112. H. J. Kitchen, I. Saratovsky and M. A. Hayward, *Dalton Transactions*, 2010, **39**, 6098-6105.
113. B. C. Hernden, J. A. Lussier and M. Bieringer, *Inorganic Chemistry*, 2015, **54**, 4249-4256.
114. C. Tassel, Y. Goto, D. Watabe, Y. Tang, H. Lu, Y. Kuno, F. Takeiri, T. Yamamoto, C. M. Brown, J. Hester, Y. Kobayashi and H. Kageyama, *Angewandte Chemie International Edition*, 2016, **55**, 9667-9670.